COPPE
Instituto Alberto Luiz Coimbra de Pós-Graduação e Pesquisa de Engenharia
UFRJ

MICROMILLING OF TITANIUM ALLOYS: A COMPARISON BETWEEN WORKPIECES PRODUCED BY CASTING, ECAP AND 3D PRINTING (SLM)

Fábio de Oliveira Campos

Tese de Doutorado apresentada ao Programa de Pós-graduação em Engenharia Mecânica, COPPE, da Universidade Federal do Rio de Janeiro, como parte dos requisitos necessários à obtenção do título de Doutor em Engenharia Mecânica.

Orientador: Anna Carla Monteiro de Araujo

Rio de Janeiro
Fevereiro de 2018

MICROMILLING OF TITANIUM ALLOYS: A COMPARISON BETWEEN WORKPIECES PRODUCED BY CASTING, ECAP AND 3D PRINTING (SLM)

Fábio de Oliveira Campos

TESE SUBMETIDA AO CORPO DOCENTE DO INSTITUTO ALBERTO LUIZ COIMBRA DE PÓS-GRADUAÇÃO E PESQUISA DE ENGENHARIA (COPPE) DA UNIVERSIDADE FEDERAL DO RIO DE JANEIRO COMO PARTE DOS REQUISITOS NECESSÁRIOS PARA A OBTENÇÃO DO GRAU DE DOUTOR EM CIÊNCIAS EM ENGENHARIA MECÂNICA.

Examinada por:

Prof. Anna Carla Monteiro de Araujo, D.Sc.

Prof. Marcelo Amorim Savi, D.Sc.

Prof. Juan Carlos Garcia de Blas, D.Sc.

Prof. Márcio Bacci da Silva, D.Sc.

Prof. Shiv Gopal Kapoor, Ph.D.

RIO DE JANEIRO, RJ – BRASIL
FEVEREIRO DE 2018

Campos, Fábio de Oliveira

Micromilling of titanium alloys: a comparison between workpieces produced by casting, ECAP and 3D printing (SLM)/Fábio de Oliveira Campos. – Rio de Janeiro: UFRJ/COPPE, 2018.

XVIII, 166 p.: il.; 29, 7cm.

Orientador: Anna Carla Monteiro de Araujo

Tese (doutorado) – UFRJ/COPPE/Programa de Engenharia Mecânica, 2018.

Referências Bibliográficas: p. 136 – 152.

1. Micromilling. 2. Titanium. 3. Machinability. I. Araujo, Anna Carla Monteiro de. II. Universidade Federal do Rio de Janeiro, COPPE, Programa de Engenharia Mecânica. III. Título.

À minha mãe, meu pai e meus irmãos.

"Llevamos un mundo nuevo en nuestros corazones."

Aknowledgements

First, I want to thank my family, parents and brothers, for the endless support and inspiration throughout my entire life. It would probably be unlikely for me to get here without it. I love you all.

Also, I want to thank my partner, Monique, that has been by my side through my Masters, stood with me even while I was doing my exchange program and never gave up on me. I love you.

I must thank my eternal professor, Anna Carla. For presenting me the Manufacturing world on my first semester at college, for welcoming me when I first looked for scientific initiation, for the orientations, the lessons, the sermons when I needed and for being such an unique professor in the academic world.

I thank the CEFCON (COPPE) technicians, Robson from the Laboratory of Material Properties (COPPE) and Laércio from the Laboratoy of Mechanical Processing of Biomaterials (COPPE) for the prompt help every time I needed. I also thank Prof. Carolina Cotta, head of the Laboratory of Nano and Microfluidics and Microsystems (COPPE) for promptly making available the digital microscope.

I thank Prof. Andre Jardini from the University of Campinas for providing the Selective Laser Melting samples and Prof. Juan Blas, from the Metallurgical and Materials Department of the Federal University of Rio de Janeiro, for providing the equal channel angular pressing samples and the support through all the research. I also thank the students Felipe Conde and Arthur Wilson for helping me with practical needs.

I also thank Prof. Shiv Kapoor for welcoming in the University of Illinois at Urbana-Champaign for six months, for the thoughts and comments that certainly helped the development of the work.

Finally, I thank my brothers and sisters of social struggle.

Resumo da Tese apresentada à COPPE/UFRJ como parte dos requisitos necessários para a obtenção do grau de Doutor em Ciências (D.Sc.)

FRESAMENTO DE LIGAS DE TITÂNIO: UMA COMPARAÇÃO ENTRE PEÇAS FABRICADAS POR FUNDIÇÃO, ECAP E IMPRESSÃO 3D (SLM)

Fábio de Oliveira Campos

Fevereiro/2018

Orientador: Anna Carla Monteiro de Araujo

Programa: Engenharia Mecânica

Propriedades como boa resistência à corrosão e biocompatibilidade assim como uma resistência mecânica satisfatória fazem do titânio e suas ligas um ótimo candidato para aplicação na indústria médica. Titânio comercialmente puro (CP-Ti) é o material metálico ideal para o uso na fabricação de implantes dentários já que a adição de elementos de liga pode alterar sua biocompatibilidade. Porém, CP-Ti apresenta limitações em suas propriedades mecânica para aplicação em certos implantes. A liga Ti-6Al-4V é a liga de titânio mais comumente usada em implantes biomédicos. Usinagem é um dos principais processos de fabricação envolvidos na fabricação de implantes e microfresamento e um dos processos que podem ser utilizados. A proposta desta tese é analisar e comparar a usinabilidade no microfresamento de quatro materiais diferentes baseados em titânio: titânio comercialmente puro convencional, Ti-6Al-4V convencional, CP-Ti processado por extrusão por canal angular (ECAP) e Ti-6Al-4V produzida por fusão seletiva a laser (SLM). A usinabilidade foi analisada considerando forças de corte, rugosidade de superfície, formação de rebarbas e morfologia dos cavacos. As propriedades mecânicas dos materiais também foram analisadas assim como sua influência nos fatores. Foi realizado um planejamento de experimentos variando o avanço por dente de 0,5 a 4,0 μm para que uma possível região de *ploughing* fosse identificada. Apesar de apresentar resistência e dureza maiores, o material produzido por SLM apresentou a melhor usinabilidade entre os materiais. Obteve melhores rugosidades de superfície, melhor formação de rebarba, um bom comportamento do cavaco e as forças de corte foram maiores apenas que o CP-Ti, que apresenta os piores valores de resistência mecânica.

Abstract of Thesis presented to COPPE/UFRJ as a partial fulfillment of the requirements for the degree of Doctor of Science (D.Sc.)

MICROMILLING OF TITANIUM ALLOYS: A COMPARISON BETWEEN WORKPIECES PRODUCED BY CASTING, ECAP AND 3D PRINTING (SLM)

Fábio de Oliveira Campos

February/2018

Advisor: Anna Carla Monteiro de Araujo

Department: Mechanical Engineering

Properties like good corrosion resistance and biocompatibility as well as satisfactory mechanical resistance make titanium and its alloys a good candidate for applications in biomedical industry. Commercially pure titanium (CP-Ti) is the ideal titanium-based material to use in the manufacturing of dental implants as alloying elements can decrease its biocompatibility. However, CP-Ti shows limited mechanical properties for a few implant applications. Ti-6Al-4V is the most common titanium alloy used in biomedical implants. Machining is one of the main manufacturing process involved in producing implants and micromilling is one of the process that can be used. The proposition of this thesis is to analyze and compare the micromilling machinability of four different titanium-based materials, indicating the better suited material regarding this manufacturing process among: standard commercially pure titanium grade 2, standard Ti-6Al-4V alloy, CP-Ti processed by equal channel angular pressing (ECAP) and Ti-6Al-4V fabricated by selective laser melting (SLM). Machinability was analyzed considering cutting forces, surface roughness, burr formation, microchips morphology as well as their mechanical properties and their influence in each factor was analyzed. It was designed a series of experiments varying feed per tooth and covering a wide range, from 0.5 to 4.0 μm, so a possible ploughing behavior could be identified. Despite presenting higher strength and hardness, SLM material presented the best machinability among the materials. It presented lower surface roughness, burr formation, a good microchip morphology and the cutting force was only higher than for CP-Ti, which has the worst mechanical properties values.

Contents

List of Figures **xi**

List of Tables **xvii**

1 Introduction **1**
1.1 Dental implants . . . 2
1.2 Material properties for dental implants . . . 4
1.3 Typical biocompatible materials for dental implants . . . 5
1.4 Motivation . . . 7
1.5 Objectives . . . 9
1.6 Thesis structure . . . 9

2 Micromilling **11**
2.1 Micromilling tools . . . 12
2.2 Machine tools . . . 13
2.3 Size effect and cutting mechanics . . . 14
2.3.1 Uncut chip thickness modelling in micromilling . . . 14
2.3.2 Material homogeneity in micromilling . . . 17
2.4 Cutting force and specific cutting force in micromilling . . . 17
2.5 Surface roughness in micromilling . . . 20
2.6 Burr formation in micromilling . . . 21
2.7 Machinability . . . 23
2.7.1 Material properties affecting machinability . . . 25

3 Machining titanium alloys **28**
3.1 Titanium and its alloys . . . 28
3.2 Titanium mechanical properties . . . 31
3.2.1 Thermal conductivity affecting cutting temperature . . . 32
3.3 Machinability of titanium and titanium alloys in conventional milling 34
3.3.1 Hardness and strength affecting cutting forces . . . 34
3.3.2 Factors affecting surface roughness . . . 36
3.4 Machinability of titanium and titanium alloys in micromilling . . . 38

4 Equal Channel Angular Pressing (ECAP) 41
4.1 ECAP process . . . 41
4.2 Accumulative strain in ECAP . . . 44
4.3 Routes in ECAP . . . 47
4.4 Consolidation of metallic powder by ECAP . . . 49
4.5 Ultra-refinement of grains in metals processed by ECAP . . . 52
4.6 Mechanical properties of metals processed by ECAP . . . 54
4.7 Commercially pure titanium and titanium alloys processed by ECAP 56
4.8 Machinability of titanium and titanium alloys processed by ECAP . . 59

5 Additive Manufacturing and Selective Laser Melting (SLM) 65
5.1 Additive manufacturing . . . 65
5.2 SLM process . . . 68
5.3 Titanium and titanium alloys processed by SLM . . . 72
5.4 Machinability of titanium and titanium alloys produced by additive manufcturing . . . 77

6 Materials and Methods 80
6.1 Materials . . . 80
6.1.1 Preparation of the samples of commercial workpieces . . . 81
6.1.2 ECAP workpiece production . . . 82
6.1.3 SLM workpiece production . . . 83
6.1.4 Characterization of materials before machining . . . 84
6.2 Equipment for micromilling experiments . . . 87
6.2.1 Machine tool . . . 87
6.2.2 Microtools and collet . . . 88
6.2.3 Cutting force measurement . . . 89
6.2.4 Roughness and burr measurement . . . 91
6.2.5 Chips and grooves analysis . . . 93
6.3 Micromilling procedure . . . 93
6.3.1 Experimental setup for micromilling . . . 93
6.3.2 Surface preparation . . . 94
6.3.3 Design of experiments . . . 94

7 Experimental Results 97
7.1 Microstructure . . . 97
7.2 Mechanical properties . . . 98
7.3 Micromilling . . . 100
7.3.1 Force treatment . . . 100
7.3.2 Maximum resultant forces . . . 105

7.3.3 Specific cutting forces results . . . 107
7.4 Roughness . . . 110
7.5 Burr formation . . . 113
7.6 Chips morphology . . . 118

8 Analysis and discussion **122**
8.1 Material characterization comparison . . . 122
8.2 Micromilling forces and specific cutting force . . . 124
8.3 Surface roughness comparison . . . 127
8.4 Burr formation comparison . . . 128
8.5 Microchips analysis comparison . . . 130

9 Conclusions **132**
9.1 Conclusions and final considerations . . . 132
9.2 Perspectives for future works . . . 134

Bibliography **136**

A Grooves images **153**

B Microchips images **162**

List of Figures

1.1 Dental implant parts: 1 - crown; 2 - screw; 3 - abutment; 4 - implant [3]. 2
1.2 Examples of commercial dental implant designs [6] 3
1.3 A zigomatic implant. [6] 4

2.1 Micromilling parameters. 11
2.2 Cutting edge radius relation to the undeformed chip thickness. 13
2.3 Cutting edge radius relation to the undeformed chip thickness [24]. . 15
2.4 Cutting mechanics in micromachining [24]. 16
2.5 Ploughing and shearing regions in full immersion micromilling. 16
2.6 Microstructure influence in micromilling cutting mechanics. 17
2.7 Specific cutting force according to Kienzle equation (adapted from [28]). 18
2.8 Cutting force simulated for specific cutting conditions. 19
2.9 Experimental maximum resultant force varying with feed per tooth [29]. 19
2.10 Specific cutting force varying with feed per tooth [24]. 20
2.11 Average roughness varying with feed per tooth [24]. 21
2.12 Average roughness varying with feed per tooth in micromilling AISI 1045 [33]. 22
2.13 Burrs types in groove machining [35]. 22
2.14 Feed per tooth influence in top burr height [36]. 23
2.15 Effect of cutting speed on tool flank wear (FW) for three cutting speeds. Hypothetical values of speed and tool life are shown for a tool life criterion of 0.50 mm flank wear [39]. 24
2.16 General view of the main factors which affect the three machinability criteria: tool life, cutting forces and surface roughness.. 27

3.1 Phase diagrams for Ti alloys. 29
3.2 Titanium microstructures. 30

3.3 Influence of temperature on the properties of Ti-6Al-4V alloy. a) Thermal conductivity; b) Rockweel hardness; c) elastic modulus; and d) ultimate tensile strength [46]. 33
3.4 Heat distribution during cutting for titanium alloy and steel [47]. . . 33
3.5 Comparison of the cutting temperature among the four metals for each cutting condition. Identical capital letters indicate no statistically significant difference among the mean values of the same cutting condition. [48]. 34
3.6 Vickers hardness of the metals [49]. 36
3.7 Cutting force magnitude in milling for four cutting conditions [49]. . . 36
3.8 Turning resultant force versus cutting distance for several cutting speeds using two cemented carbide tools, data from [51], [46]. 37
3.9 Surface roughness of cut surfaces for four different conditions [49]. . . 37
3.10 Evolution of average roughness during cutting for different cutting speeds [53]. 38
3.11 Specific cutting force and surface roughness analysis to define minimum chip thickness. 39

4.1 Titanium microstructures. 43
4.2 The principle of ECAP showing the shearing plane within the die: the elements numbered 1 and 2 are transposed by shear as indicated in the lower part of the illustration [70]. 44
4.3 Change of element geometry in ECAP for $\psi = 0°$ [68]. 45
4.4 Variation of the equivalent strain, ϵ_N, with the channel angle, ϕ, over an angular range of ϕ from 45° to 180° for values of the angle of the arc of curvature, ψ, from 0° to 90°: the strains are shown for a single pass where $N = 1$ [72]. 45
4.5 Effective strain variation across a width section A-B [71]. 46
4.6 Four fundamental routes of ECAP processing [68] and slip systems views [75]. 48
4.7 Shearing characteristics for four different processing routes [76]. . . . 49
4.8 Pure Ni pressed by ECAP using route A: (a) initial condition; (b) after 1 pass, (c) after 2 passes and (d) after 3 passes (adapted from [77]). 49
4.9 Microstructures of Ni after cold deformation via route C with number of passes (a) $N = 2$, (b) $N = 3$, (c) $N = 4$ and (d) $N = 5$ (adapted from [77]). 50

4.10 The ECAP principle used for the consolidation of aluminum alloy powder: the powder is inserted into a tight-fitting outer jacket labeled *abcd* [80]. 51
4.11 Relative density increase of the compacted powder after every ECAP pass and the peak extrusion pressure at every ECAP pass [81]. 51
4.12 Schematic of ECAP die with back pressure [79]. 52
4.13 Grain structure of an AZ31 alloy processed by ECAP from the extruded condition: (a) initial structure, (b) after 1 pass and (c) after 4 passes of ECAP using a die with 110° between the channels. [94]. . 54
4.14 A comparison of yield strength and ductility for an Al-3004 alloy processed by cold-rolling or ECAP [95]. 55
4.15 Optical and transmission electron microscopy illustration microstructure of CP-Ti grade 4: a) conventional; b) and c) ECAP + TMT [90]. 56
4.16 Stress-strain behaviors from initial CP-Ti and after 1, 3 and 5 ECAP passes [89]. 57
4.17 Optical and SEM micrographs of pure Ti: (a) as-annealed; (b), (c) and (d) after ECAP [85]. 58
4.18 Transmission electron microscope images of CP Ti after one ECAP pass. 59
4.19 Engineering stress-strain curves for CP-Ti grade 4 in different structural states [93]. 59
4.20 Cutting forces for CP-Ti before ECAP (X0), after four ECAP passes (4XH) and the alloy (#5) [17]. 60
4.21 Mean surface roughness for CP-Ti before ECAP (X0), after four ECAP passes (4XH) and the alloy (#5) [17]. 61
4.22 Thermal conductivity versus grain diameter (logarithmic scale) with thermal resistivity versus inverse grain diameter in the insert [16]. . . 61
4.23 Average chip length versus feed rate of machining at different cut depths, d_c, for UFG (solid lines) and CG (dashed lines) titanium [16]. 62
4.24 Cutting force versus feed for ultra-fined grain titanium and coarse-grained titanium [18]. 63
4.25 Maximum cutting forces achieved in milling CP-Ti and CP-Ti powder consolidated by ECAP technique [96]. 63

5.1 Additive manufacturing flowchart with all process steps. 66
5.2 Conversion of a solid model of an object into layers and one layers is shown [39]. 67
5.3 Schematic figure of selective laser melting process [100]. 69

5.4 Schematic representation of various operating parameters of SLM process [102]. 71
5.5 Balling effect at different scan speeds: a) 100 mm/s, b) 200 mm/s, c) 300 mm/s and d) 400 mm/s [103]. 72
5.6 SEM microstructure of the Cp-Ti samples produced by (a) SLM and (b) casting [104]. 73
5.7 Density 73
5.8 Properties of material used in selective laser melting 74
5.9 Implants manufactured by SLM 75
5.10 Young's modulus of elasticity of compact core and porous region of the specimens compared to ASTM values and values of cortical bone [14]. 76
5.11 SEM images of the porous Ti6Al4V implants fabricated by selective laser melting at different scan line spacing[(a) 200 μm; (b) 300 μm; (c) 400 μm; (d) 500 μm; (e) 600 μm and (f) 700 μm] [107]. 76
5.12 Cutting force in milling additive material titanium [108]. 77
5.13 Machined surface roughness as a function of the cutting parameters under dry and MQL conditions [109]. 78

6.1 Experimental procedure stages. 80
6.2 Experimental analysis. 81
6.3 McMaster-Carr commercially pure titanium raw bar and samples. . . 81
6.4 Commercially pure titanium and stainless steel set scheme (adapted from [114]). 82
6.5 Equal channel angular pressing sample production. 83
6.6 Bakelite puck with ECAP sample mounted for micromilling experiments. 83
6.7 Selective laser melting sample production. 84
6.8 Energy Dispersive X-ray Spectroscopy. 85
6.9 Procedure for metallography of the materials. 85
6.10 Metallographic analysis. 86
6.11 Three points flexural test setup. 86
6.12 Hydrostatic weighing for porosity measurement. 87
6.13 CNC Mini-Mill/GX. 88
6.14 Microtool and collet geometries. 89
6.15 Microtool geometry analysis. 90
6.16 Equipment for the experimental setup for force measurements. 91
6.17 Surface roughness and burr measurement details. 92
6.18 Surface roughness measurement procedure. 92

6.19 USB AM3715TB Dino-Lite Edge handheld digital microscope. 93
6.20 Tool, workpiece and the dynamometer: experimental setup. 94
6.21 Experiments scheme. 95

7.1 Microstructure results. 98
7.2 SLM flexure test. 99
7.3 ECAP flexure test. 100
7.4 Raw cutting force signal for CP-Ti sample using 1μm/tooth. 101
7.5 Fast Fourier Transform. 102
7.6 Comparison between unfiltered and filtered cutting force signal in X direction for CP-Ti sample using 1 μm/tooth. 103
7.7 Cutting force scheme and chip thickness in milling operations. 103
7.8 Resultant force for feed per tooth of 1 μm/tooth. 104
7.9 Cutting force results for CP-Ti grade 2. 105
7.10 Cutting force results for Ti-6Al-4V alloy. 106
7.11 Cutting force results for CP-Ti processed by ECAP. 107
7.12 Cutting force results for Ti-6Al-4V alloy produced by SLM. 108
7.13 CP-Ti. 108
7.14 Ti-6Al-4V. 109
7.15 ECAP. 109
7.16 SLM. 110
7.17 Surface roughness results for CP-Ti grade 2. 111
7.18 Surface roughness results for Ti-6Al-4V alloy. 112
7.19 Surface roughness results for standard CP-Ti processed by ECAP. . . 112
7.20 Surface roughness results for Ti-6Al-4V alloy produced by SLM. . . . 113
7.21 Top burr height measurement results for CP-Ti. 114
7.22 Grooves SEM images for CP-Ti. Upmilling: right; Downmilling: left. 114
7.23 Top burr height measurement results for Ti-6Al-4V. 115
7.24 Grooves SEM images for alloy. Upmilling: right; Downmilling: left. . 116
7.25 Top burr height measurement results for ECAP. 116
7.26 Grooves SEM images for ECAP. Upmilling: right; Downmilling: left. 117
7.27 Top burr height measurement results for SLM. 117
7.28 Grooves SEM images for SLM. Upmilling: right; Downmilling: left. . 118
7.29 Optical images of chips collected during micromilling experiments of CP-Ti. 119
7.30 Optical images of chips collected during micromilling experiments of Ti-6Al-4V. 120
7.31 Optical images of chips collected during micromilling experiments of CP-Ti processed by ECAP. 120

7.32 Optical images of chips collected during micromilling experiments of Ti-6Al-4V alloy produced by SLM. 121

8.1 Mechanical properties comparison. 123
8.2 Experimental cutting force comparison for batch A. 124
8.3 Experimental cutting force comparison for batch B. 125
8.4 Specific force comparison for batch A. 126
8.5 Specific force comparison for batch B. 126
8.6 Surface roughness comparison for batch A. 127
8.7 Surface roughness comparison for batch B. 128
8.8 Burr formation comparison for upmilling. 129
8.9 Burr formation comparison for downmilling. 129
8.10 Top SEM images of grooves for batch A with feed per tooth of 3.5 μm. 130

A.1 Groove SEM images for standard CP-Ti for batch A experiments. . . 154
A.2 Groove SEM images for standard Ti-6Al-4V alloy for batch A experiments. 155
A.3 Groove SEM images for CP-Ti processed by ECAP for batch A experiments. 156
A.4 Groove SEM images for Ti-6Al-4V alloy produced by SLM for batch A experiments. 157
A.5 Groove SEM images for standard CP-Ti for batch B experiments. . . 158
A.6 Groove SEM images for standard Ti-6Al-4V alloy for batch B experiments. 159
A.7 Groove SEM images for CP-Ti processed by ECAP for batch B experiments. 160
A.8 Groove SEM images for Ti-6Al-4V alloy produced by SLM for batch B experiments. 161

B.1 Chips analysis for standard CP-Ti. 163
B.2 Chips analysis for standard Ti-6Al-4V. 164
B.3 Chips analysis for CP-Ti processes by ECAP. 165
B.4 Chips analysis for Ti-6Al-4V produced by SLM. 166

List of Tables

1.1 Characteristic mechanical properties of various metallic biomedical materials [7]. 6

2.1 Machinability ratings and hardness for some engineering material taking SAE 1212 as the standard material [38]. 26

3.1 Titanium grades 2 and 5 composition. 30
3.2 Summary of typical mechanical, physical and thermal properties of titanium grades 2 and 5 [45]. 31
3.3 Thermal conductivity k of titanium and its alloys versus temperature [46]. 32
3.4 Selected properties of Ti-6Al-4V and commercially pure titanium [46, 50]. 35

4.1 Experimental results from different studies considering grain refinement. 54
4.2 Experimental results from different studies considering mechanical properties: σ_Y is yield strength in MPa; UTS is ultimate tensile strength in MPa; Hard. is hardness in the unity indicated; and label 1 indicates before ECAP processing, as label 2 indicates after ECAP processing. 55

5.1 Comparison between regular Cp-Ti, SLM Cp-Ti, SLM Cp-Ti produced with designed pattern and cortical bone properties [106]. 75
5.2 Mechanical properties and porosity for varying hatch space [107]. . . 77

6.1 SLM parameters 84
6.2 Technical specifications of the mini-mill used in the experiments. . . . 88
6.3 Technical specifications of the dynamometer. 90
6.4 Cutting parameters during micromilling. 96
6.5 Design of Experiments. 96

7.1 Literature data for flexural strength and modulus of CP-Ti and Ti-6Al-4V. 99

7.2 Experimental flexure test results for flexural strength and apparent modulus. 100
7.3 Hardness tests results. 100

Chapter 1

Introduction

Commercially pure titanium (CP-Ti) is the ideal titanium-based material to use in the manufacturing of dental implants because of properties such as good corrosion resistance and biocompatibility as well as satisfactory mechanical resistance. However, several notices of implant failures, specially due to fatigue failure, made it necessary to choose a material that reduces the chances of a surgery for implant removal. Due to CP-Ti high elasticity modulus and the difficulty to increase its mechanical properties without prejudicing its biocompatibility, there are a few limitations in the application of the material.

Alloying pure titanium is a common alternative to improve its mechanical properties. The titanium alloy Ti-6Al-4V presents higher mechanical resistance than CP-Ti and preserves other essential properties like good corrosion resistance and biocompatibility, being also a great candidate fabrication of dental implants. Nevertheless, in recent years, several studies have reported that Ti-6Al-4V alloy might cause some long term health problems to the patient due to the release of aluminum and vanadium inside the person organism. Diseases like Alzheimer, neuropathy and ostemomalacia have been reported as long term consequences of the presence of these elements in the body of patients as they remain in the human body for several years.

For example, Zaffe *et al.* [1] analyzed titanium plates and Ti-6Al-4V screws removed from patients that presented local inflammation and biopsies. They found out indications that biological perturbations may be related to aluminum release from the tested biomaterials. Also, Mjoberg *et al.* [2] studied 26 hip fracture patients and their conclusions agreed with the hypothesis that aluminum concentration plays a role in the development of Alzheimer's disease and bone brittleness.

Considering the specific limitations of both titanium-based materials in manufacturing dental implants, it is important the study of techniques of processing or manufacturing that helps to improve the application of these materials in this industry. Some material processing operations are being studied in order to be applied

to improve mechanical properties of commercially pure titanium, so it can be better suited for dental implants. At the same time, different manufacturing operations have been studied to optimize the fabrication of implants using Ti-6Al-4V, which is already commonly used material.

1.1 Dental implants

Dental implants are structures that are surgically inserted in the maxillary bone of a patient and are used as support for artificial teeth. Implants have the same function of roots in the original teeth. On dental implants can be mounted bridges, crowns, dentures and they can be also used in orthodontic anchorage, which are procedures made with the objective to avoid unwanted dental moving. A dental implant assembly is shown in Figure 1.1: crown, screw, abutment and the implant.

Figure 1.1: Dental implant parts: 1 - crown; 2 - screw; 3 - abutment; 4 - implant [3].

The implant is the principal component and is what actually makes contact with the bone and in order to improve biological responses, different implant shapes and surface modifications exist and are proposed. The abutment makes the connection between the implant and the prosthesis and make contact with soft tissue. Usually, the abutment is fixed to the implant by a screw, but it can also be cemented. The crown or prosthesis is the upper part which can play the role in mastigation and can be attached to the abutment also by a screw or cemented.

In order to dental implants successfully perform its function, it is necessary to occur the osteointegration (or osseointegration) between the implant and the maxillary bone, where the implant is fixed [4, 5]. Osteointegration happens if they are strongly connected to the bone, as if the implanted object and the bone were the same thing. This mechanism involves two types of cell: osteoblast and osteoclast. The former ones are related to the creation of the new bone; the latter are related to the removal of the bone tissue that died during the bone drilling. Studies indicate

that roughness, chemical composition and other characteristics of implanted material can influence osteointegration [6]. Osteointegration phenomenon occurs only with biocompatible materials, such as titanium, cobalt-chrome (Co-Cr) alloys and some ceramic materials.

According to Elias *et al.* [6], there are three general dental implant types: osseointegrated, mini-implant for orthodontic anchorage and zigomatic implant and they differ on the function they have on the organism.

Osseointegrated implant is defined as a bone-to-implant contact under load, that is, it is the implant that is placed in the bone and is under continuous stress. This type of dental implants used to be manufactured in several shapes such as hallow baskets, blades, tripods, needles, disks and others, however nowadays the most common implant is the screw shaped, as shows in Fig. 1.2. Polymers present a series of disadvantages in comparison with metals and ceramics, they are also used for dental implants. The biocompatible polymeric materials include polytetrafluroethylene (PTFE), polyethyleneterephthalate (PET), polymethylmethacrylate (PMMA) and others. In general, polymers have much lower strengths than other materials which is an important limitation factor for their application. Also, polymers are very sensitive to sterilization techniques.

Figure 1.2: Examples of commercial dental implant designs [6]

Another common dentistry implant is the temporary orthodontic mini-implant used to maintain anchorage in place in orthodontic treatments. This type of implant usually has the shape similar to osseointegrated implants and the only difference is the smaller size in diameter. As they are smaller, dental mini-implants must be manufactured with materials that have improved resistance. This type of implant does not result in osseointegration with the bone as the implant is often temporary, that is, the implant is removed before osseointegration happens.

The third implant type, zigomatic implants, are used in patients that present advance atrophy of the jaw and do not have the necessary minimum volume of bone required to have dental implants. Zigomatic implants are longer than standard dental implants and rely on the cheek bones instead on jawbone, as shown in Fig.

1.3.

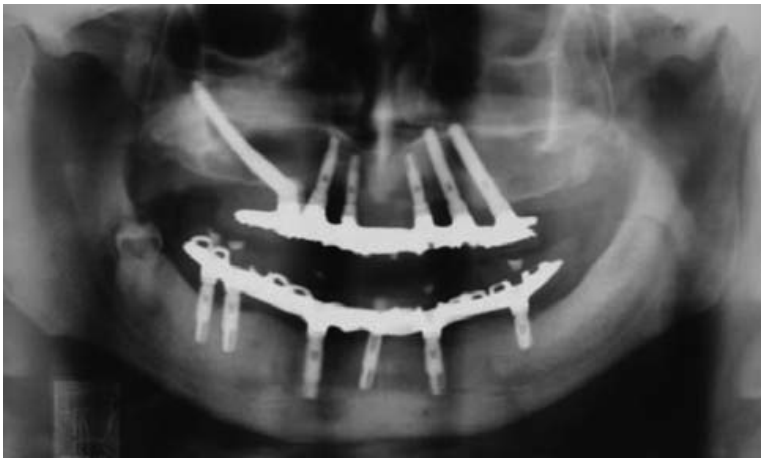

Figure 1.3: A zigomatic implant. [6]

1.2 Material properties for dental implants

Chemical, mechanical and electrical properties influence the material biocompatibility. Thus, the properties required for a biomaterial vary according to its application. The properties needed for a dental implant, for example, are different than the properties needed for an orthopedic implant. Among the main properties for a biomaterial, the following can be considered as the most important for dental implants:

- Corrosion resistance - corrosion of the dental implant can cause the implant to lose some of its original properties due to degradation, especially mechanical properties affecting resistance;
- Elastic Modulus (Young Modulus) - the material used for dental implant must possess an elastic modulus close to the cortical bone value. The difference between Young Modulus can cause the stress shielding effect, which is the loss of alveolar bone caused by the lack of bone stimulation. In every composite system composed of two materials where one component is stiffer, the stiffer component will sustain the greater part of the load. If the implant is a lot stiffer, the bone can be less stimulated, causing the stress shielding effect. Elastic modulus of cortical bone varies in a range of 10 to 30 GPa depending on the fiber density of the bone [7];
- Elongation - directly related to the elastic modulus of the material, elongation is an important issue on implants as it predicts the movement of the implant under stress. Providing the degree of relative movement in the interface bone-implant in part influences the surrounding tissue integration;

- Tensile and compressive strength - mechanical resistance of the material when submitted to tensile and compressive stresses is a very important characteristic as dental implants must be able to resist loads applied by the jaw;
- Fatigue resistance - dental implant material fatigue resistance is an important issue as teeth are constantly subjected to cyclic loads;
- Sterilizability - sterilizability is the capability of a material of not being destroyed by any typical sterilizing technique such as autoclaving, dry heat, radiation and others. These process are applied to materials in order to destroy any micro-organism existent on the part capable of causing damages to human organism [7]
- Biocompatibility - it can be defined as "the ability of a material to perform with an appropriate host response in a specific application" [7] and it is a consequence from chemical, mechanical and electrical properties of the material.

1.3 Typical biocompatible materials for dental implants

In general, there are three types of materials that are used for manufacturing dental implants: metals, ceramics and polymers. Polymers present a series of disadvantages in comparison with metals and ceramics, they are also used for dental implants. The biocompatible polymeric materials include polytetrafluroethylene (PTFE), polyethyleneterephthalate (PET), polymethylmethacrylate (PMMA) and others. In general, polymers have much lower strengths than other materials which is an important limitation factor for their application. Also, polymers are very sensitive to sterilization techniques.

Metals and metallic alloys constitute the main material category used in dental implant systems [8], including titanium, vanadium, aluminum, cobalt, chromium, molybdenum and nickel. Also, noble metals like gold and platinum are often used restore the function, integrity and morphology of missing tooth structure.

Titanium is the most used material for dental implants. It presents very high biocompatibility and together with other characteristics such as high corrosion resistance and good mechanical properties makes titanium a great option for implants. Titanium can be coupled with other metals without losing its passivity, therefore when alloyed it remains highly corrosion resistant. However, commercially pure titanium does not offer sufficient mechanical resistance in its conventional form, therefore alloys are often added to titanium in order to increase its tensile strength.

Most commonly used alloys in dentistry are Ti-30Pd (palladium), Ti-20Cu (copper), Ti-15V (vanadium) and Ti-6Al-4V (aluminum and vanadium) [8].

One of the most used materials in dental implants nowadays is the titanium alloy containing aluminum and vanadium (Ti-6Al-4V) [9, 10]. However, recent studies pointed out that in long term, this alloy can release in human organism toxic substances that could cause cancer and other problems to human organism[4, 5]. Therefore, the substitution of this alloy by the use of commercially pure titanium has been studied. Nevertheless, in order to the substitution occur, it is necessary for the pure titanium to improve its mechanical properties. Also, there has been a concern about the high elastic modulus of Ti-6Al-4V alloy in comparison with bone and stress shielding occurrence, as shown by Tab. 1.1. The elastic modulus of commercially pure titanium is closer to bone value. The table also shows mechanical properties for several metals used in dental implants, for comparison basis.

Table 1.1: Characteristic mechanical properties of various metallic biomedical materials [7].

Material	**Condition**	E **(GPa)**	**Yield stre. (MPa)**	**UTS (MPa)**
X2CrNiMo17122	Annelead	190	331	586
(AISI 316L)	30% cold worked	190	792	930
	Cold forged	190	1213	1351
Co28Cr6Mo	Cast	210	448-517	655-889
	Hot forged	210	896-1200	1399-1586
Co20Cr15W10Ni	Hot forged	210	484-648	951-1220
	44% cold worked	210	1606	1896
Co35Ni35Cr20Mo10	As wrought	232	965-1000	1206
CP-Ti	grade 2	105-110	250	390-540
Ti6Al4V	Cold worked	100-110	830-1070	920-1140
Ti6Al7Nb	-	110	810-1010	870-101
Ti5Al2.5Fe	-	110-115	780	860
Ti12Mo6Zr2Fe	-	74-85	1000-1060	1060-1100
Ti13Nb13Zr	-	64-83	435-905	705-1035
Ti29Nb13Ta4.6Zr	-	65	400	1000-1050
Ti30Nb	-	63-80	500	700
Ti30Ta	-	60-70	590	740

Other metal elements which are very used in dental implants, but in minor scale than titanium, are the CoCr (cobalt-chromium) alloys. Cobalt-chromium alloys are very resistant to corrosion and alloying, such as nickel, molybdenum or tungsten, is usually used for enhancing mechanical properties. When using CoCr alloys, stress shielding must be taken into consideration as the elastic modulus of the alloys are much higher than of cortical bone, as Tab. 1.1 presents.

Ceramics are inorganic materials composed of ionic and covalent bonds that are generally formed at very high temperatures. The biocompatible ceramics class is formed principally by alumina (aluminum oxides), zirconia (zirconium oxides), calcium phosphates, bioactive glasses and glass ceramics. Ceramic materials are

very hard and more resistant to degradation than most metals and they also present a lot of chemical similarities with bones. However, their use is limited by its natural brittleness. Thus, ceramics are very used to produce teeth replacements, that is, the prosthesis.

1.4 Motivation

Several manufacturing processes are used to produce implants. Casting followed by machining or casting followed by a plastic deformation operation, such as rolling or extrusion, are the most common. Considering the machining processes, one can use turning, milling, drilling, grinding and threading. Machining is the best process because it delivers higher surface roughness and dimensional precision. However, other processes are also used. Secondary techniques are also used to improve mechanical properties of the implant, as for example hot-isostatic pressing (HIP), used to reduce parts porosity, and heat treatments.

One of the methods that has been studied to make possible the use of CP-Ti to fabricate dental implants is the grain refinement by severe plastic deformation (SPD) in order to improve its mechanical properties. Severe plastic deformation processes consist in applying a high strain in the material, but without changing its dimensions, breaking and reducing the grain size. As a consequence, mechanical properties, such as resistance, hardness and ductility, will be affected. Equal channel angular pressing (ECAP) is one of the SPD methods used. In ECAP processing the material is pressed through a channel bent by an abrupt angle. Deformation occurs by shearing when the material passes by the angle. Several ECAP passes can be performed, achieving ultra-fine grained microstructure by accumulative strain.

Greger *et al.* [11] studied the increase in specific resistance and the grain size reduction using several ECAP passes in CP-Ti. Authors achieved, after 12 passes, three times the original resistance and a grain reduction to 100-300ηm. Estrin *et al.* [12] demonstrated that is possible to increase titanium resistance to 850 MPa, without losing its biocompatibility. Resistance limit increased almost two times the original value. However, usually an increase in resistance is followed by a decrease in ductility, that is, an increase in Young Modulus. Although CP-Ti titanium resistance can be improved after ECAP processing, it can get even stiffer than cortical bone and the stress shielding effect becomes higher.

However, other manufacturing process has been the object of studies in order to fabricate dental implants with improved properties: selective laser melting (SLM), an additive manufacturing (AM) process. Additive manufacturing processes are the ones in which, unlike conventional material removal ones, parts are fabricated by incrementally adding material by different ways until the desired shape is achieved.

Selective laser melting consists basically of solidifying metallic powder layers, previously defined by slicing a three dimensional model of the desired part, on top of each other until the part is completely fabricated [13].

Selective laser melting has been gaining a lot of attention among AM processes as it was the first one to provides bulk functional almost fully dense parts. Allying this characteristic and the versatility of AM processes which can manufacture very complex shaped parts, some works have been made towards its use to produce metallic dental implants.

Selective laser melting process allows the fabrication of implants with different porosity rate which will result in different values of the elastic modulus. Also, it is well known that rough surfaces can promote better and faster bone apposition, being more osteoconductive than a smooth surface. If the surfaces produced by SLM do not present ideal values, roughness can be modified by some conventional methods like sandblasting or acid etching in order to improve biological responses. As well, mechanical strength of CP-Ti must be improved in order to be used as the material for dental implant fabricating [14].

Attar *et al.* [15] analyzed commercially pure titanium materials with a variety of porosity percentage. The authors managed to achieve elastic modulus values very similar to cortical bone modulus value by manufacturing samples with different porosities, but still increasing ultimate tensile strength.

Equal channel angular pressing has been gaining more attention since 2001, with the number of articles published in international journals about it significantly increasing. Selective laser melting is a newer process and although it has been object of research since approximately 12 years ago, only since 2010 the number of published articles has been increasing. Both manufacturing process can be applied to produce commercially pure titanium dental implants.

There are plenty of studies covering the impact of ECAP on the mechanical properties and microstructure of metals, but almost none about the changes on the machinability of the material. Considering titanium, only three papers [16–18] and an undergraduate final project [19] were found about the machinability or machining of commercially pure titanium processed by ECAP. Taking into consideration that machining is an essential stage of dental implants manufacturing, understanding the best parameters for machining ECAP titanium is very important.

Likewise, several studies about the properties of titanium parts manufactured by SLM process and the mechanisms that lead to it have been done. When this thesis was first proposed, in 2015, there were no published research analyzing machining of additive manufacturing materials. After almost three years, a few papers have been published, but there is still a lack of knowledge in this area. Machining processes, like milling and micromilling, can be applied to materials fabricated by SLM in order

to achieve surface roughness that SLM technology can not. Also, it can be used to change the surface of parts manufactured by SLM with the objective to increase osteointegration or change implant wettability.

1.5 Objectives

This work has as general objective to compare the micromilling machinability of three different titanium bulks that are currently being used to manufacture biomedical implants and one strong candidate for future applications in this field. The four studied bulks are: standard commercially pure titanium (CP-Ti), commercially pure titanium processed by equal channel angular pressing (ECAP), standard Ti-6Al-4V alloy and Ti-6Al-4V produced by selective laser melting (SLM).

In order to achieve the general objective, the following specific objectives will be covered:

- Characterize the materials that are going to be machined: identify their microstructure, grain size and mechanical properties;
- Analyze the differences of behavior of the cutting forces during the micromilling of the materials. Analyze the effect of feed per tooth variation and correlate the cutting force with different microstructure and mechanical properties;
- Measure the roughness of the machined surfaces and compare using different cutting parameters;
- Analyze burr formation comparing different materials and cutting conditions;
- Analyze the geometry of the microchips to assess the quality of the micromilling process;
- Compare the micromilling tools before and after the experiments to qualitative analyze the tool wear;

1.6 Thesis structure

The first and present chapter of this work presented the motivation and objectives of the thesis. It also presented a brief introduction to the field of biomedical implants covering the main informations on the topic, such as the main types of implants, the materials and manufacturing processes which are used to fabricate them and the mechanical and physical properties that materials must present to be applied in the field of biomedical implants.

Chapter 2 deals with micromilling, covering the fundamental similarities and differences between the conventional macro process and miniaturized process, including the size effect and its influence in parameters like cutting forces, roughness and burr formation in machining titanium and its alloys.

The third chapter presents the basic aspects of titanium and its alloys, including the typical crystallographic structures, microstructure, properties and their machinability properties.

Chapter 4 presents the equal channel angular pressing process, giving a special attention to the application of the process to implants manufacturing. The chapter shows the fundamentals of ECAP, the technology of the process, the specifics of titanium processed by ECAP and the relationship with dental implants. It also covers the machinability of titanium processed by ECAP.

The fifth chapter deals with the selective laser melting process, showing how the operation works, the main characteristics and the mechanical properties of titanium materials fabricated by SLM. It also covers the machinability of titanium processed by SLM.

The following chapter, Materials and methods, covers the characterization of the experimental procedure used in the study. It is presented the materials and equipment used in all stages of the experimental process as well as the design of experiments and parameters used in the micromilling experiments.

The seventh chapter presents the results obtained in the characterization and analysis of the materials and also on the micromilling experiments, analyzing cutting forces, roughness, burr formation, chips and the tools. Next, Chapter 8 presents the comparison of the results between the materials analyzed.

Finally, the last chapter, Conclusions, emphasize the main contributions of the research and summarize the analysis carried out during the development of the work. It also gives a brief view on the future possibilities of research on the topic.

Chapter 2

Micromilling

The basic of micromilling can be observed in Fig. 2.1. A cylindrical tool rotates around its axis with a constant spindle speed n (rpm) and moves perpendicular to its axis with feed speed V_f (mm/min). The feed per tooth f_z (μm/tooth) and cutting speed V_c (m/min) are defined considering tool and workpiece materials in order to input n and V_f in the machine tool parameter using Eq. 2.1 and Eq. 2.2:

$$n = \frac{10^3 V_c}{\pi d} \tag{2.1}$$

$$V_f = f_z z n \tag{2.2}$$

where d is the cutting tool diameter in mm and z is the number of flutes of the tool, usually 2 in micromilling. The third cutting parameter is the axial depth of cut a_p (μm) which defined the depth of the machined groove.

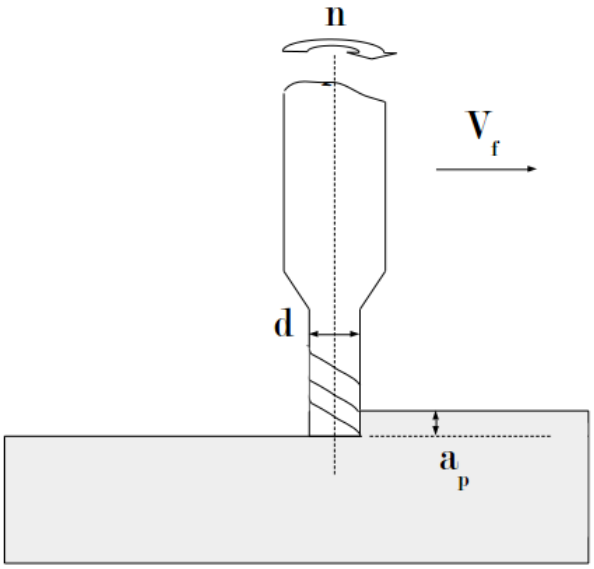

Figure 2.1: Micromilling parameters.

Despite presenting several similarities regarding the conventional macro milling operation, micromilling process has some fundamental differences which make it a more complex process. While presenting basically the same kinematics and same general characteristics, the miniaturization of the milling process leads to the size effect phenomenon which considerably affects the cutting mechanics and, as a consequence, the machining results expected [20]. Because of these similarities, the theory applied to micromilling is usually adapted to the micro scale always considering the specificities of the miniaturized process.

This chapter presents the main differences between milling and micromilling processes regarding physical aspects, the size effect and cutting mechanics as well as the consequences of the size effect phenomenon in cutting forces, roughness and burr formation results. It also presents the concepts of machinability and its application to the micromilling process.

2.1 Micromilling tools

There is not a total consensus among researchers about what limits a machining process so it can be considered a micromachining operation. One of the common definition is relative to the size of the microtool: Câmara *et al.* [21] stated that a process can be considered a micromachining operation when the microtool used presents a diameter between 1 and 1000 μm. Another common definition is regarding the volume of material removed during the engagement of the tool: Ng *et al.* [22] affirmed that a micromachining operation will occur when the size of the undeformed chip vary between 10 nm and 2 μm. During this work, the second definition will be preferred because it can be considered that the second definition includes the first one: a big diameter tool will not be able to remove such little material as it would present high cutting edge radius value. Cutting edge radius r_e is defined as the rounding of the cutting edges and, in milling tools, the principal edge is the one along the tool axis, as shown in Fig. 2.2.

The first obvious complexity of micromilling process is the diameter of the cutting tools, usually ranging from a few micrometers to 1 mm. The operator perception of the process is reduced. From the tool-part approximation to the cutting condition during the process, every step must be studied and monitored. For example, noticing a tool point breakage is impossible without the application of a monitoring system. Therefore, the use of sensors and devices capable of detecting any sign of process instability in micromilling is highly recommended.

Despite the size, the microtool geometry is overall very similar to the conventional milling tool as presented in Fig. 2.2. The main characteristics of the micromilling tool are the diameter, the helix angle λ, the flute length, the total tool length,

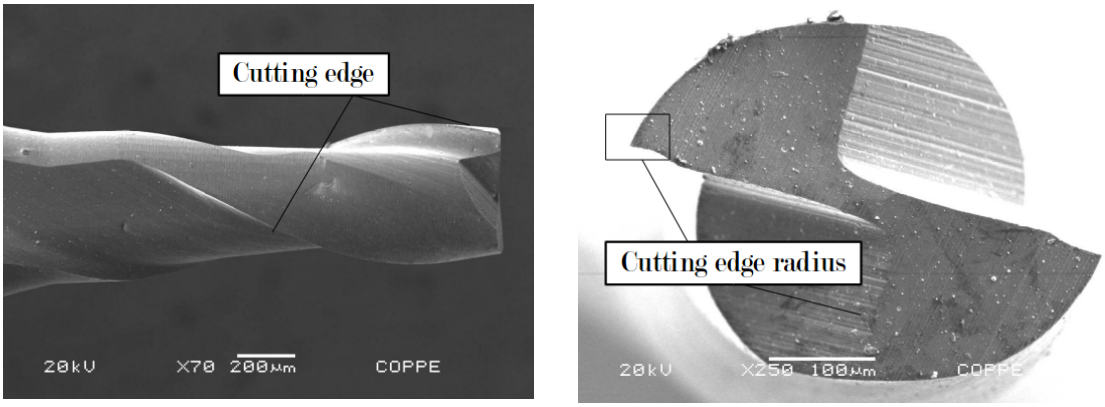

(a) (b)

Figure 2.2: Cutting edge radius relation to the undeformed chip thickness.

the cutting edge radius r_e and the tool tip radius r_{ke}. Also, micro-end-milling tools usually come only in two commercially available geometries regarding its point shape: square-end-mills and ball-end-mills.

The most used materials to manufacture micromilling tools are carbide and diamond, but carbide tools represent the majority of the market as diamond tools still present a series of limitations, inluding their high costs. In micromilling, the coatings used to improve tool life affect the tool edge radius leading to a change in cutting mechanics and an increase in cutting forces [21].

The same problems that occur in mesoscale occur in micromachining such as run-out, deflection, wear, built-up edge and breakage, but its consequences are more drastic. For example, tool breakage is difficult to perceive with naked eye and a image monitoring method must be applied so the microtools can be analyzed using a microscope. Hence, a monitoring system is essential in micromilling operations.

2.2 Machine tools

For a machine tool to be used in micromilling processes, it must present specific physical and structural characteristics. Câmara *et al.* [21] stated that a machine tool must present the following properties:

- Micromilling demands high spindle speeds. As the cutting tools present small diameter, higher spindle speeds are necessary to achieve specified cutting velocities. Spindle speeds of 60000 rpm and more are common in micromilling
- High stiffness - due to the high spindle speeds, the machine tool must present higher stiffness so vibrations do not affect the cutting process;
- High thermal stability structure - the structure of the machine tool needs to present a good thermal stability so the changes in the temperature of the

machine does not affect the temperature of the part or the microtool. Any change in the part or tool dimensions due to dilatation can have a prejudicial effect on the final dimensions of the part manufactured as it usually presents small dimensions and tight tolerances;

- Control system with high precision and low response time;
- Precision of 0.1 μm of the axis responsible for the feed and axial depth of cut control;
- Misalignment of less than 1 μm of the main axis;

2.3 Size effect and cutting mechanics

Although micromachining might seam to be just the miniaturization of the entire conventional macro process, the reduced scale introduces new issues that must be taken into account when studying machining operations in microscale, especially micromilling. Size effect is the set of differences in the characteristics of a process due to the change in their scale, which can be increasing or reducing it (35).

In micromilling size effect caused especially due to two main reasons: uncut chip thickness modeling and heterogeinity of the cut material.

2.3.1 Uncut chip thickness modelling in micromilling

Undeformed chip thickness model in milling operations was first developed by Martellotti and is given by Eq. 2.3, where f_z is the feed per tooth and ϕ is the position angle of the engaged tool. The Martellotti model did not consider secondary terms as in conventional milling they are significantly smaller than the first. Bao and Tansel [23] developed a model, showed in Eq. 2.4 for the uncut chip thickness in micromilling considering these terms as in micromilling they can not be ignored. In micromilling, undeformed chip thickness dimension is usually around the same size of the cutting edge radius of the tool. This fact completely changes the cutting mechanics of the process.

$$t_c = f_z sin\phi \tag{2.3}$$

$$t_c = f_z sin\phi - \frac{z}{2\pi r} {f_z}^2 sin\phi cos\phi + \frac{1}{2r} {f_z}^2 cos^2\phi \tag{2.4}$$

The conventional cutting mechanics in macromilling usually considers the cutting edge of the tool as perfectly sharp, as showed in Fig. 2.3a. There is almost none contact between the machined surface and the flank surface of the tool and the chip

is removed by shearing stress due to the interaction between the sharp edge and the material. It can be seen that the undeformed chip thickness, t_c, is significantly higher than the tool edge radius r_e. However, in micromilling, cutting edge radius dimension is often of similar dimension to the undeformed chip thickness, as showed in Fig. 2.3b. Differently to the conventional milling, in micromilling the chip is formed in the hight of the edge radius leading to a negative rake angle.

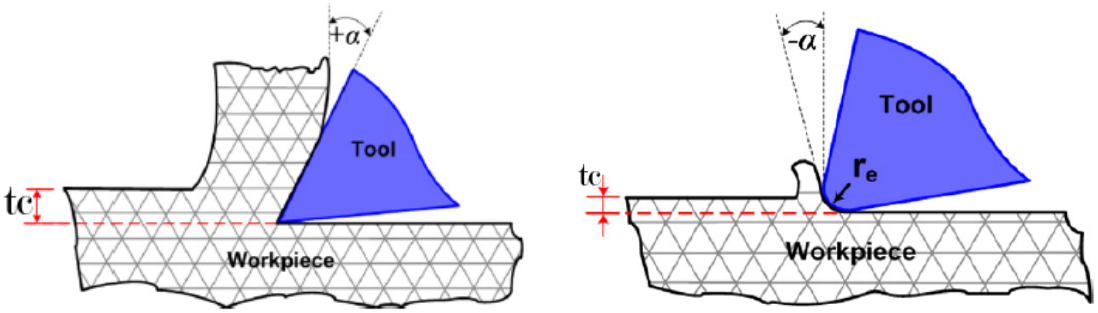

(a) Conventional milling ($r_e << t_c$). (b) Micromilling ($r_e \approx t_c$).

Figure 2.3: Cutting edge radius relation to the undeformed chip thickness [24].

This change of the cutting mechanics leads to the appearance of the minimum chip thickness t_{cm}, below which there would be no actual material cutting, but only the plastic deformation of the material followed by elastic recovery, phenomenon called ploughing. Chae *et al.* [25] proposed a basic cutting mechanism based on the relation between the chip thickness and minimum chip thickness, showed in Fig. 2.4, which works as follows:

- $t_c > t_{cm}$ - material removal will occur mainly by shearing. Ploughing can usually also be observed due to the elastic recovery of the material, as presented in Fig. 2.4a;
- $t_c \approx t_{cm}$ - ploughing phenomenon occurs, but shearing also has a role in chip removal. Here, a volume of the material is removed by shearing while the other part is plastically deformed, as showed in Fig. 2.4b;
- $t_c < t_{cm}$ - ploughing is dominant and almost the entire material volume is only plastically deformed followed by elastic recovery (Fig. 2.4c).

Micromilling presents an additional complexity which is the fact that the chip thickness is not constant as it is in turning, for example, as seen in Eq. 2.3. Therefore, in full immersion milling, three cutting phases are present according to the flute position angle. Initially, in the start of the up milling cutting until a critical angle ϕ_c, t_c is small and can be under t_{cm} and ploughing might be dominant. Then, chip thickness gets higher and shearing becomes dominant when t_c becomes bigger

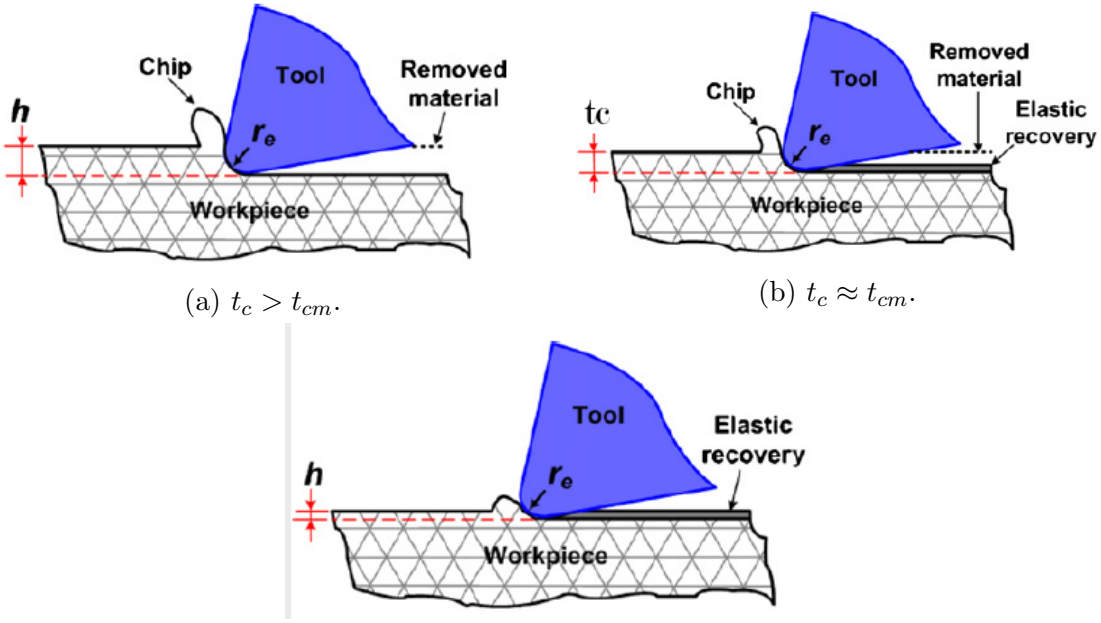

(a) $t_c > t_{cm}$.

(b) $t_c \approx t_{cm}$.

(c) $t_c < t_{cm}$.

Figure 2.4: Cutting mechanics in micromachining [24].

than t_{cm}. This part lasts until the flute is almost leaving the material, which is the end of down milling cutting, when chip thickness is again below the minimum chip thickness, as showed in Fig. 2.5.

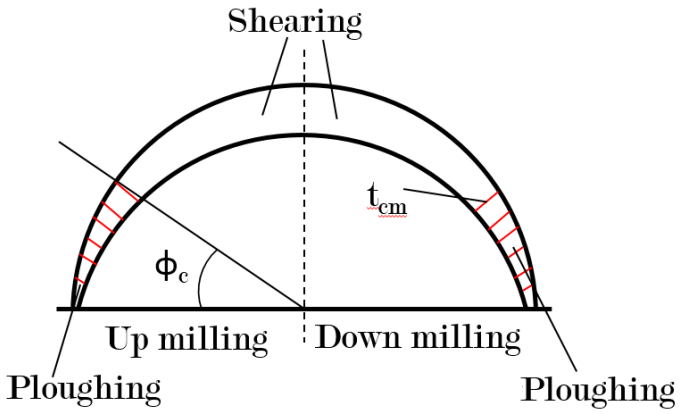

Figure 2.5: Ploughing and shearing regions in full immersion micromilling.

As a consequence, studying the minimum chip thickness of the materials and its influence in machining results is not trivial and several studies have been focusing on improving methods to define its value. Razaei *et al.* [26], for example, studied the minimum chip thickness of Ti-6Al-4V under different cutting conditions in micromilling. They varied tool diameter, cutting speed, feed per tooth, axial depth of cut and lubricant system. Different t_{cm} were found for different cutting conditions with values varying between 25 - 49% of cutting edge radius for dry cutting and between 15 - 34% using minimum quantity of lubrication (MQL).

2.3.2 Material homogeneity in micromilling

Materials which are usually considered to have a homogeneous microstructure might need to be studied as presenting heterogeneous microstructure. As the undeformed chip thickness and cutting edge radius are reduced, depending on the grain size of the material, it can be around the same dimension of the chip thickness, meaning that the tool flute can engage each time in a different microstructure phase which might present different mechanical properties.

Minimum chip thickness is directly related to the material, microtool geometry and cutting conditions and different values can be found with minimal changes in one of these factors. Besides the material properties, the microstructure also has a great influence in the process behavior for several materials. As in micromilling the cutting edge radius is reduced, but the grain sizes of the materials continue with the same dimensions, cutting edge tends to engage with one grain at a time. As each phase of a material can present very different mechanical properties, the process is highly influenced by the constituent phases of the material, as showed in Fig. 2.6.

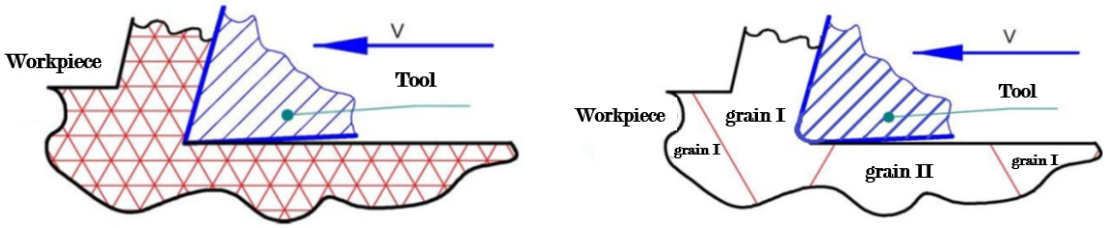

(a) Conventional milling.

(b) Micromilling.

Figure 2.6: Microstructure influence in micromilling cutting mechanics.

Attanasio *et al.* [27] studied the influence of the microstructure in micromilling of Ti-6Al-4V. Titanium alloys microstructure are connected to the history of the material in terms of processing and heat treatment. The authors achieved four different common microstructures of this alloy by carrying out annealing treatments with different times and temperatures. They analyzed mechanical properties, cutting forces, tool wear, groove shape and burr dimension during micromilling experiments using a 200 μm tool. They found out that, among the microstructure studied, a fully lamellar microstructure presented lower cutting forces and tool wear.

2.4 Cutting force and specific cutting force in micromilling

There are several models to calculate machining forces. The simpler one is expressed in Eq. 2.5 where F_c is the force tangential to the spindle speed, F_r is the

radial force and F_z is the force in the tool axis direction.

$$F(\phi) = \begin{bmatrix} F_c \\ F_r \\ F_z \end{bmatrix} = \begin{bmatrix} k_c \\ k_r \\ k_z \end{bmatrix} a_p t_c(\phi) \tag{2.5}$$

The cutting force F_c is calculated multiplying the cutting area ($a_p t_c(\phi)$) by the specific cutting force k_c. Several models have been proposed to predict the specific cutting force. In conventional milling, Kienzle [28] proposed the Eq. 2.6 where k_{s1} and z are constants of the material.

$$t_c = k_c(t_c) = k_{s1} t_c^{-z} \tag{2.6}$$

Kienzle equation leads to the curve showed in Fig. 2.7. It can be seen that when chip thickness decreases, specific force first maintain a linear behavior until it starts to rapidly increase when chip thickness reaches a specific value, turning to a non-linear behavior. Conventional milling usually works with feed per tooth values in the linear behavior region.

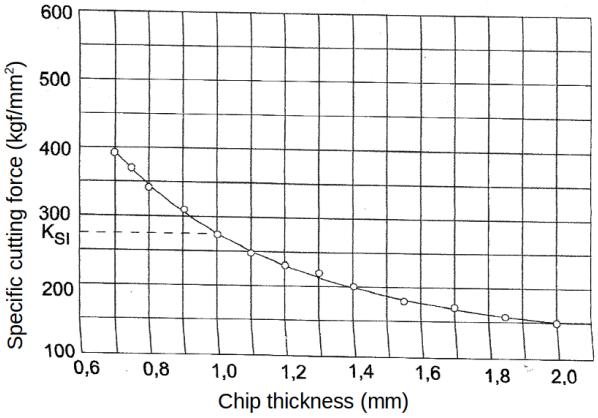

Figure 2.7: Specific cutting force according to Kienzle equation (adapted from [28]).

As an example, the cutting force for a full immersion conventional milling process (width of cut is equal to the tool diameter) considering a depth of cut of 50 μm, feed per tooth of 10 μm, specific cutting force of 20 GPa and cutting speed of 100 m/min is simulated in Fig. 2.8.

Cutting force is directly related to the chip area which is usually approximately given by feed per tooth and the axial depth of cut. In conventional milling, when increasing both parameters, cutting forces tend also to increase as a bigger volume of material is being cutting and, as a consequence, it needs more power to deform and cut the material.

Reduced chip thickness to cutting edge radius ratio often leads to experimental cutting forces present an inverse behavior for small feed per tooth values. Mougo

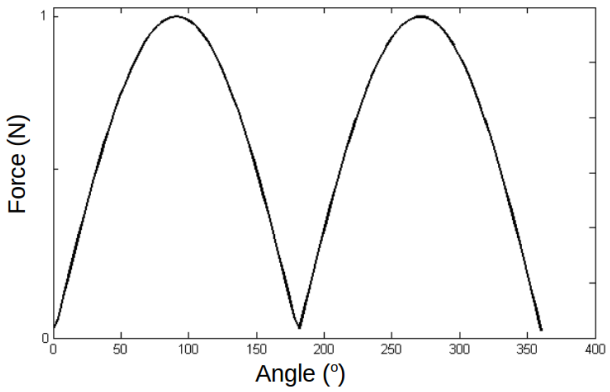

Figure 2.8: Cutting force simulated for specific cutting conditions.

te al. [29] studied the cutting forces when micromilling superduplex stainless steel for a wide range of feed per tooth. The results are presented in Fig. 2.9. Maximum resultant cutting force showed a tendency to increase when increasing feed per tooth for values above cutting edge radius r_e. But for values below the cutting edge radius, when ploughing is dominant, cutting force increased for decreasing feed per tooth.

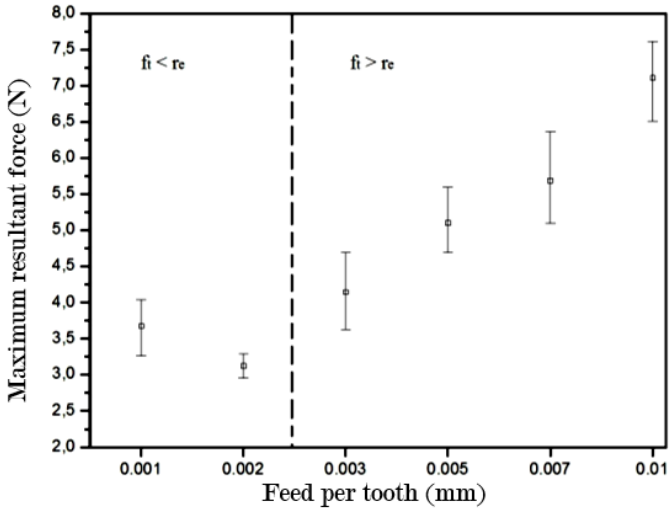

Figure 2.9: Experimental maximum resultant force varying with feed per tooth [29].

Aslantas *et al.* [30] also found a similar result when investigating the cutting performance of nano-crystalline diamond coating in micromilling of Ti6Al4V alloy in comparison with other tool coating. They concluded that for the cutting conditions used, minimum chip thickness was 0.3 the cutting edge radius and the cutting forces below this value also increased for falling values of feed per tooth.

However, this is not a fixed rule. Newby *et al.* [31] also studied the cutting force behavior for different feed per tooth values from 0.5 to 3.0 μm when micromilling an aluminum alloy. They found no inverse cutting force trend as it showed and increased pattern of growing as increased feed was used. The same result was found by Campos [32] that studied the cutting forces when varying feed per tooth and

cutting speed for micromilling of an aluminum alloy. He also found a similar result considering the feed per tooth and the cutting force showed a trend of increasing for growing feed values.

Specific cutting force is the loading necessary to remove a chip with area of 1 mm^2 and is related to the cutting force generated during the machining process. When the chip thickness to cutting edge radius ratio is decreased, the specific cutting pressure tends to present a non-linear behavior due to a higher ploughing influence. Mougo [29] computed the specific cutting pressure for superduplex stainless steel using the experimental cutting forces. She found that for small feed values, specific cutting force presents a non linear behavior rapidly increasing as feed gets lower.

Aramcharoen and Mativenga [24] studied the size effect and tool geometry influence on factors as cutting forces and specific cutting force when micromilling tool steel H13. They found that for feeds below cutting edge radius, specific cutting force presented a non-linear behavior, as showed in Fig. 2.10, and for feed above cutting edge radius, it presented an approximate linear trend.

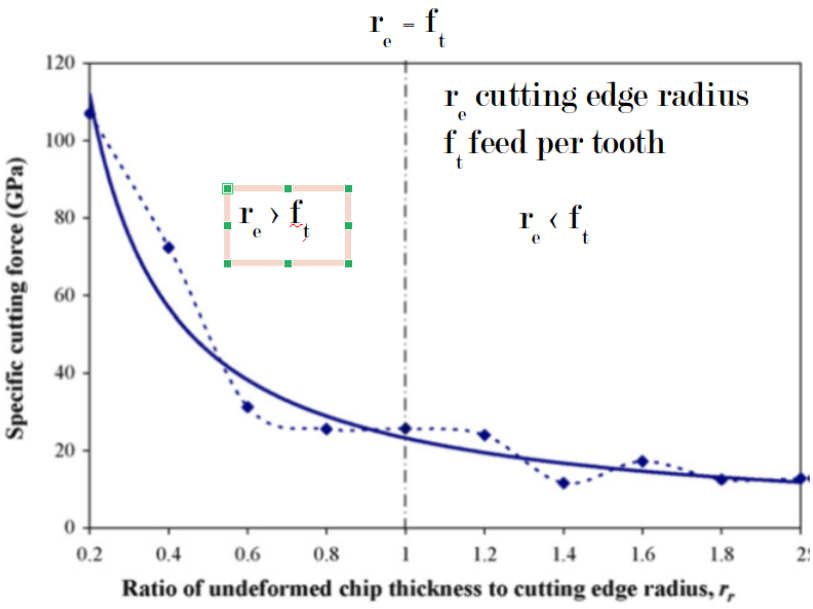

Figure 2.10: Specific cutting force varying with feed per tooth [24].

2.5 Surface roughness in micromilling

The quality of the machined surface is an essential factor during machining as machining operations are used as finishing processes to give the part the quality it needs and surface roughness is one of the parameters studied when analyzing surface integrity. Roughness represents the measure of the surface marks left by the manufacturing process used to create the surface. Along with waviness and form

curves, which present longer wavelengths, they form the surface profile measurement.

Roughness can be influenced by tool geometry, cutting parameters, process dynamics, among others. In conventional milling, usually when feed per tooth is decreased, average roughness presents smaller values as the feed marks left on the machined part would be less spaced, showing a smoother surface. However, in micromilling due to size effect, roughness does not present a standard behavior and also shows an inverse pattern when chip thickness to edge radius ratio is too small.

Aramcharoen and Mativenga [24], for example, also analyzed surface roughness in micromilling of tool steel H13 for a wide range of feed per tooth. Their result is showed in Fig. 2.11 and it can be seen that two regions of roughness behavior can be identified. For feed per tooth smaller than cutting edge radius, average roughness increased for smaller values of feed. While for feed per tooth higher than cutting edge radius, it presented a trend similar to a conventional milling process, where average roughness increases for higher feed values.

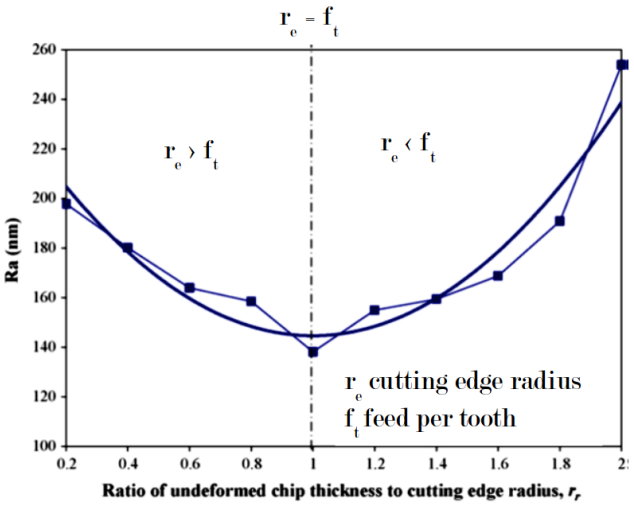

Figure 2.11: Average roughness varying with feed per tooth [24].

Mian [33] studied the size effect influence in micromilling of ferrite steel AISI 1005 and a ferrite/pearlite steel AISI 1045. Besides other parameters, he examined surface roughness using a wide range of feed per tooth values. His results showed that surface roughness presented a deeply non-linear behavior increasing for very small feed values.

2.6 Burr formation in micromilling

According to Gillespie [34], burrs can be formed by plastically deformed and sheared material during the utting process and is highly undesired because it would add an extra manufacturing process for removing it. Also, deburring process in micromachining is a very difficult operation due to the reduced scale of the processes.

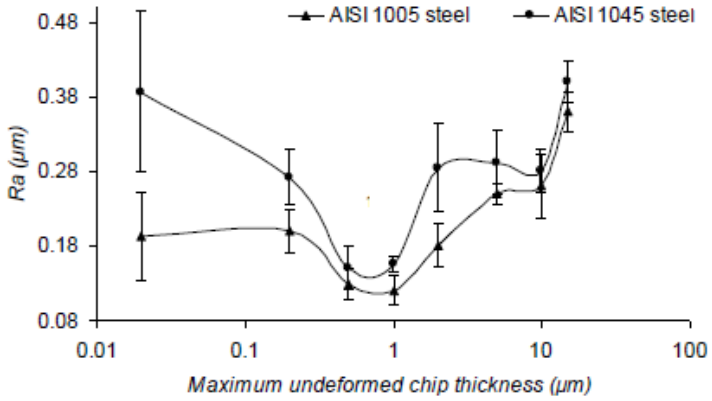

Figure 2.12: Average roughness varying with feed per tooth in micromilling AISI 1045 [33].

According to Hashimura *et al.* [35], when a groove is machined with a microtool, entrance burrs, top burrs, side burrs and exit burrs are generated, as showed in Fig. 2.13.

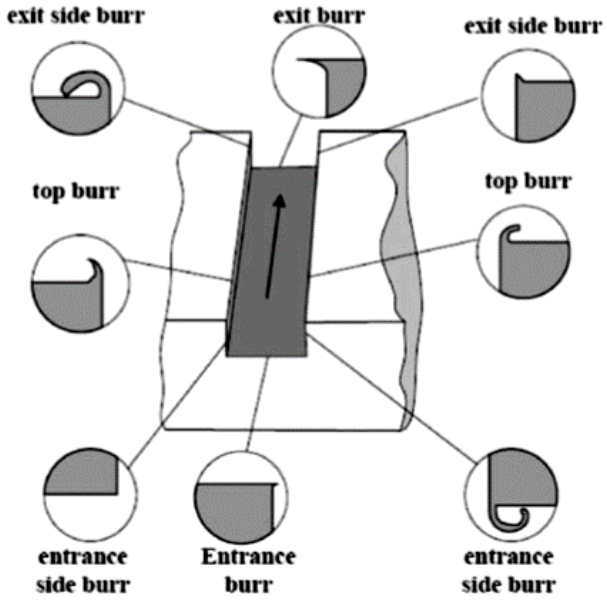

Figure 2.13: Burrs types in groove machining [35].

Hashimura *et al.* also defined the burr formation mechanism in machining. According to them, the pressing and shearing caused by the tool edge on the material surface create a primary shear zone, a plastic deformation zone and an elastic deformation zone. Next, the elastic and plastic deformation expansion causes the chip formation through the primary shear zone. Then, the chip separation occurs and the burr is formed in the part.

Burr formation is a complex and undesired issue in micromachining because, usually, in micromilling the burr size to part size ratio is a lot higher than in con-

ventional milling. Hence, burrs must be minimized in micromilling processes.

The amount of burr formation is influenced by the mechanical properties of the workpiece, tool wear and cutting parameters and, therefore, is related to the size effect in micromilling as tool wear is highly influenced by size effect. *Chern et al.* [36] studied the mechanism of burr formation in micromilling of two aluminum alloys, Al 6061-T6 and Al 3034-T4, when varying feed per tooth. As showed in Fig. 2.14, top burr height presented bigger values for smaller values of feed per tooth. Thus, the aluminum alloy that has smaller tensile and yield strength (Al 6061-T6) presented larger burrs, indicating the influence of the material properties in burr formation.

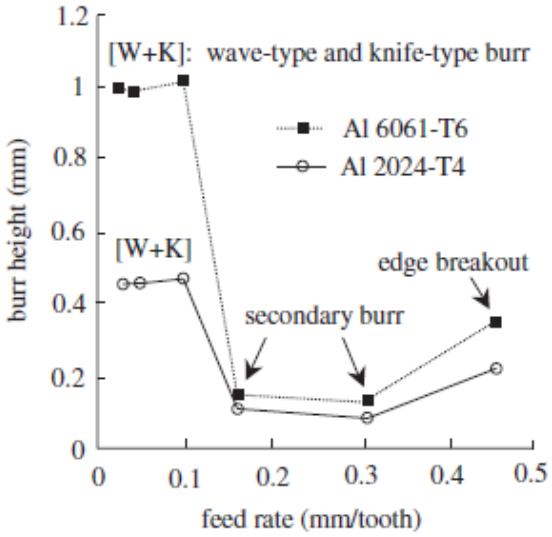

Figure 2.14: Feed per tooth influence in top burr height [36].

2.7 Machinability

Machinability is a general term used to characterize how difficult it is to cut a material. Usually, the machinability of a material is expressed relatively to three measurable machining parameters: tool life, surface finish condition or specific power consumed [37]. However, other machining parameters such as chip disposal, cutting temperatures, productivity and operator safety can be used [28, 38]. It is important to note that a material can present good machinability, or be easy to machine, taking into consideration a specific machining parameter, as tool life, but present a lower machinability when taking into consideration other parameter, as surface roughness of the machined part [28].

Therefore, the basis of comparison between two materials should be specified when comparing them by their machinability. For example, aluminum present higher machinability compared to stainless steel taking into consideration cutting forces or power consumption using optimized cutting conditions.

There are several methods used to measure the machinability of a material. In general, they can be divided into two categories: short duration and long duration methods. In **long duration** tests, tool wear is compared. The tested material and a standard material are machined until the tool life is reached or until a determined tool wear value is reached using different cutting speeds. This method allows to attain a cutting speed to a specific tool life and used only the tool life criterion to determine machinability. For example, Fig. 2.15 shows a tool life curve for a hypothetical material considering three different cutting speeds, and using 0.5 mm tool flank wear criterion to determined tool life. So, for a cutting speed of 100 m/min., the tool can be used for 41 minutes before reaching the wear of 0.5 mm. After computing cutting speed for some wear criterion of the tested and standard material, machinability rate is given by the comparison between the cutting speed of the standard material and of the tested material [28, 38].

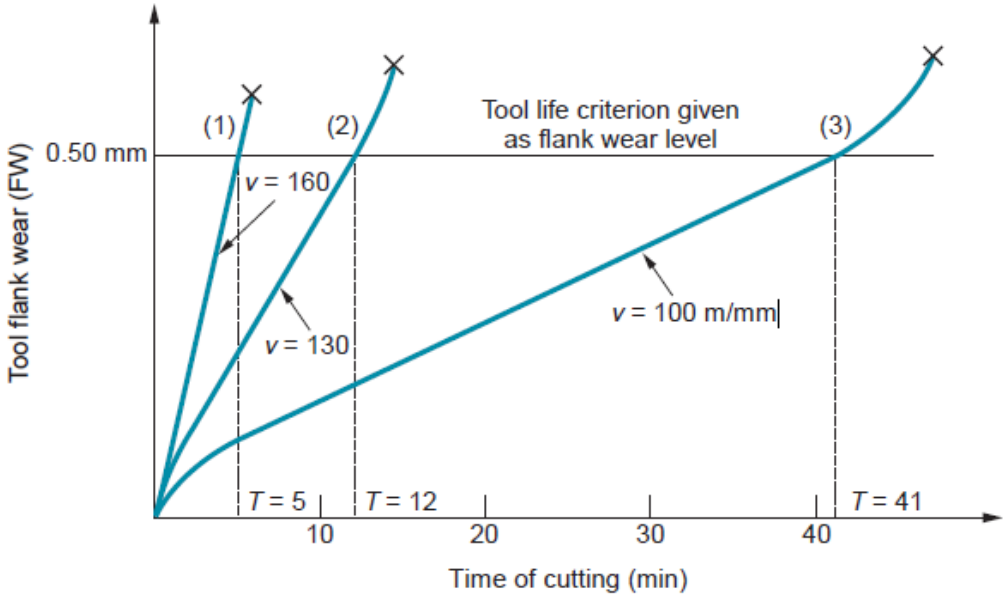

Figure 2.15: Effect of cutting speed on tool flank wear (FW) for three cutting speeds. Hypothetical values of speed and tool life are shown for a tool life criterion of 0.50 mm flank wear [39].

The most used standard material in long duration tests is the low carbon steel AISI B1112. If AISI B1112 presents a 100% machinability rating, a material with a rate lower than 100% is more difficult to machine than AISI B1112 steel and if the material rate is bigger than 100%, the material is easier to machine.

In short **duration tests**, when machinability relative to tool life is measured, forced machining conditions are used in order to achieve the end of life in a short time. Short duration tests are also performed relative to cutting forces and surface roughness because with few tool passes these parameters can be measured and machinability evaluated.

Summarizing the relation between machinability and machining criteria:

- Tool life criterion - is the most used criterion because it envolves the economic point. If a material produces more rapid tool wear, and as a consequence tool life is reached more quickly, the material presents worse machinability. The criterion of tool life is specified according to the application of the material, that is, the amount and types (crater, flank, notch and nose wear) of wear that one considers as the tool life varies;

- Energy consumed criterion - energy consumed during cutting operation is directly related to the cutting forces generated when cutting a material, which is related to the specific cutting force of the material. Specific cutting force is an empirical material property that can be determined by measuring the cutting forces during a cutting operation and using the experimental values to compute the specific cutting force. Cutting forces are related to power of the drive motor of the machine-tool, the roughness of the surface machined, the vibration during the process, tool wear and others. The larger the specific cutting force, the larger is the cutting force and worse is the machinability;

- Surface finishing criterion - a material, according to this criterion, would be more easily machined than other if, under certain machining conditions, it delivers a better surface finishing, that is, a lower surface roughness than the other.

Usually the same criteria are used to study the machinability of a material in conventional and micromilling. As an example, Teng *et al.* [40] recently investigated the machinability of magnesium based metal matrix composites in micromilling. They analyzed cutting force, surface morphology and chip formation when varying feed per tooth, spindle speed and depth of cut.

Katahira *et al.* [41] also performed an experimental machinability study in micromilling. They studied surface integrity of sapphire machined with polycrystalline diamond under different cutting conditions. Thus, Boyuan Xie [42] carried out an experimental machinability research in micromilling of amorphous materials as zirconium based bulk metallic glass and BK-7 glass. He studied tool wear, cutting forces and surface roughness under different cutting conditions.

2.7.1 Material properties affecting machinability

Machinability is not an easy characteristic to be defined. For example, steels of the same chemical composition, but different metallographic structure may have

widely different machining characteristics. Several material properties and conditions have influence on the machining: hardness and mechanical resistance, ductility, thermal conductivity, hardening rate, microstructure, chemical composition.

- Hardness and mechanical resistance - usually, materials with low hardness and mechanical resistance have better machinability as it is easier to machine softer materials. However, extremely ductile materials with low hardness can present facility to provoke built-up edge (BUE). Table 2.1 shows the machinability rating for some engineering materials regarding the Vickers hardness. For this table, SAE 1212 material is used as the standard material and it has a 100% machinability rate. Materials with rating over 100% present better machinability than SAE 1212 and materials with rating lower than 100% have worse machinability;

Table 2.1: Machinability ratings and hardness for some engineering material taking SAE 1212 as the standard material [38].

Material	**Hardness (HV)**	**Machinability rating (%)**
SAE 1212	152-162	100
SAE 1020	129-139	60
SAE 4130	180-185	45
HSS	222-232	35
Aluminum alloys	–	145
Chromium copper	–	65
Leaded copper	–	250
Forging brass	–	245
Phospher bronze	–	60

- Ductility - lower ductility values tend to benefit machinability as machining of brittle materials presents the formation of discontinuous chips and lower energy wasted caused by the friction of the chip with the tool face. However, low ductility is achieved with high hardness and vice-versa. Therefore, a good machinability is attained with a good balance between ductility and hardness [28];

- Thermal conductivity - a high thermal conductivity of the machined material means that heat generated during cutting is rapidly removed from the cutting region. Therefore, the cutting tool does not overheat and, as a consequence, does not wear quickly. So, higher thermal conductivity leads to good machinability;

- Work hardening - many metals have their hardness and resistance raised when plastically deformed by cold works such as rolling, bending, forging and shaping. This phenomenon is called hardening. A material with high hardening

rate will have its hardness significantly increased and, hence, presents worse machinability.

Figure 2.16 shows a general view of the main factors which affect the three machinability criteria: tool life, cutting forces and surface roughness. The factors are very interdependent and most of them are related with other in some way, but the figure gives an overview which are detailed next.

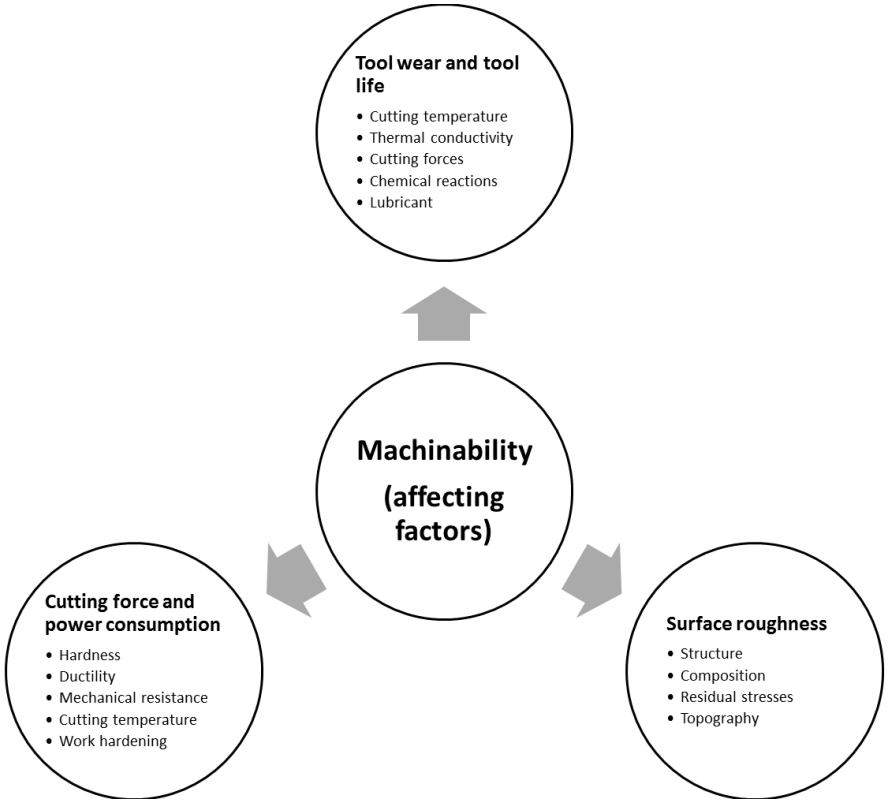

Figure 2.16: General view of the main factors which affect the three machinability criteria: tool life, cutting forces and surface roughness..

As it was seen, besides the cutting parameters and characteristics of the machining operation in question, the machinability of a material is intrinsically related to its properties, especially in micromilling. Hence, when analyzing the machinability of a material, it is essential to study and to characterize the material to be used. The next chapter covers the important aspects of titanium and its alloys regarding the present study.

Chapter 3

Machining titanium alloys

This chapter approaches the important aspects of titanium and its alloys, focusing on the commercially pure titanium and Ti-6Al-4V alloy as the following chapters deal with ECAP and SLM materials. It deals with their crystallographic transformations and microstructure characteristics, applications, properties and how these inherit characteristics can influence their machinability.

3.1 Titanium and its alloys

At room temperature and pressure, pure titanium presents a close-packed hexagonal (HCP) α structure and when it overpasses 882°C, it goes through an allotropic transformation to a body-centered cubic (BCC) β phase, which remains until the melting point which is 1668ºC.

The main aspect of alloying titanium is changing the alpha-beta transus temperature and the formation of a two-phase zone, with the presence of both alpha and beta phases. Alloying elements which presents a high solubility in the alpha phase normally raise the transformation temperature. They are called alpha stabilisers such as aluminum, oxygen, nitrogen and gallium. Elements which depress the transformation temperature, strengthen the beta phase and present low alpha solubility are called beta stabilisers, as molybdenum and vanadium. As it can be seen in Fig. 3.1, beta stabilisers can also form an eutectoid point, like copper, iron, chromium and manganese.

Beta stabilisers have two important advantages over alpha stabilisers. First, the beta phase of titanium has an inherently **lower resistance** to deformation than the alpha modification. Therefore, beta stabilisers tend to improve alloy fabricability during both hot and cold working operations. Second, when added in sufficient percentage, beta stabilisers give to the **material heat treatment** capability which allows significant strengthening to be achieved.

Despite the commercially pure category, titanium alloys are usually classified

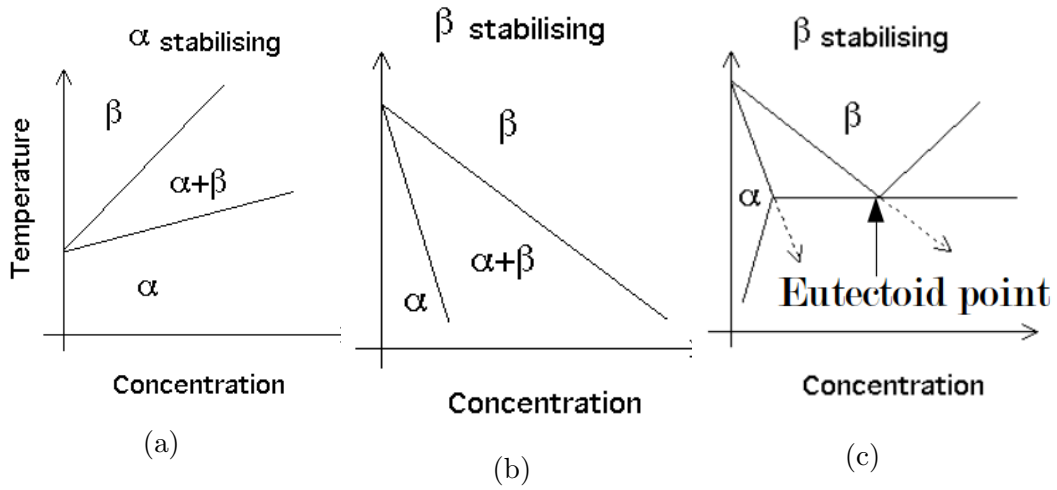

Figure 3.1: Phase diagrams for Ti alloys.

into three basic groups, considering the effect that the alloying element has on the crystallographic structure of the material, that is, on the stability of the alpha and beta phases: Alpha alloys, Beta alloys and Alpha-Beta alloys.

1. Alpha alloys - these alloys are created with alpha stabilisers or neutral elements, as tin. They are non-heat treatable, very weldable and present reliable strength at elevated temperatures. They can present 1-2% of beta stabilisers, which are called near alpha alloys;

2. Beta alloys - these alloys are created with beta stabilisers. They are heat treatable, weldable and present high strength up to intermediate temperature levels;

3. Alpha-Beta alloys - these alloys are the most commonly used as they combine the best characteristics of the other two categories, creating a balance between strength, weight and corrosion resistance. They are heat treatable and made with alpha and beta stabilisers.

The ASTM International specifies several grades of titanium alloys, according to their composition. For commercially pure titanium, the unalloyed titanium grades 1 through 4 as well as 7, 11 and 12 are specified according to the percentage of presence of other chemical compounds, like oxygen gas, iron, hydrogen gas, carbon and nitrogen gas.

In the present study, as it will be described in Chapter 6 it is used Grade 2 and Ti-6Al-4V alloy (Grade 5), which is a Beta-Alpha alloy as it has the presence of aluminum, an alpha stabiliser, and vanadium, a beta stabiliser. Hence, the next sections will focus mainly on these materials.

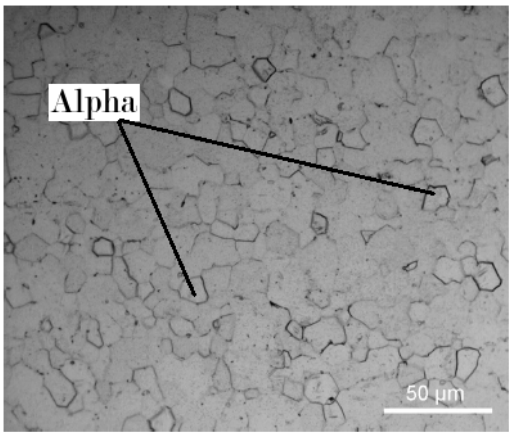

(a) Typical microstructure of CP-Ti grade 2 [43].

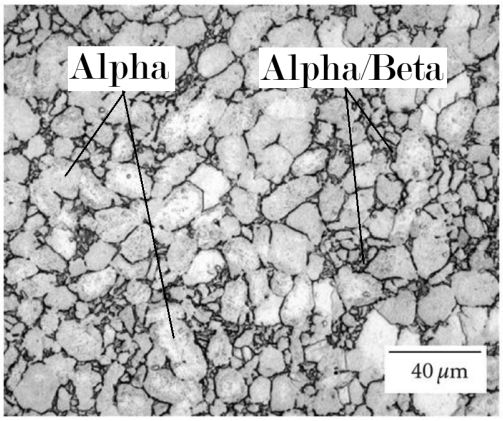

(b) Typical microstructure of Ti-6Al-4V [44].

Figure 3.2: Titanium microstructures.

Figure 3.2 shows typical microstructures for commercially pure titanium and Ti-6Al-4V alloy. Figure 3.2a shows the microstructure of an annealed grade 2 titanium bar. It consists of equiaxed alpha grains and some intergranular beta phase, which indicates that the annealing temperature was above the alpha-beta transition temperature. Figure 3.2b shows the microstructure of an annealed grade 5 titanium bar. It consists of equiaxed alpha grains (light) in transformed beta matrix (dark).

Nevertheless, titanium and its alloys microstructures are strongly dependent of their processing and heat treatment history, which means that the percentage and/or the presence of alpha and beta phases and the shape and dimensions of the grains will be influenced by the manufacturing process (forging, rolled etc.) and by the heat treatment processes and parameters used.

Titanium is a non-ferrous metallic material which combines several fundamental properties, which make it a very important material. According to ASTM International, titanium grades 2 and 5 are composed of the maximum weight percentages showed in Tab. 3.1. Also, Tab. 3.2 summarizes the main mechanical, physical and thermal properties of titanium grades 2 and 5.

Table 3.1: Titanium grades 2 and 5 composition.

Titanium components (Wt. %)								
Material	C	Fe	H	N	O	Al	V	Ti
Grade 2	max 0.1	max 0.3	max 0.015	max 0.03	max 0.25	-	-	99.2
Grade 5	-	max 0.25	-	-	max 0.2	6	4	90

3.2 Titanium mechanical properties

One of the most sought after characteristic of titanium is its weight to strength ratio. Titanium is as strong as steel, but is 45% lighter. Regarding aluminum, it is twice as resistant, but 60% heavier. This property is what makes it an ideal material for aerospace engineering applications.

The density of both titanium grades 2 and 5 are similar, as it can be seen in Tab. 3.2. However, they differ in mechanical resistance. The alloying elements, vanadium and aluminum, significantly increase the mechanical resistance of the material. The ultimate tensile strength (UTS) of the alloy is more than twice the UTS of the pure titanium.

Also, pure titanium typically presents hardness values around 160 HV while the titanium alloy presents values around 360 HV as titanium alloy can undergo heat treatment.

Another great property of the titanium is its corrosion resistance. When fresh titanium is exposed to the atmosphere or to any environment that contains oxygen, it readily forms a thin layer of oxide on its surface, providing great protection against corrosion. In general, adding alloying elements to pure titanium decreases its corrosion resistance, but titanium grade 5 still presents excellent corrosion resistance.

Table 3.2: Summary of typical mechanical, physical and thermal properties of titanium grades 2 and 5 [45].

Titanium Grade	**Grade 2**	**Grade 5**
Ultimate Tensile Strength (MPa)	485	1000
Yield Tensile Strength (MPa)	345	910
Elastic Modulus (GPa)	105-120	114
Elongation at Break (%)	28	14
Hardness (Vickers)	160	360
Density (g/cm3)	4.51	4.42
Thermal Conductivity (W/mK)	21.97	7.2

One fundamental characteristic of pure titanium and Ti-6Al-4V that makes them strong candidates for biomedical applications is their biocompatibility. Titanium and its alloys are highly known as non-toxic materials and are very well accepted by the human body. Ideally, pure titanium would be used for the fabrication of all titanium medical implants, however, for some applications where higher mechanical resistance are required, alloying elements must be used and Ti-6Al-4V is, today, the most used titanium alloy in medical implants. Despite that, several researches have raised some concerns regarding the long term performance of these alloys as it would release vanadium and aluminum in the human body. These studies indicate that this fact might be associated with health problems as Alzheimer disease, neuropathy

and ostemomalacia.

3.2.1 Thermal conductivity affecting cutting temperature

Titanium and titanium alloys thermal conductivity is relatively low when compared with that of steel (30 - 60 W/mK) or aluminum alloys (220 - 240 W/mK). Table 3.3 shows the thermal conductivity values for pure titanium and alloys when varying the temperature. It can be seeing that for pure titanium, thermal conductivity remains almost constant, but not for the alloys, occurring a big variance.

Table 3.3: Thermal conductivity k of titanium and its alloys versus temperature [46].

Temperature (°C)		**0**	**200**	**400**	**600**	**800**
k **(W/mK)**	**Pure Ti**	22	21	21	21	–
	Ti alloys	5.5 - 8.0	8.0 - 12.0	10.0 - 17.0	12.5 - 21.0	15.0 - 25.0

As already seen, low thermal conductivity causes concentration of heat on the tool cutting edge. The tool wears more quickly and, a a consequence, the tool life is reached earlier. Therefore, low thermal conductivity of the titanium and its alloys is one of the issues that causes them to present poor machinability.

Veiga *et al.* [46] did an extensive review on the machinability of titanium alloy Ti-6Al-4V, covering the relationship between the material properties and machinability, according to several published papers. Figure 3.3 shows the variance of thermal conducticity k, Rockwell hardness HRC, elastic modulus E and ultimate tensile strength UTS with material temperature. The increase of thermal conductivity and decrease of hardness and ultimate tensile strength seem to be beneficial to machinability, regarding heat removal and magnitude of cutting forces. However, the decrease of the elastic modulus results in more susceptibility for workpiece deflection and vibration during cutting.

Ezugwu *et al.* [47] wrote a review on machining titanium and its alloys, covering a variety of alloys and the influence of their properties on the machinability. Figure 3.4 shows the distribution of the heat generated during cutting when machining titanium alloy Ti-6Al-4V and steel. For the titanium alloy, about 80% of the heat generated is conducted into the tool, against only about 50% for steel, due to the low thermal conductivity of the titanium alloy. The percentage is computed dividing the heat of the tool by the total heat generated.

Kikuchi [48] did an experimental study where the cutting temperature was estimated by measuring the thermal electromotive force of the tool-workpiece thermocouple during milling of four different dental materials: pure titanium, Ti-6Al-4V, Ti-6Al-7Nb and brass. Figure 3.5 presents the results of the cutting temperature for all the materials and for four different cutting conditions, varying the cutting speed,

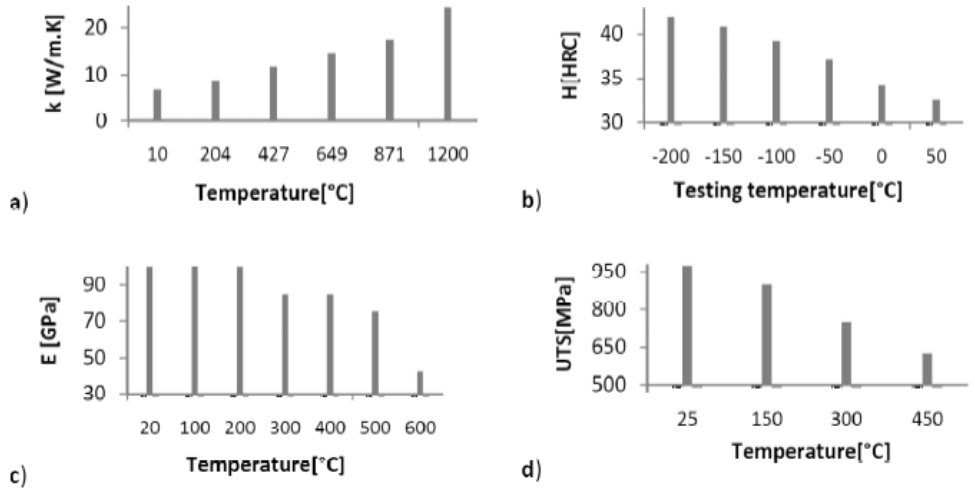

Figure 3.3: Influence of temperature on the properties of Ti-6Al-4V alloy. a) Thermal conductivity; b) Rockweel hardness; c) elastic modulus; and d) ultimate tensile strength [46].

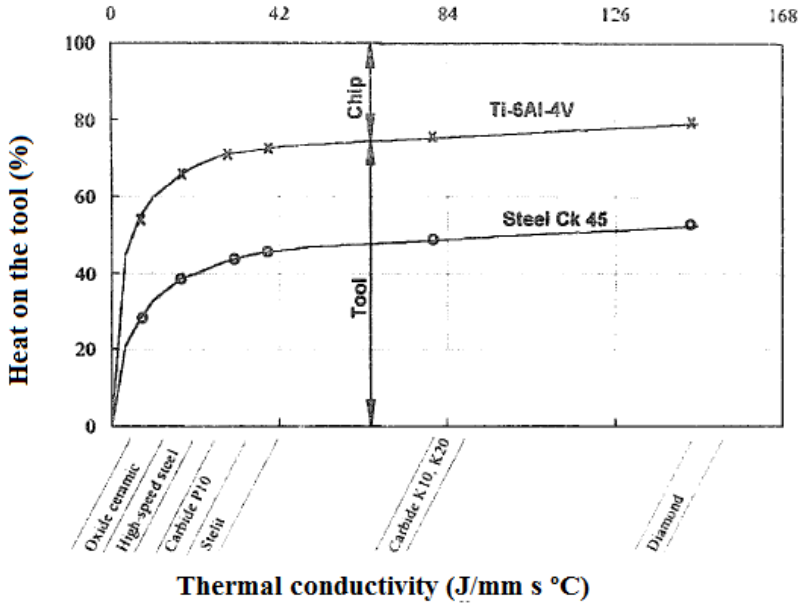

Figure 3.4: Heat distribution during cutting for titanium alloy and steel [47].

feed and depth of cut. No significant difference between the alloys was detected. However, a high difference between the cutting temperature of the alloys and pure titanium can be seeing. This is due to the lower thermal conductivity that the alloys have.

High cutting temperature on cutting titanium and titanium alloys increase the chemical reactivity of the material. Reactivity is not a wanted characteristic as when the material reacts with common gases such as oxygen, nitrogen and hydrogen, it leads to the formation of oxides, nitrides and hydrides, which cause embritlement and decrease of the fatigue strength of the material [46]. Also, an increase of the

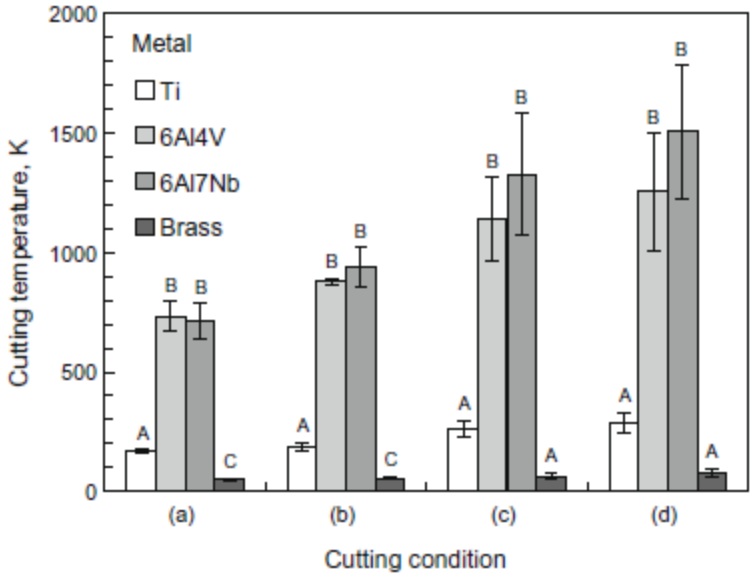

Figure 3.5: Comparison of the cutting temperature among the four metals for each cutting condition. Identical capital letters indicate no statistically significant difference among the mean values of the same cutting condition. [48].

reactivity can lead the material to react with the cutting tool material which can cause galling, smearing and chipping of the workpiece surface and rapid tool wear.

To overcome the low thermal conductivity issue and the consequent high cutting temperature, more efficient refrigeration systems have been developed in order to minimize this problem.

3.3 Machinability of titanium and titanium alloys in conventional milling

Titanium and titanium alloys are widely considered materials with low machinability [19, 46, 47]. This fact is directly related to inherent properties of the material such as low thermal conductivity, low elastic modulus, maintenance of high hardness at elevated temperatures and high chemical reactivity [49].

3.3.1 Hardness and strength affecting cutting forces

High hardness and strength materials require high cutting forces during cutting performing. Table 3.4 shows the mechanical properties for titanium alloy Ti-6Al-4V and four different grades of commercially pure titanium. It can be seeing that the alloy presents higher ultimate tensile strength and hardness than CP-Ti and the annealed Ti-6Al-4V has lower hardness and ultimate strength than the same alloy in aged condition. It is obvious that the alloy, considering these properties, has worse

machinability than pure titanium. Comparing the alloy between the annealed and aged condition, hardness and ultimate strength increase, which would mean lower machinability, however thermal conductivity also increased which would mean a better machinability.

Table 3.4: Selected properties of Ti-6Al-4V and commercially pure titanium [46, 50].

Material	**UTS (MPa)**	**YS (MPa)**	**E (GPa)**	**H (HV)**	k
CP-Ti grade 1	345	221	103	126	22
CP-Ti grade 2	483	352	103	168	22
CP-Ti grade 3	593	462	103	211	22
CP-Ti grade 4	683	559	104	263	22
Ti-6Al-4V (annealed)	895	825	110	340	7.3
Ti-6Al-4V (aged)	1035	965	–	360	7.5

Hardness and strength will greatly influence cutting forces magnitude. In machining, cutting process is generally an oblique three-dimensional operation, but it is often considered to be a bi-dimensional process to facilitate simulations. In general, the resultant cutting force acting on the tool can be divided into three components: F_x, F_y and F_z. These components are on the part reference and can be translated into the tool reference, using a rotational matrix, into radial force F_r, tangential force F_t and perpendicular force F_z.

Kikuchi and Okuno [49] carried out experiments to analyze the difference between the machinability of dental materials: CP-Ti, Ti-6Al-4V, Ti-6Al-7Nb and brass. Milling experiments were performed while measuring cutting forces for four different cutting conditions varying cutting speed, feed and depth of cut and, also, Vickers hardness and surface roughness were measured. Figure 3.6 shows the comparison between the hardness for all materials. As expected, the titanium alloys have higher hardness than pure titanium and brass.

Figure 3.7 presents the Kikuchi and Okuno [49] results for the cutting force measurements where F_{x+y} is the sum of X and Y components of the cutting force. Again as expected, cutting forces were higher for the titanium alloys, as hardness and ultimate tensile strength of these materials are higher than of pure titanium. Also, thermal conductivity of the alloys are lower, which means that cutting temperature for these materials are higher at the cutting region, helping to increase tool wear, which can affect cutting forces.

Wang *et al.* [51] carried out turning tests on Ti-6Al-4V using three different tungsten carbide tool with different cutting speeds. The authors analyzed the relationship between cutting force and cutting speed as well as cutting force and cutting distance. Figure 3.8 shows the results of the resultant force varying with cutting distance for two different tools. It can be noticed that for both tools, cutting force tends to initially increase and then decrease with increasing cutting distance. The

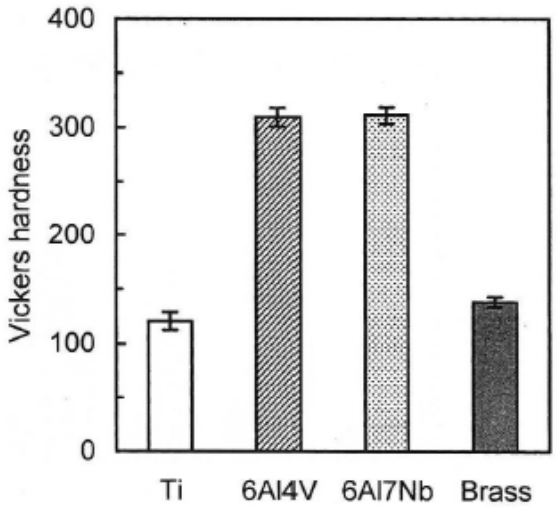

Figure 3.6: Vickers hardness of the metals [49].

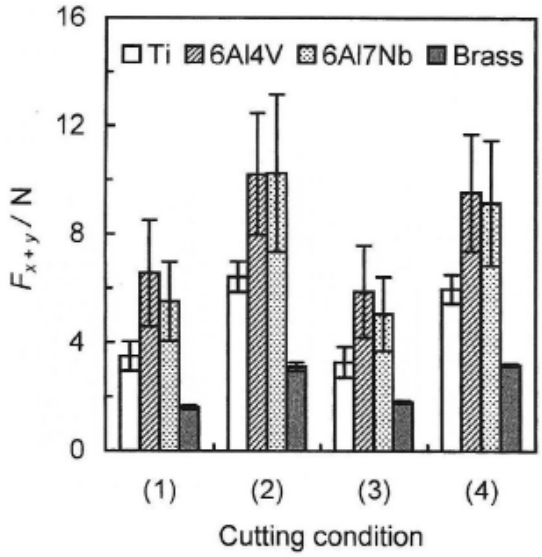

Figure 3.7: Cutting force magnitude in milling for four cutting conditions [49].

initial increase can be linked to the tool wear, while the decrease can be a result from the reduction of the depth of cut caused by excessive tool wear.

3.3.2 Factors affecting surface roughness

Surface roughness on machining titanium and its alloys are directly affected by the factors mentioned. High thermal conductivity of titanium leads to an increasing temperature at the cutting region which causes higher cutting forces and rapidly tool wear. Tool wear often generates lower surface finishing in machining as it changes the cutting edge shape by deforming and re-shaping the flank and rake face, causing changing in the cutting mechanism.

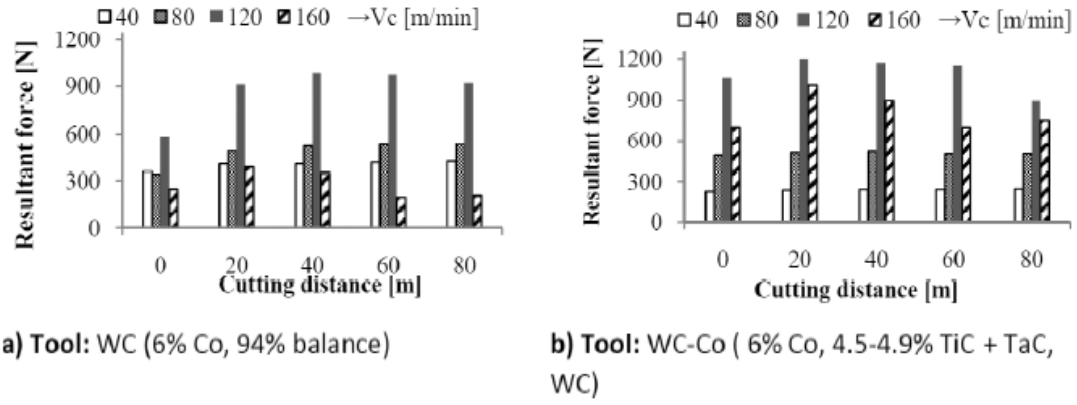

Figure 3.8: Turning resultant force versus cutting distance for several cutting speeds using two cemented carbide tools, data from [51], [46].

Ke *et al.* [52] stated that the temperature on the cutting region is so high that it can damage the finished surface of titanium alloys as chips are melted and help the adhesion of chips to the tool and machined surface.

Besides analyzing the cutting forces, Kikuchi and Okuno [49] also measured roughness of the machined surfaces after performing experiments to analyze the difference between the machinability of dental materials: CP-Ti, Ti-6Al-4V, Ti-6Al-7Nb and brass. Figure 3.9 shows the statistical results of the analysis for mean roughness and maximum roughness values. No significant difference was found between the materials for all four cutting conditions.

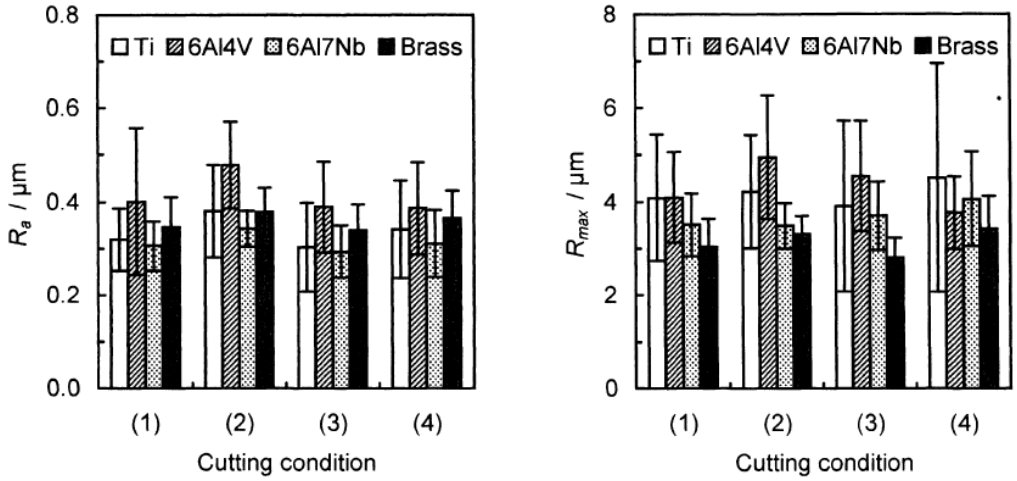

Figure 3.9: Surface roughness of cut surfaces for four different conditions [49].

CheHaron *et al.* [53] investigated the surface integrity response of Ti-6Al-4V when turning under different cutting conditions. They measured average roughness and microhardness at several depths beneath the machined surfaces. Figure 3.10 shows the evolution of average roughness during cutting for different cutting speeds. It can be seeing that roughness tends to get smoother after some time of cutting in

the beggining of the tool life. However, when approximating to the end of the tool life, roughness rapidly increases, probably because of the quick tool wear.

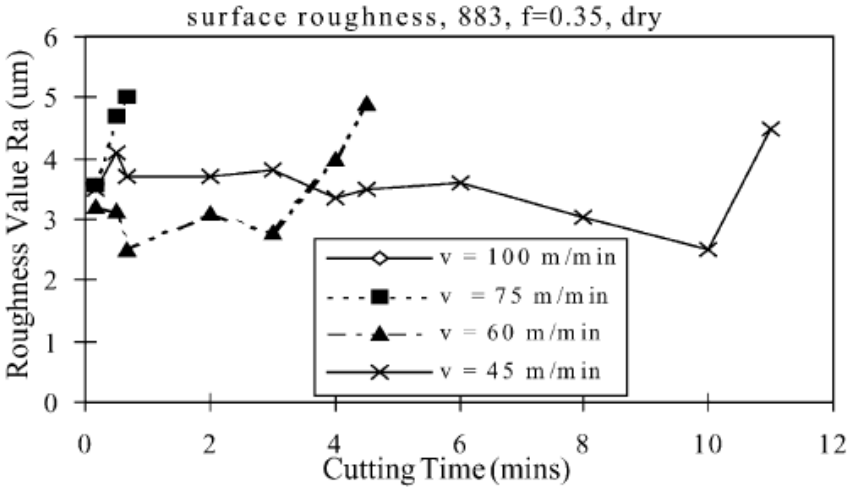

Figure 3.10: Evolution of average roughness during cutting for different cutting speeds [53].

3.4 Machinability of titanium and titanium alloys in micromilling

As it was seen in Chapter 2, machining results in micromilling can be significantly different than in conventional milling due to size effect. Micromilling of titanium alloy Ti-6Al-4V has been extensively studied in recent years. However, most published papers do not cover machinability criteria as surface roughness, burr formation, cutting forces, tool wear etc. Also, practically no study dealing with machinability of pure titanium in micromilling was published. Therefore, there is a lack of a complete study aiming to fully characterize the machinability characteristics of titanium. Besides, some of the studies provide contradictory results, which is common in micromilling as it is a highly sensitive process.

machinability of titanium in micromilling will be influenced by the same properties that affect the conventional milling machinability. However, size effect will play an additional important role and can drastically change the expected results. Recently, Carou *et al.* [54] produced a review on micromilling of titanium and its alloys. It summarized the main published papers on topics like surface integrity, cutting tools, colling systems and finite element modeling.

Rezaei *et al.* [26] aimed to define the minimum chip thickness of Ti-6Al-4V alloy during micromilling by analyzing cutting forces, specific cutting forces, surface roughness and the grooves surface images. When analyzing specific cutting force,

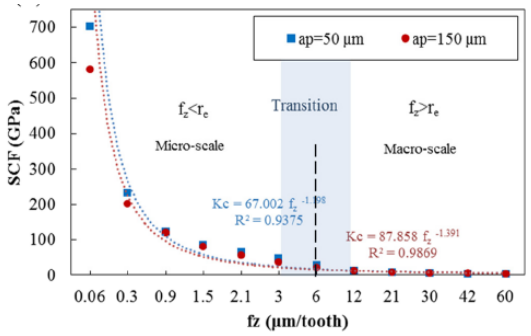

(a) Feed per tooth influence in specific cutting force [26].

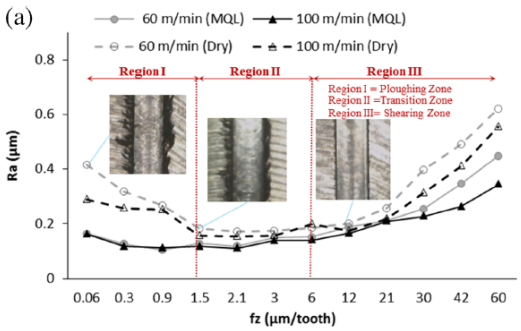

(b) Feed per tooth influence in surface roughness [26].

Figure 3.11: Specific cutting force and surface roughness analysis to define minimum chip thickness.

they defined the minimum chip thickness by characterizing the feed per tooth where specific force turns from linear to non-linear behavior, as showed in Fig. 3.11a. They also identified three different regions of roughness behavior when increasing the feed. First, roughness presented a fall, in the second region it stayed in the same level and finally, in the third region (higher feeds), it presented a strong increase. The second region was defined as transition from ploughing to shearing, as showed in Fig. 3.11b.

Ozel *et al.* [55] developed a finite element model to predict burr formation in micromilling of Ti-6Al-4V alloy considering the variation of the cutting edge radius. As titanium is a difficult to machine material, it wears the tool quickly. So, they analyzed the variation of the edge radius with cutting length and its influence in top burr height. They concluded that a bigger cutting edge radius leads to more burr formation.

Cheng *et al* [56] developed a method for minimization of burr formation in micromilling of Ti-6Al-4V by coating the surface to be machined with a resin and then removing it. In the experimental validation of the method, their results showed that feeds per tooth smaller than minimum chip thickness presented higher burr formation for downmilling cutting. Also, they found out that feed per tooth is the main parameter influencing the top burr size, as the results for different axial depths of cut did not present significant differences.

Thepsonthi and Ozel [57] applied an experimental design based on Taguchi method to verify the optimal cutting conditions for micromilling Ti-6Al-4V alloy. They used three factors (feed per tooth, spindle speed and depth of cut) with three levels each. They analyzed burr formation and surface roughness. Their result showed that higher feed rates lead to better surface finishing and higher depths of cut lead to less burr formation.

Kim *et al.* [58] developed one of the most complete published works in mi-

cromilling of Ti-6Al-4V. They analyzed the effects of cutting speed and feed per tooth in cutting forces, surface roughness, burr formation and microchips morphology. They found out that lower feeds lead to higher burrs and that cutting speed did not present a big influence in burr formation. Also, they found that increased cutting speed lead to smoother surface finishing as well as higher feeds. However, their study lacked a material characterization which could explain some of the results they presented.

It was seen the main aspects of titanium alloys and their relation to the study of machinability in macro and micromilling. However, titanium alloys can undergo some processing so their properties can be changed according to the application in which they will be used. For an example, commercially pure titanium can undergo a process to increase its mechanical resistance so its application range can be widen. Equal channel angular pressing, that is the topic of the next chapter, is one of the process used to achieve this improvement in commercially pure titanium.

Chapter 4

Equal Channel Angular Pressing (ECAP)

This chapter presents the severe plastic deformation (SPD) process of equal channel angular pressing (ECAP). It explains the technology and stages involved in the process as well as the effects that ECAP causes in the materials and the mechanisms that lead to these changes. Also, the application of the process in commercially pure titanium is handled as well as a review of machinability studies on titanium processedby ECAP.

4.1 ECAP process

Severe plastic deformation technique can be defined as the metal forming process in which a large strain is introduced into a bulk material with the objective to create ultra-fine grained (UFG) metals without the introduction of any significant change in the overall dimensions of the solid [59–61]. The grain size of a polycrystalline metal is directly related to the strength and fracture toughness by Eq. 4.1, the Hall Petch equation [62].

$$\sigma_y = \sigma_0 + k_y {d_g}^{-1/2} \tag{4.1}$$

where σ_y is yield stress, d_g is grain size and σ_0 and k_y are specific constants of the material. Equation 4.1 describes that the yield stress increases with decreasing square root of the grain size and it was experimentally proved by Petch [63]. The decrease of grain size leads to a higher tensile strength without reducing the toughness [64]. Azushima *et al.* [64] states that conventional metal forming processes like rolling, forging and extrusion usually impose plastic strain smaller than 2.0, because when plastic strain is greater than 2.0, the thickness of the material becomes very thin and is not suitable to be used as structural parts. In order to

impose extremely large strain on a bulk material without changing its shape, severe plastic deformation processes have been developed.

Severe plastic deformation operations have been used to improve mechanical properties of metals for a long time. For example, Bridgman [65] carried out a series of experiments, more than 60 years ago, where metals were subjected to large deformation under high applied pressures in attempts to improve mechanical properties of materials that were inherently brittle. However, SPD techniques have gained more attention in metallurgy only since Segal *et al.* [66] work from 1974, in which he established the equal channel angular pressing process guidelines, then called equal channel angular extrusion (ECAE), and lead him to patent the technique [67].

After the work of Segal and co-workers, a long list of severe plastic deformation technologies have been proposed, developed and evaluated, besides ECAP, These techniques include high-pressure torsion (HPT), multi-axial forging, twist extrusion (TE), cylinder covered compression, accumulative roll-bonding (ARB), friction stir processing (FSP) and submerged friction stir processing (SFSP), some of which are already very well-established methods for achieving UFG materials with grain sizes in the range of 70 to 500 nm, depending upon the crystal structure [68, 69].

Azushima *et al.* [64], Toth *et al.* [59], Verlinden [60], Estrin [61] and Vinogradov and Valiev [61] works present extensive reviews over main SPD techniques, the impact on materials microstructure, the mechanical properties of metals processed by SPD and the application of ultra-fine grained metals.

Equal channel angular pressing is now the most popular and developed SPD technique [61] and according to Valiev and Langdon [68], it is an especially attractive processing technique for several reasons, as:

- It can be applied to large billets, therefore having the potential for producing materials which can be used in a wide range of structural applications;
- It is a relatively simple procedure that is easily performed on a wide range of alloys and uses equipment that is available in most laboratories;
- Reasonable homogeneity is attained through most of the as-pressed billet;
- The process may be scaled-up for the pressing of relatively large samples.

Conventional ECAP process is shown schematically in Fig. 4.1a. The metal sample is pressed by a plunger into the die through a channel that is bent by an abrupt angle and has the same cross sectional area through the hole extension. The material is plastically deformed by simple shear as it passes on the intersection of the channels and the more abrupt is the angle, greater the strain imposed to the

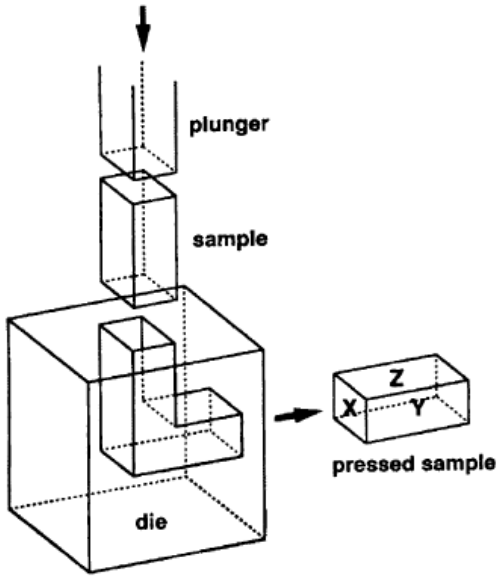

(a) Schematic illustration of a typical ECAP matrix [68].

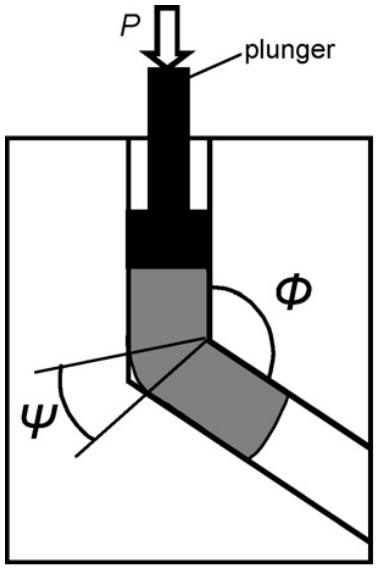

(b) Schematic representation of ECAP process [64].

Figure 4.1: Titanium microstructures.

metal billet will be. The sample can be fabricated in the form of a rod or a bar and is machined to fit within the channel. Despite the introduction of a very large strain when the sample passes through the shear plane, it finally emerges from the die without experiencing any change in the cross-sectional dimensions, as illustrated by the figure. This figure also defines three separate orthogonal planes: X is the transverse plane, perpendicular to the flow direction; Y is the flow plane which is parallel to the side face of the billet; and Z is the longitudinal plane parallel to the top surface of the billet.

Figure 4.1b shows the schematic of the cross-section of an ECAP die and some of the main parameters of the process: ϕ is the angle of the bent channel (equal to 90° in Fig. 4.1a); ψ represents the outer arc of curvature where the two channels intersect (equal to 0° in Fig. 4.1b); and the pressure P made by the plunger onto the sample into the channel.

The nature of the imposed deformation is simple shear which occurs as the sample passes through the angle ϕ of the channel, as shown in Fig. 4.2. In the figure, ϕ is equal 90°, so the shearing plane is located exactly at the intersection of the channels and makes a 45° with the channels. If ϕ was different, the inclination of the shearing plane would also be different [70].

As it is also shown in Fig. 4.2, the element numbered 1 of the sample is deformed into element numbered 2 by the shear plane. Due to the die design, that avoid the flow of material in other directions rather than longitudinal to the channel, the sample emerges without any dimension change, despite the introduction of very

intense strain.

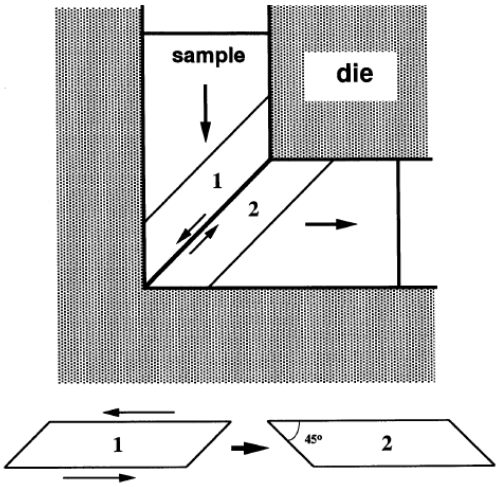

Figure 4.2: The principle of ECAP showing the shearing plane within the die: the elements numbered 1 and 2 are transposed by shear as indicated in the lower part of the illustration [70].

Since the cross-sectional area of the sample remains the same, it can be pressed repetitively using the same ECAP die to attain very large accumulative strains and ultra-fined grain sizes [19, 68], performing as many passes of the sample through the channel as one may need.

4.2 Accumulative strain in ECAP

During each pass of the sample through the die, sample is deformed when passing through the shearing plane and an effective strain is induced in the material. When multiple ECAP passes are carried out, large accumulative strains are attained. The magnitude of this strain can be estimated by an analytical approach based on the various possible configurations of the die, illustrated schematically in Fig. 4.3 in two-dimensional representation.

In the figure, a square element labeled *abcd* is deformed into the element $a'b'c'd'$ when passing through the shearing plane for $\psi = 0°$. The accumulative strain ϵ_N induced by ECAP in each pass is dependent basically of ϕ and ψ, the angle between the channels and the angle of curvature of the outer arc, respectively, as shown by Eq. 4.2 [71].

$$\epsilon_N = N\frac{[2cot(\phi/2+\psi/2)+\psi cosec(\phi/2+\psi/2)]}{\sqrt{3}} \tag{4.2}$$

where N is the number of ECAP passes performed. This equation is deduced by geometric relations regarding die parameters. It means that a higher intersect and

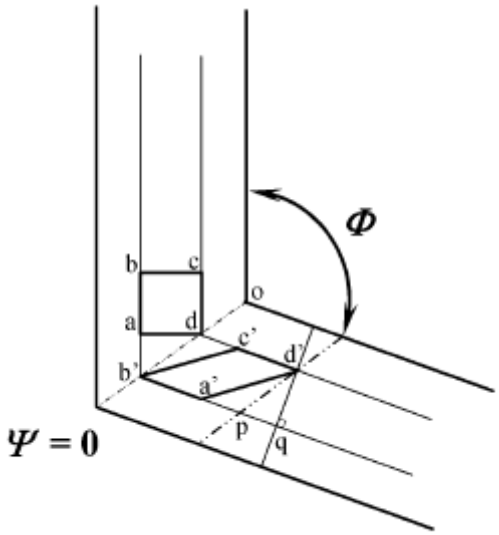

Figure 4.3: Change of element geometry in ECAP for $\psi = 0°$ [68].

curvature angles lead to increasing strain values. For example, setting ϕ angle to 90°, strain decrease from a maximum of 1.15 to a minimum of 0.907, while changing the corner angle from $\psi = 0°$ to 90°. Figure 4.4 shows the results for Eq. 4.2 for a single ECAP pass with $N = 1$ where the channel angle ϕ ranges from 45° to 180° for several values of ψ angle.

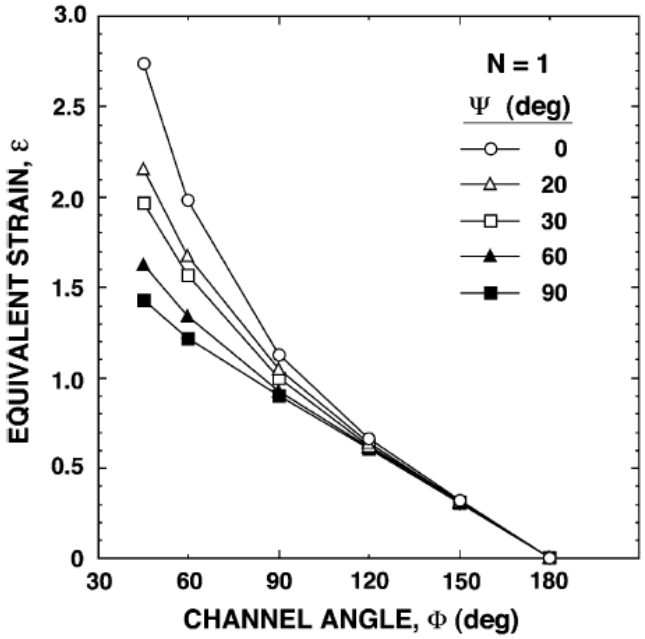

Figure 4.4: Variation of the equivalent strain, ϵ_N, with the channel angle, ϕ, over an angular range of ϕ from 45° to 180° for values of the angle of the arc of curvature, ψ, from 0° to 90°: the strains are shown for a single pass where $N = 1$ [72].

From Fig. 4.4, some conclusions can be reached: first, the angle of curvature has practically no influence on strain for channel angles higher than 90°; second, very

high strains can be achieved in a single ECAP pass when constructing a die with very low values for ϕ and ψ; andd third, for conventional dies that use $\phi = 90°$, equivalent strain is close to 1 for a single pass and is essentially independent of the angle of curvature [68].

Nagasekhar *et al.* [71] used Eq. 4.2 and simulated using finite element analysis the influence of ϕ angle in the range of 60° to 150° on the effective strain while keeping ψ equal to 10°. Figure 4.5 presents the equivalent plastic effective strain (PEEQ) variation along a section A-B of the second channel for various channel angles, being A a point on the top surface of the channel and B a point on the bottom surface of the channels. The graph shows the general values of effective strain versus normalized width of section A-B, that is, the dimension along A-B divided by the dimension of the whole section. The figure shows how homogeneous/heterogeneous the strain values are through the channel section. Higher ϕ angles lead to more homogeneous strain.

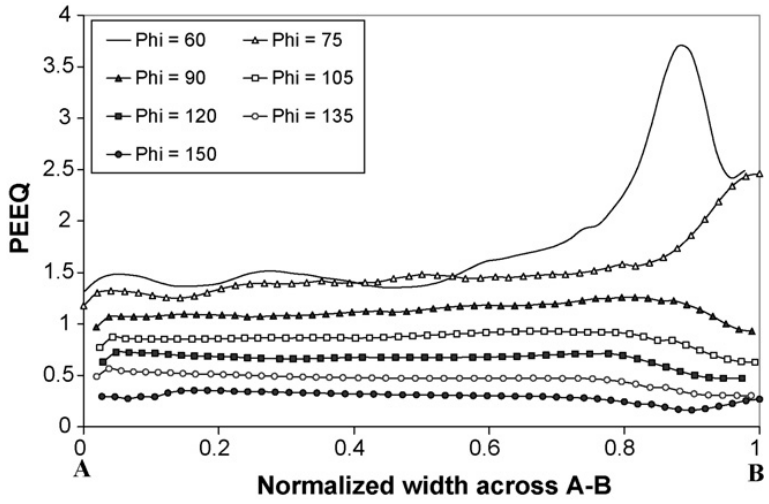

Figure 4.5: Effective strain variation across a width section A-B [71].

However, Eq. 4.2 does not take into consideration two important factors that influence on the equivalent strain: strain hardening and friction between the die and the sample. Nagasekhar *et al.* [73] compared the theoretical effective strain with effective strain simulated by finite element and taking into consideration strain hardening and the friction between the sample and the die. They analyzed the results in three different points: a point closer to the outer surface of the die, a point in the center of the channel and a point closer to the inner surface of the die. They found that theoretical results were lower than the effective strains taking into consideration strain hardening and the friction for all channel angles used.

4.3 Routes in ECAP

An important consequence of the continuity characteristic of ECAP technique, that is, the possibility of several number of passes of the sample through the die be performed, is that it is possible to invoke different slip systems on each consecutive pass by rotating the samples after each pass [74]. Each different combination of rotation of the sample is called route. There are four fundamental routes used in ECAP technologies, as presented on the left of Fig. 4.6:

- Route A - the sample is pressed repetitively without any rotation between each pass;
- Route B_A - the sample is rotated by 90° in alternate directions, that is, after the first pass, the sample is rotated clockwise and after the second pass, the sample is rotated counter-clockwise and so on;
- Route B_C - the sample is rotated in the same sense (clockwise or counterclockwise) by 90° between each consecutive pass;
- Route C - where the sample is rotated by 180° between passes.

The different slip systems associated with each route is shown on the right of Fig. 4.6, where X, Y and Z are the planes presented in Fig. 4.1a. The labels 1 to 4 represent the number of consecutive ECAP passes. Routes C and B_C are considered redundant strain processes as the strain is restored after a specific number of passes because the direction of the shear is reversed on each pass, although the shearing plane is the same. In route C, the slip is canceled after every even number of passes and in route B_C as the slip in the first pass is canceled by slip in the third and the slip in the second pass is canceled by the one in the fourth pass. Routes A and B_A are not redundant, as the shearing planes are different in each pass. There is a cumulative build-up of additional strain on each separate pass through the die [75].

Figure 4.7 shows the influence of each route on the deformation of a cubic element of the sample viewed on the three planes for up to 8 passes. The analysis of shearing characteristics is better visualize on plane Y, which is the plane parallel to the flow direction of the material. For route A, as the slip plane changes after each pass, the distortion of the material becomes more acute after each pass and, as a consequence, the material microstructure presents grain more elongated in the flow direction. Figure 4.8 shows the microstructure evolution of pure Ni processed by ECAP using route A after 1, 2 and three passes. Analyzing the Fig. 4.7 for route B_A on plane Y, it is clear that distortion behavior is similar to the one for route A, as slip system changes after each pass. Therefore, microstructure behavior similar to route A is expected.

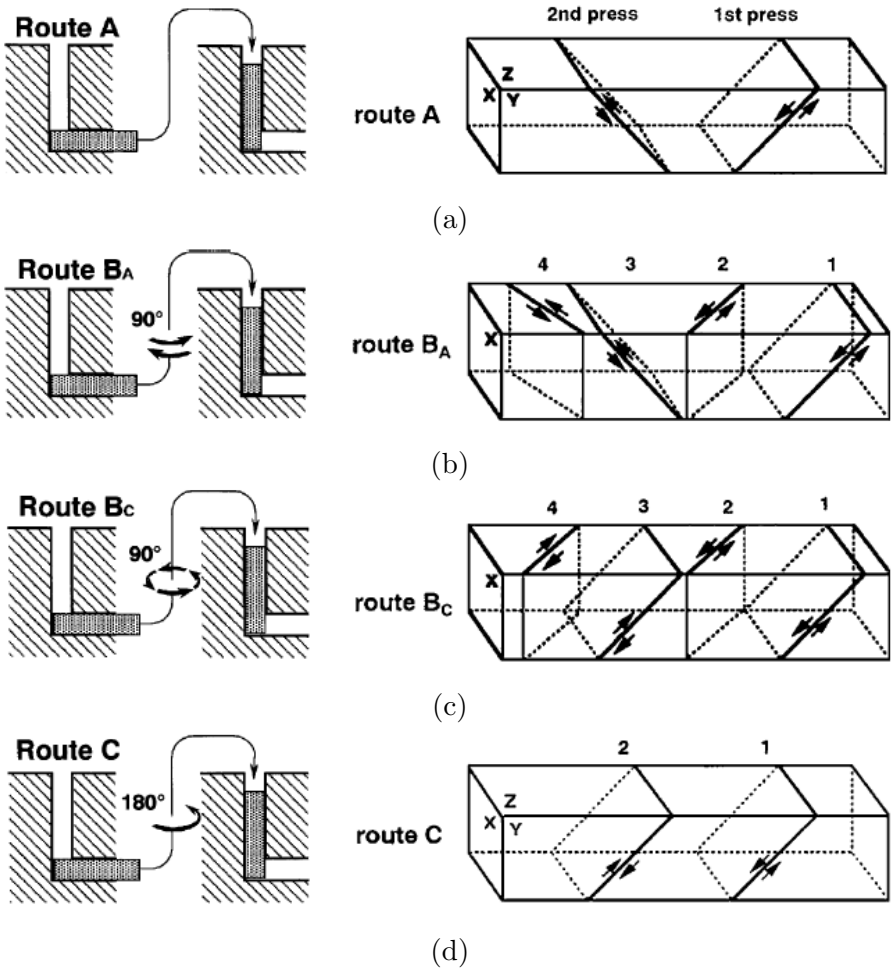

Figure 4.6: Four fundamental routes of ECAP processing [68] and slip systems views [75].

For route B_C, Fig. 4.7 shows that every 4 passes, the cubic element shape is restored because the slip occurred in first two passes are canceled by the next two passes and so on. Therefore, equiaxed grains are expected every 4 passes using route B_C. In a similar way, for route C, every 2 passes, the cubic element shape is restored because the slip of the first pass is canceled by next one and so on. So, equiaxed grains are expected every 2 passes using route C. Figure 4.9 present the microstructure evolution for pure Ni for 2, 3, 4 and 5 ECAP passes. It can be seen that for 2 and 4 passes, equiaxed grains are present in the microstructure f the material and for even number of passes, distorted grains are present.

It is clear that the cubic element is restored every 2 passes using route C and every 4 passes using route B_C, whereas the distortions become more acute when using routes A and B_A [76]. These distortions have great influence on the final microstructure of the sample.

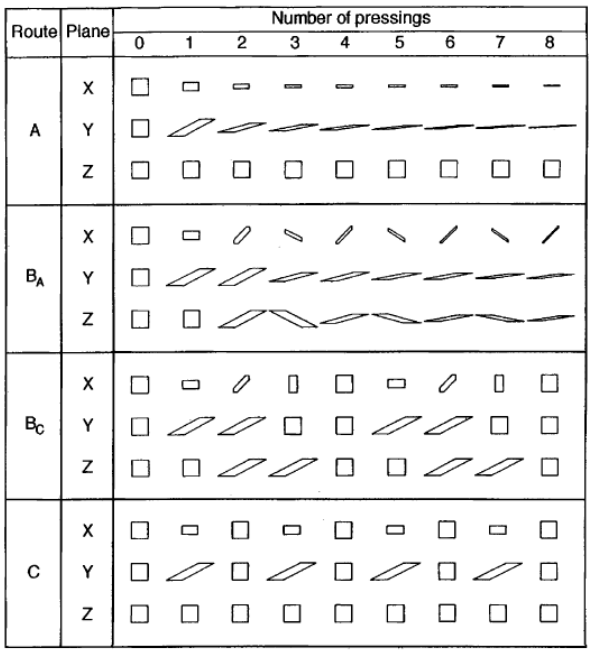

Figure 4.7: Shearing characteristics for four different processing routes [76].

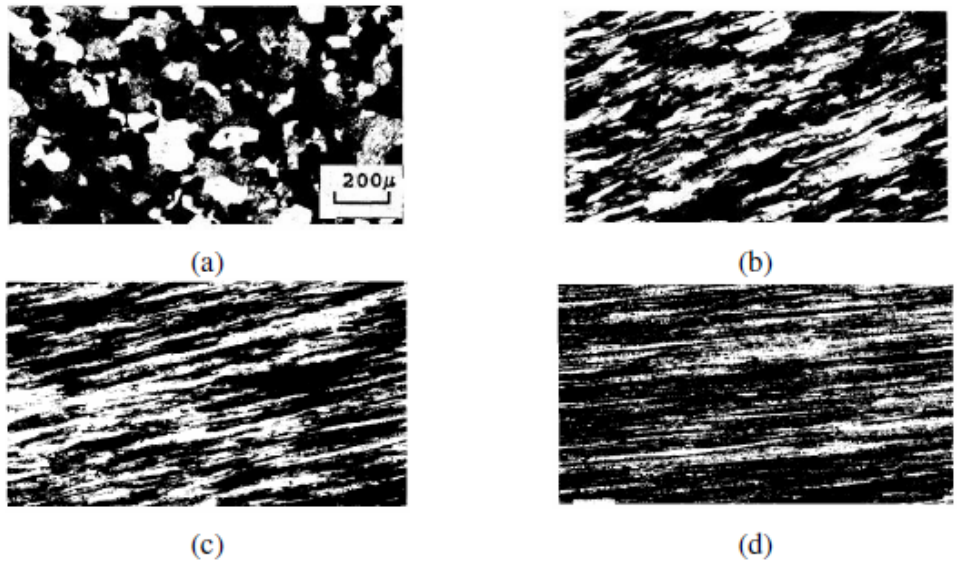

Figure 4.8: Pure Ni pressed by ECAP using route *A*: (a) initial condition; (b) after 1 pass, (c) after 2 passes and (d) after 3 passes (adapted from [77]).

4.4 Consolidation of metallic powder by ECAP

There are several conventional technologies used for consolidation of metallic powder, however in conventional powder metallurgy, consolidation is accomplished through sintering at hight temperatures, which can lead to change the special microstructure of the particles. Although equal channel angular pressing is mostly related with processing of solid metals, it can also be used for consolidation of metallic powder [78–81]. The severe shear deformation imposed to the material in

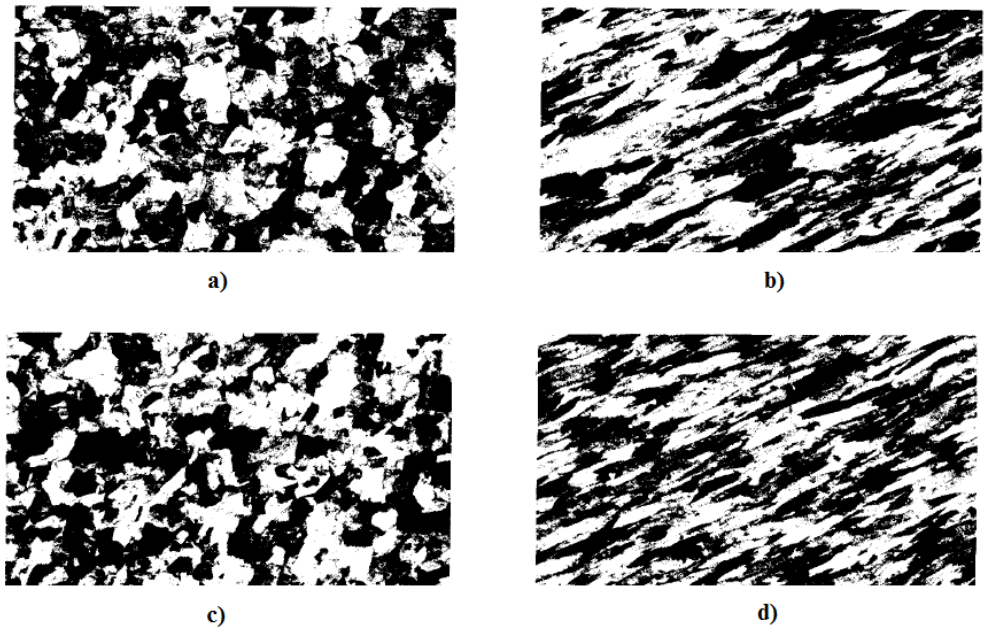

Figure 4.9: Microstructures of Ni after cold deformation via route C with number of passes (a) $N = 2$, (b) $N = 3$, (c) $N = 4$ and (d) $N = 5$ (adapted from [77]).

the process is believed to be able to disrupt the surface oxide layer and create good contact between particles and, consequently, consolidation can be carried out in much lower temperatures [79].

Figure 4.10 shows the setting used by Matsuki *et al.* [80] to consolidate Al-2004 alloy powder. The powder was cold isostatic pressed (CIP) to a billet size with 20 mm diameter and 70 mm length. To avoid cracking during the process, the powder was inserted into a tight-fitting outer jacket fabricated of Al-2024 alloy, showed in Fig. 4.10 by the *abcd* label. The channels inside the die intersect at an angle of 105° and there was an outer arc with 75° curvature. The ECAP pressing was repeated up to three times for each specimen. The study results showed that almost fully dense material consolidation was achieved without surface cracks and significant hardness increase is attained by a single pressing.

Senkov *et al.* [81] used ECAP technique to consolidate $Al_{85}Ni_{10}Y_{2.5}La_{2.5}$ alloy powder. The material was cold compacted inside a copper can which was pressed by 4 ECAP passes at 280° using a die with channel angular of 90° and route B_C. Authors concluded that feasibility of $Al_{85}Ni_{10}Y_{2.5}La_{2.5}$ alloy is possible and 99% of full density material was attained. Figure 4.11 shows the increase in density of the powder after every ECAP pass. A volume-averaged increase in density of about 28% relative to initial cold compacted condition was detected after first pass and 145% after fourth pass. The figure also shows the ECAP pressure peaks for each pass.

Xia and Wu [79] processed aluminum powder by, instead of compacting and canning the powder, wrapping the powder in an aluminum foil and using ECAP

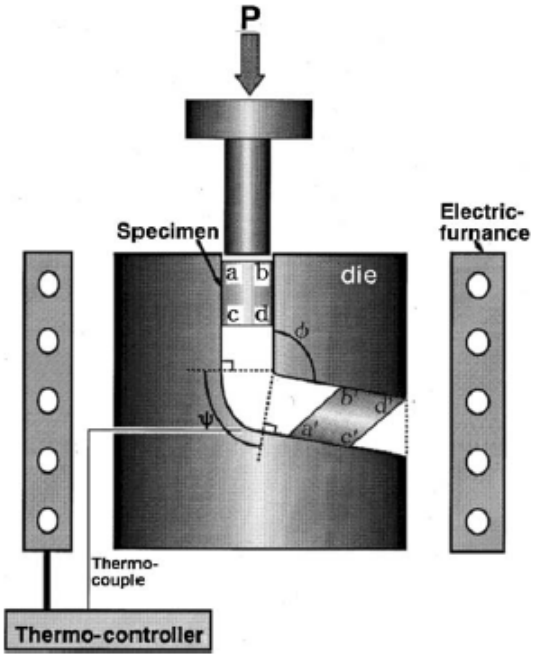

Figure 4.10: The ECAP principle used for the consolidation of aluminum alloy powder: the powder is inserted into a tight-fitting outer jacket labeled *abcd* [80].

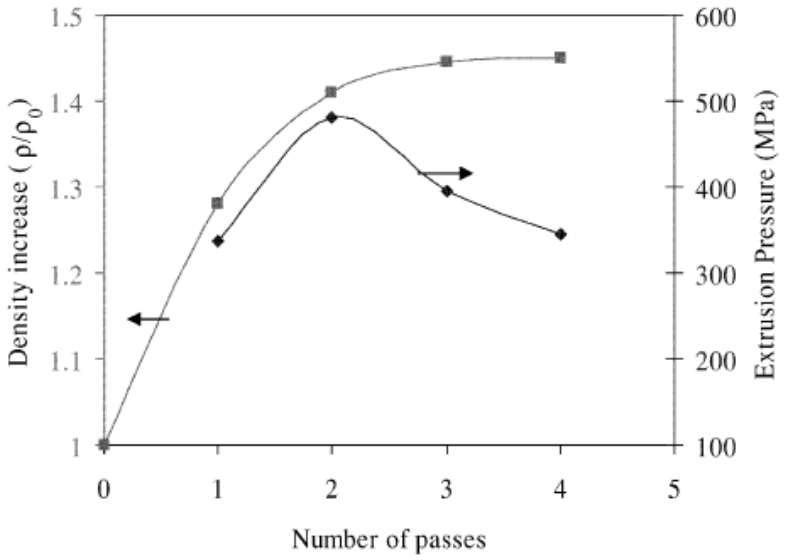

Figure 4.11: Relative density increase of the compacted powder after every ECAP pass and the peak extrusion pressure at every ECAP pass [81].

procedure with back pressure as shown in Fig. 4.12. In addition to the forward plunger in the entrance channel, a back plunger was placed in the exit channel to provide a constant back pressure during the process. According to the authors, pure aluminum particles were successfully synthesized into fully dense bulk material.

Balog *et al.* [78] also studied the consolidation of aluminum powder using ECAP techniques. Authors compared the properties of samples compacted by equal chan-

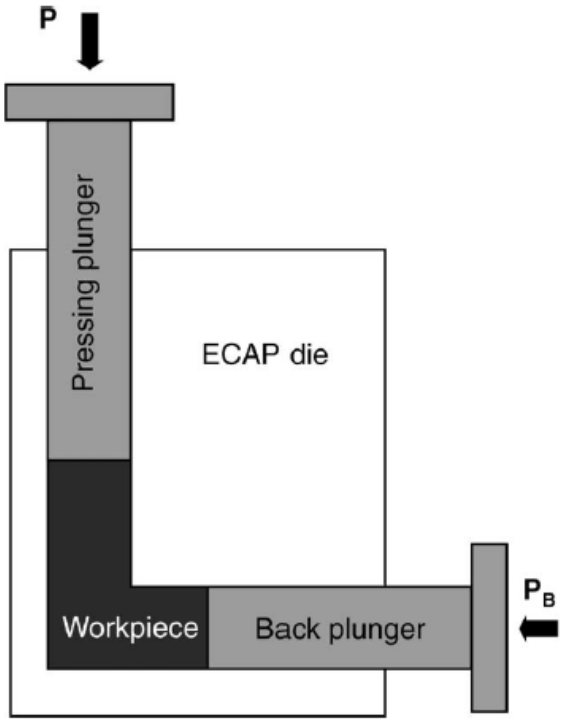

Figure 4.12: Schematic of ECAP die with back pressure [79].

nel angular pressing and direct extrusion. The authors succeed in achieving fully dense material, but stated that the used of back pressure seamed inevitable to avoid formation of cracks.

The results from studies which experimentally researched the feasibility of consolidate metallic powder through ECAP pressing confirm that it is possible to use this technology to achieve fully dense bulk material and that the use of back pressure is very important to avoid cracking during the process.

4.5 Ultra-refinement of grains in metals processed by ECAP

Equal channel angular pressing can lead to materials with grain sizes in submicron (100 - 1000 ηm) and nanocrystalline ($<$ 100 ηm) range depending on the material processed and process parameters [82]. It is well known that grain refinement by severe plastic deformation implies the creation of new high angle grain boundaries (HAB) [60, 83]. High angle boundaries are the grain boundaries with mis-orientation over 15°, while low angle boundaries (LAB) are the ones with mis-orientation smaller than 15° [59]. Materials with fined grains are harder and stronger because the boundaries act as a barrier to dislocation motion, that is what causes deformation. Also, high angle boundary grains do not let dislocations pass. The

dislocations tend to "pile up" at the grain boundaries [62].

Sun *et al.* [83] established that the main high angle boundary formation mechanism is by grain subdivision. Grain subdivision starts at low to medium strains when grains break up in cell and cell blocks. With increasing strain, this substructure evolves to lamellar structure and during this process high angle boundaries are formed.

Understanding the mechanism of grain refinement is an important issue in severe plastic deformation processing because it determines the characteristics of the material after the process, i.e., the strength, hardness, ductility and others [84]. The mechanism is different when processing face-centered cubic (FCC) metals, like aluminum, and hexagonal close-packed metals (HCP), like titanium [85].

Face-centered cubic (FCC) metals possesses a lot of slip systems, so grain refinement is relatively easy. After the first pass, the material presents an elongated cell or subgrain structure with boundaries having mostly low angle mis-orientation. Each separate pass introduces new deformation and the various structures will re-arrange and be destroyed in a manner consistent with the low-energy dislocation structure (LEDS) [84, 86].

Differently, HCP metals present fewer slip planes in comparison to FCC materials, so the deformation process is different. When subjected to large strains, HCP metals accommodates the excess strain through twinning deformation, as presented by Dheda and Mohamed [86] and Chen *et al.* [87].

Table 4.1 presents the experimental results from different studies considering grain refinement. The table includes the material or alloy used, the number of ECAP passes made (∅P = zero passes, 1P = one pass, 2P = two passes and so on), the route used, the grain size of the coarse grained material, the grain size after each ECAP pass and the reference of the work. All studies were successful in achieving grain refinement through ECAP processing. The level of refinement varies with several factors such as material, number of passes, die angle ϕ, outer arc angle ψ, route and others [68].

For example, Fig. 4.13 presents the microstructure of the magnesium alloy AZ31 (Mg-3%, Al-1%, Zn) before ECAP processing, after 1 pass and after 4 passes using a die with 110° between the channels. It is clear that after only one pass, the area fraction of the newly formed ultrafine grains is reasonably large and the volume of the smaller grains becomes homogeneous and extends through the sample [94].

As a consequence of having achieved grain refinement, mechanical properties of the material will accompany the changing. Therefore, modification in properties like strength, hardness and ductility are expected.

Table 4.1: Experimental results from different studies considering grain refinement.

Material	**Route**	**∅P (μm)**	**1P (μm)**	**2P (μm)**	**3P (μm)**	**4P+ (μm)**	**Ref.**
Aluminum	A	1000	0.60	0.55	0.50	0.50	[74]
Aluminum	B_C	1000	0.60	0.60	1.20	1.30	[74]
Aluminum	C	1000	0.60	0.55	0.55	0.55	[74]
6082Al-Mg-Si	C	1000	–	–	–	0.3	[88]
CP-Ti	A	41600	4.7	–	1.76	0.96	[89]
CP-Ti G4	B_C	25	–	–	–	0.150	[90]
CP-Ti G4	A	30	0.02	–	–	–	[86]
CP-Ti G1	B_C	10	–	–	–	0.30	[91]
CP-Ti G1	A	30	0.08	–	–	–	[85]
CP-Ti G2	B_C	28	0.4	0.35	–	0.25	[92]
CP-Ti G4	A	25	–	–	–	0.23	[93]

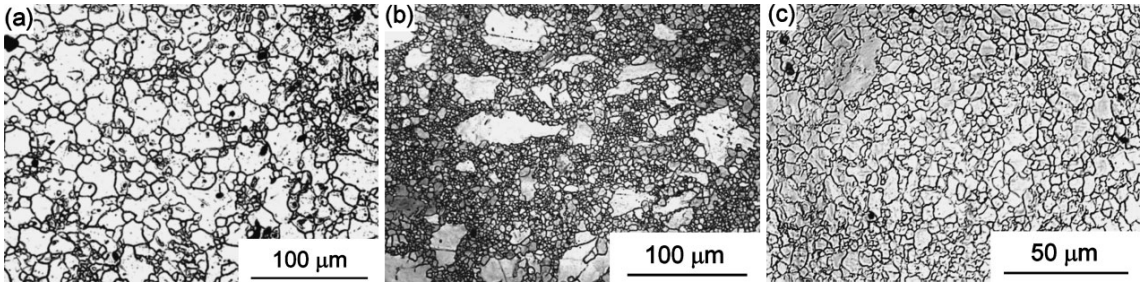

Figure 4.13: Grain structure of an AZ31 alloy processed by ECAP from the extruded condition: (a) initial structure, (b) after 1 pass and (c) after 4 passes of ECAP using a die with 110° between the channels. [94].

4.6 Mechanical properties of metals processed by ECAP

As stated in Eq. 4.1, the relation between grain size of a material and its yield stress is given by the Hall-Petch equation. Strength and ductility are the main mechanical properties of any material, i.e., usually a material is wanted to combine high strength with sufficient ductility, along with high fatigue toughness [61, 68]. However, strength and ductility typically have opposing characteristics. Materials can be strong or ductile, but they are rarely both. The reason for this is that plastic deformation mechanisms associated with the generation and movement of dislocations are not effective in ultra-fine grains. Most ECAP processed material present low relatively ductility, but they usually demonstrate significantly higher strength than their coarse-grained counterparts [68], as a consequence of the Hall-Petch equation.

Equal channel angular pressing usually leads to a reduction in the ductility smaller than in more conventional plastic deformation processes such as rolling and drawing. Zhu and Langdon [95] conducted experiments to compare strength and ductility of 3004 aluminum alloy processed by ECAP and cold rolling. As Fig. 4.14 show, yield strength increased with each rise of the strain, which is equivalent to

accumulative passes, in both ECAP and rolling processing. However, ductility had a different behavior. Equal channel angular pressing decreased the ductility after the first pass, but then it kept stable. Cold rolling, otherwise, decreased the ductility after first pass by the same magnitude of ECAP and then it continued to decrease with increasing strain. Consequently, ECAP processing lead ultimately to a greater retention of ductility than conventional cold-rolling.

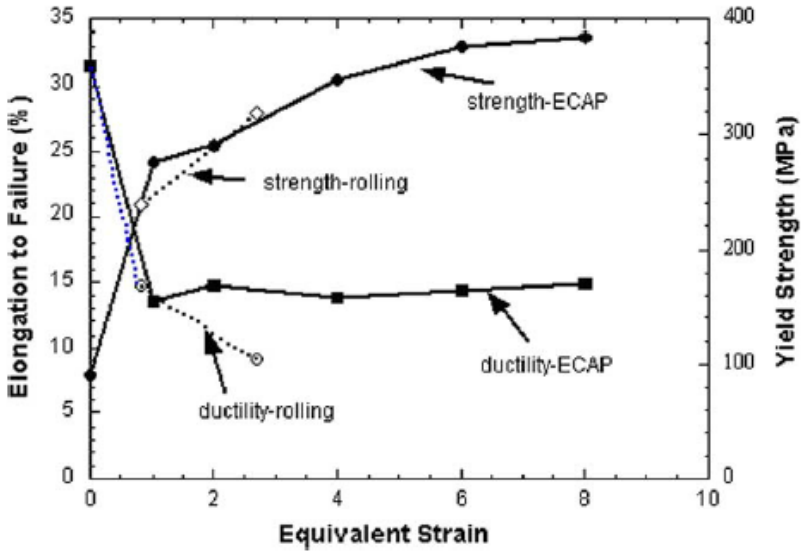

Figure 4.14: A comparison of yield strength and ductility for an Al-3004 alloy processed by cold-rolling or ECAP [95].

Another important mechanical property is the material hardness. Hardness, as the yield stress, has a direct relationship with the grain size: the smaller is the grain dimensions, the higher is the material hardness and the relation is also given by the Hall-Petch equation [62].

Table 4.2 presents the experimental results of several studies considering mechanical properties, especially the yield strength, where GX represents the titanium grade. It includes the material used in the study, total number of ECAP passes made, the final properties values after all ECAP passes and the work reference.

Table 4.2: Experimental results from different studies considering mechanical properties: σ_Y is yield strength in MPa; UTS is ultimate tensile strength in MPa; Hard. is hardness in the unity indicated; and label 1 indicates before ECAP processing, as label 2 indicates after ECAP processing.

Material	**Passes**	$\sigma_Y 1$	$\sigma_Y 2$	UTS_1	UTS_2	$Hard_1$	$Hard_2$	**Ref.**
CP-Ti	B_C	202.6	530.4	292.5	665.5	–	–	[89]
CP-Ti G4	B_C	530	1200	700	1240	–	–	[90]
CP-Ti G4	A	–	–	–	–	1621 MPa	2073 MPa	[86]
CP-Ti G1	B_C	380	650	460	810			[91]
CP-Ti G2	B_C	390	680	474	773	1589 MPa	2486 MPa	[92]
CP-Ti G4	A	625	1190	760	1230	–	–	[93]

As Table 4.2 presents, several studies have been performed to analyze the impact of equal channel angular pressing in materials properties. Also, different types of metallic materials have been studied, including face-centered cubic metals, like aluminum and aluminum alloys and copper, and hexagonal close-packed metals, such as magnesium and titanium and titanium alloys. As the present work deals mostly with commercially pure titanium and titanium alloys, especially the Ti-6Al-4V, it is necessary to present more deeply the studies results using these materials.

4.7 Commercially pure titanium and titanium alloys processed by ECAP

It is of great importance to studies that analyzed the impact of ECAP on commercially pure titanium to compare the improved properties, like strength and hardness, with the mechanical properties of Ti-6Al-4V alloy, which for many years have been used in manufacturing dental implants. Therefore, a lot of studies, besides testing the results of ECAP on CP-Ti properties, also compare them with the alloy properties.

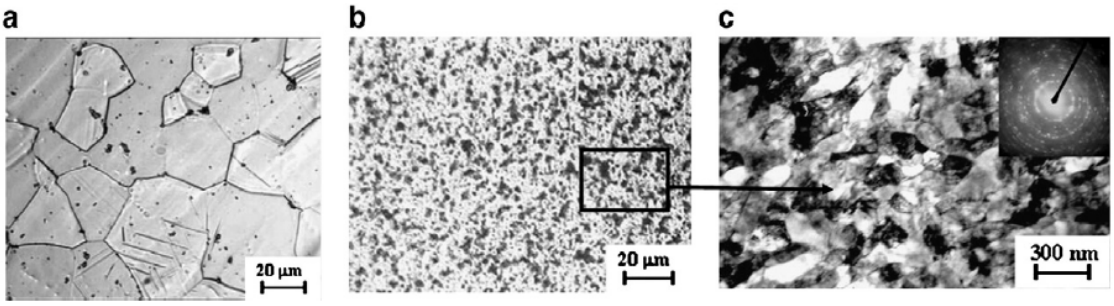

Figure 4.15: Optical and transmission electron microscopy illustration microstructure of CP-Ti grade 4: a) conventional; b) and c) ECAP + TMT [90].

There are four grades of commercially pure titanium: grade 1, 2, 3 and 4. They differ between each other mostly by the oxygen percentage in their chemical composition. From grade 1 to 4, the tensile and yield strength increase and the corrosion resistance decreases.

Serra *et al.* [90] compared nanostructured CP-Ti (ηTi) grade 4 (C - . %, O_2 - 0.34%, Fe - 0.3%, N - 0.015%, Ti - bal.) with CP-Ti and Ti-6Al-4V alloy in order to prove the hypothesis if it could be possible to substitute the titanium alloy for nanostructured CP-Ti as the material base for orthodontic mini-implants. The (ηTi) was produced by processing CP-Ti rods by four ECAP passes at 450°C using route B_C followed by thermo-mechanical treatment (TMT). The samples were tested and then machined to fabricate mini-implants that were, later, tested by a torque test.

The grain size was reduced from 25 μm to 150 ηm, as showed by Fig. 4.15. Also, ultimate tensile strength increased from 700 to 1240 MPa, but without the drastic ductility reduction normally seen after rolling or drawing. The elongation during tensile test decreased from 25% only to 12%. The study concluded that it can be suggested that (ηTi) can replace Ti-6Al-4V alloy.

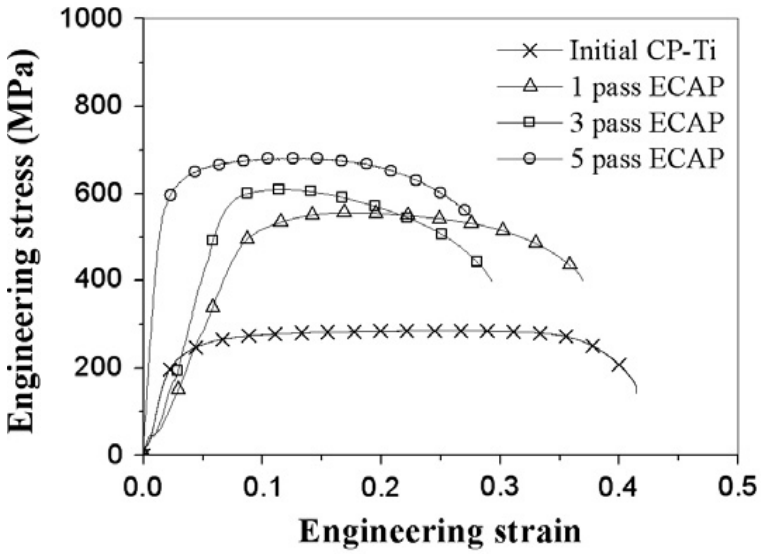

Figure 4.16: Stress-strain behaviors from initial CP-Ti and after 1, 3 and 5 ECAP passes [89].

Kang and Kim [89] conducted a multi-pass ECAP experiment followed by cold-extrusion in order to improve CP-Ti grade 2 mechanical properties. Equal channel angular pressing process was performed at 450°C, using $\phi = 90°$ and $\psi = 0°$ and a combination of routes A and C. Figure 4.16 shows the stress-strain behaviors from initial CP-Ti and after 1, 3 and 5 ECAP passes. The yield strength increased from 202.6 to 530.4 MPa and the ultimate tensile strength from 292.5 to 665.5 MPa. The loss in ductility was also relatively small: the elongation decreased from 44.5% to 26%.

Dheda and Mohamed [86] did an investigation to find out if the initial microstructure of CP-Ti affects the microstructure of the material resulting after one pass of ECAP. Three annealing conditions were used to analyze different initial conditions: non-annealed, annealed at 7600°C for 2 hours and annealed at 900°C for 4 hours. The authors concluded that the initial condition of the microstructure had influence on the material after one pass of ECAP mostly related with the difference in the presence of dislocations within the grains and with the size and distribution of the second phase, which was formed by the presence of Fe impurities in the initial material.

Vinogradov *et al.* [91] explored the fatigue performance of the ultra-fine grained titanium produced by ECAP. Samples were processed through ECAP at $400 - 450°$,

using route B_C and eight passes were made. The investigation concluded that ultra-fine grained titanium presented considerable increase in fatigue life and fatigue limit under constant load testing when compared with titanium in coarse-grain state.

Kim *et al.* [85] analyzed the deformation structures of commercially pure titanium grade 1 during 1 ECAP pass. After 1 pass of ECAP, they achieved a grain reduction from 30 to 0.08 μm and the results from microstructure analysis indicate that twinning plays a critical role in plastic deformation by ECAP, as showed by Fig. 4.17. Figure 4.17*c*) presents the twinning deformation mechanism labeled by letters A and B.

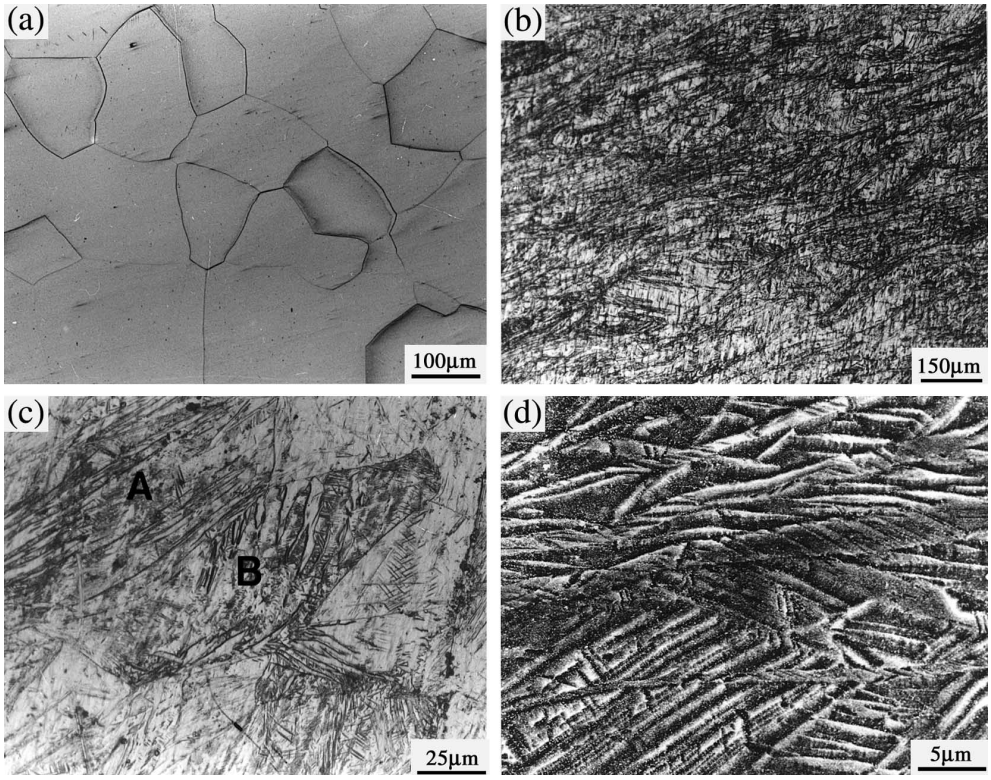

Figure 4.17: Optical and SEM micrographs of pure Ti: (a) as-annealed; (b), (c) and (d) after ECAP [85].

Xirong *et al.* [92] processed CP-Ti grade 2 by ECAP at room temperature, but with larger angle between the channels inside the die, using $\phi = 120°$. The samples were processed by route B_C and a grain reduction from 28 to 0.25 μm was achieved. Also, an improvement of the mechanical properties from 390 to 680 MPa in yield strength and 474 to 773 MPa in ultimate tensile strength. In addition, twinning deformation mechanism was also detected during ECAP passes, as shown by Fig. 4.18.

Gunderov *et al.* [93] stated that severe plastic deformation materials are stringly dependant not only of the refined grain size, but also on grain boudaries state, defect densities, texture and others. Therefore, the authors studied the evolution of microstructure, macrotexture and mechanical properties of CP-Ti grade 4 processed

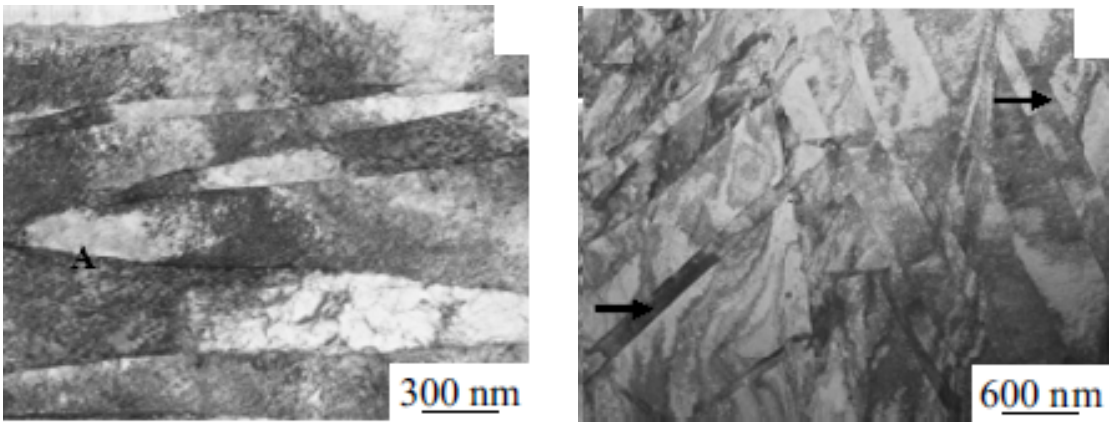

(a) Shear bands. (b) Twinning.

Figure 4.18: Transmission electron microscope images of CP Ti after one ECAP pass.

by ECAP. After 6 ECAP passes, ultra-fine grained microstructure was formed with equiaxed grains/subgrains with 200 ηm. Commercially pure titanium properties were increased and the ductility showed opposite tendency, as shows Fig. 4.19.

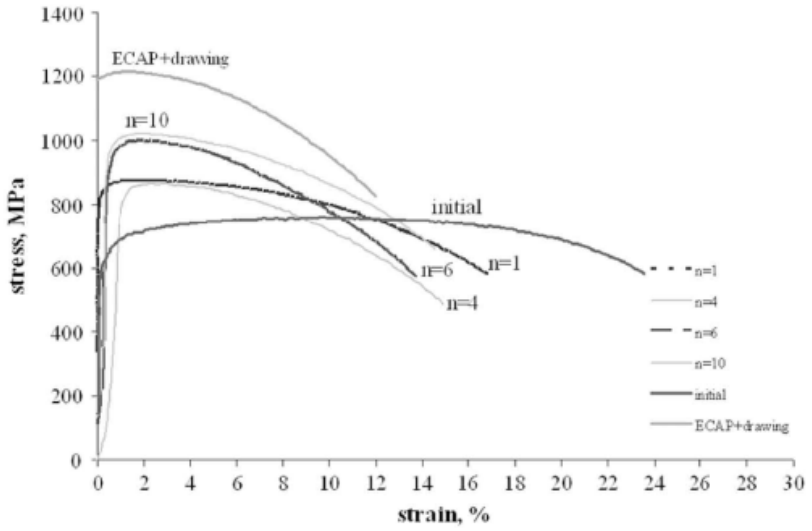

Figure 4.19: Engineering stress-strain curves for CP-Ti grade 4 in different structural states [93].

4.8 Machinability of titanium and titanium alloys processed by ECAP

Equal channel angular pressing is expected to improve mechanical properties of processed material. Therefore, ultimate tensile strength and hardness are properties that usually increase after a number of ECAP, while a loss in ductility is also often

expected.

Antonialli *et al.* [17] evaluated how ECAP processing affected the machinability of Grade 2 CP-Ti after four ECAP passes by measuring cutting forces during turning and compared the results with the Ti-6Al-4V alloy. In addition, the authors examined the flank and rake faces of the tool in order to detect differences regarding the main wear mechanism. Figure 4.20 shows the results for cutting forces for Grade 2 CP-Ti before ECAP (0X), after four ECAP passes (4XH) and the alloy (#5). It can be seeing that ECAP processing almost doubled the main cutting force required for the operation and reached values close to the required by Ti-6Al-4V alloy.

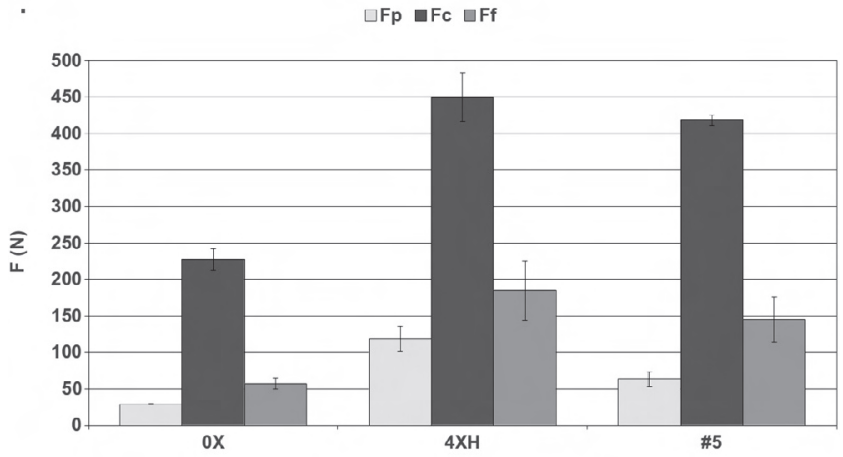

Figure 4.20: Cutting forces for CP-Ti before ECAP (X0), after four ECAP passes (4XH) and the alloy (#5) [17].

It was also measured the surface roughness achieved after machining the materials. Figure 4.21 shows that for pure titanium surface roughness was higher than for Ti-6Al-4V alloy and between CP-Ti and ECAP CP-Ti, no significant difference was detected. This fact is probably due to different chip types obtained from the different materials during the turning tests: coarse-grained or ultra-fine grained titanium produced longer chips than the alloy. Continuous chips may scratch the newly machined surface, thus causing damage to the samples surface roughness. The authors concluded that ECAP pressing decreases machinability as specific force for ECAP titanium achieved values similar to Ti-6Al-4V alloy. In addition, attrition was the main wear mechanism found when machining CP-Ti, regardless its condition, as a strong adhesion of workpiece material followed by tool particles pull out was observed on the tool rake face.

Lapovok *et al.* [16] conducted a comparative study of turning coarse grained and ultra-fine grained Grade 2 CP-Ti processed by ECAP focused on thermal characteristics. The length and hardness of the chips were measured and thermal conductivity was calculated by performing heating experiments. Figure 4.22 shows the thermal

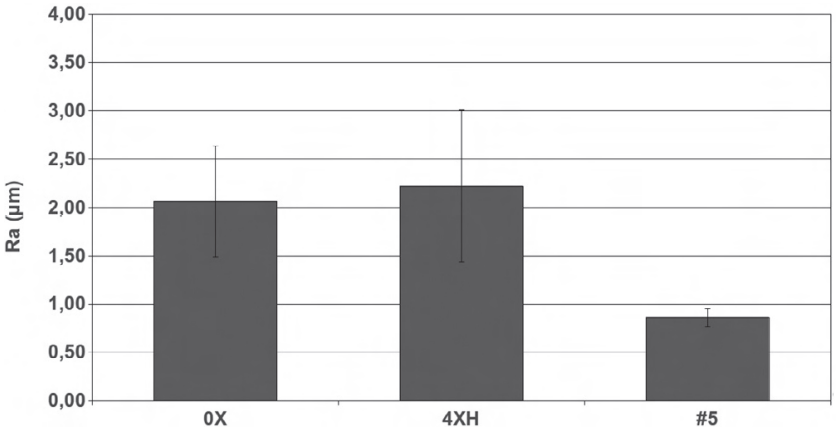

Figure 4.21: Mean surface roughness for CP-Ti before ECAP (X0), after four ECAP passes (4XH) and the alloy (#5) [17].

conductivity calculation results for increasing grain sizes. According to the experiments results, increasing grain sizes lead to an increase in thermal conductivity. Although thermal conductivity decreased for UFG titanium, the author concluded that an improvement of machinability was achieved by processing CP-Ti by ECAP and suggest that to achieve a gain in machinability of CP-Ti by virtue of reduced thermal conductivity, the microstructure of the material should be in the UFG range.

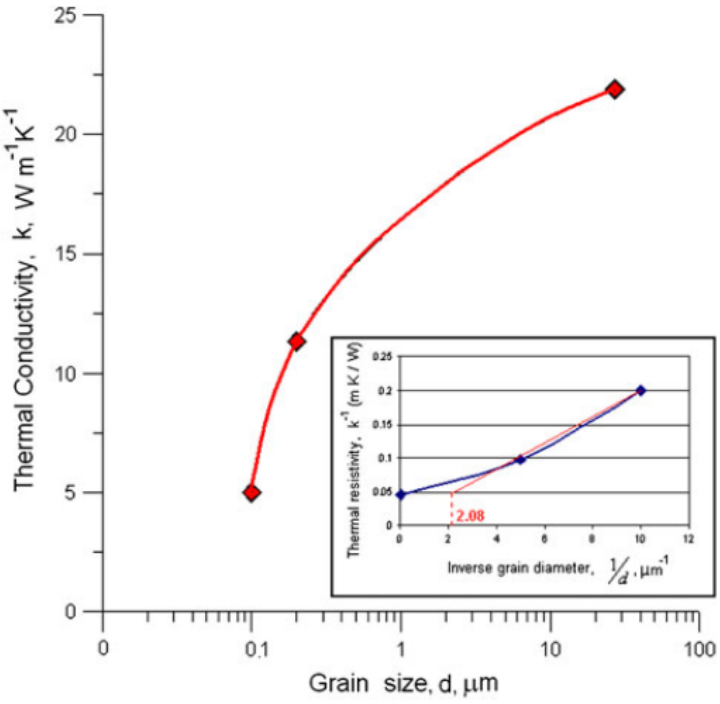

Figure 4.22: Thermal conductivity versus grain diameter (logarithmic scale) with thermal resistivity versus inverse grain diameter in the insert [16].

Their conclusion is based on the reduction of chip length when machining UFG titanium in comparison to machining coarse-grained titanium, as showed by Fig.

4.23. The figure shows that, for different depths of cut, average chip length decreased with feed rate decreased when machining UFG titanium in comparison with machining coarse-grain titanium. Long chips are detrimental to the cutting tool as a long chip has a tendency to wrap around the tool and damage the surfaces of the workpiece and the tool, according to the authors [16]. However, although the improvement on machinability may have been achieved by ECAP processing, the authors neglected any effect that the machining process had on the tool or even the cutting forces required or the surface roughness achieved by machining.

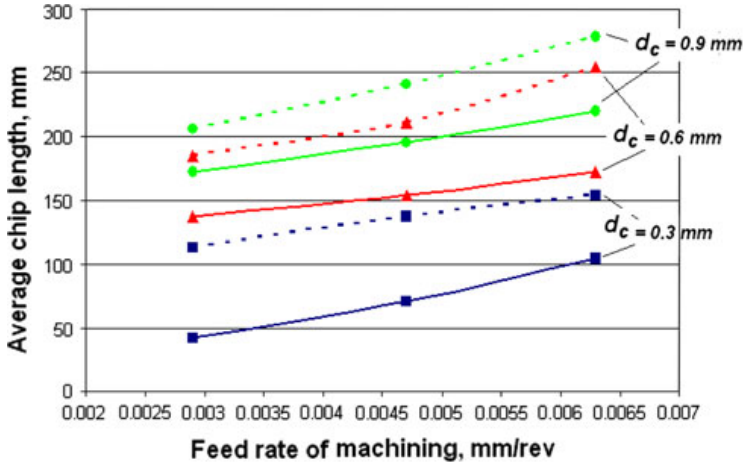

Figure 4.23: Average chip length versus feed rate of machining at different cut depths, d_c, for UFG (solid lines) and CG (dashed lines) titanium [16].

Morehead *et al.* [18] performed turning experiments to analyze the machinability of UFG pure titanium processed by ECAP using cutting forces data and compare it to coarse-grained titanium at different cutting conditions. Figure 4.24 shows the cutting force result for cutting speed of 120 m/min., depth of cut of 40 μm and feed varying. The forces are showed in the tangential direction, F_x, radial direction, F_y, and axial direction, F_z, for coarse-grained titanium and ultra-fined grain titanium. The graph shows that no significance variance can be seen between machining both materials. In addition, authors measured surface roughness for UFG titanium, but did not measure for coarse-grained material, so the comparison was not possible. Flank wear was also measured and no accentuated difference could be detected between both materials. The authors concluded that a difference between the machinability of UFG and coarse-grained titanium could not be confirmed under the cutting conditions used.

Campos *et al.* [96] conducted a study on the mechanical behavior and machinability of Grade 2 CP-Ti powder consolidated by ECAP processing after two passes. Mechanical behavior was investigated by carrying out bending tests, but the samples were extremely fragile, probably because of hydrides contamination. This fact

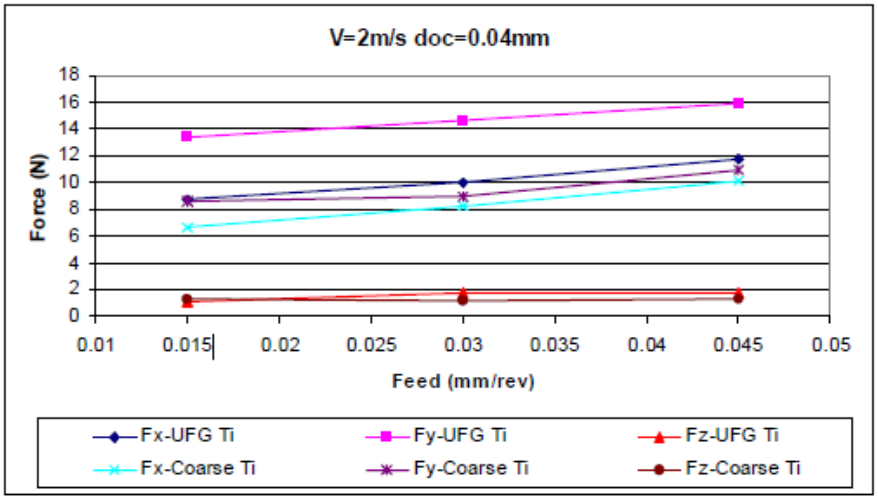

Figure 4.24: Cutting force versus feed for ultra-fined grain titanium and coarse-grained titanium [18].

harmed the machinability tests, which was performed by measuring cutting forces during milling process. Figure 4.25 shows the cutting force results for machining CP-Ti and CP-Ti powder consolidated by ECAP. No significant difference between machining both materials were detected. However, the study was successful in producing CP-Ti powder consolidated by ECAP with ultra-fine grain structure.

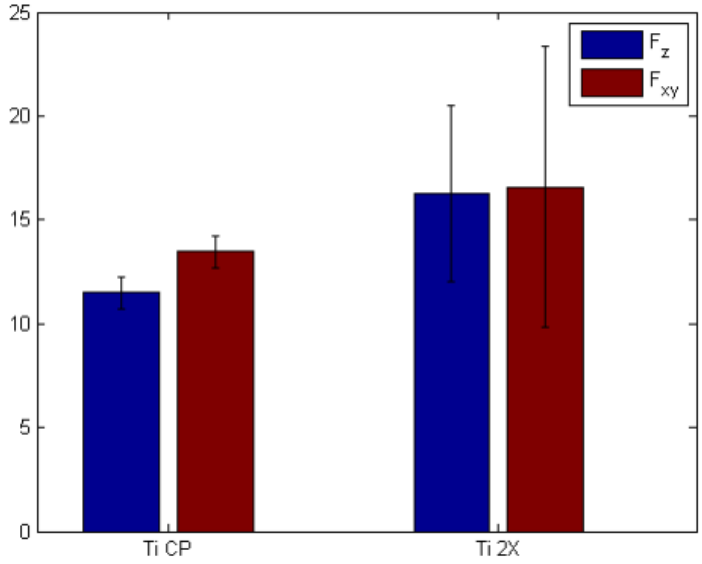

Figure 4.25: Maximum cutting forces achieved in milling CP-Ti and CP-Ti powder consolidated by ECAP technique [96].

It is well established, by the bibliography used in this work, that equal channel angular pressing process is able to introduce ultra-fined grain structures in coarse-grain materials and also to improve mechanical properties such as yield and tensile

strength and hardness, while material ductility usually decreases during the process. Also, according to the studies, twinning mechanism plays an important role on the deformation mechanism of commercially pure titanium during severe plastic deformation process, allowing slip to occur on more favorable directions.

The changes introduced on the material can considerably influence the machining processes which will be necessary to produce implants after ECAP processing. Therefore, it is important to analyze how ECAP process can affect the machinability of CP-Ti.

Also, other alternatives for producing bulk commercially pure titanium with improved properties have been studied, like selective laser melting, an additive manufacturing process which is covered in next chapter.

Chapter 5

Additive Manufacturing and Selective Laser Melting (SLM)

This chapter aims to introduce the additive manufacturing (AM) processes, focusing on selective laser melting (SLM). It deals with the definition and stages of the process as well as specific characteristics in comparison with other additive manufacturing processes. In addition, mechanical properties of materials manufactured by SLM, especially titanium alloys, as well as machinability studies using SLM titanium alloys are presented.

5.1 Additive manufacturing

Additive manufacturing processes are the ones in which, unlike conventional material removal ones, parts are fabricated by adding material incrementally by different ways until the desired shape is achieved. Additive manufacturing technology has experienced more than 20 years of development and is now being rapidly developed worldwide as an advanced manufacturing technique [97]. This approach was first used for fabricating engineering parts prototypes on the minimum time possible, referred as rapid prototyping (RP) processes.

However, advances in materials, processes and machine hardware meant that parts could be produced with sufficient properties to allow functional applications and industrial manufacturing. Additive manufacturing is the general term used for manufacturing processes that uses additive technologies and RP is used to described one application of AM technologies [98].

Additive manufacturing processes present several advantages in comparison with machining and deformation processes: there are less constraints on the shape of the final geometry; lower interaction with the operator, letting most work to computers and AM machine; there is almost zero waste of material, that is a huge difference

over machining processes; general prices are very reduced in comparison to some machining processes, considering initial and operating costs; overall production times are smaller than in machining process.

According to Gibson *et al.* [99], any AM technology can be broken down into 7 steps which are presented in Fig. 5.1 and detailed next.

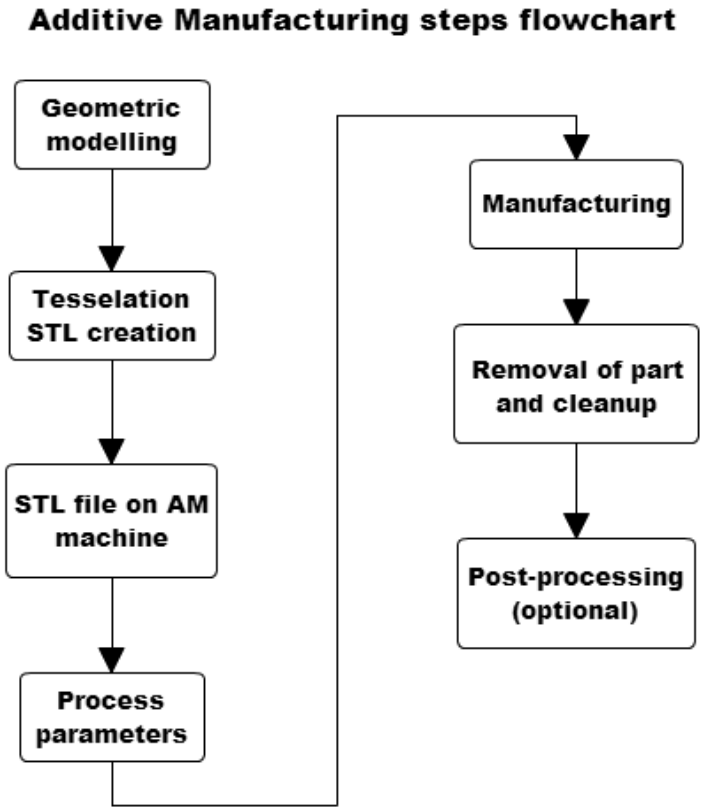

Figure 5.1: Additive manufacturing flowchart with all process steps.

1. **Geometric modeling** - Initially, the product to be manufactured must be modeled using a Computer Aided-Design (CAD) software. Softwares such as SolidWorks, Autodesk Inventor, CATIA, Rhinoceros 3D and many others can be used. Solid modeling is preferred rather than surface modeling as it provides a complete and unambiguous mathematical representation of the part geometry;

2. **Tessellation of the geometric model** - CAD model must be converted into a format that approximates part surfaces by triangles and polygons. This is called tessellation of the model. The most common file format is the STL (STereoLitography or Standard Tessellation Language) file, that is used by almost every AM systems. The 3D model in the STL format is sliced into spaced parallel horizontal layers. The space between the layers is called the

thickness of the layer and it is an important parameter of the processes that is decided by the user. The layers are then used by AM system to construct the physical model. For each layer on the XY plane orientation, a curing path is generated. This path will be followed by the AM system to cure/solidify the layer. Figure 5.2 shows this stage and a separate layer of the sliced object;

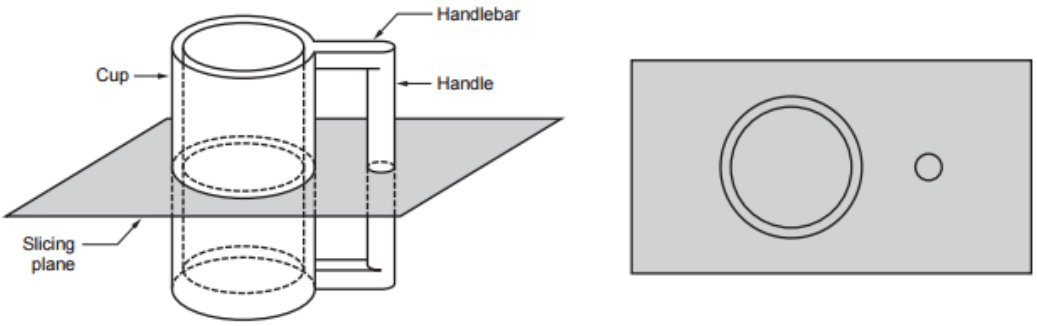

Figure 5.2: Conversion of a solid model of an object into layers and one layers is shown [39].

3. **Loading of the STL model in the AM machine environment** - Once the STL model has been oriented, supported and layered, it can be transferred into the AM machine environment. At this stage, different parts can be added into the AM machine for simultaneous fabrication;

4. **Set up of process parameters** - Here, the process parameters can be set up. These parameters determine the quality and properties of the built up part and must be adequately chosen. They will depend on the AM process and the initial material;

5. **Building time** - The process is launched and the part is created one layer at the time;

6. **Removal and cleanup** - Once the part is completed, it will be taken off the platform and the supporting structures, if there is any, and the surrounding build material must be taken off the object;

7. **Post-processing (optional)** - This stage is specific for each intended application and can include polishing, surface treatments, properties improvement by thermal or non-thermal treatments and others.

The general classification of AM processes is based on the form of the starting material: liquid-based, solid-based and powder-based [39]. The most common AM processes are:

- Liquid-based systems - The starting material in these technologies is a liquid. The main liquid-based additive manufacturing processes are: stereolithography (STL), that is a process for fabricating a solid plastic part, where a laser beam is used to solidify a photosensitive liquid polymer layer onto another according to the path and layer thickness defined in the programming stage; solid ground curing (SGC) which consists of solidifying a photosensitive polymer layer by exposing the entire layer to an ultraviolet light source, but using a mask that let the light to pass only in the layer shape; and droplet deposition manufacturing (DDM), where small droplets of melted material are deposited by a spray nozzle workhead onto a previously formed layer, following the defined layer path, to form a new one. Droplet deposition manufacturing can also be used with metals with low melting point;

- Solid-based systems - The starting material is solid. The two principal AM systems of this category are: laminated-object manufacturing (LOM) where adhesive sheet shaped material is fed on a platform and a laser beam cut the sheet to an outline corresponding to the cross-sectional shape of the layer and the excess material of each layer is used as support to the next one; and fused-deposition modeling (FDM) where a filament of wax or polymer is extruded onto a substrate or the previous layer from a workhead to complete each new layer and then the material is solidified;

- Powder-based systems - The starting material is powder. Three of the main technologies of these types of systems are: three dimensional printing (3DP) that consists of an ink-jet printer that ejects an adhesive bonding material onto successive layers of powders and this binder holds the powders together at the cross-section defined before as the loose material is removed later; and selective laser melting (SLM) and selective laser sintering (SLS) which are covered in the next section.

5.2 SLM process

Selective laser melting is a *powder-based* additive manufacturing process in which a fiber laser melts a powder layer by following a path defined in the slicing of the model stage, as showed in Fig. 5.3. As the layer passes, the melted parts are solidified by cooling and get ready to receive the next layer of powder which is delivered by a layering system. The thickness of each layer is previously defined and the platform where the part is being fabricated is lowered by the thickness dimension to receive the next layer. The process occur inside a vacuum building chamber with a tightly controlled protective atmosphere of an inert gas to avoid

unwanted chemical reactions with the melted powder material, as showed by Fig. 5.3.

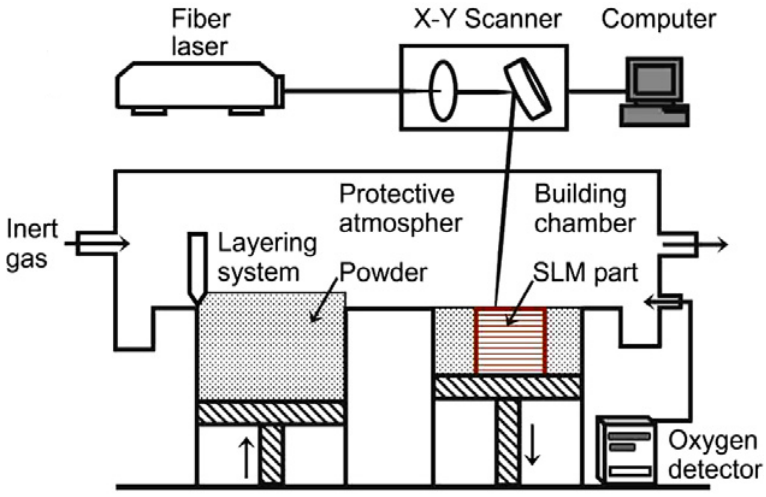

Figure 5.3: Schematic figure of selective laser melting process [100].

Selective laser melting has evolved from selective laser sintering (SLS) process. Selective laser sintering is based on a liquid-phase sintering mechanism involving a partial melting of the powder. Direct metal laser sintering (DMLS) is a nomenclature used for SLS processes using metallic powder, whereas SLS is used to refer to a variety of materials such as polymers and ceramics. Selective laser melting is based on a complete melting/solidification mechanism, which is a big difference as it allows the manufacturing of fully dense parts with characteristics compared to ones of bulk material [97, 101]. Full melting of metals became possible as developments in laser processing conditions were improved, such as high laser power, smaller focused size and thinner layer thickness [97].

Selective laser melting parameters play a large role in determining the metallurgical characteristics of the molten pool and resultant microstructural and mechanical properties of SLM processed materials. The SLM process parameters can be divided into four general categories [99]:

- Laser-related parameters - laser power, energy density, spot size, pulse duration, pulse frequency and others;
- Scan-related parameters - scan speed, scan spacing and scan pattern;
- Powder-related parameters - particle shape, size and distribution, powder bed density, layer thickness, material properties etc.;
- Temperature-related parameters - powder bed temperature, powder feeder temperature, temperature uniformity etc.

Among these parameters, several of them are strongly interdependent. For example, the required laser power for fully melt a determined material increases with the melting point and with a lower powder bed temperature. Between them, the following are the most important ones:

- Layer thickness - the layer thickness is specified when slicing the CAD model and it defines the dimension of each powder layer, as presented by Fig. 5.4. Higher layer thickness will result on a rougher surface part and on smaller production time, as a lower number of layers will be performed;

- Part orientation - part orientation is the position in which the part will be manufactured on the SLM system substrate and it determines the building direction. Part orientation takes into consideration the surfaces which will be sliced and the shape of the part and will influence the microstructure of the manufactured part;

- Spot size - is the dimension of the laser spot. A great advantage of SLM over DMLS technique is that modern laser beam can be focused to a spot size on the powder ben and therefore the level of resolution and accuracy that SLM can achieve is undisputed. Also, smaller spot sizes lead to smaller molten pool and, as a consequence, surface finish of the as-built component is often superior.;

- Laser power - is the power of the laser beam. Using higher laser power, the powder will melt more quickly;

- Scan speed - is the speed with which the laser beam will pass on the powder for it to melt;

- Hatch space - hatch space is the distance between two side-by-side laser paths in the scanning strategy of the SLM procedure, as shown in Fig. 5.4. In the figure, each black line inside the boundary contour is the laser path.

- Boundary contour - boundary contour is the laser path that can be used in SLM operations where the laser contours the shape of the part layer. So, to scan a layer, the laser will scan the boundary contour and also inside the boundary. Without the boundary contour, the laser would scan only inside, as shown in Fig. 5.4;

- Energy density - is the amount of energy supplied by laser beam to a volumetric unit of powder material and it is defined by Eq. 5.1, where P is the laser power (W), v is the laser scan speed (mm/s), h is the hatching distance (mm) and t is the layer thickness (mm).

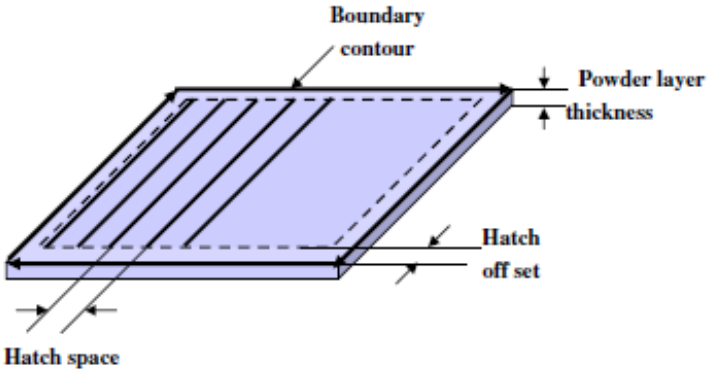

Figure 5.4: Schematic representation of various operating parameters of SLM process [102].

$$E = \frac{P}{vht} \tag{5.1}$$

For the laser beam to fully melt the material, high energy levels must be achieved which is possible using high laser power and thin powder layer thickness. This way, SLM can suffer from instability of the molten pool due to the full melting mechanism used. Also, SLM is characterized by the high temperature gradients and the rapid solidification. These aspects can bring the following issues [13]:

- "Balling" effect - is the spheroidization of the liquid within the molten pool caused by the molten pool instability. Balling can be caused, for example, by low scan speed as it results on a long liquid lifetime because the solidification is slower. Balling is also caused by high scan speed as it drives to enhanced instability of the liquid. Figure 5.5 shows images of a titanium part produced by SLM at different scan speeds: 100, 200, 300 and 400 mm/s. The higher balling occurrence can be detected at 100 and 400 speeds. Balling effect can lead to discontinuous scan tracks, porosity due to non-uniform deposition of fresh powder over previously powder bed and delamination due to poor inter-layer bonding [103];

- Microstructure - uncontrollable development of non-equilibrium phases and microstructures caused by the rapid solidification. Basically, rapid colling rate can lead to non-finished phase changing;

- Distortion - in selective laser melting, there is a high rate of colling of the powder bed in order to receive the next layer, resulting on high temperature gradients [100]. Therefore a large degree of shrinkage tends to occur during liquid-solid transformation. The thermal residual stresses during cooling can be responsible for distortions and a flat powder bed surface can become a

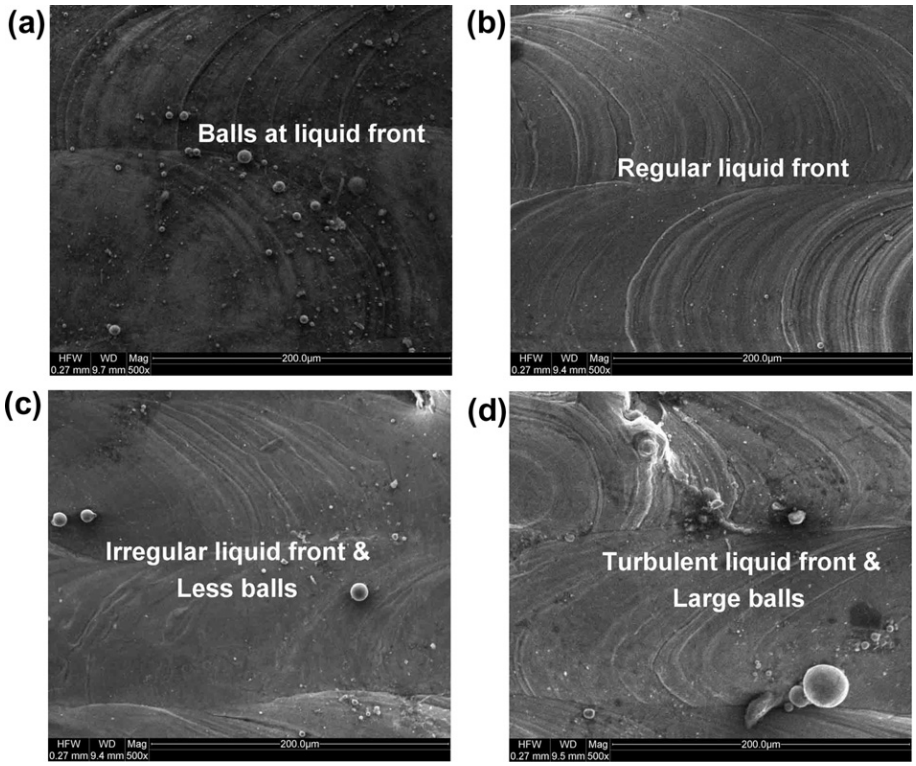

Figure 5.5: Balling effect at different scan speeds: a) 100 mm/s, b) 200 mm/s, c) 300 mm/s and d) 400 mm/s [103].

curved surface due to rapid densification Thermal stresses can also lead to formation of cracks and pores in the material.

5.3 Titanium and titanium alloys processed by SLM

Attar *et al.* [15], aiming to compare wear properties of Cp-Ti parts produced by SLM and by casting, presented the microstructure achieved by both process, showed in Fig. 5.6. It can be seen that for the SLM part, acicular α' martensitic microstructure is present with width of 0.82 μm, while casting part presents a microstructure with plate-like shape and width of 1.57 μm. Selective laser melting processed sample has finer microstructure which is probably due to high colling rates as for casting process moderate cooling rates are used. As a consequence of this finer microstructure, SLM part presented a hardness of 261 HV and casting part a hardness of 210 HV.

Considering density of titanium and titanium alloys manufactured by SLM, studies have showed that almost fully dense parts can be achieved, but with optimized processing parameters. Therefore, parts produced by SLM can present densities inside a wide range of values and with varying porosities. The higher the part porosity

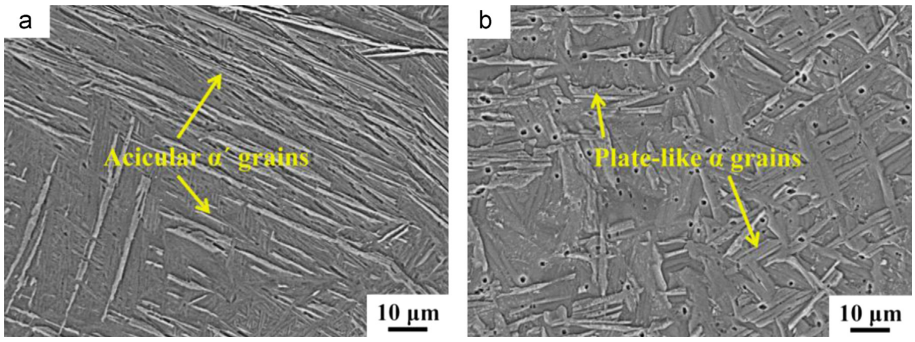

Figure 5.6: SEM microstructure of the Cp-Ti samples produced by (a) SLM and (b) casting [104].

is, the lower the density is. Generally, the almost fully dense parts are achieved by a combination of high laser power, sufficient to fully melt the metallic powder, and moderate scanning speed.

Pattanayak *et al.* [102] studied the effect of SLM processing parameters such as laser power, scanning speed and scanning strategy on the density of pure titanium by fabricating plate specimens with the objective of producing porous structures analogous to human trabecular bone. The effect of laser power to scanning speed ratio is showed in Fig. 5.7a with and without boundary contour, where theoretical density of Ti (5.1 g/cm) is achieved with increased laser power. Figure 5.7b shows the density varying with the plate specimen thick for two different hatch spaces. Theoretical density was nearly achieved for thickness over 1.8 mm.

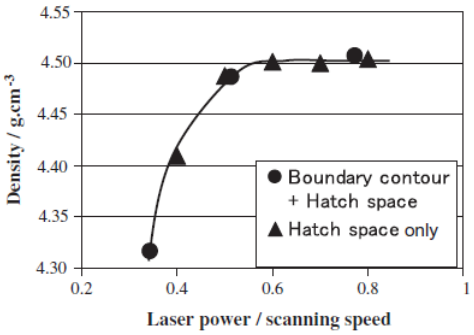

(a) The effect of laser power to scanning speed ratio on density [102].

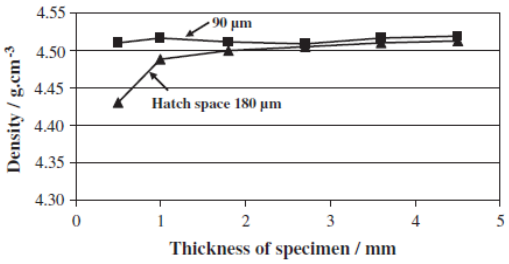

(b) Density varying with the plate specimen thick for two different hatch spaces [102].

Figure 5.7: Density

Gu *et al.* [97] studied the relationship between processing parameters with material properties such as densification, hardness and wear using Cp-Ti grade 2. Figure 5.8a and 5.8b show, respectively, the particle morphology and the accumulative particle size distribution of the starting Cp-Ti powder. Ti powder had spherical shape and a maximum size of 43.3 μm. Figure 5.8c shows the microstructure of processed Ti and the result is similar to Fig. 5.6. 99% dense pure titanium parts were achieved

when using scanning speed of 200 and 300 mm/s. With lower and higher speeds, microcracks and micropores were formed and balling effect occurred. As a consequence of the densification behavior, hardness results for the almost fully dense parts were higher than for parts that presented microcracks and pores, as showed by Fig. 5.8d.

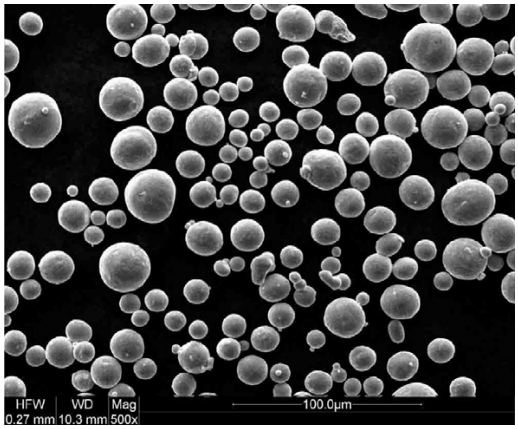

(a) Particle morphology of Cp-Ti powder [97].

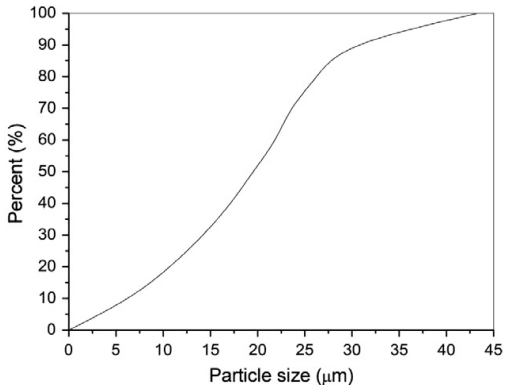

(b) Particle size distribution of Cp-Ti powder [97].

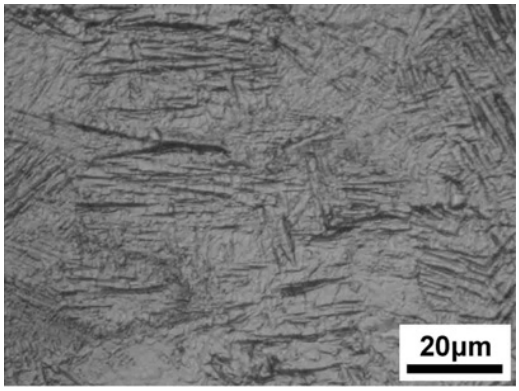

(c) Microstructure of SLM part [97].

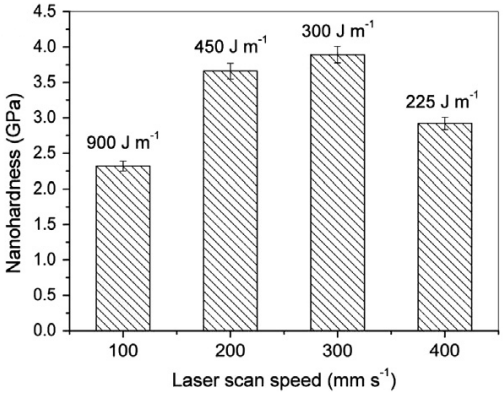

(d) Nanohardness varying with laser scan speed [97].

Figure 5.8: Properties of material used in selective laser melting

Chen *et al.* [105] evaluated the density, surface roughness and mechanical properties of a custom-made Cp-Ti grade 2 dental implant manufactured by SLM with two shapes, threaded and no threaded, using scanning speed of 275 mm/s, laser power of 100 W and layer thickness of 30 μm. More than 99% density was achieved and average surface roughness measured was 4.735 μm. The paper does not explained how or in which part of the manufactured implants roughness was measured. Also, a yield strength of 559 MPa was attained which is a much higher value than conventional Cp-Ti. The no threaded and threaded implants are shown in Fig. 5.9a and 5.9b.

Barbas *et al.* [106] evaluated the mechanical properties of Cp-Ti grade 2 processed by SLM and, also, an elementary pattern for the part was designed to approximate the properties of human bone and increase implant osteointegration. Table

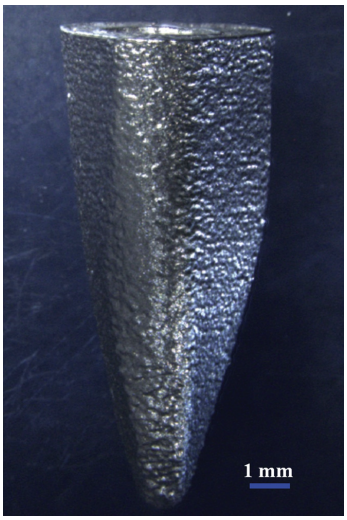

(a) Root-analog implant [105].

(b) Root-analog threaded implant. [105].

Figure 5.9: Implants manufactured by SLM

5.1 summarizes the results. Selective laser melting part presented improved properties in relation to regular Cp-Ti, with higher ultimate tensile strength and yield strength. The part produced with a designed pattern achieved the objective of approaching cortical bone properties. Elastic modulus, for example, is a lot closer to bone value, which can drastically decrease stress shielding occurrence.

Table 5.1: Comparison between regular Cp-Ti, SLM Cp-Ti, SLM Cp-Ti produced with designed pattern and cortical bone properties [106].

Properties	**Regular**	**SLM (bulk)**	**SLM (designed)**	**Cortical bone**
Elastic Modulus (GPa)	-	101	38	17.4
Yield Strength (MPa)	230	533	133.3	182
Tensile Strength (MPa)	345	617	143.6	195

Traini *et al.* [14] fabricated parts by selective laser melting using Ti-6Al-4V alloy powder with particle size of 1-10 μm and used acid etching techniques to improve surface microstructure. According to the authors, surface roughness could not be measured as an extremely variable level of values was found, varying in the range of 0-400 μm. However, elastic modulus values of porous and compact Cp-Ti processed by SLM were measured and compared to ASTM machined Cp-Ti and cortical bone, as shown by Fig. 5.10. Porous Cp-Ti reached values closer to cortical bone than the others, which can reduce stress shielding effect.

Zhang *et al.* [107] studied the influence of the hatch space on the mechanical properties of parts produced by SLM using Ti-6Al-4V powder. A scanning speed of 300 mm/s, laser power of 130 W and 35 μm layer thickness was used. The scanning strategy used was that scan lines of each subsequent layer is perpendicular to the former one and hatch spaces in a range of 200-700 μm with 100 μm step. Figure 5.11

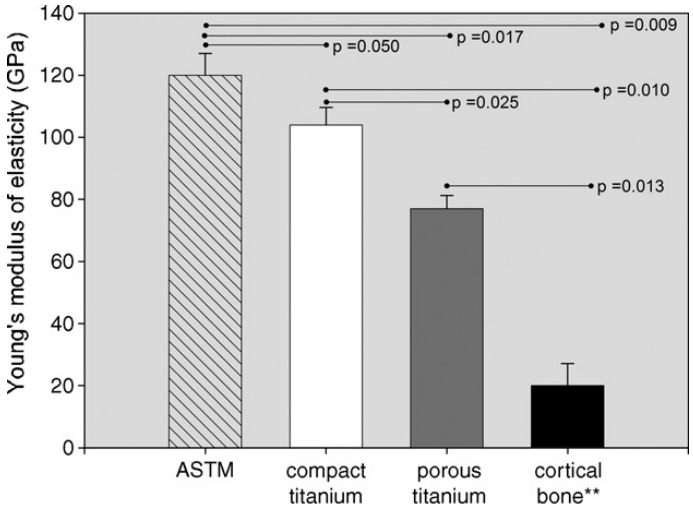

Figure 5.10: Young's modulus of elasticity of compact core and porous region of the specimens compared to ASTM values and values of cortical bone [14].

shows the pores of the parts for all hatch spaces. It can be seen that for increased hatch spaces, pore sizes also increase and from hatch space of 400 μm on, open pores were detected. Table 5.2 shows the results for mechanical properties and porosity. Elastic modulus decreases with increased hatch space, which is advantageous for dental implants, however yield strength also decreases.

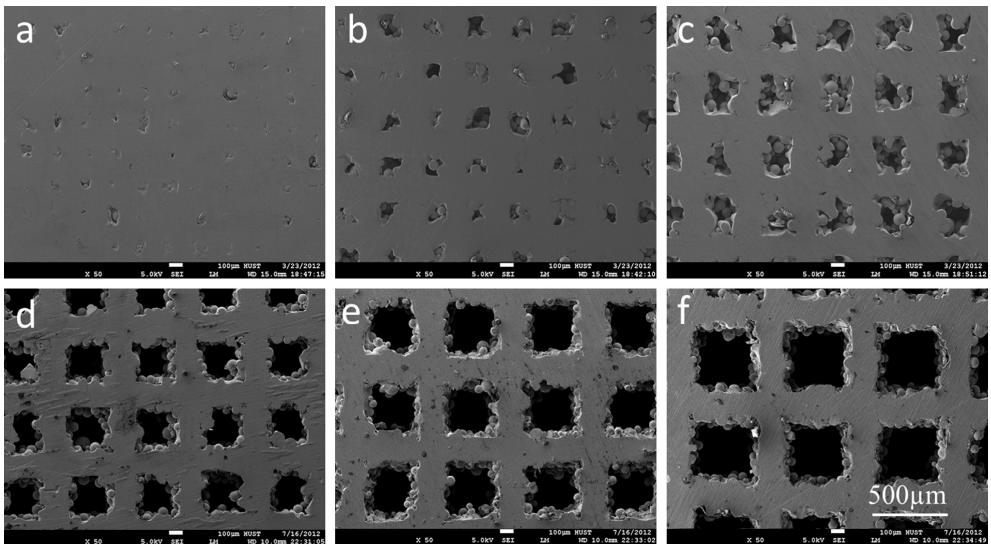

Figure 5.11: SEM images of the porous Ti6Al4V implants fabricated by selective laser melting at different scan line spacing[(a) 200 μm; (b) 300 μm; (c) 400 μm; (d) 500 μm; (e) 600 μm and (f) 700 μm] [107].

Table 5.2: Mechanical properties and porosity for varying hatch space [107].

Hatch space (μm)	Yield strength (MPa)	Elastic Modulus (GPa)	Porosity (%)
200	862	85	11
300	770	58	18
400	686	44	23
500	603	28	39
600	559	20	44
700	467	16	49

5.4 Machinability of titanium and titanium alloys produced by additive manufcturing

Machining metallic materials produced by additive manufacturing processes is a field of research that still is in development and until 2016 there were no studies on the topic published on relevant journals. To this day, there is no study covering machining of titanium produced by selective laser melting in macromilling nor micromilling. However, there are a few recent studies covering a few different machining processes, different additive manufacturing processes and different materials.

Montevecchi *et al.* [108] studied the influence of two different additive manufacturing processes, Laser-Engineered-Net-Shaping (LENS) and Wire-Arc-Additive-Manufacturing (WAAM), in the cutting forces during milling experiments of AISI-H13 using a 4 mm diameter solid carbide tool. The results showed that the additive manufacturing material for both processes presented increased hardness and, as a consequence, increased cutting forces, as showed in Fig. 5.12 However, the author missed in analyzing why the additive manufacturing processes produced harder AISI-H13 parts.

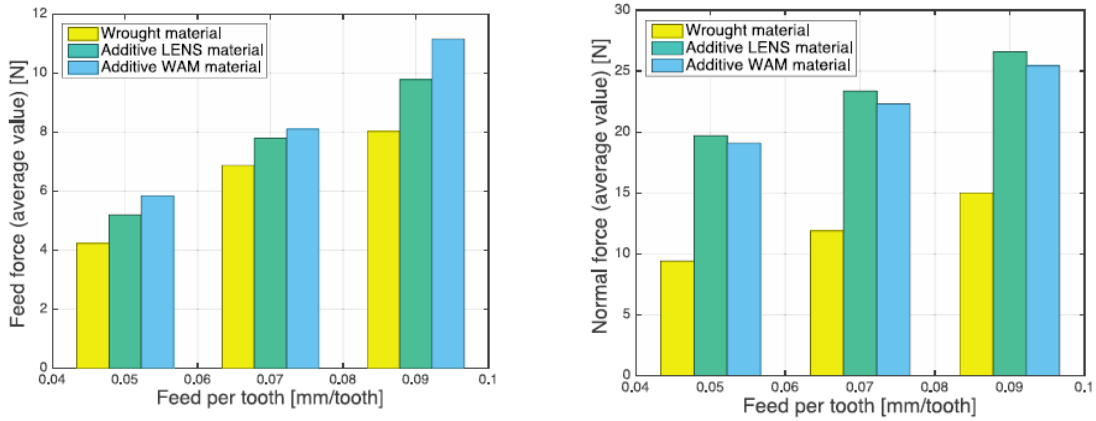

(a) Average feed force.

(b) Average normal force.

Figure 5.12: Cutting force in milling additive material titanium [108].

Bruschi *et al.* [109] analyzed different lubrication methods during micromilling of Ti-6Al-4V produced by the additive manufacturing process Electron Beam Melting.

They analyzed surface integrity using Minimum Quantity Lubrication (MQL), dry cutting and cryogenic colling aiming applications in biomedical industry in which the cleaner the manufacturing environment is, the better is for the material. The authors concluded, analyzing roughness and burr formation, that dry cutting condition delivered the same performance than MQL, being the most suitable option as ensures a clean environment. Figure 5.13 shows the results for surface surface and it can be seen that for most feeds, the differences between dry cutting and MQL are not relevant.

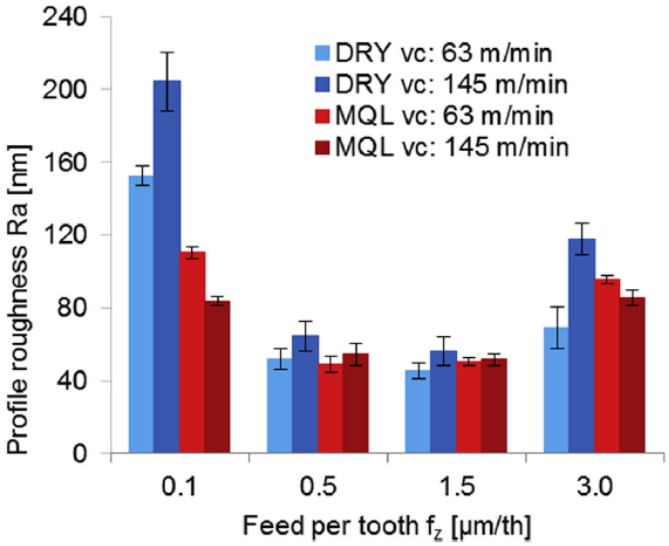

Figure 5.13: Machined surface roughness as a function of the cutting parameters under dry and MQL conditions [109].

Rysava *et al.* [110] tested different cutting conditions in microdrilling of Ti-6Al-4V produced by DMLS and analyzed the feasibility of threading the holes aiming the fabrication of internal threaded holes of dental pins. They concluded that the best parameters for the microdrilling process is 60 m/min and feed per tooth of 10 μm and they succeeded in producing internal threads.

Khorasani *et al.* [111] carried out a study milling a fully dense prosthetic acetabular shell (for hip implants) made of Ti-6Al-4V focusing on developing a static model for tool deflection using a ball-end-milling tool. Therefore, they did not focused on the influence of the manufacturing process on the machining operation.

Polishetty *et al.* [112] studied the differences between standard Ti-6Al-4V and the same material produced by selective laser melting in turning, considering cutting forces and surface roughness. They found out that the cutting forces were higher for the SLM material due to increased strength presented by the material. Thus, SLM material presented lower surface roughness because of their increased hardness and brittleness.

Finally, Bonaiti *et al.* [113] investigated the machinability in micromilling of Ti-

6Al-4V produced by LENS, analyzing cutting forces, roughness and burr formation. They found several differences when comparing the AM material with the standard titanium alloy: AM material presented higher hardness due to a finer microstructure; standard titanium presented higher surface roughness than AM titanium; despite presenting increased hardness, AM titanium presented lower cutting forces; and standard titanium presented better results considering burr formation.

According to the published papers reviewed, it can be seen that it is possible to obtain almost fully dense parts using selective laser melting procedures. Also, porous structures can be achieved, which leads to smaller elastic modulus values, closer to cortical bone. Therefore, stress shielding can be minimized. But increasing porosity of the part, besides decreasing elastic modulus value, will also affect part strength. So, a balance between these properties must be achieved. And to achieve these properties, processing parameters must be carefully chosen.

Chapter 6

Materials and Methods

This chapter presents the experimental methodoly and describes the equipment used in the experimental procedure. It is divided in two separate groups: first the experimental activities until the micromachining of samples, as shown in Fig. 6.1; and secondly the analysis of the machining results, as shown in Fig. 6.2.

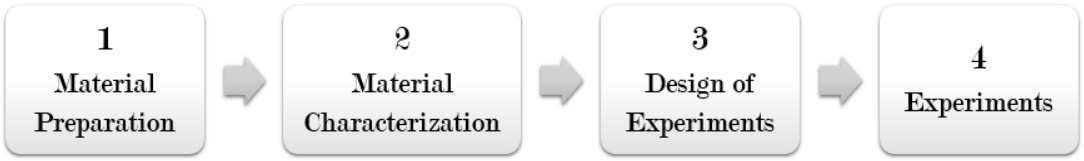

Figure 6.1: Experimental procedure stages.

It is presented the equipment and tools used to perform the micromilling experiments and to measure the cutting forces; the equipment used to measure roughness, burr and to analyze the chips and grooves; the equipment and procedure used to characterize the materials and samples used in the experiments; and the design of experiments.

6.1 Materials

This section details bulk manufacturing and the preparation of the workpieces used in this work: standard annealed commercially pure titanium (Grade 2), standard annealed titanium alloy Ti-6Al-4V (Grade 5), commercially pure titanium processed by equal channel angular pressing and titanium alloy Ti-6Al-4V fabricated through selective laser melting. It also covers the parameters, procedures and equipment used to characterize these materials.

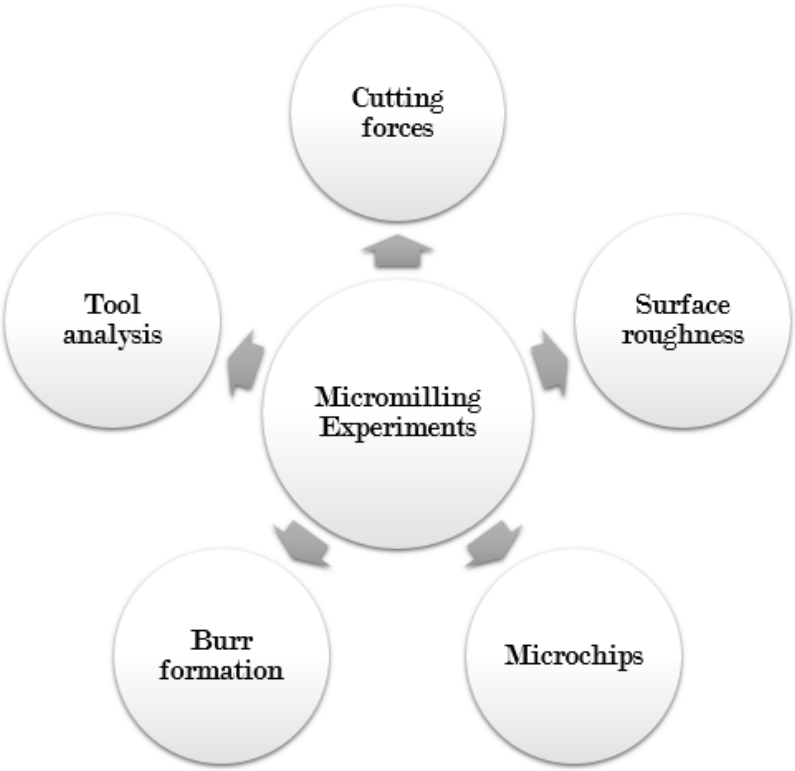

Figure 6.2: Experimental analysis.

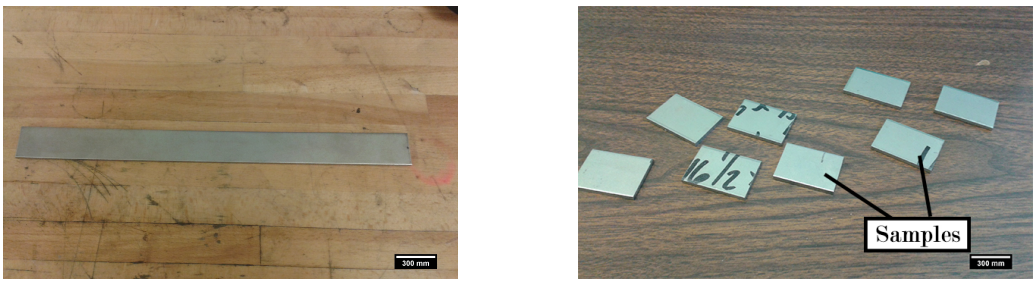

(a) Initial bar. (b) Samples.

Figure 6.3: McMaster-Carr commercially pure titanium raw bar and samples.

6.1.1 Preparation of the samples of commercial workpieces

For simplification purposes, during the explanation of this study, the commercially pure titanium (CP-Ti) samples will be referred to as 'CP-Ti' samples, the Ti-6Al-4V samples will be referred to as 'alloy' samples, the samples processed by ECAP as 'ECAP' samples and the samples manufactured by SLM as 'SLM' samples.

The CP-Ti and alloy workpieces were cut out of raw material bars purchased in McMaster-Carr Supply Company, as showed in Fig. 6.3. According to the supplier, both titanium materials meet the specifications of ASTM B265 standard.

6.1.2 ECAP workpiece production

The commercially pure titanium ECAP sample was supplied by the *Laboratório de Processamento Termomecânico – Biomateriais* (Thermomechanical Processing Laboratory - Biomaterials) from COPPE/UFRJ. It was produced by processing titanium powder through ECAP, using the process for metallic powder consolidation along with grain refinement. The procedure consisted of the following stages:

- Titanium powder was insert in an ASTM 304 stainless austenitic steel tube with a bottom fix lid and a sliding up lid, as showed in Fig. 6.4 and Fig. 6.5a. 2g of titanium powder was insert at a time;
- The powder was pressed by a manual press with 4 tons of force by two seconds every time, until it reached a distance of 10 mm from the top of the tube;
- To reduce the friction during the ECAP processing, the tube was lubricated using MoS_2 and involved with polytetrafluoroethylene (PTFE) tape;
- The ECAP processing was carried out with the matrix at 375°C, below the recrystallization temperature of titanium, and it was performed 4 passes using route C, where the sample is turned 180° by the longitudinal axis after each pass. Also, the sample was heated inside the matrix for 10 minutes before the process begin;

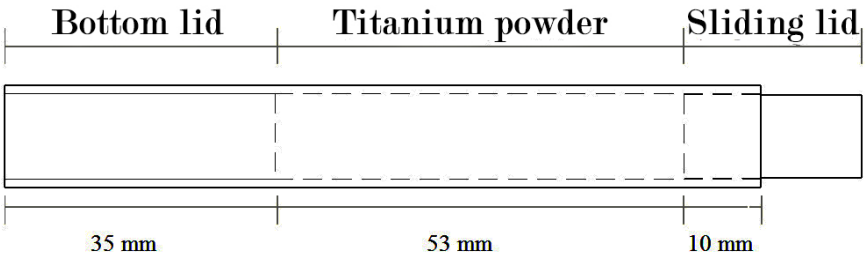

Figure 6.4: Commercially pure titanium and stainless steel set scheme (adapted from [114]).

After the ECAP processing and consolidation of the titanium powder, the material was cut in pure titanium small bars as showed in Fig. 6.5b. From these small bars, a few samples for flexure and hardness tests were manufactured. The samples used in the micromilling experiments were the same used in the mechanical tests in order to ensure that there was no differences in the mechanical properties of the samples tested and the samples that were machined.

Due to the small dimensions of the samples that were tested and, as a consequence, used in the machined tests, they were mounted on bakelite pucks so they

(a) Stainless steel tube with lids.

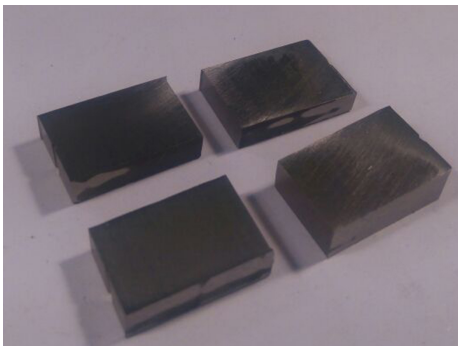

(b) Titanium parts cut out of consolidated titanium.

Figure 6.5: Equal channel angular pressing sample production.

could be fixed on the dynamometer for the micromilling tests, as shown in Fig. 6.6. Thus, the bakelite pucks were cut so that the milling tool could cut the titanium workpiece without having to cut the bakelite first as it could already cause tool wear and prejudice the experiments results.

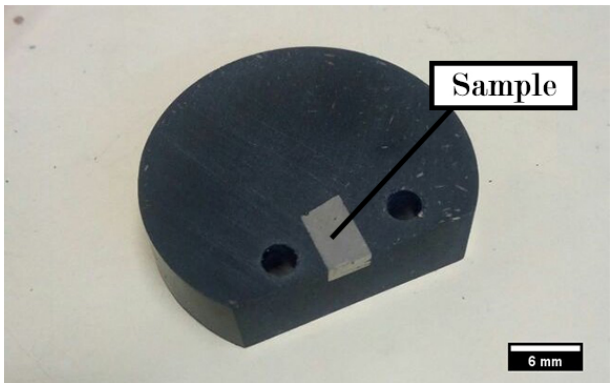

Figure 6.6: Bakelite puck with ECAP sample mounted for micromilling experiments.

6.1.3 SLM workpiece production

The SLM Ti-6Al-4V sample was supplied by *Biofabris - Instituto Nacional de Ciência & Tecnologia em Biofabricação* (National Institute of Science and Technology in Biomanufacturing). It was manufactured by SLM using a EOS M270 machine. The morphology of the Ti-6Al-4V powder used is shown in Fig. 6.7a. The particles presented a spherical morphology with varying diameter.

The process parameters like laser energy, scanning speed and layer thickness can be seen in Tab. 6.1. They were specified so that a fully dense Ti-6Al-4V alloy sample was obtained. The sample suffered a stress relief process to reduce residual stresses and avoid warpage and it is shown in Fig. 6.7b.

Table 6.1: SLM parameters

Parameter	Value
Laser power	170 W
Scaning speed	1250 mm/s
Layer thickness	0.03 mm
Hatch space	0.1 mm

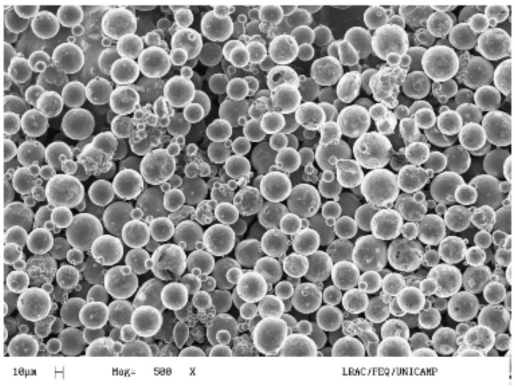

(a) Ti-6Al-4V powder.

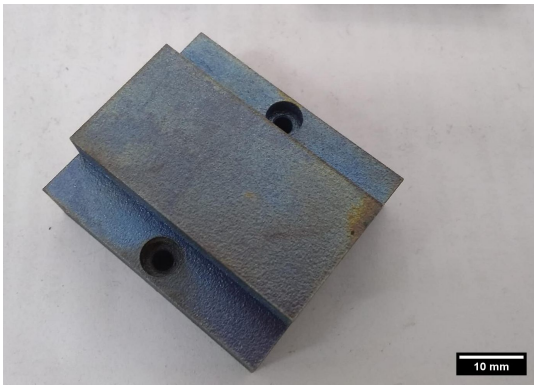

(b) Selective laser melting sample.

Figure 6.7: Selective laser melting sample production.

6.1.4 Characterization of materials before machining

The first stage for characterization of the materials was performing an Energy Dispersive X-ray Spectroscopy (EDS) in order to identify the chemical elements present in each sample. This technique is performed through a scanning electron microscope (SEM) equipment.

The CP-Ti sample presented practically 100% presence of titanium.

The SLM sample presented a major peak for titanium presence and secondary peaks for aluminum and vanadium and the ECAP sample also presented practically 100% of titanium.

For the alloy sample, the peak related to the vanadium presence is not appearing, but it was probably masked by the second titanium peak and they overlapped.

The next step for characterization of the materials was performing a metallographic analysis which was held at the *Laboratório de Microscopia Ótica* of the Materials and Metallurgical Department from COPPE/UFRJ (Optic Microscopy Laboratory). The samples surface which would be analyzed passed through a series of procedures, as shown in Fig. 6.9, and detailed as follows:

- Conventional grinding using sandpapers from 100 to 2400 μm/;
- First stage of polishing using a solution of 100 g of alumina, 50 ml of oxalic acid and 400 ml of distilled water;

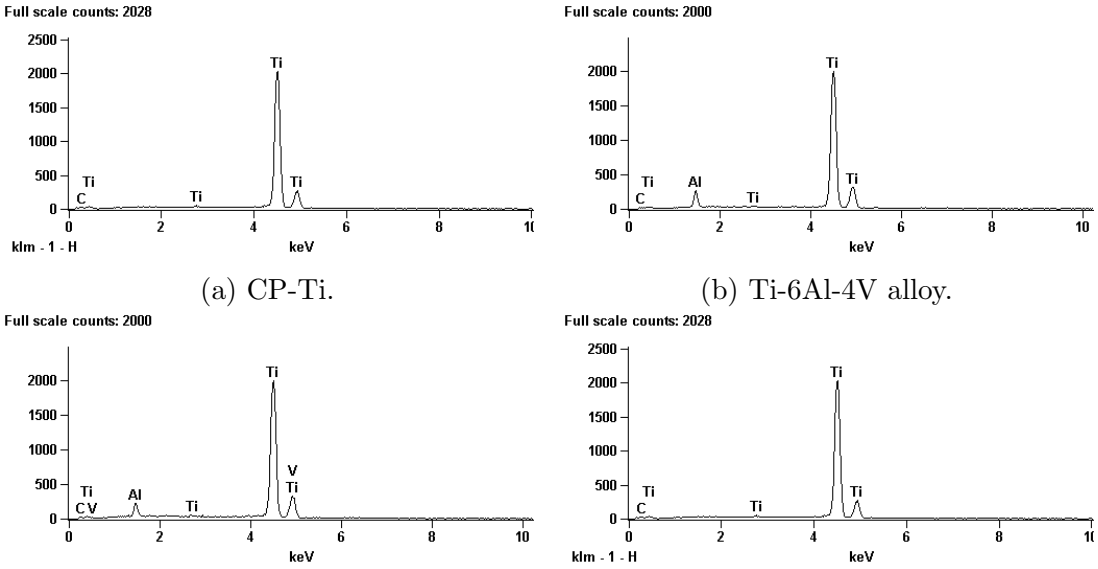

(a) CP-Ti.

(b) Ti-6Al-4V alloy.

(c) SLM.

(d) ECAP.

Figure 6.8: Energy Dispersive X-ray Spectroscopy.

Figure 6.9: Procedure for metallography of the materials.

- Second stage of polishing using a colloidal silica dispersion;
- Chemical attack with Kroll's reagent, composed of 250 ml of distilled water, 20 ml of nitric acid and 2 ml of hydrofluoric acid as shown in Fig. 6.10a;
- Image analysis using a setup with an optical microscope, a camera (LG LVC-SX810HM), a computer and a software (Snappy 4.0) to record the images, as shown in Fig. 6.10b.

Following the microstructure analysis, some mechanical properties were measured so it would be possible to compare the materials behaviors during the machining tests.

Hardness tests were carried out at the *Laboratório de Propriedades Mecânicas* (Laboratory of Mechanical Properties) of the Materials and Metallurgical Department from COPPE/UFRJ. It was performed Vickers hardness tests with loads of 30 kgf for cycles of 20 s using an Indentec universal tester. It was taken five measurements of hardness for each material and the average was computed.

Also, **flexure tests** were performed to measured the apparent flexural modulus (modulus of elasticity in bending) and the flexural strength of the materials. It

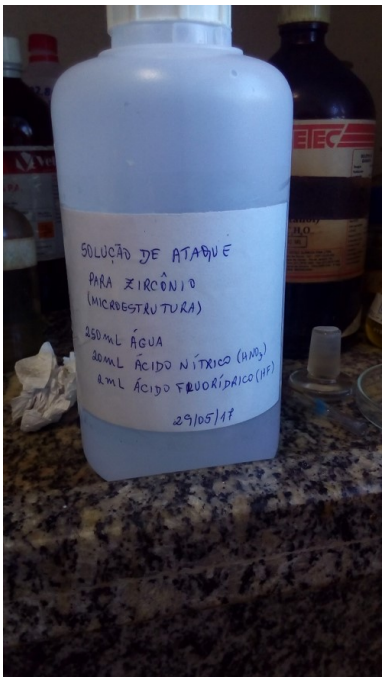

(a) Kroll's reagent

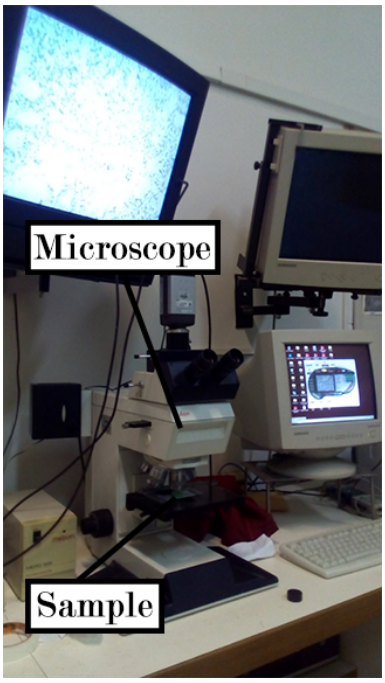

(b) Equipment for microstructure images.

Figure 6.10: Metallographic analysis.

was carried out three points flexural tests at the *Instituto Naiconal de Tecnologia* (National Institute of Technology) using samples with dimensions of 10 x 4 x 2 mm. It was used an especial device for the support of the sample adapted for an universal equipment of tests INSTRON 3382, as shown in Fig. 6.11.

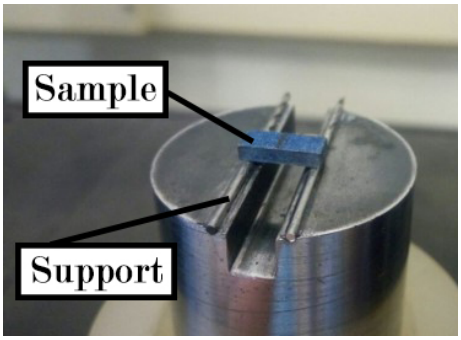

(a)

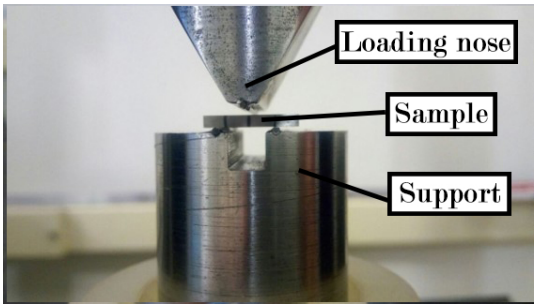

(b)

Figure 6.11: Three points flexural test setup.

Additionally to the hardness and flexure tests, considering the nature of the selective laser melting process, a **porosity test** was made to measure the percentage of density of the SLM sample. It was used the Archimedes method and it was carried out at the Laboratório de Polímeros (Polymers Laboratory) from the Materials and Metallurgical Department from COPPE/UFRJ. The Archimedes method of measuring the porosity of a sample consists of using hydrostatic weighing, as shown in Fig. 6.12 to measure the apparent and real masses of the sample. Using the

apparent mass, the real mass and real volume of the sample, it is possible to compute the apparent porosity of the sample. The porosity measured for the SLM sample was 1.7%.

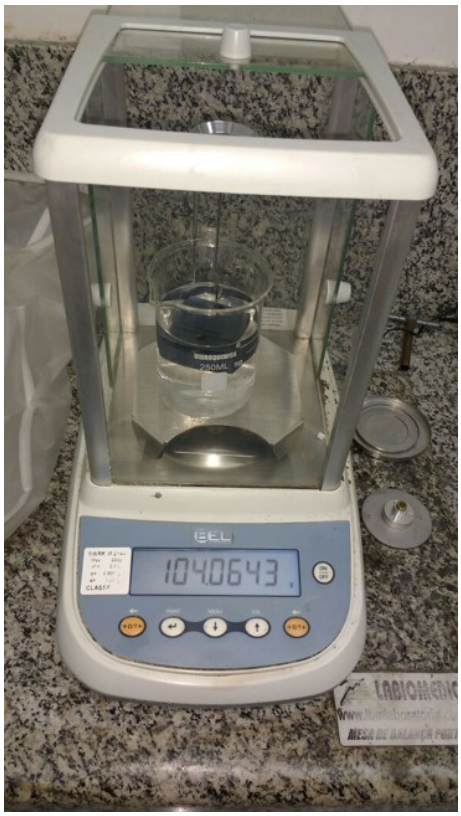

Figure 6.12: Hydrostatic weighing for porosity measurement.

6.2 Equipment for micromilling experiments

In this section, the equipment, tools and experimental setup used for each stage of the micromilling experiments and analysis of the cutting forces, roughness, burr formation and microchips are detailed.

6.2.1 Machine tool

The machining experiments were performed in the Micromilling Laboratory (LMM) which is part of the *Centro de Estudos em Fabricação e Comando Numérico (CEFCON)*, a laboratory of COPPE/UFRJ. The machine tool used in this work was the CNC Mini-Mill/GX from the Minitech Machinery Corporation, showed in Fig. 6.13. This machine has three axis of translation between the workpiece and the machine. The axis are moved by stepper motors using ball screws, ball bearings anf linear slides with caged balls which provide little friction during the moving process.

Figure 6.13: CNC Mini-Mill/GX.

The mini-mill is controlled by CNC, using the software Mach3. The tool controller provides a Nakanish motor with a maximum rotational speed of 60000 rpm, with refrigeration by compressed air. The machine technical specifications are given in Tab. 6.2.

Table 6.2: Technical specifications of the mini-mill used in the experiments.

Base material	Granite
x **Axis Travel**	300 mm
y **Axis Travel**	228 mm
z **Axis Travel**	228 mm
Table size	152.4 x 444.5 mm
Hold down provision	1/4-20 tapped holes on 2.54 mm centers
Maximum rpm	60.000 rpm

6.2.2 Microtools and collet

The microtool used to perform the micromilling experiments was a 500 μm 2 flute Mitsubishi Materials carbide square end mill without coating. Besides the diameter, the microtool geometry consists of a shaft with 4 mm diameter, a flute length of 1 mm and a total length of 40 mm, as showed in Fig. 6.14a. According to the manufacturer, this tool is indicated for general use. To fix the microtool in the spindle, it was used a NAKANISHI collet specific for fixing tools with shaft diameter of 4 mm, as shown in Fig. 6.14b. It has an external maximum diameter of 10.5 mm and an internal diameter of 4 mm.

The tools were analyzed using a scanning electron microscope from Zeiss, model DSM 940, of the *Laboratório Multiusuário de Microscopia Eletrônica e Microanálise* from the Materials and Metallurgical Engineering Department (COPPE/UFRJ). It was measured the cutting edge radius, the helix angle and the point radius of the tool.

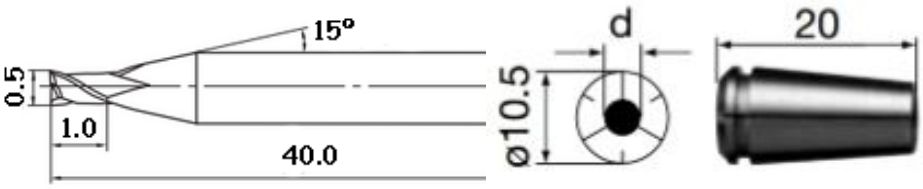

(a) Square end mill geometry. (b) Microtool collet.

Figure 6.14: Microtool and collet geometries.

Cutting edge radius plays an important role on micromilling as it is usually around the same size of the feed per tooth. Using feeds per tooth lower than the cutting edge of the tool can cause the tool to work on ploughing region, which can cause the consequences discussed in Chapter 2. Edge radius measurement was performed according to the images in Fig. 6.15c and Fig. 6.15a.

Also, the depth of cut used in micromilling operations must be bigger than the point radius of the tool, otherwise the tool will not be able to fully cut the specified depth of cut. Measurement of the point radius of the microtool was made as showed in Fig. 6.15d.

Thus, it is important to know the helix angle of the tool because they are responsible to determine how significant cutting forces in the tool axis and tool periphery directions will be. As the helix angle increase, side loading on the tool decreases as well as the amount of heat generated during the cutting process. Helix angle measurement is shown in Fig. 6.15b.

The measurements of these values were made using the *ImageJ* software which is used for image processing. The results were 2 to 2.5 μm cutting edge radius, 10 μm tip radius and 26° helix angle.

6.2.3 Cutting force measurement

For the cutting force signal acquisition, an experimental setup was assembled with a dynamometer, a signal amplifier, an acquisition board and a computer with a software for data reading.

A Kistler dynamometer 9256C2, shown in Fig. 6.16a, with cable 1697A was used for the cutting force signal acquisition. This type of dynamometer was design specifically for measurement of force signals with values below 250 N. It has low minimum flow of signal, which is the minimum signal for acquisition, and sensitivity three times higher than the ones from conventional dynamometers, hence making it possible the measurement of small cutting forces.

This dynamometer has a positioning region for the workpiece of 55 × 80 mm. Its fixation on the machine table can be done using M4 Allen screws or by pressure and it

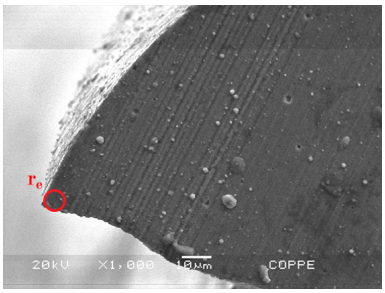

(a) Cutting edge radius

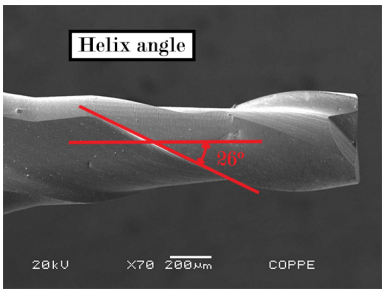

(b) Helix angle

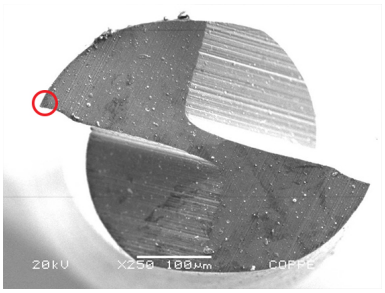

(c) Cutting edge radius measurement

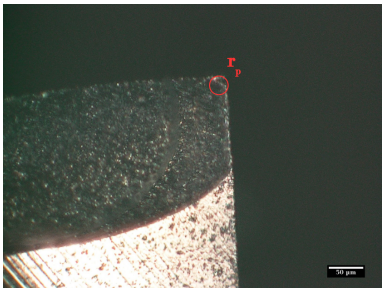

(d) Tool tip radius

Figure 6.15: Microtool geometry analysis.

has M3 holes for the workpiece fixation on the sensor. Some technical specifications like sensitivity, minimum flow and measure range are shown in Tab. 6.3. It acquires forces in three directions: F_x, F_y and F_z.

Table 6.3: Technical specifications of the dynamometer.

Measurement range	-250 a 250 N
Minimum flow	<0,002
Sensitivity for F_x	-25,61 pC/N
Sensitivity for F_y	-12.86 pC/N
Sensitivity for F_z	-25.86 pC/N
Dimensions	80 × 91 × 25 mm

The force signal is transmitted to a charge amplifier where the signal is converted from electrical charge to a proportional voltage value. A 5070A10100 Kistler amplifier, shown in Fig. 6.16b was used in the experiments. In the charge amplifier, it is adjusted the sensitivities of the dynamometer indicated by the manufacturer for each channel in the data sheet.

Also, it is specified in the amplifier the amplification rate, in accordance with the signal range that will be measured. It is possible to apply an analog filter using the amplifier. However, for the experiments carried out in this work, no previous filter was applied, so the rough signal could be analyzed and a digital filter applied if necessary.

The charge amplifier is connected to an acquisition board, which converts the experimental analog signal into digital signal, so it can be read by a computer

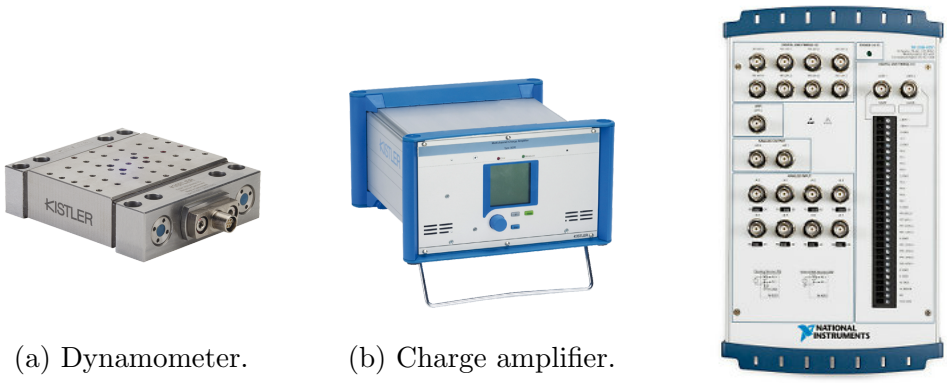

(a) Dynamometer. (b) Charge amplifier. (c) Acquisition board.

Figure 6.16: Equipment for the experimental setup for force measurements.

through a communication software. The digital file of the experimental cutting force signal is compound of a three columns matrix, one for each force component. The National Instrument acquisition board NI USB-6551, shown in Fig. 6.16c, and the LabView Signal Express 2012 for data reading was used. In the software, it is specified the acquisition frequency, which is the number of data points that will be acquired per second. The determination of this frequency depends on the tool spindle speed. It must be high enough so the cutting force profile per tool revolution can be identified in the force signal.

The dynamometer, the charge amplifier and the acquisition board used are shown in Fig. 6.16.

6.2.4 Roughness and burr measurement

For burr and roughness analysis, it was used a Taylor Hobson profilometer, Form Talysurf Intra 0120. This equipment has a maximum transversal displacement of 50 mm and 1 mm vertical range. It has a vertical resolution of 16 nm and a horizontal data spacing of 0.5 μm. It was also used the standard stylus 112/2009, series SY 0637. This stylus has an arm length of 57.5 mm and the distance between the arm and the surface being measured is 14.7 mm. The stylus presents a 90° angle between its walls and diamond tip with a diameter of 2 μm, as showed in Fig. 6.17a.

To perform burr formation analysis, the profile of the grooves was measured with the profilometer as showed in Fig. 6.17b. The profile was taken in five different positions of the groove. Next, top burr heights were measured for up and down milling using as a reference the top surface of the samples. The average and standard deviation from all five measurements were then computed.

To perform the roughness analysis, the profile of the topography of the surface was measured. Next, it was necessary to separate the raw profile measured in two

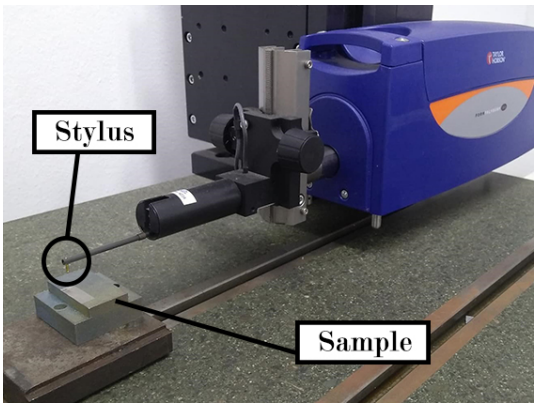

(a) Taylor Hobson profilometer and stylus used in burr and roughness analysis.

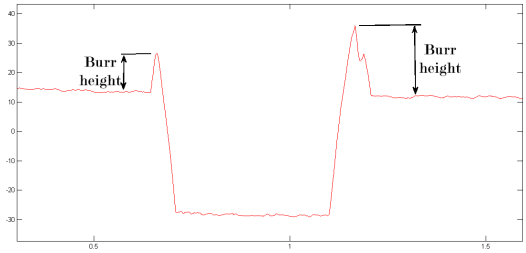

(b) Burr measurement procedure.

Figure 6.17: Surface roughness and burr measurement details.

curves: the primary texture (roughness) and the secondary texture (waviness). To achieve that, it was used the appropriate profile cut-off filter (λ_c). The cut-off was defined considering the ISO 4288-1996 recommendation of five times the expected spacing of the profile features which, for milling experiments, corresponds to the feed per tooth. As it will be seen in the Section 6.2.2, feed per tooth range of this work was from 0.5 μm to 4.0 μm. Therefore, considering the cut-off values available, it was used 0.08 mm. To perform this analysis, it was used the *Ultra Surface Finish V5* software.

Surface roughness measurement was performed in three different positions in the bottom surface of the groove with distance of 100 μm from each other, as shown in Fig. 6.18, and the average and standard deviation were computed. The samples were moved using a translation platform. Thus, all measurements were carried out in the longitudinal direction of the groove and in the feed direction.

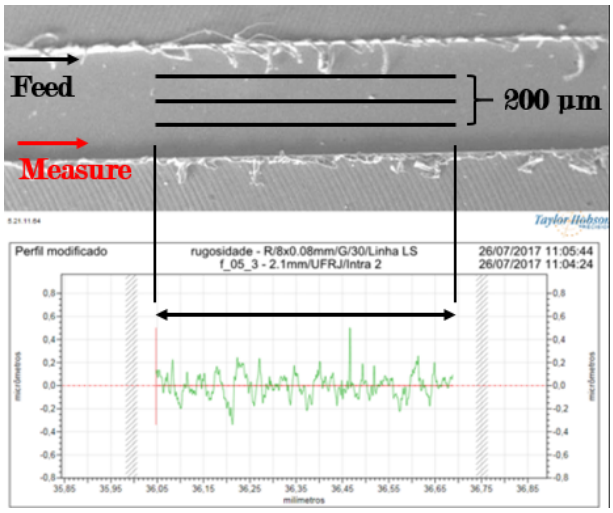

Figure 6.18: Surface roughness measurement procedure.

6.2.5 Chips and grooves analysis

In order to analyze the microtool, chips and the grooves, it was used a couple of different equipment. First, it was used a USB AM3715TB Dino-Lite Edge handheld digital microscope to get general images of the chips. This camera, showed in Fig. 6.19, has a maximum magnification of 220 times and a higher resolution output image of 640 x 480 pixels. Second, for better images of the chips and also to analyze the grooves, it was used a scanning electron microscope (SEM) from Zeiss, model DSM 940, of the Laboratório Multiusuário de Microscopia Eletrônica e Microanálise from the Materials and Metallurgical Engineering Department (COPPE/UFRJ).

Figure 6.19: USB AM3715TB Dino-Lite Edge handheld digital microscope.

The microchips were collected after each experiment using an adhesive tape. The process was carried out so that the microchips were not damaged.

6.3 Micromilling procedure

After characterizing the materials that would be machined and the microtools that would be used, next step was to define the experimental setup and the design of experiments for the micromilling tests.

6.3.1 Experimental setup for micromilling

The experimental setup for the micromilling tests consisted of the machine-tool, the computer to control the machine-tool, the dynamometer, the charge amplifier, the acquisition board and a second computer to read the cutting force signals. The microtool is fixed in the spindle using the appropriate collet and the workpiece is fixed on the dynamometer using screws, as showed in Fig. 6.20. The setup was arranged so the feed direction coincided with the 'x' direction.

During the cutting process, the dynamometer acquires the experimental cutting force signal in the directions as presented in Fig. 6.20: F_x, F_y and F_z. The force signal goes from the dynamometer to the charge amplifier which amplifies the signal, transforming the signal from electric current to voltage. The signal goes then to the

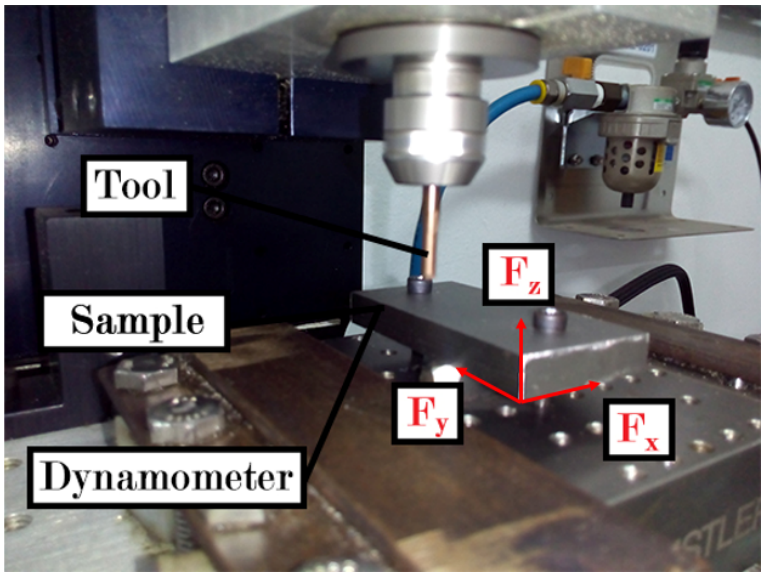

Figure 6.20: Tool, workpiece and the dynamometer: experimental setup.

acquisition board which transforms the analog signal to digital so it can be read in the computer, using the Labview software.

6.3.2 Surface preparation

Before actually performing the micromilling experiments, the surface of the workpieces must be prepared. This preparation consists of making a pre-machining with a conventional tool in order to make the surface plain to receive the micro grooves. If this step is not made, during the cutting process in the micromilling experiment, the axial depth of cut could vary, influencing the cutting force values and tool wear. It ensures that the depth of cut will remain constant during the whole process.

The surface preparation was carried out for all the workpieces with a carbide 3 mm end mill using always the same cutting parameters: cutting velocity of 37.7 m/min (4000 rpm), feed velocity of 120 m/min (feed per tooth of 15 μm/tooth), depth of cut of 30 μm and tool overlapping of 66% f the tool diameter. It was used low values of depth of cut and feed per tooth so the end mill would not wear too fast and the surface would be smooth to receive the microgrooves.

6.3.3 Design of experiments

In order to define the cutting parameters and the number of experiments that would be performed and their orders, it was first defined which parameters would be constant and which ones would vary. As the objective of the study was to compare the machinability of four different materials, it was chosen to vary the feed per tooth, which is the parameter that generally has more effect on measurements like cutting

forces, roughness and burr formation and is a critical parameter in micromilling. As it was seen in Chapter 2, when the feed per tooth used is smaller than the minimal chip thickness, the cutting mechanics changes and ploughing becomes dominant over cutting.

So it was defined a wide range of feed per tooth, including small values so the tool would also work in the ploughing region and its behavior could be defined for critical cutting edge radius-feed per tooth ratio ($r_e = 2 - 2.5\mu m$). Feed per tooth range was defined from 0.5 to 4.0 μm/tooth, which has values below and above the cutting edge radius.

The axial depth of cut was chosen using a value commonly used in the literature, ensuring only that it is higher than the point radius of the microtool which is 4 μm. Also, it was not chosen a value too high because of the low machinability of the titanium alloys. Using higher depth of cut, the microtool would wear too fast and a higher number of tools would have to be used to finish the experiments.

The experiments were performed in full immersion, which means that the radial depth of cut was the same value of the tool diameter. Therefore, in each groove the tool was cutting half time in upmilling and halftime in downmilling, as shown in the scheme of the Fig 6.21. The length of each groove was 4 mm and a dry cutting system was used.

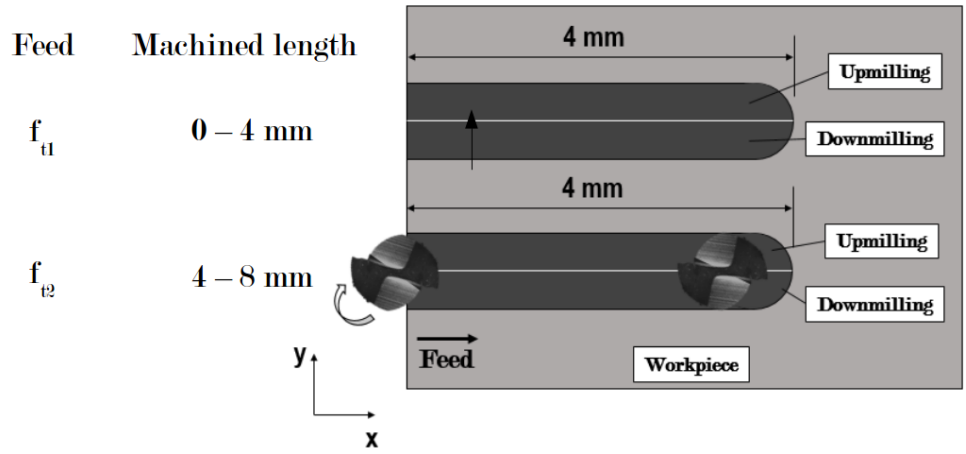

Figure 6.21: Experiments scheme.

To define the cutting speed and the spindle speed, a series of experiments were performed varying the spindle speed from 12000 to 24000 rpm. It was analyzed the burr formation for each speed and a cutting velocity of 28.3 mm/min (18000 rpm) presented better results.

A summary of the parameters used in the experiments is presented in Tab. 6.4.

To define the design of experiments, it was taken into consideration that the objective of the study was to compare how difficult the materials are rather than to exactly quantify the parameters to be measured. So, it was defined that one test and

Table 6.4: Cutting parameters during micromilling.

Tool Diameter (μm)	500
Spindle speed (rpm)	18000
Cutting speed (m/min)	28.3
Feed per tooth (μm/tooth)	0.5, 1.0, 1.5, 2.0, 2.5, 3.0, 3.5, 4.0
Axial depth of cut (μm)	40
Radial depth of cut (μm)	500 (full immersion)
Cutting length (mm)	4
Cutting system	Dry cutting

Table 6.5: Design of Experiments.

Material	**Batch**	**Tool**	**Exp.**	**Feed (μm/tooth)**	**Machined length (mm)**
CP-Ti, Ti-6Al-4V, SLM, ECAP	Batch A	Tool Batch A	1	0.5	4
			2	1.0	4-8
			3	1.5	8-12
			4	2.0	12-16
			5	2.5	16-20
			6	3.0	20-24
			7	3.5	24-28
			8	4.0	28-32
	Batch B	Tool Batch B	8	4.0	4
			7	3.5	4-8
			6	3.0	8-12
			5	2.5	12-16
			4	2.0	16-20
			3	1.5	20-24
			2	1.0	24-28
			1	0.5	28-32

one replica would be performed with each combination of the cutting parameters. For the first batch of experiments, it would be used an increasing feed (test) per tooth and for the second batch (replica), a decreasing feed. Using this configuration of the design of experiments, it would be possible to analyze the impact of tool wear in the parameters measured, like cutting force and surface roughness, as well as to compare the machinability of the materials. The first batch, performed in increasing feed order will be called batch A and the second one, performed in decreasing feed order, will be called batch B.

For each batch of experiment and for each material, it was used a new microtool. Table 6.5 shows the design of experiments. The results are presented in Chapter 7.

Chapter 7

Experimental Results

This chapter presents the results for the material characterization and micromilling experiments in standard commercially pure titanium, standard Ti-6Al-4V alloy, commercially pure titanium processed by ECAP and Ti-6Al-4V produced by SLM. The results presented are the microstructure and mechanical properties; machining force, roughness, burr measurement and microchips analysis results as well as microtool evaluation.

7.1 Microstructure

Optical microscope images from the microstructure of working materials are presented in Fig. 7.1. Figure 7.1a shows the microstructure of the commercially pure titanium grade 2 and, as expected, it shows a typical structure of a neutral titanium. It is composed by equiaxed coarsed alpha grains with dimension in the order of 20-30 μm and it is in agreement with literature results [43].

The microstructure of standard Ti-6Al-4V alloy is presented in Fig. 7.1b and is composed by equiaxed alpha grains mixed with alpha/beta small regions in between them. The alpha grains size varied from 10-20 μm and it is in agreement with literature results [115].

For the ECAP sample, due to the reduced grain size and the limitation of the optical microscope used, it was not possible to apply a higher magnification so the microstructure could not be fully identified, as showed in Fig. 7.1c. As the microstructure of ECAP materials are usually composed of ultra-fined grain, often with sub-micron dimensions, a higher magnification was necessary. However, it is of common knowledge that CP-Ti processed by ECAP presents refined fined alpha grains.

Figure 7.1d presents the microstructure of SLM fabricated Ti-6Al-4V and shows an acicular α' martensitic microstructure. This phase is a consequence of beta transformation and can be achieved through quenching, that is, cooling the material at

a rapid rate. Selective laser melting process has a rapid cooling rate unlike forging processes, that presents slow cooling rate. As it can be seen, the microstructure presents refined grains in comparison with Ti-6Al-4V standard annealed alloy. The acicular martensite grains presented width dimensions varying between 1-2 μm. It is important to notice that the microstructure did not present any sign of defects that can occur in SLM materials like balling effect and distortion. Also the microstructure showed no sign of voids, indicating that an almost fully dense material was achieved, as confirmed by the porosity test result. This result is in agreement with the literature presented [15].

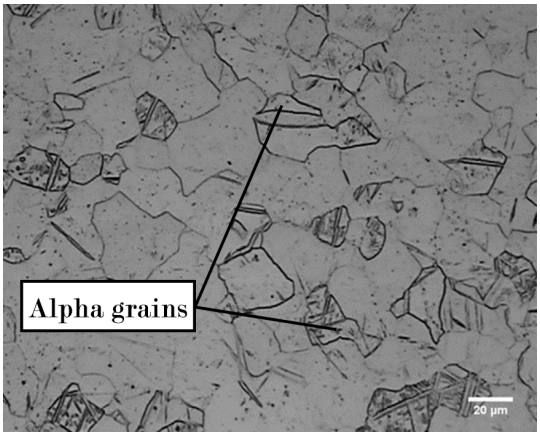

(a) CP-Ti grade 2.

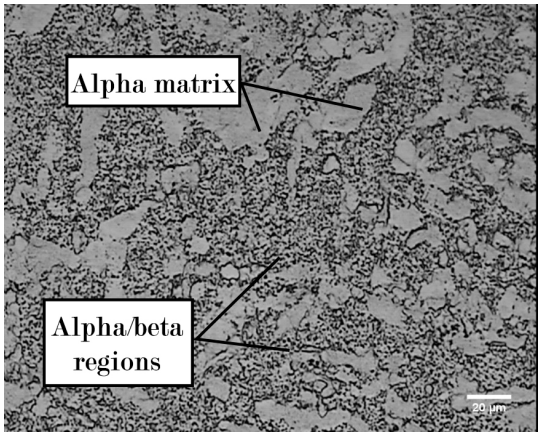

(b) Ti-6Al-4V alloy.

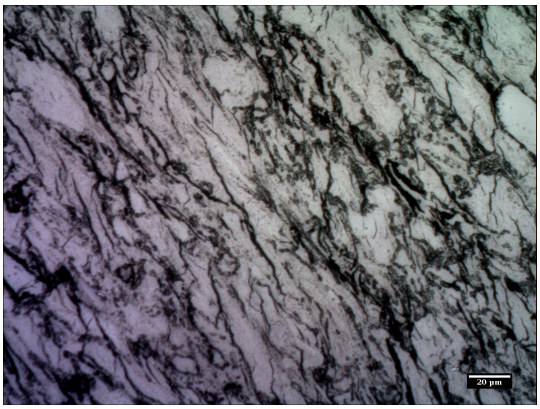

(c) CP-Ti processed by ECAP.

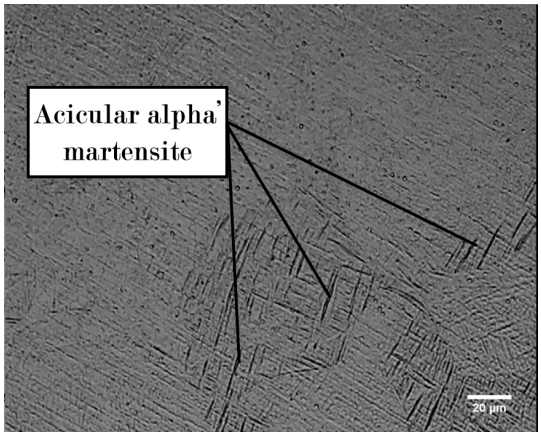

(d) Ti-6Al-4V alloy produced by SLM.

Figure 7.1: Microstructure results.

7.2 Mechanical properties

Flexure tests were carried out in the non-conventional materials, ECAP and SLM samples, in order to characterize their flexural strength and apparent flexural modulus. Flexural modulus corresponds to the elastic modulus measured in the tensile testing and for homogeneous materials they usually coincide. It represents

how easily a material bends or the stiffness of a material. The lower the flexural modulus, the softer the material is and less load is needed for it to bend. The flexural strength corresponds to the tensile strength of the tensile testing. It represents the highest stress which the sample suffered at the moment of yielding and it corresponds to the mechanical resistance of the material.

The ECAP samples presented a brittle behavior, as can be seen by the graph format showed in Fig. 7.3. All the samples fractured still in the elastic region, presenting no plastic deformation.

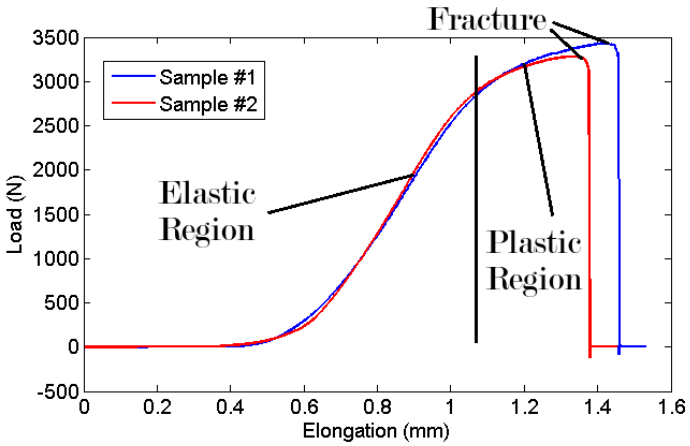

Figure 7.2: SLM flexure test.

The SLM samples presented elastic and plastic behavior, as can be seen by the graph generated during the tests showed in Fig. 7.2, presenting the load versus extension curve. The initial linear behavior represents the elastic region. After reaching the elastic limit point, the linearity ends and the plastic region initiates. The samples showed little plastic deformation fracturing short after reaching the yielding point. The tangent modulus method was used to compute the flexural modulus.

Table 7.1 summarizes the flexure test numerical results for the ECAP and SLM samples, presenting flexural strength and apparent flexural modulus. Table 7.2 presents the literature properties for commercially pure titanium grade 2 and Ti-6Al-4V alloy according to ASTM International Standards [116].

Table 7.1: Literature data for flexural strength and modulus of CP-Ti and Ti-6Al-4V.

	Flexural strength	**Flexural modulus**
CP-Ti (Literature)	345 (MPa)	105 (GPa)
Ti-6Al-4V (Literature)	900 (MPa)	113.8 (GPa)

Table 7.3 shows the Vickers Hardness testing results and the standard deviation for each material.

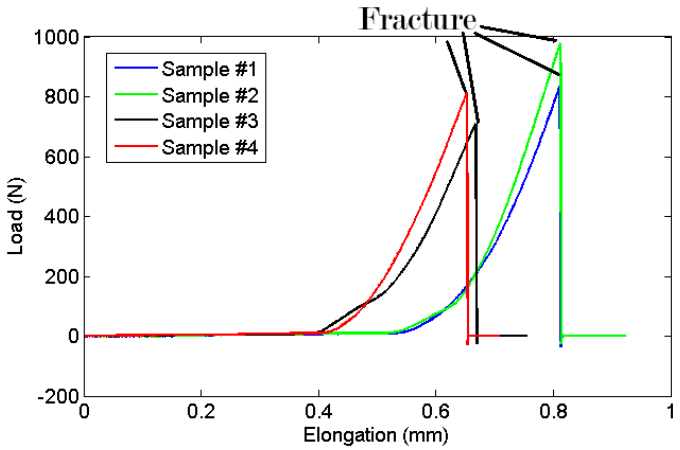

Figure 7.3: ECAP flexure test.

Table 7.2: Experimental flexure test results for flexural strength and apparent modulus.

	Flexural strength	**Apparent flexural modulus**
SLM - Ti-6Al-4V	2011 (MPa)	18.93 (GPa)
ECAP - CP-Ti	630 (MPa)	17.49 (GPa)

Table 7.3: Hardness tests results.

	Vickers Hardness (HV30)	**Std. Deviation (HV30)**
CP-Ti	167.9	1.8
Ti-6Al-4V	317.6	4.2
SLM - Ti-6Al-4V	369.2	6.3
ECAP - CP-Ti	320.0	7.0

7.3 Micromilling

This section presents the analysis of the machining forces acquired in the micromilling experiments for each material, considering two important results: maximum resultant forces and secific cutting force.

7.3.1 Force treatment

The measurement of machining forces output is a matrix with three columns, where each one corresponds to X, Y and Z directions, and the number of lines depends on the acquisition frequency and the length machined during the experiment.

When plotting the raw data on *MATLAB*, the graphs for all experiments have the general aspect as showed in Fig. 7.4. The first part of the graph represents the approximation of the tool to the part, already moving in the cutting feed direction, that is, the tool is not cutting yet. The presence of force signal in this part 1 can be a consequence of electrical noise or machine vibration. The second part of the

graph is where the tool flutes are actually cutting the material and, therefore, the force signal is considerably higher than in the other parts. The third part is related to the path of the tool where it is getting away from the part, by going up in Z direction and then in the opposite direction of the feed. Again, force presence in this part can be related to electrical noise and machine vibrations. For the analysis of the cutting force signal, the first and third part of the signal were ignored as the tool is not cutting the material. By the Fig. 7.4, it is possible to notice that the noise of the non-cutting parts are significantly high.

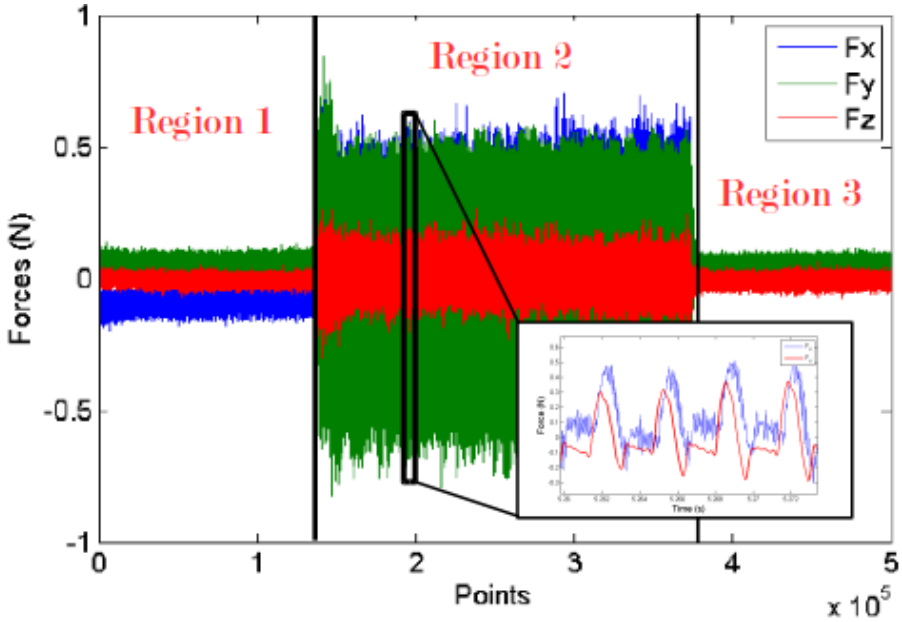

Figure 7.4: Raw cutting force signal for CP-Ti sample using 1μm/tooth.

Thus, when analyzing the signal, it can be noted the presence of undesired frequencies, which can affect the profile of the cutting forces and their general values. When a 2 flute milling tool is cutting, the typical expected profile of the cutting force for one tool revolution represents a periodical curve with two peak forces. The main frequencies which are expected to be present in the signal are the one given by Eq. 7.1, spindle speed frequency, by Eq. 7.2, tooth passing frequency, and the harmonic frequencies related to it ($2f_{tooth}$, $3f_{tooth}$ etc.):

$$f_{sp} = \frac{n}{60} = \frac{18000}{60} = 300Hz \tag{7.1}$$

$$f_{tooth} = z \times f_{sp} = 2 \times 300 = 600Hz \tag{7.2}$$

where z is the number of flutes of the tool and n is the spindle speed. In order to analyze the main frequencies present in the cutting force signal, it was necessary to apply a fast Fourier transform (FFT) on the signal. The FFT transforms the signal, which is in the time domain, in a sum of sine waves with their own frequencies and

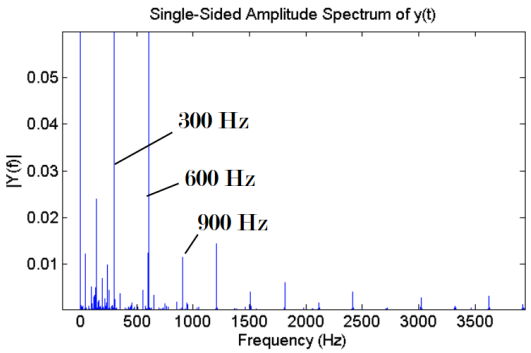

(a) Amplitude spectrum of unfiltered cutting force signal for CP-Ti sample using 1 μm/tooth.

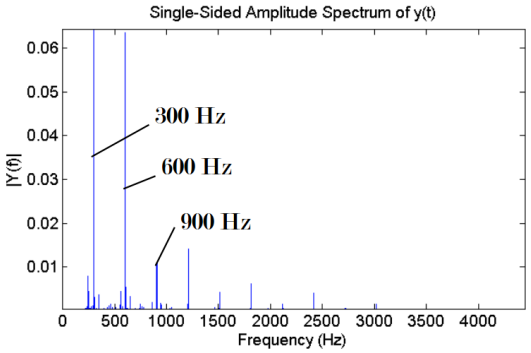

(b) Amplitude spectrum of filtered cutting force signal for CP-Ti sample using 1 μm/tooth.

Figure 7.5: Fast Fourier Transform.

amplitudes. Doing that, it is possible to analyze the main frequencies of the signal, which are the ones with higher amplitudes. Therefore, according to Eq. 7.1 and Eq. 7.2, as the spindle speed of the experiments of this work was constant and of 18000 rpm, the spindle speed frequency was 300 Hz and the tooth passing frequency was 600 Hz.

Applying the FFT on the force signals, the frequency results obtained are shown in Fig. 7.5a. It can be seen that besides the expected main frequencies (300 Hz, 600 Hz, 900 Hz, 1200 Hz etc.), there are several other noise frequencies that presented significant amplitudes, especially below 150 Hz. Therefore, it was necessary to apply a filter to the cutting force signals to remove the undesired frequencies. As there are frequencies with high amplitudes below and above 150 Hz, it was designed a band-pass digital filter using *MATLAB*. Also, Fig. 7.5b presents the frequencies amplitudes that were left on the signals and it can be seen that it became a lot closer to what was expected. All cutting force signals were filtered before being analyzed.

A comparison between the cutting force signal in feed direction for feed of 1 μm/tooth before and after being filtered is showed in Fig. 7.6. It is clear the effects of filtering. Most unwanted frequencies which were masking the original force profile were removed and the result is a lot closer to the force profile usually seen in milling experiments.

Cutting forces can be analyzed considering many aspects: using each force component separately, using the force average, change the reference frame of the force matrix to others. As one of the main goals of this work is to compare the machinability of different materials, it was preferred to quantify the cutting force considering the maximum force per revolution.

Thus, it was preferred to use the resultant force value as it gives an idea of the

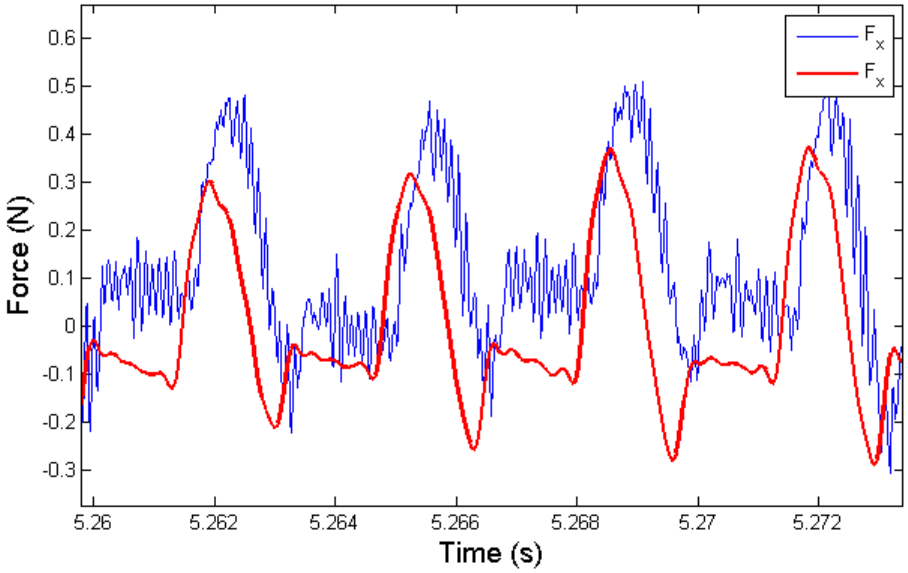

Figure 7.6: Comparison between unfiltered and filtered cutting force signal in X direction for CP-Ti sample using 1 μm/tooth.

cutting force values in all directions. Because cutting force is directly related to the chip area and this area is often computed using the undeformed chip thickness, the force will be maximum when chip thickness, t, is maximum, which is when ϕ is equal to 90°, as showed in Fig. 7.7, positions 2 and 3.

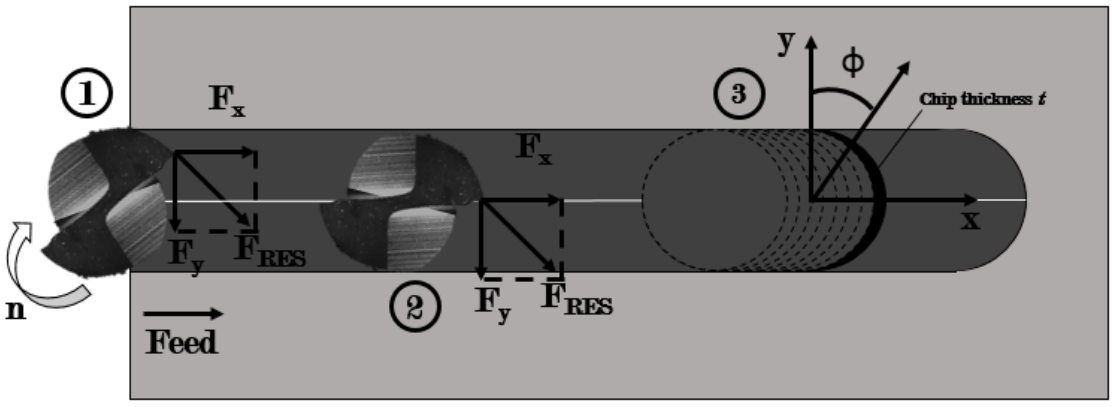

Figure 7.7: Cutting force scheme and chip thickness in milling operations.

Also, in milling experiments, cutting forces in Z direction are usually significantly smaller than the forces in X and Y directions. Forces in this direction are perpendicular to the working plane and only occur due to the presence of the helix angle in the tool geometry. Therefore, F_z is often ignored when computing the resultant force in milling or micromilling. Resultant cutting force was calculated using only F_x and F_y. Figure 7.8 shows an example of the resultant force for an experiment using feed per tooth of 1 μm/tooth with the positions 2 from Fig. 7.7 specified for each tool revolution.

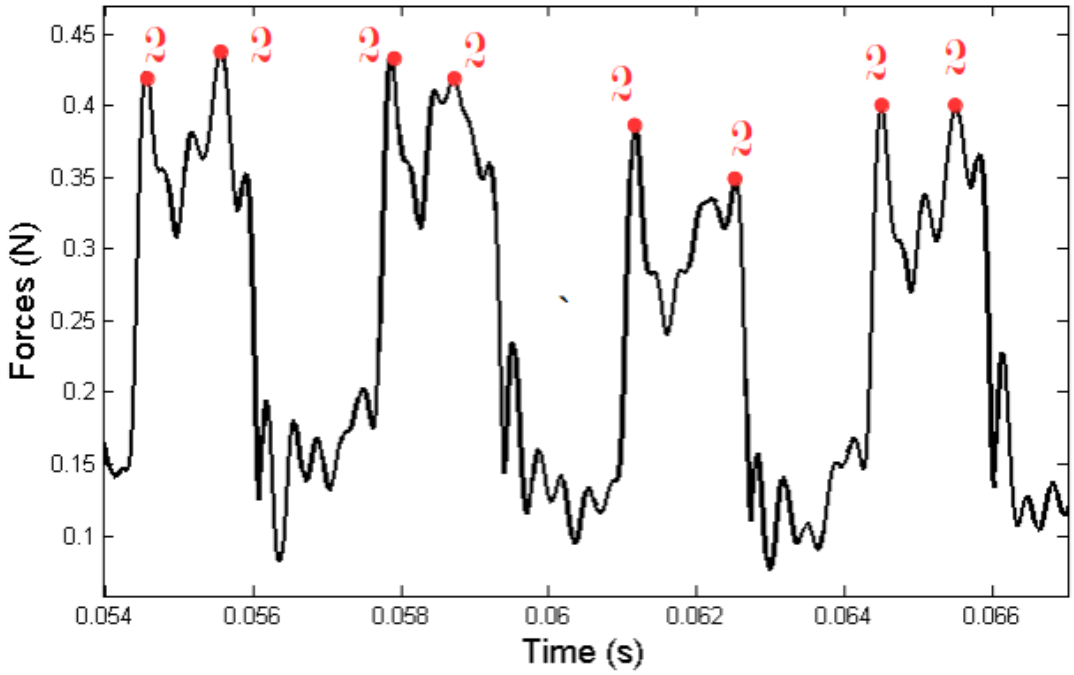

Figure 7.8: Resultant force for feed per tooth of 1 μm/tooth.

As the microtools used in this study presents two flutes and the experiments were performed using full immersion of the tool, each flute engaged with the material at different time and, therefore, theoretically, the cutting force signal should present two maximum resultant cutting force peaks of the same value per tool revolution. However, several factors during the machining operation can affect the cutting force behavior and these force peaks can be different. For the force quantitative analysis, the highest force was considered.

Thus, as it can be seen in the position 2 of Fig. 7.4, if nothing unusual happen during the process, the maximum cutting force values per tool revolution maintains a constant level throughout each experiment, excluding the entrance and exit of the tool from the material. When the tool is entering the material, the flute is still not cutting the entire specified feed per tooth, so it takes a few tool revolutions until the maximum force level is kept constant. The same happens when the tool is exiting, where the tool is stopping to make contact with material. Therefore, it would be useless to use the whole force signal. It was opted to use the the average of the maximum resultant force for 40 tool revolutions. Using the average and standard deviation, besides the maximum stress to which the tool is subjected, the variation of the force can also be analyzed. The error bar for each force point was computed considering a significance level of 0.05 and the standard deviation.

7.3.2 Maximum resultant forces

As detailed in Chapter 6, it was carried out two batches of experiments for each material: one increasing the feed per tooth (batch A) and the other decreasing the feed per tooth (batch B). Figure 7.9 presents the influence of feed per tooth in the cutting force of CP-Ti sample, regarding the maximum resultant force average for 40 tool revolutions, considering each batch separately. The general force behavior corresponds to the expected result: experimental cutting force increases when increasing feed per tooth as the cutting area is linearly proportional to f_t.

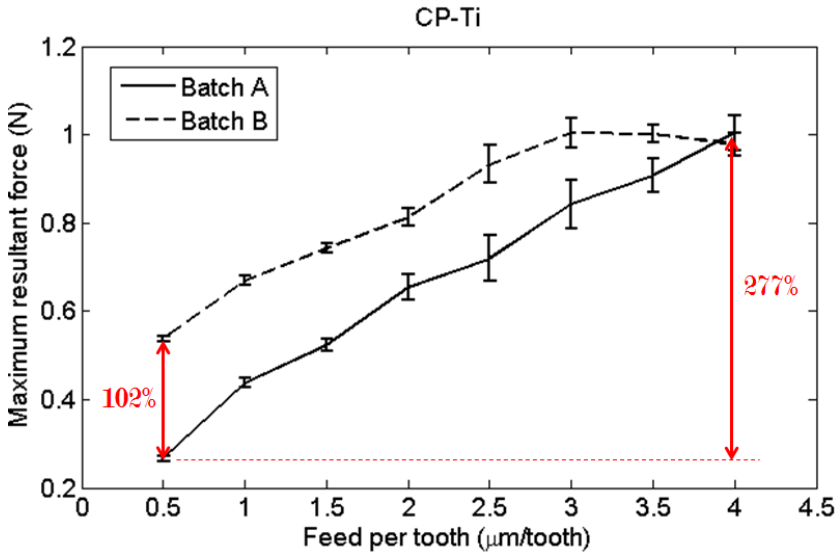

Figure 7.9: Cutting force results for CP-Ti grade 2.

The first important thing to notice is that tool wear plays an important role in machining titanium, which was also expected as titanium and its alloys are hard to machine materials. If there was no tool wear, the points for both batches should be overlapped. However, this only happened for the feed of 4 μm/tooth, using new tool in batch B and used tool in batch A. Thus, analyzing batch B, it can be seen that for the feeds 3, 3.5 and 4 μm/tooth, the force remained at the same level. This probably happened because the tool was new for the highest feed and tool wear compensated the reduction in the feed.

For feed the feed per tooth of 0.5 μm/tooth, performed with new tool for batch A and used tool for batch B, the difference was more than 100 %. As tool wear has such an important impact, the correspondent experiments of each batch can not be considered a replica. Hence, it would not be correct to compute the force average. So, each batch will be analyzed separately and used in the comparison among the materials, instead of the force average.

Figure 7.9 also shows that for both batches, A and B, lower feeds presented smaller standard deviation. This fact is related to machine vibrations and can also

be seen analyzing the entire raw force signals. The graphs show that when increasing feed per tooth, noise signal in feed direction, F_x, also shows significant increase. The digital filtering, as explained, aimed to reduce the effect of this noise, but some might have remained.

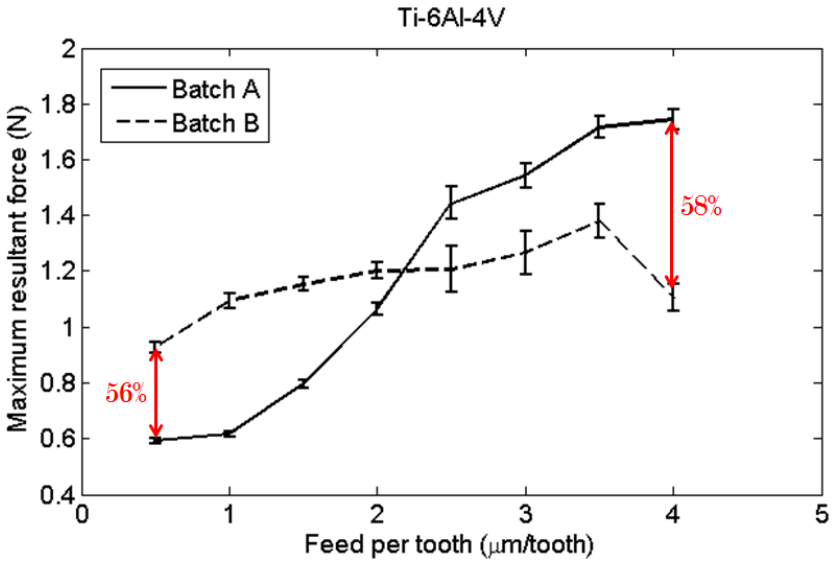

Figure 7.10: Cutting force results for Ti-6Al-4V alloy.

The experimental force results trend for the Ti-6Al-4V alloy for batch A is similar to the CP-Ti, as it can be seen in Fig. 7.10. Although the correspondent feed points of both batches did not overlap, the general force behavior when increasing feed per tooth is that it rises, being consisted with what was expected. The tool wear seamed to highly affect the alloy machining as for a feeds of 0.5 and 4 μm/tooth, there is a big difference between the batches. It means that the results for the same feed using a new tool and an used tool are considerably different.

For batch B, the force curve trend did not show a wide angular coefficient as batch A. That is because when decreasing feed per tooth, at the same time that the cutting force should be smaller because the feed is smaller, it also should be higher as tool wear increases. So, tool wear ends even up the feed per tooth effect in the cutting force.

Analyzing the error bar for both batches, it can be seen that the error bars for lower feeds per tooth are smaller than for higher feeds which is related to increasing noise presence in the cutting force when rising feed per tooth.

Examining the cutting force results for the ECAP samples, considering batches A and B, showed in Fig. 7.11, it can be seen an unexpected force result when feed is increased from 1.5 to 2 μm/tooth for batch A. The cutting force presents a strong growth, indicating that something could have happened during the micromilling experiment. Taking this into consideration, a second batch A was performed. However, there was limited machining space in the samples as they had small dimensions.

Hence, it was not possible to perform the experiments for the last three feeds.

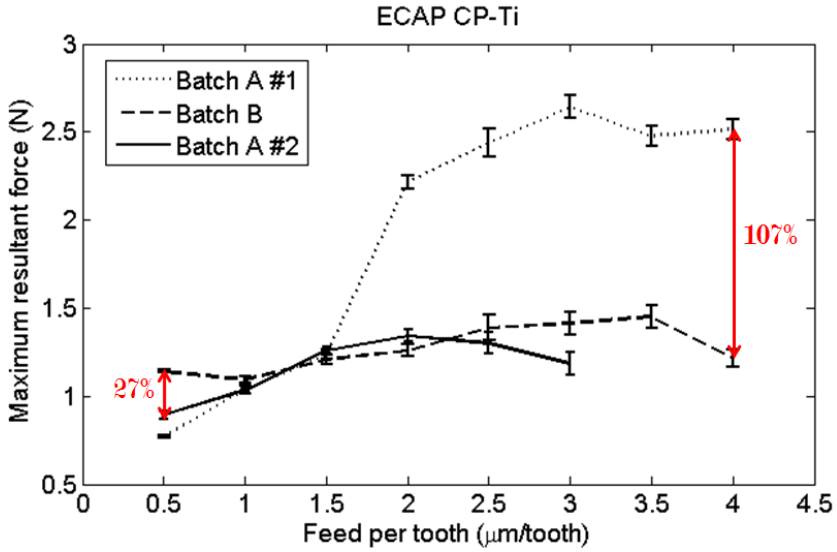

Figure 7.11: Cutting force results for CP-Ti processed by ECAP.

The second batch A presented a more regular force behavior with no unexpected occurrence. Batch B shows a strong tool wear as the cutting force presents almost the same level for all feeds. This means that the tool wear effect of increasing the cutting force when tool wear rises compensated the feed per tooth effect of decreasing the cutting force when feed per tooth decreases. Also, batch A #2 showed similar force values regarding batch A, except for 0.5 μm feed per tooth that presented a difference of 27 %.

Cutting force results for the SLM sample for batches A and B are showed in Fig. 7.12. Although a couple of correspondent points overlapped, the general behavior is the same with high presence of tool wear given the great difference between the forces for 4 μm/tooth and the small difference between the forces for the higher feed values for batch B. This is due to the tool wear evening up the feed per tooth increasing effect in the force.

7.3.3 Specific cutting forces results

Using the maximum resultant cutting force and the chip area, it is possible to compute the maximum specific cutting force resultant from Eq. 7.3.

$$K_{RES_{MAX}} = \frac{F_{RES_{MAX}}}{f_z.a_p} \tag{7.3}$$

where f_z is feed per tooth and a_p is axial depth of cut.

Figure 7.13 shows the specific force for CP-Ti. It is seen that batch B presented higher values than batch A with a higher difference of 102 %. That means that

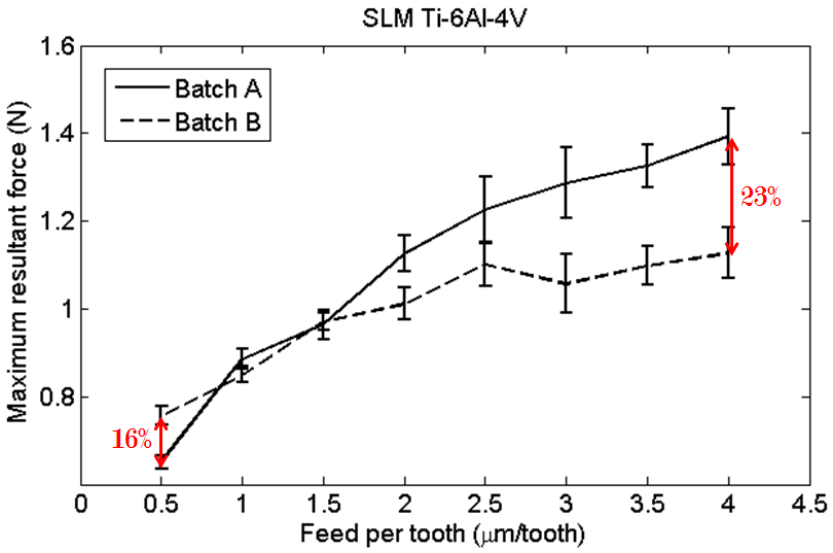

Figure 7.12: Cutting force results for Ti-6Al-4V alloy produced by SLM.

the tool spent more energy to machine the material for the same parameters. This fact is related to the tool wear which increases the cutting edge radius and, as a consequece, more energy must be used to cut the material.

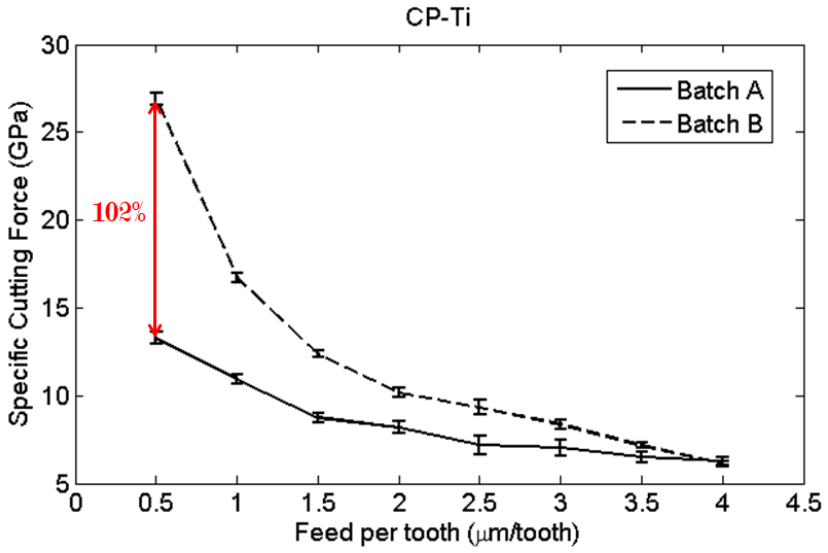

Figure 7.13: CP-Ti.

For the alloy sample, the results show that for feeds higher than 2 μm/tooth, batch A presented higher specific force results while for feeds equal or smaller, batch B presented higher results. The results are shown in Fig. 7.14

Figure 7.15 shows the results for specific force results for the ECAP samples. Despite the unusual behavior of batch A #1, the other batches presented similar values with higher difference of 28 % for batch B.

The results for the SLM sample are presented in Fig. 7.16. It can be seen that both batches presented similar values with a higher difference of 16 % for batch B.

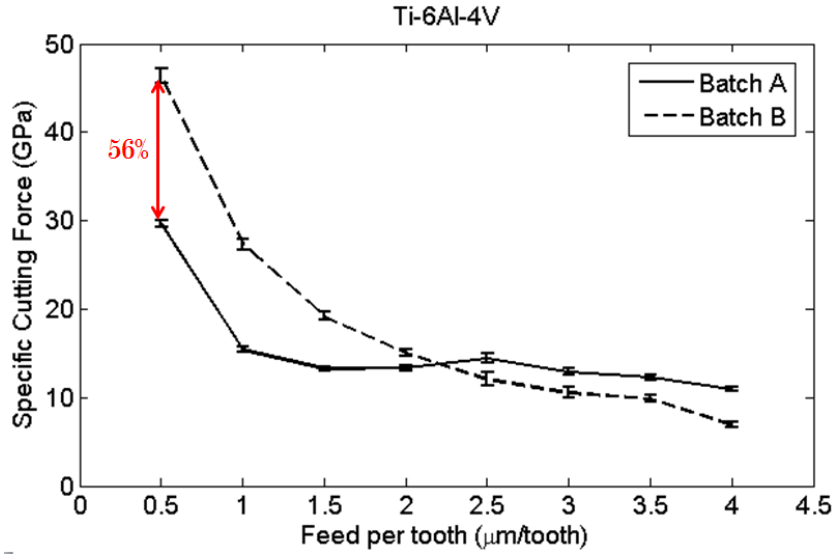

Figure 7.14: Ti-6Al-4V.

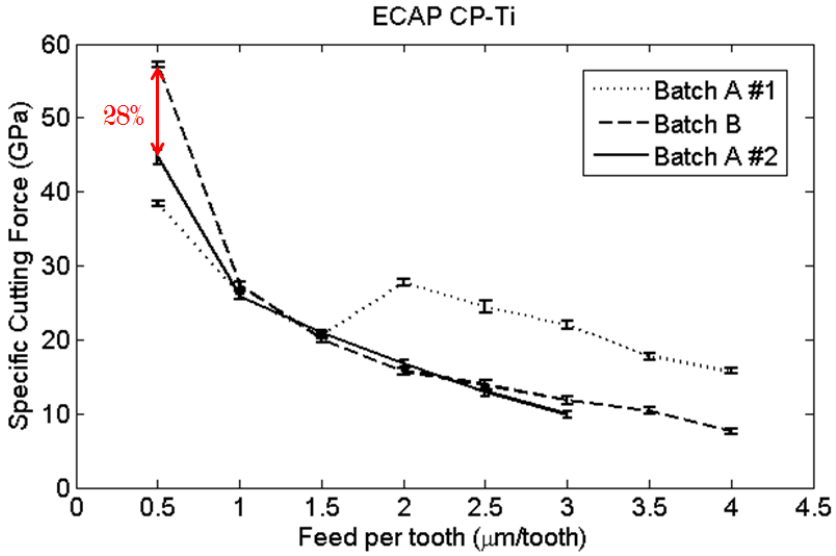

Figure 7.15: ECAP.

All four materials presented the expected specific cutting force behavior for varying feed per tooth: a decrease in the value while feed per tooth is growing. Both A and B batches show a change from an almost linear behavior to a non-linear behavior when feed decreases. As feed values is lowered, specific cutting force tends to quickly increase, while increasing the feed it tends to approximate to a constant level. This is an indicative of ploghing phenomenon becoming more present as feed per tooth decreases.

Examining the graphs, it can be seen that for all the materials, for a feed of 0.5 μm/tooth, batches B presented higher values for the specific force than for A batches, while for 4.0 μm/tooth, the opposite occurred. This is an indication of the tool wear role in the specific cutting force values. The specific force can be understood as the

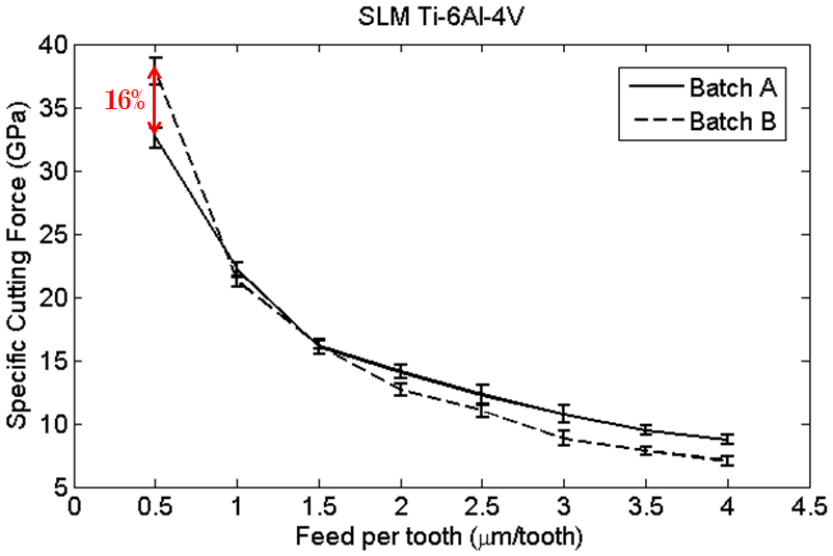

Figure 7.16: SLM.

force needed for the tool to cut a chip with 1 mm^2 area. Therefore, it is influenced by many factors, including the tool geometry. When the tool wears, the cutting edge radius and point radius change, affecting the force needed tu cut the material.

7.4 Roughness

Surface roughness was measured in three different transversal position on the bottom surface of the slots. The results are given through plots of the roughness averages versus feed per tooth with bar errors corresponding to a significance level of 0.05. In conventional milling, usually surface roughness increases when feed per tooth is raised due to geometric relations considering among other parameters the feed per tooth and the tip radius of the tool. However, in micromilling, several results show that roughness can present a different behavior when varying feed per tooth as presented in Section 2.5.

Roughness results for CP-Ti sample is presented in Fig. 7.17. At first, it can be seen that the surface roughness behavior when increasing feed per tooth does not follow the conventional milling standard results. It presents different tendencies according to the feed range it is analyzed. It is possible to roughly specified three different parts in the roughness behavior according to feed per tooth.

The first part is characterized by a decrease in roughness values when increasing feed from 0.5 to more or less 1.5 μm/tooth. This part might be explained by the ploughing phenomenon which can de dominant in this window of feed and cause an uneven plastic flow of material and can prejudice surface finishing. The second part, when feed per tooth is increased from 1.5 to 3.5 μm/tooth, shows an unstable behavior, initially increasing and then decreasing or staying more or less at the same

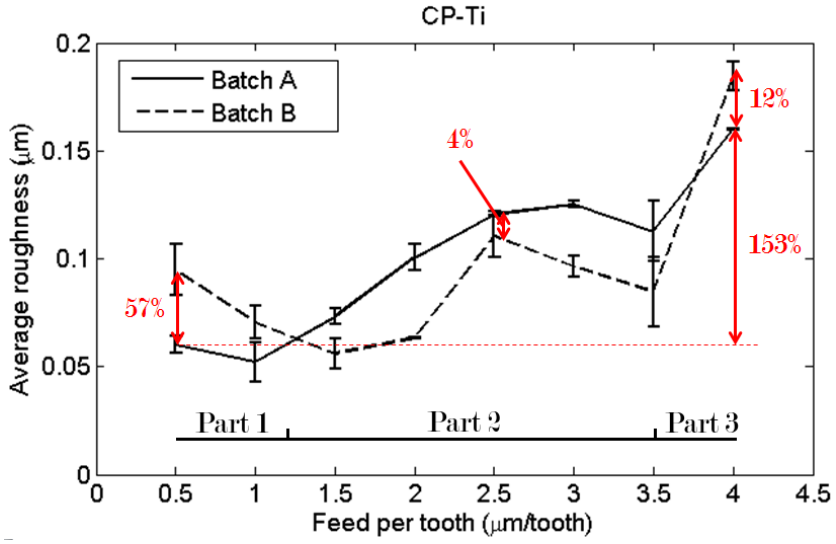

Figure 7.17: Surface roughness results for CP-Ti grade 2.

level when rising feed per tooth. The second part window coincide with the cutting edge radius value of the microtool and it can be a possible reason for the instability of the roughness results. The third part, which is related to the increase of feed from 3.5 to 4 μm/tooth represents a strong rise in the roughness values. This feed window represents the same trend expected for conventional milling and it shows that in this range feed per tooth is distancing from the ploughing and unstable behavior.

Additionally, it is noticed that tool wear did not present as much influence as it presented for the cutting force results. Despite the fact that the correspondent points did not overlap, both batches presented very similar trend. Also, the roughness differences between the correspondent points were not so high. For example, for 4 μm/tooth, which represents the final experiment for the increasing batch and a new tool for the decreasing batch, the roughness difference is not so significant.

Similarly to the analysis made for the commercially pure titanium sample, for the alloy sample, roughness results varying with feed per tooth also can be divided into three parts and using the same feed windows as before, as can be seen in Fig. 7.18 that shows the surface roughness results for the alloy sample. The general behavior of the surface roughness is also similar for each part with just a few specific details different. Although both batches present a couple of overlapped correspondent points, there are also a couple of points with very significantly different result. Surface integrity is deeply connected to the cutting edge radius and tool point radius, including their shape. Depending on how the tool wear is affecting the tool shape, it can sometimes favor or prejudice surface roughness. The rapid grow of roughness values from 2 to 2.5 μm/tooth and the later return to normal values can be a consequence of this wear shape.

For the ECAP samples, it is presented the results for the batches that were

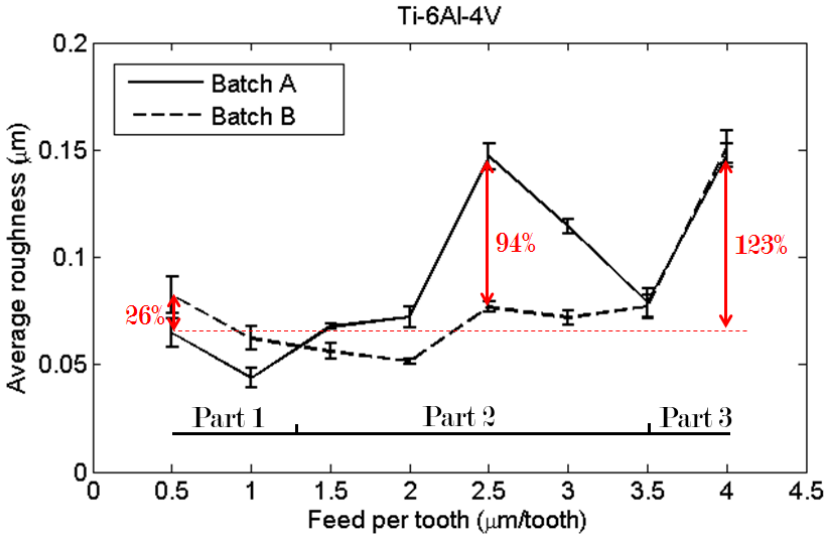

Figure 7.18: Surface roughness results for Ti-6Al-4V alloy.

finished until the last feed per tooth in Fig. 7.19. Again, three parts can be clearly defined considering the roughness trend behavior. For batch A, similarly to the SLM sample, the first part seems to go from 0.5 to somewhere between 1.5 and 2 μm/tooth and presenting the same trend as for the previous materials. However, the second part, which goes until 3.5 μm/tooth, shows a little different trend. While for most previous batches for all the materials, roughness decreased or stayed at the same level between 2.5 and 3.5 μm/tooth, ECAP sample presents an increase trend. Nevertheless, it is important to notice that the error bar limits for these points are very close one to the other. For the third part, the trend is equal to all the other batches of all materials, showing a strong increase in roughness value when feed grows from 3.5 to 4 μm/tooth. batch B presented higher roughness values than batch A, but a similar trend behavior.

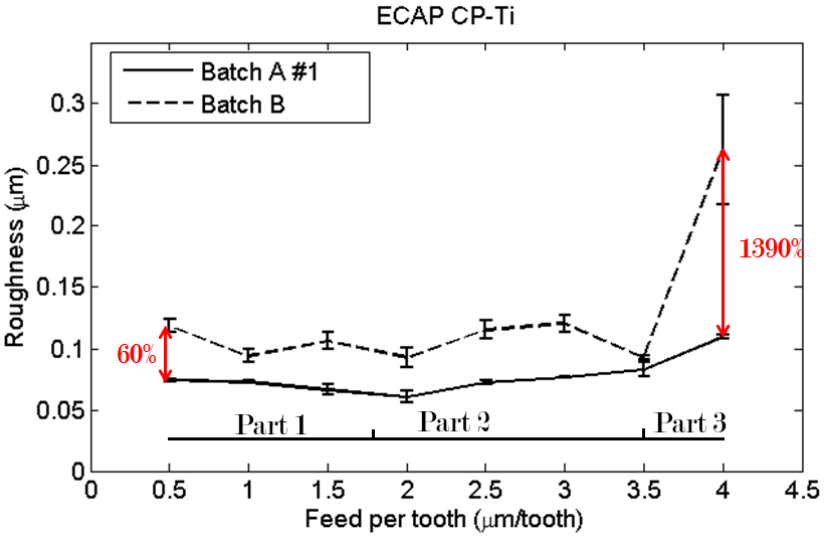

Figure 7.19: Surface roughness results for standard CP-Ti processed by ECAP.

Figure 7.20 presents the roughness related to feed per tooth results for the SLM sample. The general roughness behavior for both batches is similar to the previous ones and it also shows three different parts. However, for SLM, the first part seems to finish after 1.5 μm/tooth. Differently from the previous materials, for SLM sample almost all the correspondent points overlapped, considering the error bars. This means that tool wear did not play a so important role as played to the CP-Ti and Ti-6Al-4V samples as using a new tool or an used tool did not changed the results.

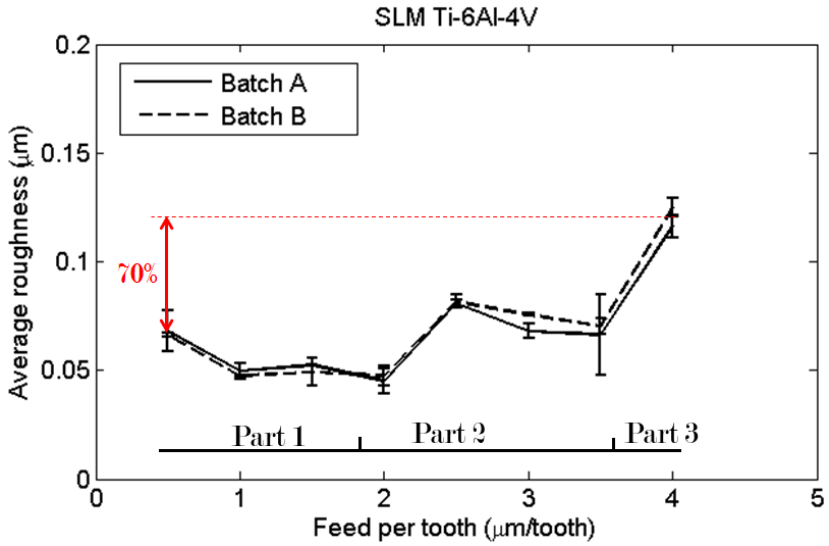

Figure 7.20: Surface roughness results for Ti-6Al-4V alloy produced by SLM.

Analyzing the roughness results for the different materials, it can be seen that all presented a similar general behavior presenting three clear different pars considering the trend behavior which can be connected to the ploughing phenomenon and the cutting edge radius of the microtool. Also, it was noticed that tool wear played different roles for each material, affecting more or less the results. For a better understanding of the surface integrity generated by micromilling of these materials, top burr formation was measured and analyzed.

7.5 Burr formation

Burr formation was analyzed through top burr height measurement using a profilometer and through scanning electron microscope top images of the grooves. Burr measurement can be really tricky as there is not a standard procedure to follow and burrs configuration can vary a lot. Therefore, burr measurements can be influenced by several factors: the burr can be deformed, the burr can present a small dimension in the measurement direction and a higher dimension in a different direction, burrs can be irregularly distributed by the groove and others. Because of this, burr formation analysis will take into consideration both top burr height measurements

and visual examination. All the SEM top images of the grooves for all materials are presented in the Appendix A.

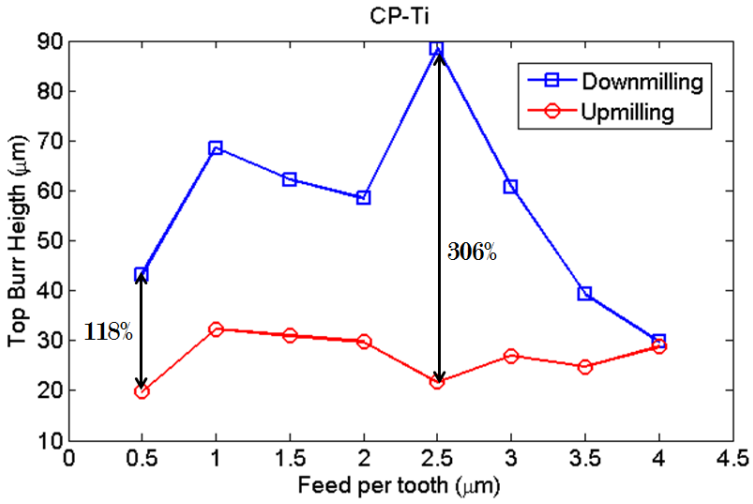

Figure 7.21: Top burr height measurement results for CP-Ti.

Top bur height measurements results for downmilling and upmilling in CP-Ti are presented in Fig. 7.21. As burr measurement is inherently variable, it was chosen to work with the average between the batches A and B, presuming that it would give a better idea of burr formation behavior when varying feed per tooth.

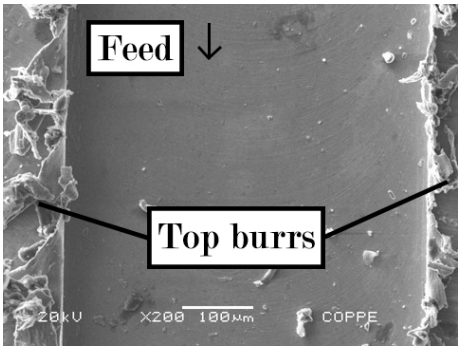

(a) Increasing feed - $f_t = 1.0$ μm/tooth.

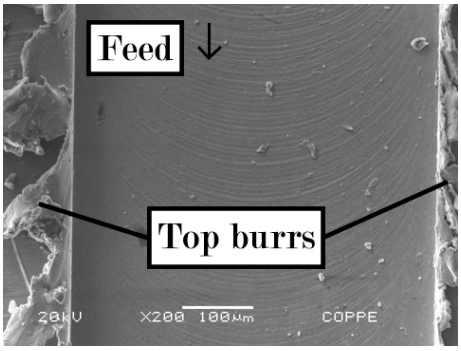

(b) Increasing feed - $f_t = 3.5$ μm/tooth.

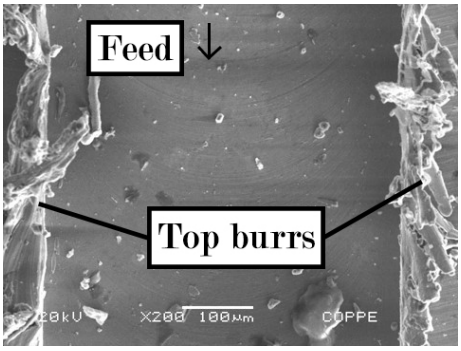

(c) Decreasing feed - $f_t = 1.0$ μm/tooth.

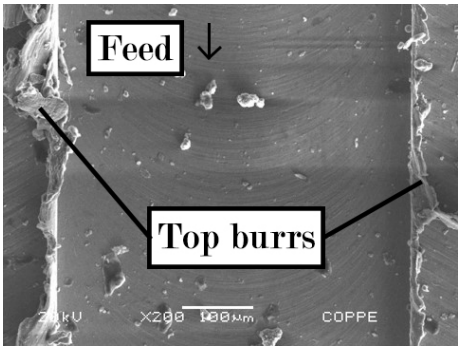

(d) Decreasing feed - $f_t = 3.5$ μm/tooth.

Figure 7.22: Grooves SEM images for CP-Ti. Upmilling: right; Downmilling: left.

It can be seen in the graph that during the upmilling part of the cutting ma-

chining process there was significantly less burr formation than in downmilling, presenting differences of more than 100 % for most feeds. Also, it can be noticed a general burr formation trend of decreasing burr dimensions when feed per tooth is increased. This trend is especially clear for the downmilling part.

These results are confirmed when analyzing the SEM images of the grooves showed in Fig. 7.22. It presents the top image for feeds per tooth of 1.0 and 3.5 μm/tooth for increasing the feed and when decreasing the feed batches. Visually, it is noticed that the grooves machined with feed of 3.5 μm/tooth present less or smaller burrs than the ones machined with 1.0 μm/tooth. This happened for both batches: increasing and decreasing feed. Also, for both batches, downmilling presented more burr formation than upmilling.

Figure 7.23 shows the burr measurement results for the alloy sample. Again, a general burr formation trend can be identified when varying feed per tooth: it decreases when increasing feed. Although for small feed values this trend is not identifiable, after 2.0 μm/tooth, it becomes clear. When comparing downmilling with upmilling, the latter presented a better results considering the burr measurements with differences up to 100 %, especially for feeds higher than 2 μm/tooth.

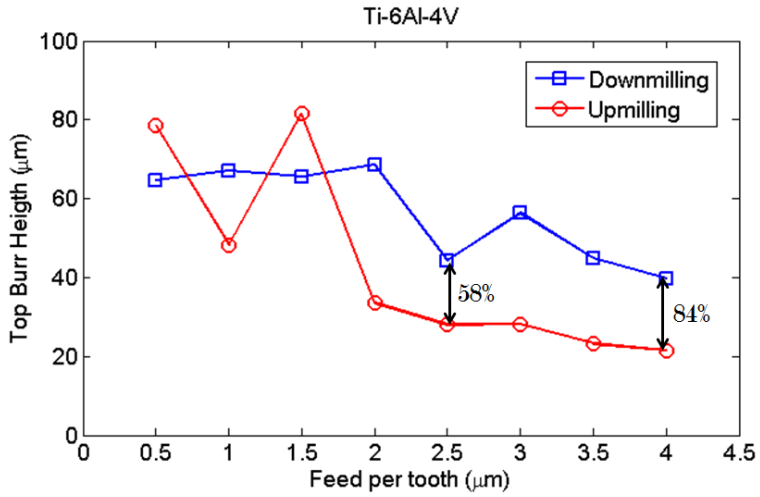

Figure 7.23: Top burr height measurement results for Ti-6Al-4V.

The visual analysis of the top image from the grooves machined with feeds of 1.0 and 3.5 μm/tooth, showed in Fig. 7.24, confirms the previous analysis. It can be seen that burr formation for 3.5 μm/tooth was clearly smaller than for 1.0 μm/tooth. Thus, in general, upmilling presented less burr formation or smaller burrs than downmilling. For further confirmation, it can be examined the images for the entire feed range, presented in Appendix A.

Analyzing the top burr height measurements for the ECAP, showed in Fig. 7.25, it can be seen that upmilling and downmilling presented similar results for all feeds per tooth, except for the two highest feeds, where upmilling presented a better

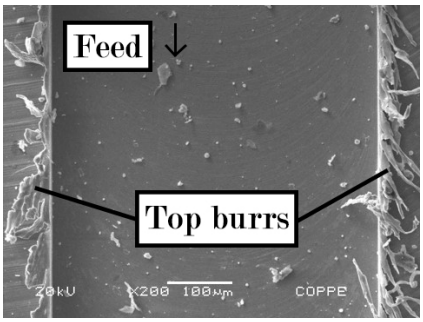

(a) Increasing feed - $f_t = 1.0$ μm/tooth.

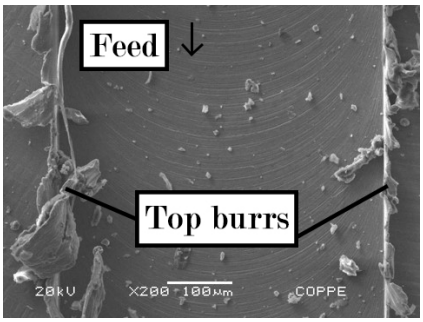

(b) Increasing feed - $f_t = 3.5$ μm/tooth.

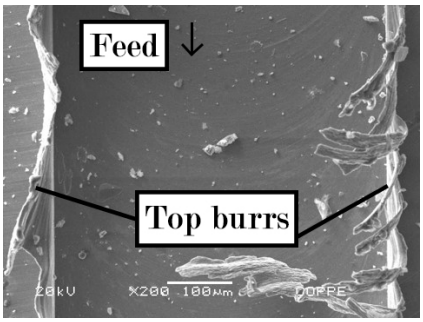

(c) Decreasing feed - $f_t = 1.0$ μm/tooth.

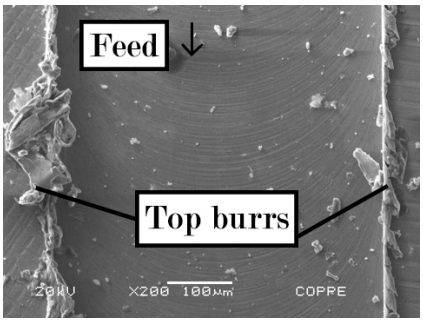

(d) Decreasing feed - $f_t = 3.5$ μm/tooth.

Figure 7.24: Grooves SEM images for alloy. Upmilling: right; Downmilling: left.

result. Thus, for all feeds, burr formation seams to maintained a constant level with the exception of the two highest feeds, where upmilling presented a decrease in the top burr height. Figure 7.26 confirms that burr formation were similar for up and downmilling as well as when varying feed per tooth.

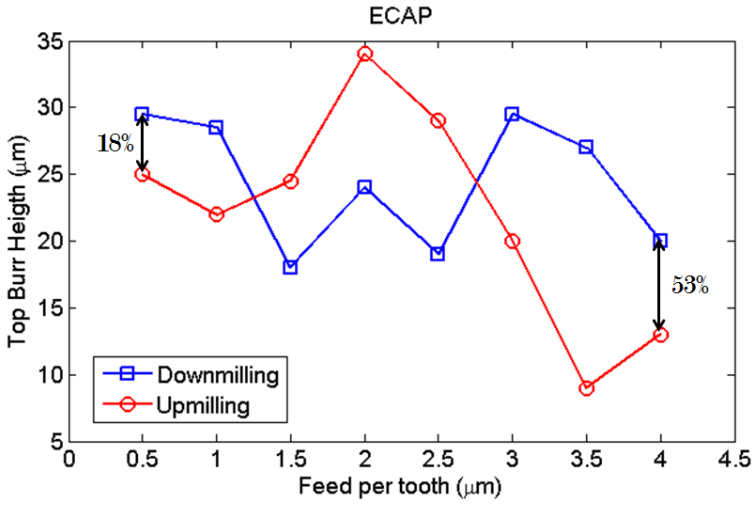

Figure 7.25: Top burr height measurement results for ECAP.

For the SLM sample, it is clear that increasing feed per tooth influenced positively burr formation for up and downmilling, as showed in Fig. 7.27. Burrs height decreased while feed per tooth was increased. Also, it can be noticed that, as occurred for the previous materials, downmilling presented a worst result than upmilling for

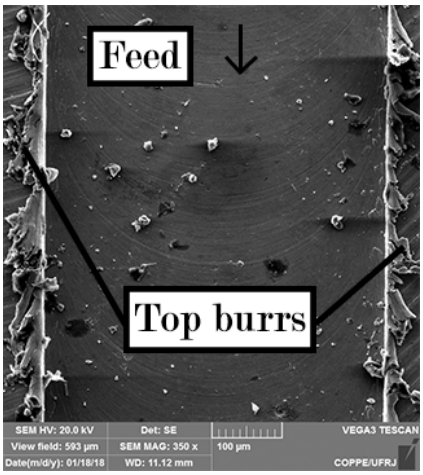

(a) Increasing feed - $f_t = 1.0$ μm/tooth.

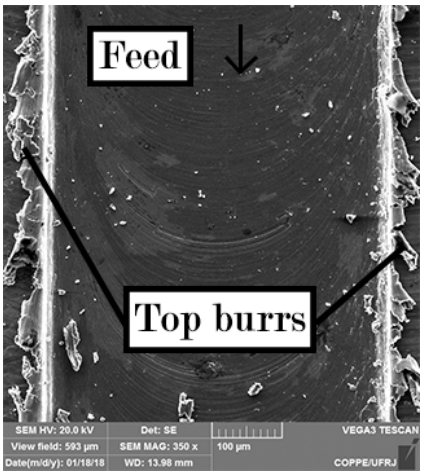

(b) Increasing feed - $f_t = 3.5$ μm/tooth.

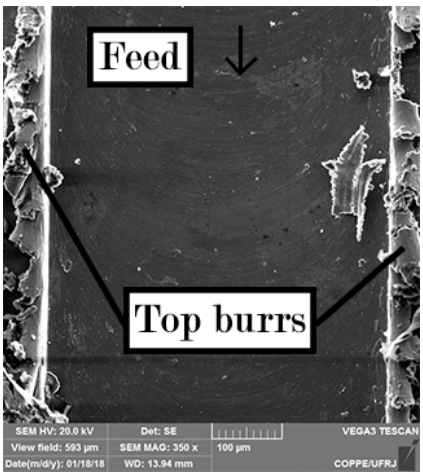

(c) Decreasing feed - $f_t = 1.0$ μm/tooth.

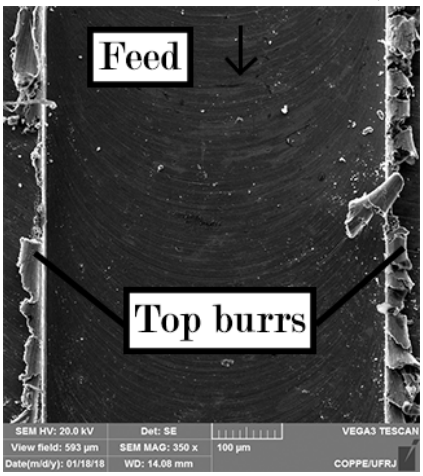

(d) Decreasing feed - $f_t = 3.5$ μm/tooth.

Figure 7.26: Grooves SEM images for ECAP. Upmilling: right; Downmilling: left.

all feeds.

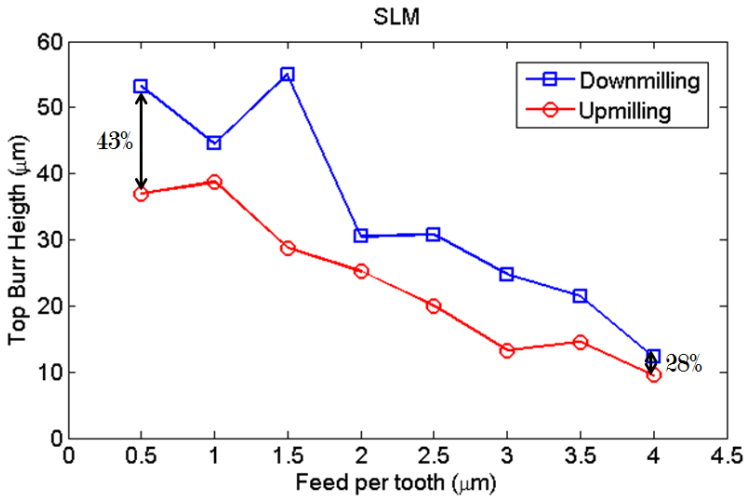

Figure 7.27: Top burr height measurement results for SLM.

Top SEM images of the grooves machined in the SLM sample are shown in Fig.

7.28 for feeds of 1.0 and 3.5 μm/tooth for both batches, increasing and decreasing the feed. The visual analysis of the images confirms that results presented in Fig. 7.27: higher feeds presented less burr formation than small feeds and downmilling showed more burr formation than upmilling.

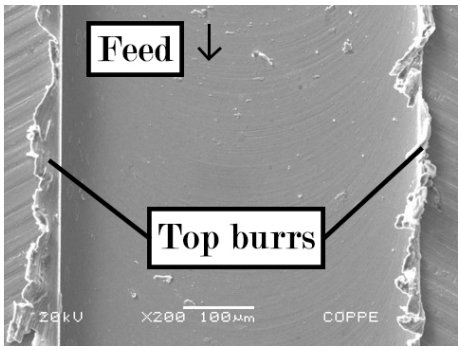

(a) Increasing feed - $f_t = 1.0$ μm/tooth.

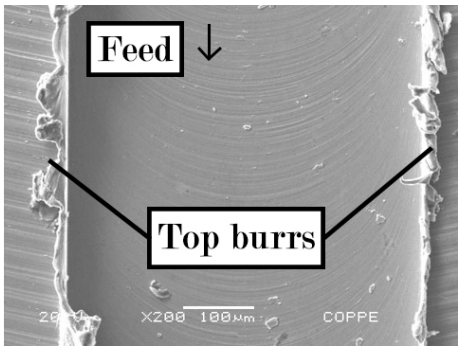

(b) Increasing feed - $f_t = 3.5$ μm/tooth.

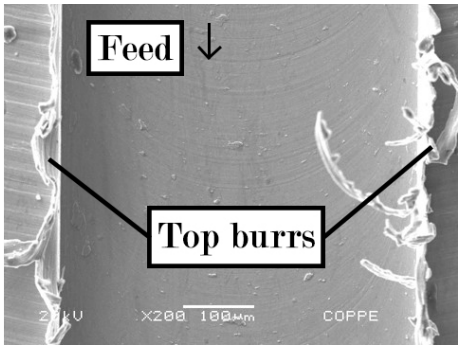

(c) Decreasing feed - $f_t = 1.0$ μm/tooth.

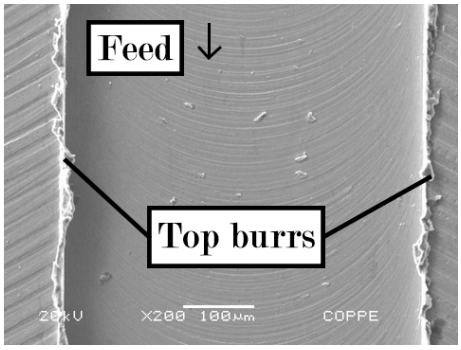

(d) Decreasing feed - $f_t = 3.5$ μm/tooth.

Figure 7.28: Grooves SEM images for SLM. Upmilling: right; Downmilling: left.

7.6 Chips morphology

Microchips from all experiments were collected and analyzed using a digital microscope. Also, for some experiments, it was possible to analyze them using SEM images. Appendix B presents the optical images of the microchips for all four materials and the entire range of feeds per tooth used.

Microchips images for the commercially pure titanium experiments using feeds per tooth of 0.5 and 4.0 μm/tooth, the bottom and up limits of the feed range, can be seen in Fig. 7.29. Analyzing the images, along with the images presented in the appendix, the first thing noticed is that lower feeds generated long and connected chips. Thus, when increasing feed per tooth, microchips became very short going from a length of more than 1 mm for 0.5 μm feed per tooth to around 200 μm for 4 μm/tooth. Usually, short chips are preferred when machining a workpiece as long chips can roll up the tool and have more chances to be cut again during the process, which can prejudice surface finish. Also, chips are responsible for removing heat

from the cutting region. So, the longer a chip takes to break away, the longer it is taking to remove heat and cool the tool-material contact region.

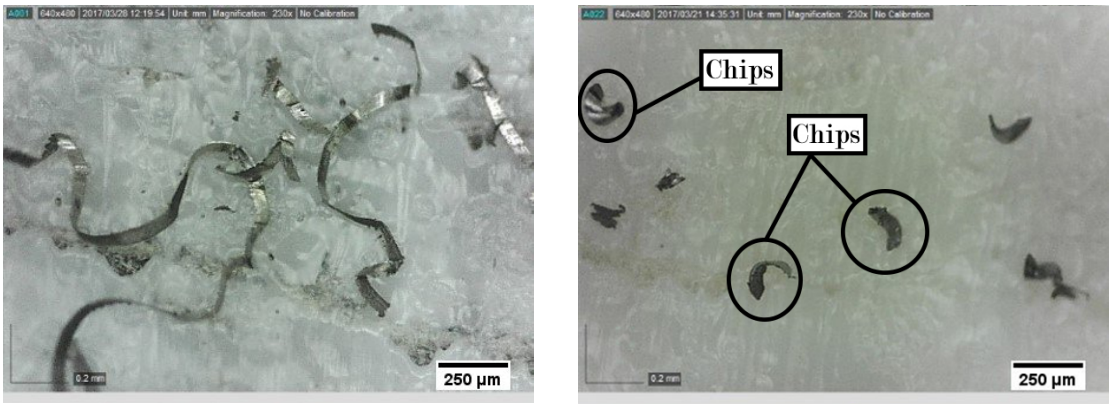

(a) Feed per tooth of 0.5 μm/tooth. (b) Feed per tooth of 4.0 μm/tooth.

Figure 7.29: Optical images of chips collected during micromilling experiments of CP-Ti.

However, it can be seen that chips length rapidly decrease, presenting small length for feeds above 1.5 μm/tooth. The long chips for the small feeds probably happened because the chip thickness is given by the feed per tooth. The thicker the chips, more difficult it is for them to curl while in contact with the rake surface of the microtool. Probably, the chips break when they start to curl during the cutting process.

Microchips generated during the experiments with the alloy sample are presented in Fig. 7.30. It is showed the chips for 0.5 and 4.0 μm/tooth. It can be seen that the chip length decreases when increasing feed per tooth varying from a length of around 0.5 mm for 0.5 μm feed per tooth to around 200 μm for 4 μm/tooth. Analyzing the entire feed range, it is noticed that feeds higher than 2.0 μm/tooth cleary shows smaller dimension. For 0.5 and 1.0 μm/tooth feeds, despite them being longer than for other feeds, they present a curly shape, which is a more desirable shape than the snarled one as it is less likely to cause damages to the tool or the machined surface.

The chips morphology results for the ECAP samples are presented in 7.31 for 0.5 and 4.0 μm/tooth and the behavior is similar. As feed per tooth grows, chip turn from the snarled format to loose chips. The chip length varied from around 1 mm for 0.5 μm feed per tooth to around 400 μm for 4 μm/tooth

The microchips collected during the experiments with the SLM sample are showed in Fig. 7.32. Chips for 0.5 and 4.0 μm/tooth are presented. It can be seen that the chip morphology showed the same behavior than for the previous materials: long and connected chips for small feeds and short chips for the higher feeds. It varied from a length of more than 2 mm for 0.5 μm feed per tooth to around 250 μm for 4 μm/tooth. For feeds greater than 2.0 μm/tooth, chips show a significantly

(a) Feed per tooth of 0.5 μm/tooth.

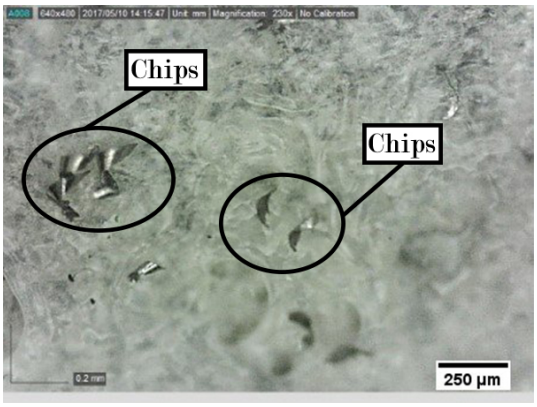

(b) Feed per tooth of 4.0 μm/tooth.

Figure 7.30: Optical images of chips collected during micromilling experiments of Ti-6Al-4V.

(a) Feed per tooth of 0.5 μm/tooth.

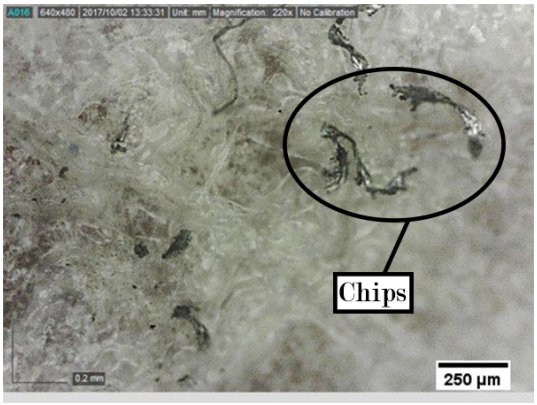

(b) Feed per tooth of 4.0 μm/tooth.

Figure 7.31: Optical images of chips collected during micromilling experiments of CP-Ti processed by ECAP.

smaller length, as can be seen in Appendix B.

This chapter presented the experimental and testing results and comments for each separate material (CP-Ti, alloy, SLM and ECAP) concerning material microstructure, mechanical properties, cutting force, specific cutting force, surface roughness, burr formation and microchips.

It is important now to compare the results between the materials and quantitatively analyze their machinability so it is possible to have an idea of the better process and material, among the ones used, to use in a specific application. The comparison is presented in Chapter 8.

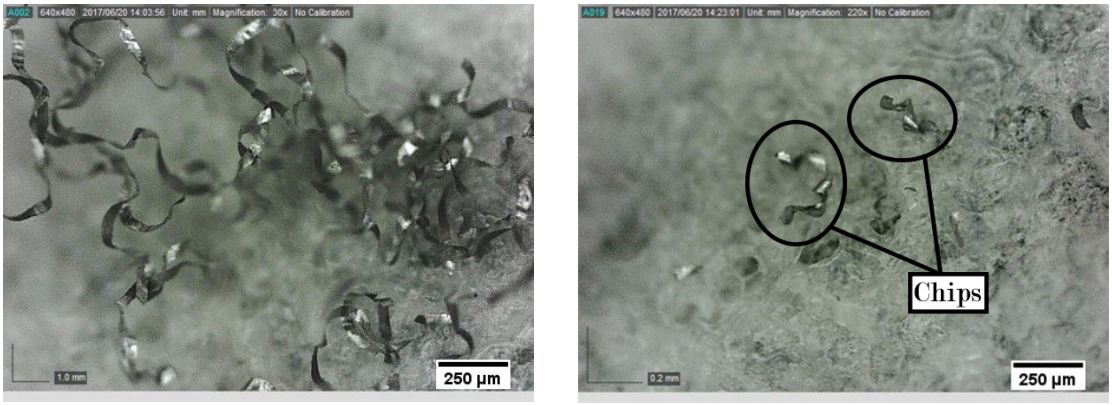

(a) Feed per tooth of 0.5 μm/tooth.

(b) Feed per tooth of 4.0 μm/tooth.

Figure 7.32: Optical images of chips collected during micromilling experiments of Ti-6Al-4V alloy produced by SLM.

Chapter 8

Analysis and discussion

This chapter presents a comparative analysis and discussion of the results exposed in the Chapter 7 between the commercially pure titanium, the Ti-6Al-4V alloy, commercially pure titanium processed by ECAP and Ti-6Al-4V produced by SLM. It is covered the material characterization, cutting force, specific cutting force, surface roughness, burr formation and microchips and microtool results.

8.1 Material characterization comparison

Figure 8.1 summarizes the mechanical properties results and includes the cortical bone properties according to the literature. The mechanical properties differences between the materials can be explained by their microstructure. According to literature information, CP-Ti grade 2 has a flexural strength of 345 MPa while the flexure testing showed that CP-Ti processed by ECAP has a 630 MPa strength, representing an increase of 83%. This result was expected as ECAP processing turns a coarsed alpha grain microstructure into fined alpha grains. As a consequence, by the Hall-Petch equation, the strength of the material is increased, due to the higher presence of grain boundaries and the difficulty for the dislocations motion.

A similar analysis can be made for the comparison between the titanium alloy and the SLM fabricated alloy. Titanium alloy flexural strength presented more than two times increase when being fabricated by SLM. Analyzing their microstructure, it is clear that happened a strong grain refinement process, and the same mechanism of strengthening occurred and it would be expected to reduce machinability. The SLM material also presented a more brittle behavior than the standard titanium alloy showed in the literature.

Comparing the CP-Ti processed by ECAP and the SLM fabricated alloy, it can be seen that there is a great difference between the materials resistance, but their apparent flexural modulus is similar. Thus, the ECAP samples presented a strong brittle behavior, while the SLM samples presented a more ductile characteristic in

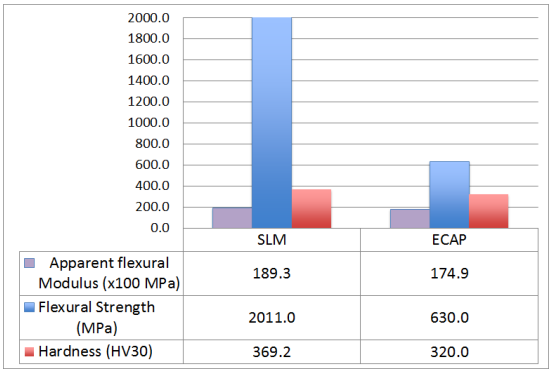

	SLM	ECAP
Apparent flexural Modulus (x100 MPa)	189.3	174.9
Flexural Strength (MPa)	2011.0	630.0
Hardness (HV30)	369.2	320.0

(a) SLM alloy and CP-Ti ECAP.

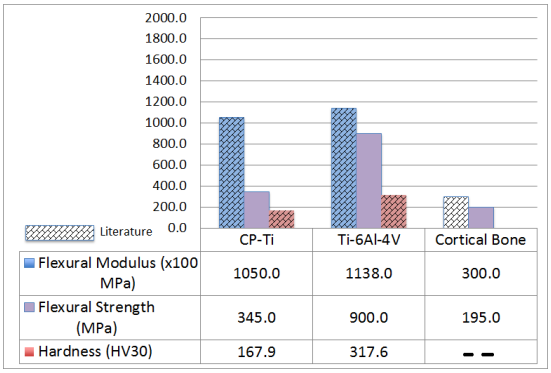

	CP-Ti	Ti-6Al-4V	Cortical Bone
Flexural Modulus (x100 MPa)	1050.0	1138.0	300.0
Flexural Strength (MPa)	345.0	900.0	195.0
Hardness (HV30)	167.9	317.6	– –

(b) CP-Ti, Ti-6Al-4V and bone.

Figure 8.1: Mechanical properties comparison.

comparison, fracturing with more than twice the strain of ECAP samples. Although it was not possible to measure the grain size for the ECAP samples, the higher resistance indicate that fined microstructure was achieved.

As in flexure tests it was measured the apparent flexural modulus for SLM and ECAP samples, it is not possible to compare them with the literature values for CP-Ti and Ti-6Al-4V. However, as the apparent modulus results were significantly smaller than the literature flexural modulus and the difference between them usually is not that high, it can indicate that SLM alloy and ECAP CP-Ti presented a decrease in stiffness. The decrease in stiffness would be a good material improvement considering the biomedical implants application. The flexural modulus of bone can vary between 7 and 30 GPa, as showed in Fig. 8.1b. The stiffness presented by the ECAP and SLM materials would be closer to the human bone value which can overcome a long issue involving the use of metallic implants: the loss of bone stiffness.

The Vickers hardness tests results followed the flexural strength trends. Selective laser melting sample presented the highest value (369 HV30) followed by the ECAP (320 HV30) and alloy (318 HV30) samples and then by the CP-Ti sample. Commercially pure titanium processed by ECAP presented the same result as the alloy, considering the standard deviation.

Summarizing the properties between all the materials, it can be said that SLM and ECAP processing presented an increase of strength and hardness regarding the standard materials as well as a decrease in the stiffness and a more prominent brittle behavior. Regarding thermal conductivity, which is an important property in titanium alloys, it would hardly be changed if the chemical composition and the physical state of the material are the same.

8.2 Micromilling forces and specific cutting force

Cutting force in machining operations usually are deeply connected to the properties of the workpiece material such as strength, hardness, ductility and thermal conductivity. In micromilling, additional factors can also play an important role, as the material microstructure.

As detailed in Chapter 7, batch A for the ECAP sample was performed twice as the first one presented a suddenly and unexpected increase of force during the third experiment. However, both results are being presented. The cutting force results for the CP-Ti, Ti-6Al-4V, SLM and ECAP samples for batch A, with both ECAP batches, are presented in Fig. 8.2. And the force results for batch B is showed in Fig. 8.3.

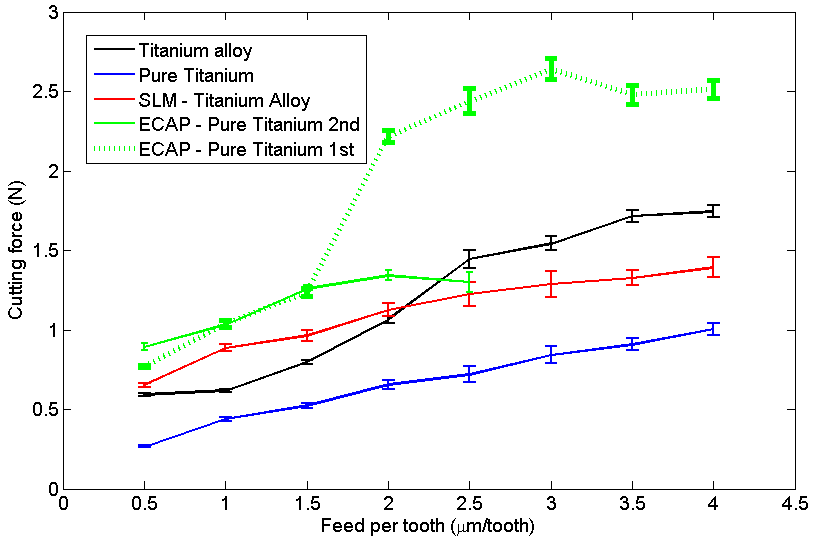

Figure 8.2: Experimental cutting force comparison for batch A.

It can be seen that cutting forces for the standard CP-Ti were the lowest among the materials for all feeds per tooth and all batches. This result was expected as it presented the lowest hardness and strength values and has higher thermal conductivity than the titanium alloy, which is a key factor in tool wear when machining titanium. Additionally, it is noticed that the ECAP samples presented the higher forces between the materials, including both A batches. The increase of cutting force milling ECAP processed CP-Ti when comparing with standard CP-Ti was expected as it presents significant higher strength and hardness.

The results for the standard titanium alloy and the alloy produced by SLM showed in general an inverse result, considering the hardness tests values. Although SLM material presented significantly higher strength and hardness, it presented lower cutting forces. For the increased feed batch, initially the SLM sample presented

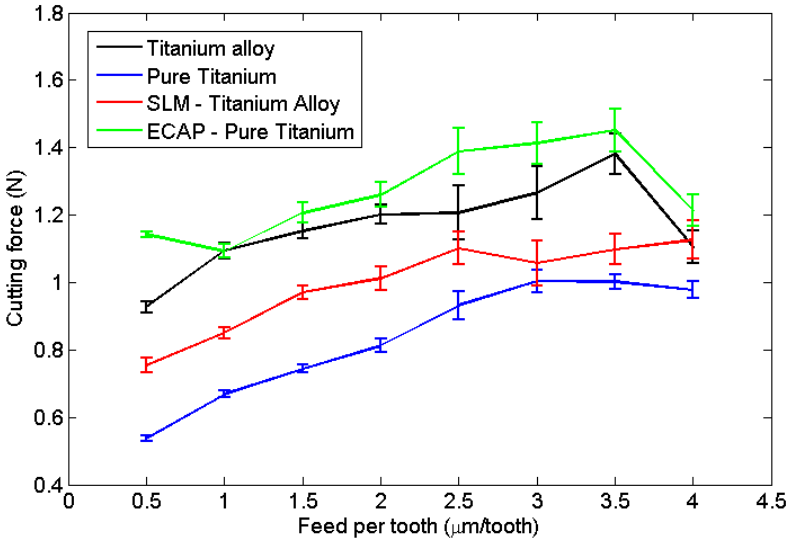

Figure 8.3: Experimental cutting force comparison for batch B.

higher forces, but this behavior changes after 2 μm/tooth when the standard alloy start to present higher forces. For batch B, SLM presented smaller forces throughout all the feeds. Thus, standard alloy and SLM alloy cutting force results were higher than standard CP-Ti, but lower than the ECAP CP-Ti.

This result is in compliance with other studies in micromilling of titanium alloys where cutting forces were found smaller for higher hardness material. Bonaiti *et al.*, for example, found lower cutting forces when milling additive manufacturing Ti-6Al-4V with different porosities using a 500 μm tool and different feed per tooth in comparison with standard Ti-6Al-4V.

There are a couple of possible reasons that could help that to happen. In micromilling, microstructure of the material can play an important role, specially in machining forces. Despite the differences in grain size, standard alloy and SLM alloy presented different phases and grains shape. While the standard alloy presented near equiaxed alpha grains with alpha/beta regions in between, SLM sample presented acicular alpha‘ martensite in alpha matrix.

Despite the microstructure, tool wear can have influenced the cutting force during the experiments. Analyzing batch A, Fig. 8.2, the force relation between the materials changes in the middle of the experiments. As this fact did not occurred for batch B, it can mean that when the tool was new, forces for SLM was higher, but as the tool for standard alloy worn more than for the SLM alloy (as showed in Chapter 7), the cutting force for the standard alloy became higher. For batch B, the force for SLM material was higher in all feeds because as it started with a high feed per tooth, the difference in tool wear might have been significant from the first experiment. Too wear increased cutting edge radius from 2 μm to 5 μm, making

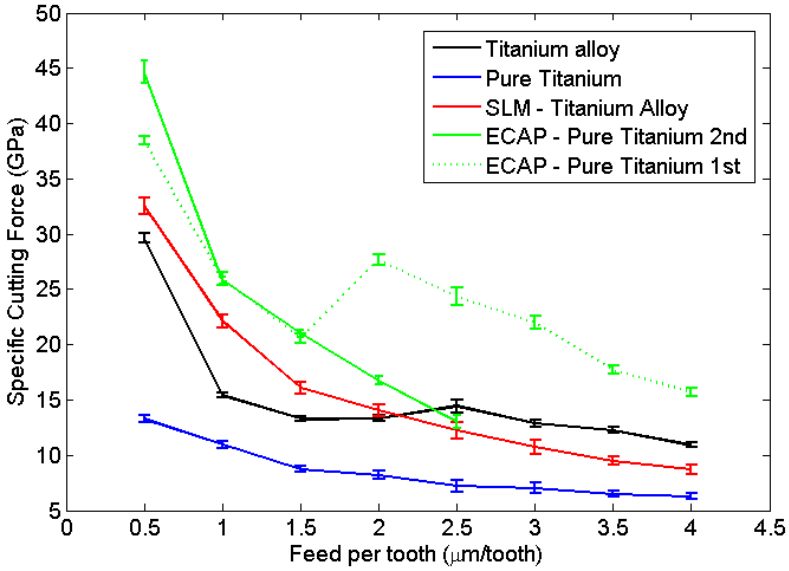

Figure 8.4: Specific force comparison for batch A.

it more difficult to cut the material and, as a consequence, increasing cutting force necessary.

Cutting forces are directly related to the specific cutting force of the materials. As showed in Fig. 8.4 and Fig. 8.5, the comparison between the materials are similar to the cutting force analysis. Equal channel angular pressing samples presented higher specific force than the other materials, while CP-Ti presented the smaller ones. And the SLM alloy sample presented a smaller specific force than the standard alloy. This means that SLM alloy requires less energy to be cut.

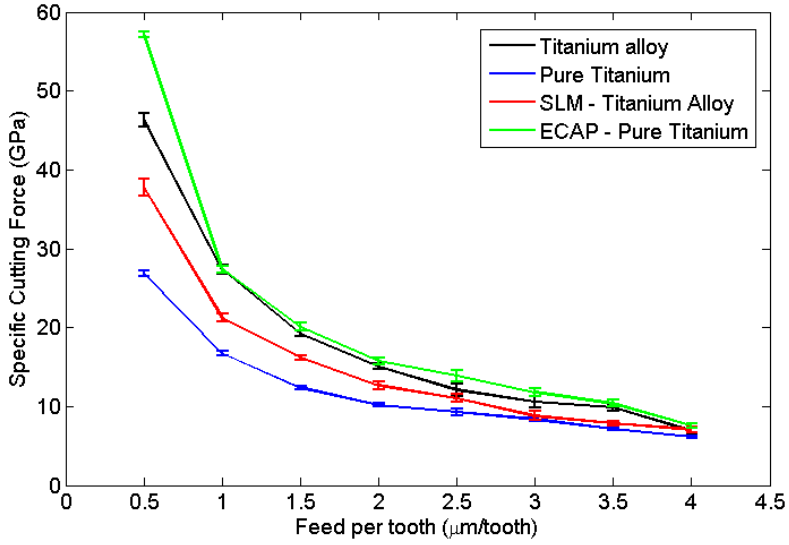

Figure 8.5: Specific force comparison for batch B.

One important factor to point out is that the SLM sample was the material which

was less affected by the tool wear considering the cutting force and specific force. Comparing the results from both batches, A and B, for SLM alloy, the specific force values presented small differences (highest of 19 %) while for the other materials the differences reached more than 100 %.

8.3 Surface roughness comparison

Surface integrity is an essential factor for analyzing and comparing machinability of materials and surface roughness is an important parameter to characterize surface integrity of a machined surface. As detailed in Chapter 7, roughness results showed three well defined regions considering the feed per tooth range and these regions will be used to divide the comparison. This general behavior of roughness was also found by other studies [33].

For batch A, which is showed for all materials in Fig. 8.6, the materials presented a similar result, except the ECAP sample that showed higher roughness values. In the second part, standard Ti-6Al-4V and CP-Ti presented a strong increase followed by a decrease in the results, while the SLM and ECAP samples kept more or less the same level of roughness. In the third part, again the standard alloy and CP-Ti presented similar results while the others showed lower roughness values. Analyzing point to point, SLM sample presented the lowest roughness values throughout almost the entire batch.

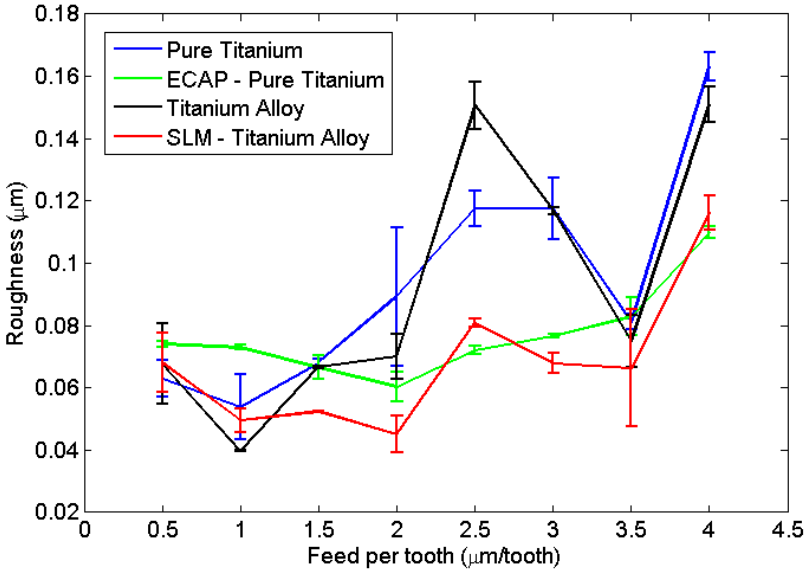

Figure 8.6: Surface roughness comparison for batch A.

Following the same pattern to analyze batch B, it can be seen that the results were more consistent than for the other batch. For all regions of the surface roughness result, showed in Fig. 8.7, ECAP sample presented the highest roughness

values, followed by the CP-Ti. Standard alloy and SLM alloy presented similar results, but in general the SLM material showed lower roughness values.

Roughness is strongly related to the mechanical properties of the material and tool wear. For example, built-up edge can negatively influence surface roughness (although it does not form when cutting pure metals), while other wear mechanism can positively affect it. Depending on how the tool is wearing, it can lead to a sharper cutting edge and improve surface roughness.

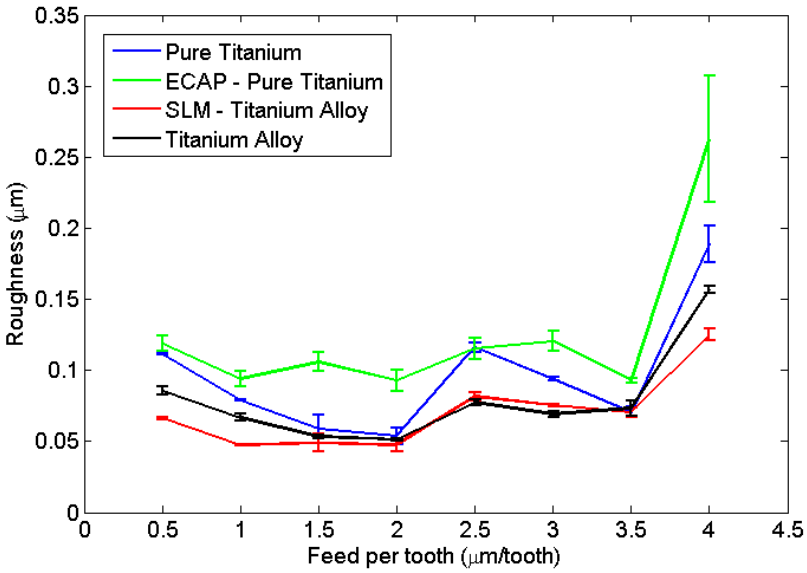

Figure 8.7: Surface roughness comparison for batch B.

8.4 Burr formation comparison

As presented in Section 2.6, burr formation in an important factor for analyzing surface integrity, specially in micromilling as the procedure for deburring a workpiece machined by micromilling is very complex due to the miniaturized dimensions of the part.

The results for burr formation regarding all four materials showed that SLM and ECAP samples presented lower burr formation than the other materials, as presented in Fig. 8.8 and Fig. 8.9 for upmilling and downmilling, respectively.

In micromilling, size effect is crucial when studying burr formation because it is related to the cutting edge radius of the tool and the feed per tooth, besides other factors as material properties. As seen in the top burr height measurements presented in the figures, burrs tend to decrease when increasing feed per tooth in micromilling. This happens because as feed per tooth gets closer to the cutting edge radius, shearing of the material starts to be replaced by ploughing mechanism where the material is plastic deformed more than cut off.

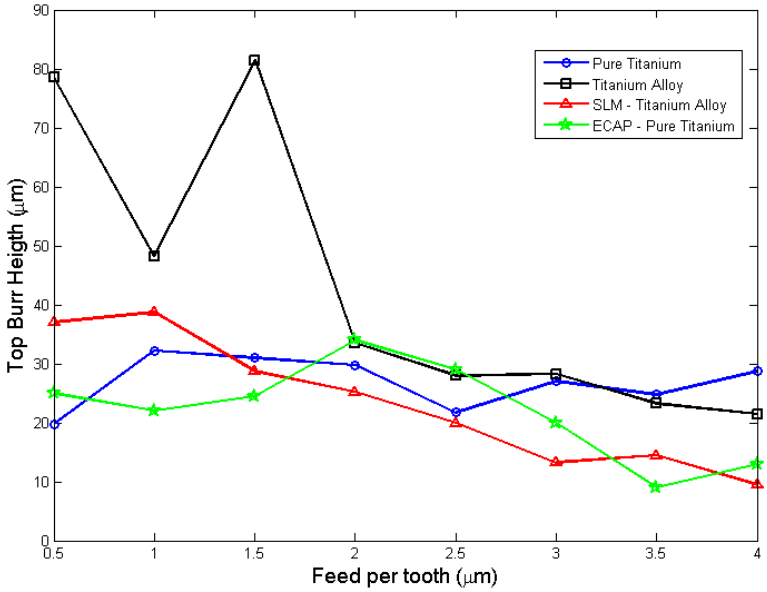

Figure 8.8: Burr formation comparison for upmilling.

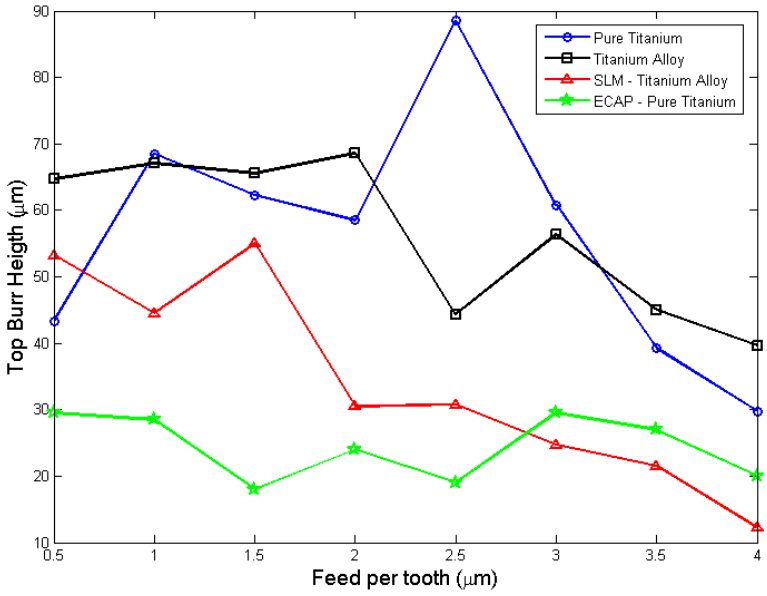

Figure 8.9: Burr formation comparison for downmilling.

Therefore, during a micromilling process, the microtool wears quickly and the edge radius increases, burr formation tends to also be higher and that is one of the reasons why SLM sample showed less burr formation: it also presented less tool wear.

When comparing the Ti-6Al-4V sample with the SLM alloy, besides presenting less tool wear and lower cutting forces, the SLM sample also has a more brittle behavior, which contributes with the smaller burr values. The chips tend to break

and be cut off the material more easily and do not stay connected to the workpiece. The same reason might explain why ECAP sample showed less burr in comparison to the other materials. ECAP sample showed extreme brittle behavior during flexure testing and it can have influenced the amount of burrs formed in the experiments.

Top images of the grooves confirm the previous result as shown in Fig. 8.10. It presents a comparison between the grooves for each material during batch A for 3.5 μm/tooth. The images for all experiments are shown in Appendix A. It is noticed that indeed SLM and ECAP samples presented less burr formation than the other materials for the same cutting conditions.

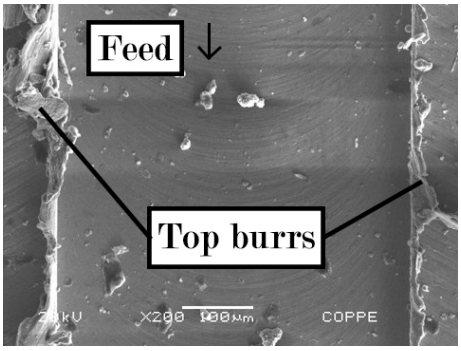

(a) CP-Ti.

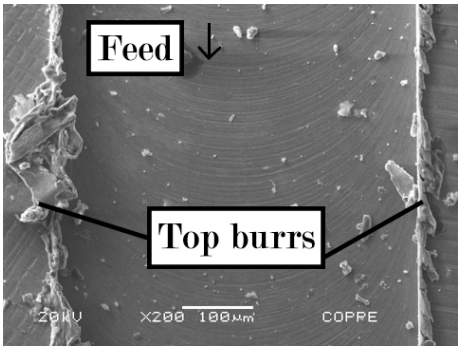

(b) Ti-6Al-4V.

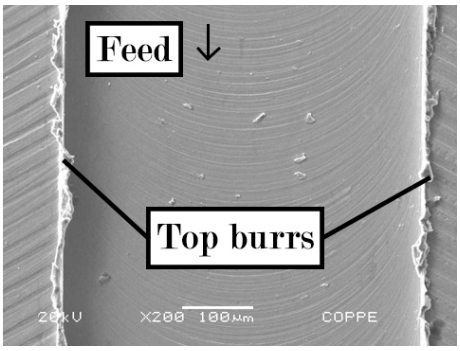

(c) SLM.

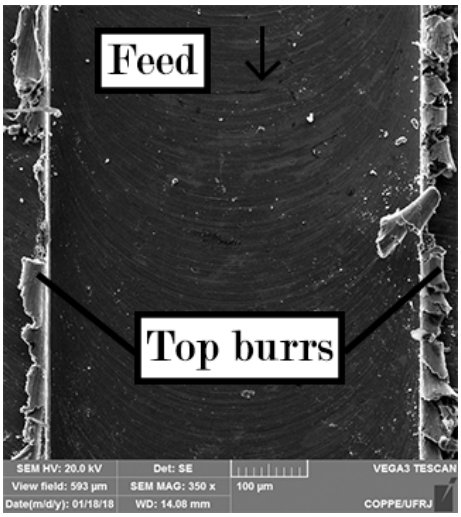

(d) ECAP.

Figure 8.10: Top SEM images of grooves for batch A with feed per tooth of 3.5 μm.

8.5 Microchips analysis comparison

Analyzing the microchips through all the cutting conditions for all materials, as shown in Appendix B, it can be seen that the microchips for all four material presented the same general behavior. Microchips presented a longer length for small feeds, especially below 1.5 μm/tooth.

Increasing the feed per tooth made microchips length decreased. However, the shape of the chips was different when comparing the pure titanium samples (standard and ECAP) with the Ti-6Al-4V samples (standard and SLM). For higher feeds, the chips for pure titanium went from long snarled chips to loose arc shape, while for the alloy based samples it went from snarled to helical short chips.

Chapter 9

Conclusions

The present chapter presents the main conclusions and contributions of the research considering the analysis of the experimental results for each material studied and the comparison made between the machinability of each material. It also broaches a few suggestions and perpectives to continue this study.

9.1 Conclusions and final considerations

This study dealt with four different titanium-based materials: standard commercially pure titanium grade 2, standard Ti-6Al-4V alloy, CP-Ti processed by ECAP and Ti-6Al-4V fabricated by SLM. It was compared and analyzed the micromilling machinability of each material considering cutting forces, surface roughness, burr formation, microchips morphology as well as their mechanical properties and the influence of each parameter.

It was designed a series of experiments varying feed per tooth and covering a wide range, from 0.5 to 4.0 μm. Two batches of experiments were carried out for each material: one increasing feed per tooth (batch A) and the other decreasing feed per tooth (batch B). The experiments consisted of micromilling 4 μm length grooves. During the experiments, cutting forces were acquired and the microchips were collected. Thus, surface roughness and top burr height were measured and top images of each groove were analyzed using a scanning electron microscope.

The following main conclusions and considerations can be established:

- Considering the microstructure, standard CP-Ti and Ti-6Al-4V presented typical phase constitutions, SLM and ECAP material showed fined grain structures. The SLM material presented acicular alpha' martensite in alpha matrix and ECAP presented alpha distort particles and fined grains;

- Selective laser melting and ECAP samples presented an increase of strength and hardness regarding their standard related materials as well as a more

prominent brittle behavior. Also, SLM sample presented higher strength and hardness than the ECAP sample. This is due to the fined grain microstructure both presented;

- Regarding each cutting force behavior, all materials presented the expected trend related to the feed per tooth: increasing the cutting force with the increase of feed per tooth. The SLM sample showed to be less affected by tool wear than the other materials as both batches of experiments presented similar numerical results;

- Despite presenting the higher strength and hardness, the SLM sample presented lower cutting force values than the standard alloy and the ECAP samples. This result can be related to its microstructure as well as to the fact that the tool was less affected by tool wear;

- Specific cutting force was computed using the resultant force experimental result and it confirmed the previous analysis. The selective laser melting material showed the lowest variation between both batches, confirming that tool wear did not affect the micromilling results as affected the other materials, specially ECAP sample;

- All materials presented the same general roughness behavior when varying feed per tooth. It showed three different regions considering the feed per tooth range: from 0.5 to around 2.0 μm/tooth where roughness decreases; 2.0 to 3.5 μm/tooth where it shows a non pattern behavior, initially increasing and then decreasing or staying more or less at the same level; and from 3.5 to 4.0 μm/tooth where a strong rise in the roughness values occurred. The first region might be explained by the ploughing region as feeds are very small, while the second region can be related to the cutting edge radius of the microtool, which was 2-2.5 μm;

- Selective laser melting sample presented the lowest surface roughness results for almost all feeds per tooth. This is probably related also to the low tool wear in comparison with the other materials as well as its mechanical properties;

- All materials presented more burr formation during downmilling than upmilling as well as a trend of decreasing burr formation when increasing feed per tooth. Hence, when machining these materials, it is suggested to plan the milling process for the tool to work only in downmilling and to use higher feeds per tooth, considering the values used in this study;

- Selective laser melting and ECAP sample presented less burr formation than the other materials which might be explained by the smaller tool wear occurred

during the process which affected less the cutting edge radius that is directly related to burr formation. Thus, both materials had more brittle behavior than the others which also might explain the better results;

- Analyzing microchips morphology, all four material presented the same general behavior. Microchips presented a longer length for small feeds, especially below 1.5 μm/tooth, and small length for higher feeds;

- Considering all the factors analyzed, SLM produced Ti-6Al-4V presented the higher machinability, considering its mechanical properties and the cutting force, roughness, burr formation and chips analysis. The only analyzed factor where SLM sample presented worst results was in cutting force where standard CP-Ti presented lower forces. However, CP-Ti presents low mechanical properties in comparison with SLM material. Thus, it does not present strength necessary for implant applications, except for dental implants that do not require great loading.

9.2 Perspectives for future works

Despite finding that SLM Ti-6Al-4V presented a higher machinability than the other materials according to the experiments performed during this work, this titanium alloy presents a few limitations regarding its chemical composition as explained in Chapter 1. Thus, titanium machinability is a complex issue, presenting several factors that can influence the process characterization.

Therefore, considering these observations, a few suggestions and perspectives of futures works are highlighted:

- It is important to analyze tool wear as it presented a key participation in micromilling titanium-based materials. There is not an easy and well developed methodology for microtool wear analysis, but it can be analyzed the cutting edge radius and tool diameter evolution, analyzing the mechanisms which lead SLM material to have a better behavior;

- Ti-6Al-4V alloy has the limitation of being alloyed with aluminum and vanadium, which can cause health issues for a patient, considering biomedical implants application. Therefore, it is necessary to analyze the machinability of CP-Ti produced by SLM as it will probably present improved mechanical properties regarding standard CP-Ti. It is suggested to subtitute the alloy powder for CP-Ti powder;

- Surface roughness has an important role in biomedical implants as it is related to the biological adaptation and the rate of cell growing around the implant.

Therefore, in vivo studies using different machined surface roughness in SLM produced implants is suggested;

Bibliography

[1] ZAFFE, D., BERTOLDI, C., CONSOLO, U. "Accumulation of aluminium in lamellar bone after implantation of titanium plates, Ti–6Al–4V screws, hydroxyapatite granules", *Biomaterials*, v. 25, n. 17, pp. 3837 – 3844, 2004. ISSN: 0142-9612. doi: https://doi.org/10.1016/j.biomaterials.2003.10.020. Disponível em: <http://www.sciencedirect.com/science/article/pii/S0142961203009359>.

[2] MJÖBERG, B., HELLQUIST, E., MALLMIN, H., et al. "Aluminum, Alzheimer's disease and bone fragility", *Acta Orthopaedica Scandinavica*, v. 68, n. 6, pp. 511–514, 1997. doi: 10.3109/17453679708999016. Disponível em: <https://doi.org/10.3109/17453679708999016>.

[3] IMPLANT, . "Taking Care of Your Dental Implants". 2012. Disponível em: <http://www.1888implant.com/dental-implants-care.html>.

[4] E M. B. OSKOOEE E N. SHAFIEI, S. O. "Finite element analysis of an ultrafine grained Titanium dental implant covered by different thicknesses of hydroxyapatite layer", *Indian Journal of Dentistry*, v. 4, n. 1, pp. 1 – 4, 2013. ISSN: 0975-962X. doi: http://dx.doi.org/10.1016/j.ijd.2012.10.002. Disponível em: <http://www.sciencedirect.com/science/article/pii/S0975962X12001141>.

[5] E M. B. OSKOOEE, S. O. "Analysis of stress concentration in bone–implant interface using different shapes of the implant: Porous Ti and ultrafine grained Ti", *Indian Journal of Dentistry*, v. 4, n. 3, pp. 125 – 128, 2013. ISSN: 0975-962X. doi: http://dx.doi.org/10.1016/j.ijd.2013.07.008. Disponível em: <http://www.sciencedirect.com/science/article/pii/S0975962X13000695>.

[6] E M. A. MEYERS E R. Z. VALIEV E S. N. MONTEIRO, C. N. E. "Ultrafine grained titanium for biomedical applications: An overview of performance", *Journal of Materials Research and Technology*, v. 2, n. 4, pp. 340 – 350, 2013. ISSN: 2238-7854.

[7] BAUER, S., SCHMUKI, P., VON DER MARK, K., et al. "Engineering biocompatible implant surfaces: Part I: Materials and surfaces", *Progress in Materials Science*, v. 58, n. 3, pp. 261 – 326, 2013. ISSN: 0079-6425. doi: https://doi.org/10.1016/j.pmatsci.2012.09.001. Disponível em: <http://www.sciencedirect.com/science/article/pii/S007964251200062X>.

[8] MUDDUGANGADHAR, B., SIDDHI, G. A., SUCHISMITA, T., et al. "Biomaterials for Dental Implants: An Overview", *International Journal of Oral Implantology and Clinical Research*, v. 2, n. 1, pp. 13 – 24, 2011. Disponível em: <http://www.jaypeejournals.com/eJournals/ShowText.aspx?ID=1032&Type=FREE&TYP=TOP&IN=_eJournals/images/JPLOGO.gif&IID=89&isPDF=NO>.

[9] RACK, H., QAZI, J. "Titanium alloys for biomedical applications", *Materials Science and Engineering: C*, v. 26, n. 8, pp. 1269 – 1277, 2006. ISSN: 0928-4931. ¡ce:title¿Proceedings of the First TMS Symposium on Biological Materials Science¡/ce:title¿.

[10] NIINOMI, M. "Mechanical biocompatibilities of titanium alloys for biomedical applications", *Journal of the Mechanical Behavior of Biomedical Materials*, v. 1, n. 1, pp. 30 – 42, 2008. ISSN: 1751-6161.

[11] E L. KANDER E V. MASEK, M. G. "Ultrafine-grain titanium using for medical applications, structure and properties", *NANOCON 2010: 2nd International Conference*, pp. 502 – 507, 2013.

[12] E H. KIM E R. LAPOVOK E H. P. NG E J. JO, Y. E. "Mechanical Strength and Biocompatibility of Ultrafine-Grained Commercial Purity Titanium", *BioMed Research International*, v. 2013, 2013. doi: 10.1155/2013/914764.

[13] KRUTH, J.-P., LEVY, G., KLOCKE, F., et al. "Consolidation phenomena in laser and powder-bed based layered manufacturing", {*CIRP*} *Annals - Manufacturing Technology*, v. 56, n. 2, pp. 730 – 759, 2007. ISSN: 0007-8506. doi: http://dx.doi.org/10.1016/j.cirp.2007.10.004. Disponível em: <http://www.sciencedirect.com/science/article/pii/S0007850607001540>.

[14] TRAINI, T., MANGANO, C., SAMMONS, R., et al. "Direct laser metal sintering as a new approach to fabrication of an isoelastic functionally graded material for manufacture of porous titanium dental implants", *Dental Materials*, v. 24, n. 11, pp. 1525 – 1533, 2008. ISSN: 0109-5641. doi: http://

dx.doi.org/10.1016/j.dental.2008.03.029. Disponível em: <http://www.sciencedirect.com/science/article/pii/S0109564108000833>.

[15] ATTAR, H., LÖBER, L., FUNK, A., et al. "Mechanical behavior of porous commercially pure Ti and Ti–TiB composite materials manufactured by selective laser melting", *Materials Science and Engineering: A*, v. 625, n. 0, pp. 350 – 356, 2015. ISSN: 0921-5093. doi: http://dx.doi.org/10.1016/j.msea.2014.12.036. Disponível em: <http://www.sciencedirect.com/science/article/pii/S0921509314015366>.

[16] LAPOVOK, R., MOLOTNIKOV, A., LEVIN, Y., et al. "Machining of coarse grained and ultra fine grained titanium", *Journal of Materials Science*, v. 47, n. 11, pp. 4589–4594, 2012. ISSN: 0022-2461. doi: 10.1007/s10853-012-6320-7. Disponível em: <http://dx.doi.org/10.1007/s10853-012-6320-7>.

[17] ÍTALO SETTE ANTONIALLI, A., DE ANDRADE MENDES FILHO, A., SORDI, V. L., et al. "The Machinability of Ultrafine-grained Grade 2 Ti Processed by Equal Channel Angular Pressing", *Journal of Materials Research and Technology*, v. 1, n. 3, pp. 148 – 153, 2012. ISSN: 2238-7854. doi: http://dx.doi.org/10.1016/S2238-7854(12)70026-1. Disponível em: <http://www.sciencedirect.com/science/article/pii/S2238785412700261>.

[18] MOREHEAD, M. *Machinability and Microstructure Stability During the mahicning of Pure Copper and Titanium Processed by Equal Channel Angular Pressing*. Tese de Doutorado, Clemson University, 2007.

[19] SCHRODER, F. C. "Estudo das forças de usinagem e da resistência mecânica do titânio puro processado por extrusão angular em canal", *Undergraduation project*, v. Universidade Federal do Rio de Janeiro, 2014.

[20] VOLLERTSEN, F., BIERMANN, D., HANSEN, H., et al. "Size effects in manufacturing of metallic components", *CIRP Annals*, v. 58, n. 2, pp. 566 – 587, 2009. ISSN: 0007-8506. doi: https://doi.org/10.1016/j.cirp.2009.09.002. Disponível em: <http://www.sciencedirect.com/science/article/pii/S0007850609001693>.

[21] CÂMARA, M., RUBIO, J. C., ABRÃO, A., et al. "State of the Art on Micromilling of Materials, a Review", *Journal of Materials Science & Technology*, v. 28, n. 8, pp. 673 – 685, 2012. ISSN: 1005-0302. doi: https://doi.org/10.1016/S1005-0302(12)60115-7. Disponível em: <http://www.sciencedirect.com/science/article/pii/S1005030212601157>.

[22] NG, C. K., MELKOTE, S. N., RAHMAN, M., et al. "Experimental study of micro- and nano-scale cutting of aluminum 7075-T6", *International Journal of Machine Tools and Manufacture*, v. 46, n. 9, pp. 929 – 936, 2006. ISSN: 0890-6955. doi: https://doi.org/10.1016/j.ijmachtools.2005.08.004. Disponível em: <http://www.sciencedirect.com/science/article/pii/S0890695505002130>.

[23] BAO, W., TANSEL, I. "Modeling micro-end-milling operations. Part I: analytical cutting force model", *International Journal of Machine Tools and Manufacture*, v. 40, n. 15, pp. 2155 – 2173, 2000. ISSN: 0890-6955. doi: https://doi.org/10.1016/S0890-6955(00)00054-7. Disponível em: <http://www.sciencedirect.com/science/article/pii/S0890695500000547>.

[24] ARAMCHAROEN, A., MATIVENGA, P. "Size effect and tool geometry in micromilling of tool steel", *Precision Engineering*, v. 33, n. 4, pp. 402 – 407, 2009. ISSN: 0141-6359. doi: https://doi.org/10.1016/j.precisioneng.2008.11.002. Disponível em: <http://www.sciencedirect.com/science/article/pii/S0141635908001529>.

[25] CHAE, J., PARK, S., FREIHEIT, T. "Investigation of micro-cutting operations", *International Journal of Machine Tools and Manufacture*, v. 46, n. 3, pp. 313 – 332, 2006. ISSN: 0890-6955. doi: https://doi.org/10.1016/j.ijmachtools.2005.05.015. Disponível em: <http://www.sciencedirect.com/science/article/pii/S0890695505001306>.

[26] REZAEI, H., SADEGHI, M. H., BUDAK, E. "Determination of minimum uncut chip thickness under various machining conditions during micro-milling of Ti-6Al-4V", *The International Journal of Advanced Manufacturing Technology*, Nov 2017. ISSN: 1433-3015. doi: 10.1007/s00170-017-1329-3. Disponível em: <https://doi.org/10.1007/s00170-017-1329-3>.

[27] ATTANASIO, A., GELFI, M., POLA, A., et al. "Iinfluence of Materials Microstructures in Micromilling of Ti6Al4V Alloy", *Materials*, v. 6, n. 9, pp. 4268–4286, 2013. ISSN: 1996-1944. doi: 10.3390/ma6094268. Disponível em: <https://www.mdpi.com/1996-1994/6/9/4268>.

[28] DINIZ, A. *Tecnologia da Usinagem dos Materiais*. Artliber Editora, 2006.

[29] MOUGO, A. *Microfresamento do Aço Superduplex: uma comparação mecanística com os aços inoxidáveis austenítico e ferritico para as forças*

de usinagem e avaliação da superfície usinada. Tese de Doutorado, Universidade Federal do Rio de Janeiro, 2016.

[30] ASLANTAS, K., HOPA, H., PERCIN, M., et al. "Cutting performance of nano-crystalline diamond (NCD) coating in micro-milling of Ti6Al4V alloy", *Precision Engineering*, v. 45, pp. 55 – 66, 2016. ISSN: 0141-6359. doi: https://doi.org/10.1016/j.precisioneng.2016.01.009. Disponível em: <http://www.sciencedirect.com/science/article/pii/S0141635916000118>.

[31] NEWBY, G., VENKATACHALAM, S., LIANG, S. "Empirical analysis of cutting force constants in micro-end-milling operations", *Journal of Materials Processing Technology*, v. 192-193, pp. 41 – 47, 2007. ISSN: 0924-0136. doi: https://doi.org/10.1016/j.jmatprotec.2007.04.026. Disponível em: <http://www.sciencedirect.com/science/article/pii/S092401360700386X>. The Seventh Asia Pacific Conference on Materials Processing (7th APCMP 2006).

[32] CAMPOS, F. D. O. *Estudo das Forcas de Corte no Microfresamento da*. Tese de Mestrado, Universidade Federal do Rio de Janeiro, the Netherlands, 2012.

[33] MIAN, A. J. *Size Effect in Micromachining*. Tese de Doutorado, University of Manchester, 2011.

[34] GILLESPIE, L. K., BLOTTER, P. T. "The Formation and Properties of Machining Burrs", *Journal of Engineering for Industry*, v. 98, n. 1, pp. 66–74, Feb 1976. ISSN: 1087-1357. doi: 10.1115/1.3438875. Disponível em: <http://dx.doi.org/10.1115/1.3438875>.

[35] M. HASHIMURA, Y. P. C., DORNFELD, D. "Analysis of Burr Formation Mechanism in Orthogonal Cutting", *Journal of Manufacturing Science and Engineering*, v. 121, n. 1, pp. 1 – 7, 1999. ISSN: 0022-1817. doi: doi:10.1115/1.2830569. Disponível em: <http://manufacturingscience.asmedigitalcollection.asme.org/article.aspx?articleid=1434469>.

[36] CHERN, G.-L. "Experimental observation and analysis of burr formation mechanisms in face milling of aluminum alloys", *International Journal of Machine Tools and Manufacture*, v. 46, n. 12, pp. 1517 – 1525, 2006. ISSN: 0890-6955. doi: https://doi.org/10.1016/j.ijmachtools.2005.09.006. Disponível em: <http://www.sciencedirect.com/science/article/pii/S0890695505002658>.

[37] SHAW, M. *Metal Cutting Principles*. Oxford University Press, 2005.

[38] B.L. JUNEJA, G. S. *Fundamentals of Metal Cutting and Machine Tools*. New Age international Publishers, 2012.

[39] GROOVER, M. P. *Principles of Modern Manufacturing*. Jon Wiley & Sons, 2011. ISBN: 9780470505922.

[40] TENG, X., HUO, D., WONG, W. L. E., et al. "Machinability Investigation in Micro-milling of Mg Based MMCs with Nano-Sized Particles". In: Solanki, K. N., Orlov, D., Singh, A., et al. (Eds.), *Magnesium Technology 2017*, pp. 61–69, Cham, 2017. Springer International Publishing. ISBN: 978-3-319-52392-7.

[41] KATAHIRA, K., MATSUMOTO, Y., KOMOTORI, J., et al. "Experimental investigation of machinability and surface quality of sapphire machined with polycrystalline diamond micro-milling tool", *The International Journal of Advanced Manufacturing Technology*, v. 93, n. 9, pp. 4389–4398, Dec 2017. ISSN: 1433-3015. doi: 10.1007/s00170-017-0881-1. Disponível em: <https://doi.org/10.1007/s00170-017-0881-1>.

[42] XIE, B. *Investigation on the Machinability in the Micro-Milling of Amorphous Materials*. Tese de Doutorado, Oklahoma State University, 2016.

[43] WANG, Z.-B., HU, H.-X., LIU, C.-B., et al. "Corrosion Behaviors of Pure Titanium and Its Weldment in Simulated Desulfurized Flue Gas Condensates in Thermal Power Plant Chimney", *Acta Metallurgica Sinica (English Letters)*, v. 28, n. 4, pp. 477–486, Apr 2015. ISSN: 2194-1289. doi: 10.1007/s40195-015-0222-z. Disponível em: <https://doi.org/10.1007/s40195-015-0222-z>.

[44] YEOM, J.-T., KIM, J. H., HONG, J.-K., et al. "Prediction of Microstructure Evolution in Hot Backward Extrusion of Ti-6Al-4V Alloy", *Journal of Metallurgy*, v. 2012, 2012. doi: doi:10.1155/2012/989834.

[45] GEETHA, M., SINGH, A., ASOKAMANI, R., et al. "Ti based biomaterials, the ultimate choice for orthopaedic implants – A review", *Progress in Materials Science*, v. 54, n. 3, pp. 397 – 425, 2009. ISSN: 0079-6425. doi: https://doi.org/10.1016/j.pmatsci.2008.06.004. Disponível em: <http://www.sciencedirect.com/science/article/pii/S0079642508001126>.

[46] C. VEIGA, J.P. DAVIM, J. L. "Review on Machinability of Titanium Alloys: The Process Perspective", *Reviews on Advanced Materials Science*, v. 34, pp. 148 – 164, 2013.

[47] EZUGWU, E., WANG, Z. "Titanium alloys and their machinability—a review", *Journal of Materials Processing Technology*, v. 68, n. 3, pp. 262 – 274, 1997. ISSN: 0924-0136. doi: http://dx.doi.org/10.1016/S0924-0136(96)00030-1. Disponível em: <http://www.sciencedirect.com/science/article/pii/S0924013696000301>. Superplasticity and Superplastic Technology in Japan.

[48] KIKUCHI, M. "The use of cutting temperature to evaluate the machinability of titanium alloys", *Acta Biomaterialia*, v. 5, n. 2, pp. 770 – 775, 2009. ISSN: 1742-7061. doi: http://dx.doi.org/10.1016/j.actbio.2008.08.016. Disponível em: <http://www.sciencedirect.com/science/article/pii/S1742706108002596>.

[49] KIKUCHI, M., OKUNO, O. "Machinability evaluation of titanium alloys", *Dental Materials Journal*, v. 23, n. 1, pp. 37 – 45, 2004.

[50] PERFORMANCE, S. H. "Titanium Catalog". 2014. Disponível em: <http://www.smithshp.com/downloads/CPGrade4_SHP.pdf>.

[51] WANG, X. Q., AI, X., ZHAO, J., et al. "Experimental Investigation on Cutting Force and Tool Wear of Carbide Tools in Ti6Al4V Turning". In: *Advances in Machining & Manufacturing Technology IX*, v. 375, *Key Engineering Materials*, pp. 231–235. Trans Tech Publications, 8 2008. doi: 10.4028/www.scientific.net/KEM.375-376.231.

[52] LIN KE, Y., YUE DONG, H., LIU, G., et al. "Use of nitrogen gas in high-speed milling of Ti-6Al-4V", *Transactions of Nonferrous Metals Society of China*, v. 19, n. 3, pp. 530 – 534, 2009. ISSN: 1003-6326. doi: https://doi.org/10.1016/S1003-6326(08)60307-6. Disponível em: <http://www.sciencedirect.com/science/article/pii/S1003632608603076>.

[53] CHE-HARON, C., JAWAID, A. "The effect of machining on surface integrity of titanium alloy Ti–6% Al–4% V", *Journal of Materials Processing Technology*, v. 166, n. 2, pp. 188 – 192, 2005. ISSN: 0924-0136. doi: https://doi.org/10.1016/j.jmatprotec.2004.08.012. Disponível em: <http://www.sciencedirect.com/science/article/pii/S0924013604010313>.

[54] CAROU, D., RUBIO, E., HERRERA, J., et al. "Latest advances in the micro-milling of titanium alloys: a review", *Procedia Manufacturing*, v. 13,

pp. 275 – 282, 2017. ISSN: 2351-9789. doi: https://doi.org/10.1016/j.promfg.2017.09.071. Disponível em: <http://www.sciencedirect.com/science/article/pii/S2351978917307060>.

[55] ÖZEL, T., OLLEAK, A., THEPSONTHI, T. "Micro milling of titanium alloy Ti-6Al-4V: 3-D finite element modeling for prediction of chip flow and burr formation", *Production Engineering*, v. 11, n. 4, pp. 435–444, Oct 2017. ISSN: 1863-7353. doi: 10.1007/s11740-017-0761-4. Disponível em: <https://doi.org/10.1007/s11740-017-0761-4>.

[56] CHENG, J., JIN, Y., WU, J., et al. "Experimental study on a novel minimization method of top burr formation in micro-end milling of Ti-6Al-4V", *The International Journal of Advanced Manufacturing Technology*, v. 86, n. 5, pp. 2197–2217, Sep 2016. ISSN: 1433-3015. doi: 10.1007/s00170-015-8312-7. Disponível em: <https://doi.org/10.1007/s00170-015-8312-7>.

[57] THEPSONTHI, T., ÖZEL, T. "Multi-objective process optimization for micro-end milling of Ti-6Al-4V titanium alloy", *The International Journal of Advanced Manufacturing Technology*, v. 63, n. 9, pp. 903–914, Dec 2012. ISSN: 1433-3015. doi: 10.1007/s00170-012-3980-z. Disponível em: <https://doi.org/10.1007/s00170-012-3980-z>.

[58] KIM, D. H., LEE, P.-H., LEE, S. W. "Experimental Study on Machinability of Ti-6Al-4V in Micro End-Milling". In: *Proceedings of The World Congress Engineering Vol. II*, London, jul. 2014.

[59] TOTH, L. S., GU, C. "Ultrafine-grain metals by severe plastic deformation", *Materials Characterization*, v. 92, n. 0, pp. 1 – 14, 2014. ISSN: 1044-5803. doi: http://dx.doi.org/10.1016/j.matchar.2014.02.003. Disponível em: <http://www.sciencedirect.com/science/article/pii/S1044580314000576>.

[60] VERLINDEN, B. "Severe plastic deformation of metals", *Journal of Metallurgy*, v. 126, pp. 165 – 179, 2006.

[61] ESTRIN, Y., VINOGRADOV, A. "Extreme grain refinement by severe plastic deformation: A wealth of challenging science", *Acta Materialia*, v. 61, n. 3, pp. 782 – 817, 2013. ISSN: 1359-6454. doi: http://dx.doi.org/10.1016/j.actamat.2012.10.038. Disponível em: <http://www.sciencedirect.com/science/article/pii/S1359645412007859>. The Diamond Jubilee Issue Materials Challenges in Tomorrow's World Selected Topics in Materials Science and Engineering.

[62] CALLISTER, W. D. *Materials science and engineering: an introduction*. Jon Wiley & Sons, 2009. ISBN: 2009023130.

[63] PETCH, N. "The influence of grain boundary carbide and grain size on the cleavage strength and impact transition temperature of steel", *Acta Metallurgica*, v. 34, n. 7, pp. 1387 – 1393, 1986. ISSN: 0001-6160. doi: https://doi.org/10.1016/0001-6160(86)90026-X. Disponível em: <http://www.sciencedirect.com/science/article/pii/000161608690026X>.

[64] AZUSHIMA, A., KOPP, R., KORHONEN, A., et al. "Severe plastic deformation (SPD) processes for metals", {*CIRP*} *Annals - Manufacturing Technology*, v. 57, n. 2, pp. 716 – 735, 2008. ISSN: 0007-8506. doi: http://dx.doi.org/10.1016/j.cirp.2008.09.005. Disponível em: <http://www.sciencedirect.com/science/article/pii/S0007850608001947>.

[65] BRIDGMAN, P. W. *Studies in large plastic flow and fracture*. Mc-Grew-Hill, 1952.

[66] SEGAL, V. M. "Plastic working of metals by simple shear", *Russ Metall.*, v. 1, pp. 99 – 106, 1981.

[67] SEGAL, V. "Invention Certificate of the USSR", *Russ Metall.*, p. No. 575892, 1977.

[68] VALIEV, R. Z., LANGDON, T. G. "Principles of equal-channel angular pressing as a processing tool for grain refinement", *Progress in Materials Science*, v. 51, n. 7, pp. 881 – 981, 2006. ISSN: 0079-6425. doi: http://dx.doi.org/10.1016/j.pmatsci.2006.02.003. Disponível em: <http://www.sciencedirect.com/science/article/pii/S0079642506000120>.

[69] VALIEV, R., ISLAMGALIEV, R., ALEXANDROV, I. "Bulk nanostructured materials from severe plastic deformation", *Progress in Materials Science*, v. 45, n. 2, pp. 103 – 189, 2000. ISSN: 0079-6425. doi: http://dx.doi.org/10.1016/S0079-6425(99)00007-9. Disponível em: <http://www.sciencedirect.com/science/article/pii/S0079642599000079>.

[70] NAKASHIMA, K., HORITA, Z., NEMOTO, M., et al. "Development of a multi-pass facility for equal-channel angular pressing to high total strains", *Materials Science and Engineering: A*, v. 281, n. 1–2, pp. 82 – 87, 2000. ISSN: 0921-5093. doi: http://dx.doi.org/10.1016/S0921-5093(99)00744-3. Disponível em: <http://www.sciencedirect.com/science/article/pii/S0921509399007443>.

[71] NAGASEKHAR, A., TICK-HON, Y., SEOW, H. "Deformation behavior and strain homogeneity in equal channel angular extrusion/pressing", *Journal of Materials Processing Technology*, v. 192–193, n. 0, pp. 449 – 452, 2007. ISSN: 0924-0136. doi: http://dx.doi.org/10.1016/j.jmatprotec.2007.04.093. Disponível em: <http://www.sciencedirect.com/science/article/pii/S0924013607004517>. The Seventh Asia Pacific Conference on Materials Processing (7th {APCMP} 2006).

[72] FURUNO, K., AKAMATSU, H., OH-ISHI, K., et al. "Microstructural development in equal-channel angular pressing using a 60 die", *Acta Materialia*, v. 52, n. 9, pp. 2497 – 2507, 2004. ISSN: 1359-6454. doi: http://dx.doi.org/10.1016/j.actamat.2004.01.040. Disponível em: <http://www.sciencedirect.com/science/article/pii/S1359645404000229>.

[73] NAGASEKHAR, A., TICK-HON, Y., LI, S., et al. "Stress and strain histories in equal channel angular extrusion/pressing", *Materials Science and Engineering: A*, v. 423, n. 1–2, pp. 143 – 147, 2006. ISSN: 0921-5093. doi: http://dx.doi.org/10.1016/j.msea.2005.09.127. Disponível em: <http://www.sciencedirect.com/science/article/pii/S0921509306001110>. Mechanical Behaviour of Micro- and Nanoscale Systems.

[74] IWAHASHI, Y., HORITA, Z., NEMOTO, M., et al. "The process of grain refinement in equal-channel angular pressing", *Acta Materialia*, v. 46, n. 9, pp. 3317 – 3331, 1998. ISSN: 1359-6454. doi: http://dx.doi.org/10.1016/S1359-6454(97)00494-1. Disponível em: <http://www.sciencedirect.com/science/article/pii/S1359645497004941>.

[75] LEE, S., LANGDON, T. G. "Influence of Equal-Channel Angular Pressing on the Superplastic Properties of Commercial Aluminum Alloys". In: *Symposium HH – Superplasticity-Current Status & Future Potential*, v. 601, *MRS Online Proceedings Library*, 1999. doi: 10.1557/PROC-601-359. Disponível em: <http://journals.cambridge.org/article_S1946427400180455>.

[76] FURUKAWA, M., IWAHASHI, Y., HORITA, Z., et al. "The shearing characteristics associated with equal-channel angular pressing", *Materials Science and Engineering: A*, v. 257, n. 2, pp. 328 – 332, 1998. ISSN: 0921-5093. doi: http://dx.doi.org/10.1016/S0921-5093(98)00750-3. Disponível em: <http://www.sciencedirect.com/science/article/pii/S0921509398007503>.

[77] SEGAL, V. "Materials processing by simple shear", *Materials Science and Engineering: A*, v. 197, n. 2, pp. 157 – 164, 1995. ISSN: 0921-5093. doi: http://dx.doi.org/10.1016/0921-5093(95)09705-8. Disponível em: <http://www.sciencedirect.com/science/article/pii/0921509395097058>.

[78] BALOG, M., SIMANCIK, F., BAJANA, O., et al. "{ECAP} vs. direct extrusion—Techniques for consolidation of ultra-fine Al particles", *Materials Science and Engineering: A*, v. 504, n. 1–2, pp. 1 – 7, 2009. ISSN: 0921-5093. doi: http://dx.doi.org/10.1016/j.msea.2008.12.014. Disponível em: <http://www.sciencedirect.com/science/article/pii/S0921509308013853>.

[79] XIA, K., WU, X. "Back pressure equal channel angular consolidation of pure Al particles", *Scripta Materialia*, v. 53, n. 11, pp. 1225 – 1229, 2005. ISSN: 1359-6462. doi: http://dx.doi.org/10.1016/j.scriptamat.2005.08.012. Disponível em: <http://www.sciencedirect.com/science/article/pii/S1359646205004999>.

[80] MATSUKI, K., AIDA, T., TAKEUCHI, T., et al. "Microstructural characteristics and superplastic-like behavior in aluminum powder alloy consolidated by equal-channel angular pressing", *Acta Materialia*, v. 48, n. 10, pp. 2625 – 2632, 2000. ISSN: 1359-6454. doi: http://dx.doi.org/10.1016/S1359-6454(00)00061-6. Disponível em: <http://www.sciencedirect.com/science/article/pii/S1359645400000616>.

[81] SENKOV, O., MIRACLE, D., SCOTT, J., et al. "Equal channel angular extrusion compaction of semi-amorphous $Al_{85}Ni_{10}Y_{2.5}La_{2.5}$ alloy powder", *Journal of Alloys and Compounds*, v. 365, n. 1–2, pp. 126 – 133, 2004. ISSN: 0925-8388. doi: http://dx.doi.org/10.1016/S0925-8388(03)00682-0. Disponível em: <http://www.sciencedirect.com/science/article/pii/S0925838803006820>.

[82] SAUVAGE, X., GANEEV, A., IVANISENKO, Y., et al. "Grain Boundary Segregation in UFG Alloys Processed by Severe Plastic Deformation", *Advanced Engineering Materials*, v. 14, n. 11, pp. 968–974. doi: 10.1002/adem.201200060. Disponível em: <https://onlinelibrary.wiley.com/doi/abs/10.1002/adem.201200060>.

[83] SUN, P., KAO, P., CHANG, C. "High angle boundary formation by grain subdivision in equal channel angular extrusion", *Scripta Materialia*, v. 51, n. 6, pp. 565 – 570, 2004. ISSN: 1359-6462. doi: http://dx.doi.org/10.1016/j.

scriptamat.2004.05.031. Disponível em: <http://www.sciencedirect.com/science/article/pii/S1359646204003112>.

[84] FIGUEIREDO, R. B., LANGDON, T. G. "Using severe plastic deformation for the processing of advanced engineering materials", *Materials Transactions*, v. 50, n. 7, pp. 1613–1619, 2009. Disponível em: <http://eprints.soton.ac.uk/72193/>.

[85] KIM, I., JEONG, W.-S., KIM, J., et al. "Deformation structures of pure Ti produced by equal channel angular pressing", *Scripta Materialia*, v. 45, n. 5, pp. 575 – 580, 2001. ISSN: 1359-6462. doi: http://dx.doi.org/10.1016/S1359-6462(01)01065-X. Disponível em: <http://www.sciencedirect.com/science/article/pii/S135964620101065X>.

[86] DHEDA, S. S., MOHAMED, F. A. "Effect of initial microstructure on the processing of titanium using equal channel angular pressing", *Materials Science and Engineering: A*, v. 528, n. 28, pp. 8179 – 8186, 2011. ISSN: 0921-5093. doi: http://dx.doi.org/10.1016/j.msea.2011.07.032. Disponível em: <http://www.sciencedirect.com/science/article/pii/S0921509311008112>.

[87] CHEN, Y., LI, Y., WALMSLEY, J., et al. "Microstructure evolution of commercial pure titanium during equal channel angular pressing", *Materials Science and Engineering: A*, v. 527, n. 3, pp. 789 – 796, 2010. ISSN: 0921-5093. doi: http://dx.doi.org/10.1016/j.msea.2009.09.005. Disponível em: <http://www.sciencedirect.com/science/article/pii/S0921509309010223>.

[88] CABIBBO, M., EVANGELISTA, E., VEDANI, M. "Influence of severe plastic deformations on secondary phase precipitation in a 6082 Al-Mg-Si alloy", *Metallurgical and Materials Transactions A*, v. 36, n. 5, pp. 1353–1364, May 2005. ISSN: 1543-1940. doi: 10.1007/s11661-005-0226-9. Disponível em: <https://doi.org/10.1007/s11661-005-0226-9>.

[89] KANG, D.-H., KIM, T.-W. "Mechanical behavior and microstructural evolution of commercially pure titanium in enhanced multi-pass equal channel angular pressing and cold extrusion", *Materials & Design*, v. 31, Supplement 1, n. 0, pp. S54 – S60, 2010. ISSN: 0261-3069. doi: http://dx.doi.org/10.1016/j.matdes.2010.01.004. Disponível em: <http://www.sciencedirect.com/science/article/pii/S026130691000018X>. Advanced Component Manufacture from Light Materials International Conference on Materials for Advanced Technologies 2009.

[90] SERRA, G., MORAIS, L., ELIAS, C. N., et al. "Nanostructured severe plastic deformation processed titanium for orthodontic mini-implants", *Materials Science and Engineering: C*, v. 33, n. 7, pp. 4197 – 4202, 2013. ISSN: 0928-4931. doi: http://dx.doi.org/10.1016/j.msec.2013.06.012. Disponível em: <http://www.sciencedirect.com/science/article/pii/S0928493113003718>.

[91] VINOGRADOV, A., STOLYAROV, V., HASHIMOTO, S., et al. "Cyclic behavior of ultrafine-grain titanium produced by severe plastic deformation", *Materials Science and Engineering: A*, v. 318, n. 1–2, pp. 163 – 173, 2001. ISSN: 0921-5093. doi: http://dx.doi.org/10.1016/S0921-5093(01)01262-X. Disponível em: <http://www.sciencedirect.com/science/article/pii/S092150930101262X>.

[92] XIRONG, Y., XICHENG, Z., WENJIE, F. "Deformed Microstructures and Mechanical Properties of CP-Ti Processed by Multi-Pass {ECAP} at Room Temperature", *Rare Metal Materials and Engineering*, v. 38, n. 6, pp. 955 – 957, 2009. ISSN: 1875-5372. doi: http://dx.doi.org/10.1016/S1875-5372(10)60039-2. Disponível em: <http://www.sciencedirect.com/science/article/pii/S1875537210600392>.

[93] GUNDEROV, D., POLYAKOV, A., SEMENOVA, I., et al. "Evolution of microstructure, macrotexture and mechanical properties of commercially pure Ti during ECAP-conform processing and drawing", *Materials Science and Engineering: A*, v. 562, n. 0, pp. 128 – 136, 2013. ISSN: 0921-5093. doi: http://dx.doi.org/10.1016/j.msea.2012.11.007. Disponível em: <http://www.sciencedirect.com/science/article/pii/S0921509312015559>.

[94] FIGUEIREDO, R. B., LANGDON, T. G. "Principles of grain refinement and superplastic flow in magnesium alloys processed by {ECAP}", *Materials Science and Engineering: A*, v. 501, n. 1–2, pp. 105 – 114, 2009. ISSN: 0921-5093. doi: http://dx.doi.org/10.1016/j.msea.2008.09.058. Disponível em: <http://www.sciencedirect.com/science/article/pii/S0921509308011386>.

[95] ZHU, Y., LANGDON, T. "The fundamentals of nanostructured materials processed by severe plastic deformation", *JOM*, v. 56, n. 10, pp. 58–63, 2004. ISSN: 1047-4838. doi: 10.1007/s11837-004-0294-0. Disponível em: <http://dx.doi.org/10.1007/s11837-004-0294-0>.

[96] DE OLIVEIRA CAMPOS, F., DE CASTRO MONTE SCHRODER, F., ARAUJO, A. C., et al. "Cutting Forces and Mechanical Resistance of Pure Titanium Processed by Equal Channel Angular Pressing", *Procedia CIRP*, v. 46, pp. 222 – 225, 2016. ISSN: 2212-8271. doi: https://doi.org/10.1016/j.procir.2016.04.038. Disponível em: <http://www.sciencedirect.com/science/article/pii/S2212827116301937>. 7th HPC 2016 – CIRP Conference on High Performance Cutting.

[97] GU, D., HAGEDORN, Y.-C., MEINERS, W., et al. "Densification behavior, microstructure evolution, and wear performance of selective laser melting processed commercially pure titanium", *Acta Materialia*, v. 60, n. 9, pp. 3849 – 3860, 2012. ISSN: 1359-6454. doi: http://dx.doi.org/10.1016/j.actamat.2012.04.006. Disponível em: <http://www.sciencedirect.com/science/article/pii/S1359645412002522>.

[98] THOMAS, D. *The Development of Design Rules for Selective Laser Melting*. Tese de Doutorado, University of Wales Institute, Cardiff., 2009.

[99] I. GIBSON, D.W. ROSEN, B. S. *Additive Manufacturing Technologies: Rapid Prototyping to Direct Digital Manufacturing*. Springer, 2010. ISBN: 1441911197.

[100] THIJS, L., VERHAEGHE, F., CRAEGHS, T., et al. "A study of the microstructural evolution during selective laser melting of Ti–6Al–4V", *Acta Materialia*, v. 58, n. 9, pp. 3303 – 3312, 2010. ISSN: 1359-6454. doi: https://doi.org/10.1016/j.actamat.2010.02.004. Disponível em: <http://www.sciencedirect.com/science/article/pii/S135964541000090X>.

[101] SIMONELLI, M. *Microstructure evolution and mechanical properties of selective laser melted Ti-6Al-4V*. Tese de Doutorado, Loughborough University., Madison, 2014.

[102] PATTANAYAK, D. K., FUKUDA, A., MATSUSHITA, T., et al. "Bioactive Ti metal analogous to human cancellous bone: Fabrication by selective laser melting and chemical treatments", *Acta Biomaterialia*, v. 7, n. 3, pp. 1398 – 1406, 2011. ISSN: 1742-7061. doi: https://doi.org/10.1016/j.actbio.2010.09.034. Disponível em: <http://www.sciencedirect.com/science/article/pii/S1742706110004447>.

[103] GU, D., SHEN, Y. "Balling phenomena in direct laser sintering of stainless steel powder: Metallurgical mechanisms and control methods", *Materials & Design*, v. 30, n. 8, pp. 2903 – 2910, 2009. ISSN: 0261-3069. doi: https:

//doi.org/10.1016/j.matdes.2009.01.013. Disponível em: <http://www.sciencedirect.com/science/article/pii/S0261306909000181>.

[104] ATTAR, H., PRASHANTH, K., CHAUBEY, A., et al. "Comparison of wear properties of commercially pure titanium prepared by selective laser melting and casting processes", *Materials Letters*, v. 142, pp. 38 – 41, 2015. ISSN: 0167-577X. doi: https://doi.org/10.1016/j.matlet.2014.11.156. Disponível em: <http://www.sciencedirect.com/science/article/pii/S0167577X14021594>.

[105] CHEN, J., ZHANG, Z., CHEN, X., et al. "Design and manufacture of customized dental implants by using reverse engineering and selective laser melting technology", *The Journal of Prosthetic Dentistry*, v. 112, n. 5, pp. 1088 – 1095.e1, 2014. ISSN: 0022-3913. doi: https://doi.org/10.1016/j.prosdent.2014.04.026. Disponível em: <http://www.sciencedirect.com/science/article/pii/S0022391314002406>.

[106] BARBAS, A., BONNET, A.-S., LIPINSKI, P., et al. "Development and mechanical characterization of porous titanium bone substitutes", *Journal of the Mechanical Behavior of Biomedical Materials*, v. 9, pp. 34 – 44, 2012. ISSN: 1751-6161. doi: https://doi.org/10.1016/j.jmbbm.2012.01.008. Disponível em: <http://www.sciencedirect.com/science/article/pii/S1751616112000288>.

[107] ZHANG, S., WEI, Q., CHENG, L., et al. "Effects of scan line spacing on pore characteristics and mechanical properties of porous Ti6Al4V implants fabricated by selective laser melting", *Materials & Design*, v. 63, pp. 185 – 193, 2014. ISSN: 0261-3069. doi: https://doi.org/10.1016/j.matdes.2014.05.021. Disponível em: <http://www.sciencedirect.com/science/article/pii/S0261306914003902>.

[108] MONTEVECCHI, F., GROSSI, N., TAKAGI, H., et al. "Cutting Forces Analysis in Additive Manufactured AISI H13 Alloy", *Procedia CIRP*, v. 46, pp. 476 – 479, 2016. ISSN: 2212-8271. doi: https://doi.org/10.1016/j.procir.2016.04.034. Disponível em: <http://www.sciencedirect.com/science/article/pii/S2212827116301895>. 7th HPC 2016 – CIRP Conference on High Performance Cutting.

[109] BRUSCHI, S., TRISTO, G., RYSAVA, Z., et al. "Environmentally clean micromilling of electron beam melted Ti6Al4V", *Journal of Cleaner Production*, v. 133, pp. 932 – 941, 2016. ISSN: 0959-6526. doi: https:

//doi.org/10.1016/j.jclepro.2016.06.035. Disponível em: <http://www.sciencedirect.com/science/article/pii/S0959652616307107>.

[110] RYSAVA, Z., BRUSCHI, S., CARMIGNATO, S., et al. "Micro-drilling and Threading of the Ti6Al4V Titanium Alloy Produced through Additive Manufacturing", *Procedia CIRP*, v. 46, pp. 583 – 586, 2016. ISSN: 2212-8271. doi: https://doi.org/10.1016/j.procir.2016.04.030. Disponível em: <http://www.sciencedirect.com/science/article/pii/S2212827116301858>. 7th HPC 2016 – CIRP Conference on High Performance Cutting.

[111] KHORASANI, A. M., GIBSON, I., CHEGINI, N. G., et al. "An improved static model for tool deflection in machining of Ti–6Al–4V acetabular shell produced by selective laser melting", *Measurement*, v. 92, pp. 534 – 544, 2016. ISSN: 0263-2241. doi: https://doi.org/10.1016/j.measurement.2016.06.031. Disponível em: <http://www.sciencedirect.com/science/article/pii/S0263224116303128>.

[112] POLISHETTY, A., SHUNMUGAVEL, M., GOLDBERG, M., et al. "Cutting Force and Surface Finish Analysis of Machining Additive Manufactured Titanium Alloy Ti-6Al-4V", *Procedia Manufacturing*, v. 7, pp. 284 – 289, 2017. ISSN: 2351-9789. doi: https://doi.org/10.1016/j.promfg.2016.12.071. Disponível em: <http://www.sciencedirect.com/science/article/pii/S2351978916302347>. International Conference on Sustainable Materials Processing and Manufacturing, SMPM 2017, 23-25 January 2017, Kruger.

[113] BONAITI, G., PARENTI, P., ANNONI, M., et al. "Micro-milling Machinability of DED Additive Titanium Ti-6Al-4V", *Procedia Manufacturing*, v. 10, pp. 497 – 509, 2017. ISSN: 2351-9789. doi: https://doi.org/10.1016/j.promfg.2017.07.104. Disponível em: <http://www.sciencedirect.com/science/article/pii/S2351978917302871>. 45th SME North American Manufacturing Research Conference, NAMRC 45, LA, USA.

[114] SILVA, M. V. A. *Consolidação de pós de Titânio via Extrusão Angular em Canal*. Tese de Doutorado, Universidade Federal do Rio de Janeiro, 2016.

[115] MOTYKA, M., KUBIAK, K., SIENIAWSKI, J., et al. "Hot Plasticity of Alpha Beta Alloys". In: Amin, A. N. (Ed.), *Titanium Alloys - Towards Achieving Enhanced Properties for Diversified Applications*, InTech, cap. 5, Rijeka, 2012. doi: 10.5772/34806. Disponível em: <http://dx.doi.org/10.5772/34806>.

[116] FROUM, S. *Dental Implant Complications: Etiology, Prevention, and Treatment*. John Wiley & Sons, 2016.

Appendix A

Grooves images

This appendix presents the scanning electron microscope images of the machined grooves after the micromilling experiments for all the materials studies in this work, including both batches, A and B.

They are presented as follows:

- Figure A.1 - grooves for batch A of micromilling standard commercially pure titanium grade 2;
- Figure A.2 - grooves for batch A of micromilling standard Ti-6Al-4V alloy;
- Figure A.3 - grooves for batch A of micromilling commercially pure titanium grade 2 processed by equal channel angular pressing;
- Figure A.4 - grooves for batch A of micromilling Ti-6Al-4V alloy produced by selective laser melting;
- Figure A.5 - grooves for batch B of micromilling standard commercially pure titanium grade 2;
- Figure A.6 - grooves for batch B of micromilling standard Ti-6Al-4V alloy;
- Figure A.7 - grooves for batch B of micromilling commercially pure titanium grade 2 processed by equal channel angular pressing;
- Figure A.8 - grooves for batch B of micromilling Ti-6Al-4V alloy produced by selective laser melting;

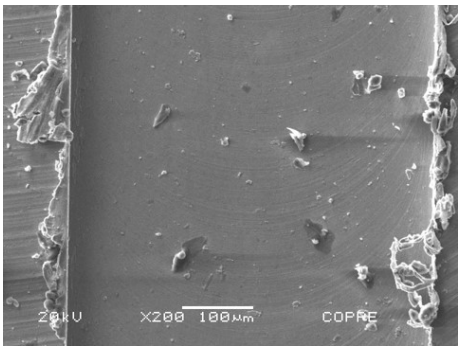

(a) $f_t = 0.5$ μm.

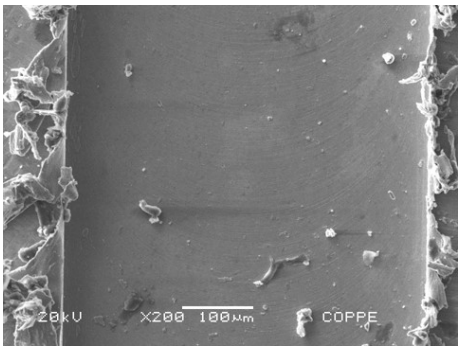

(b) $f_t = 1.0$ μm.

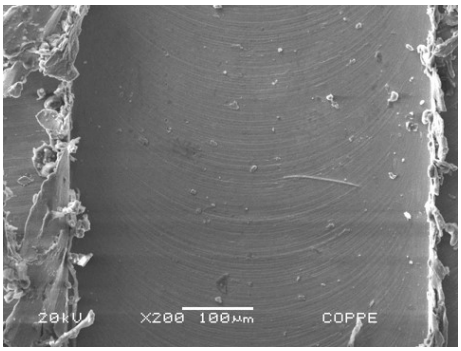

(c) $f_t = 1.5$ μm.

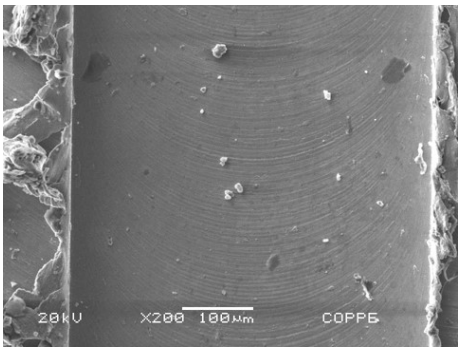

(d) $f_t = 2.0$ μm.

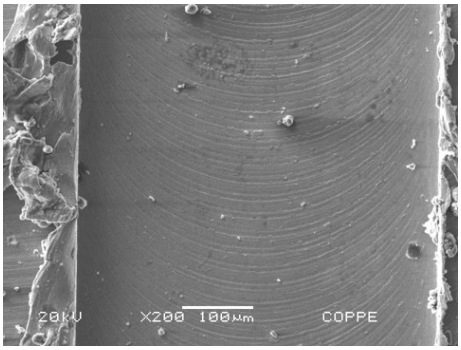

(e) $f_t = 2.5$ μm.

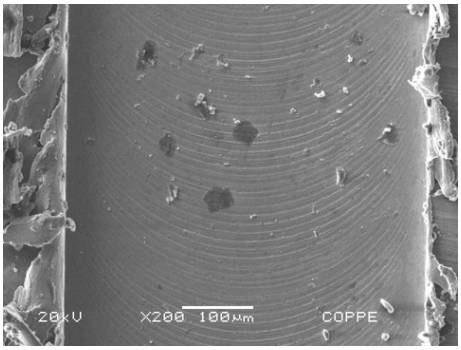

(f) $f_t = 3.0$ μm.

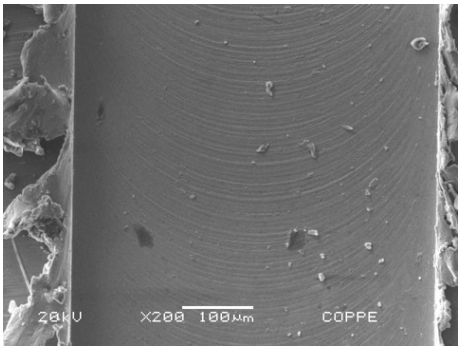

(g) $f_t = 3.5$ μm.

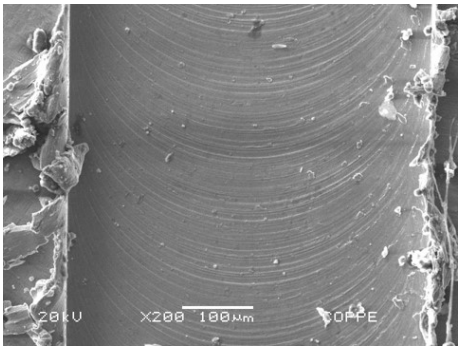

(h) $f_t = 4.0$ μm.

Figure A.1: Groove SEM images for standard CP-Ti for batch A experiments.

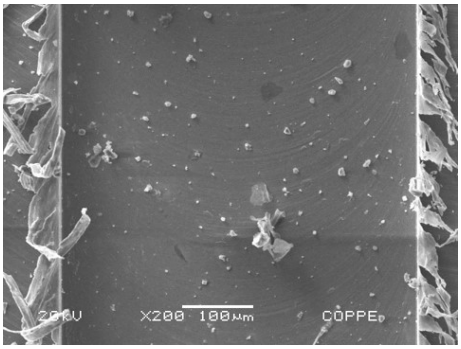

(a) $f_t = 0.5$ μm.

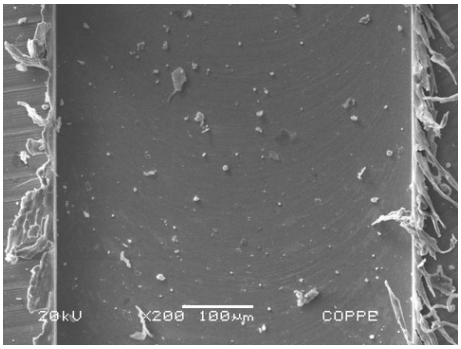

(b) $f_t = 1.0$ μm.

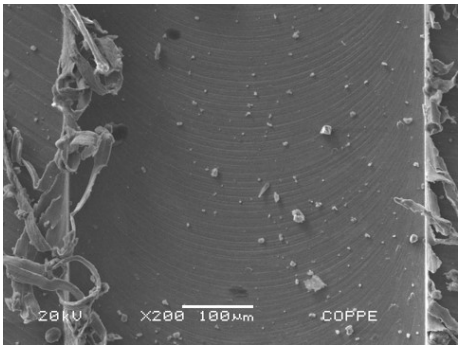

(c) $f_t = 1.5$ μm.

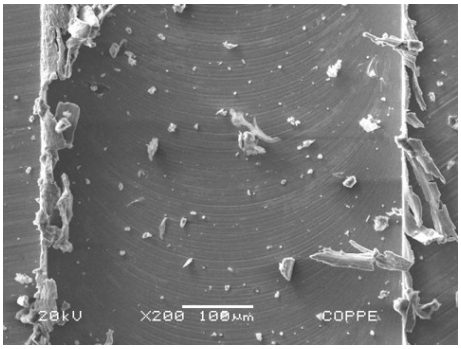

(d) $f_t = 2.0$ μm.

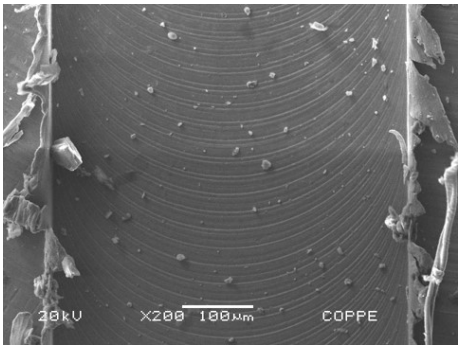

(e) $f_t = 2.5$ μm.

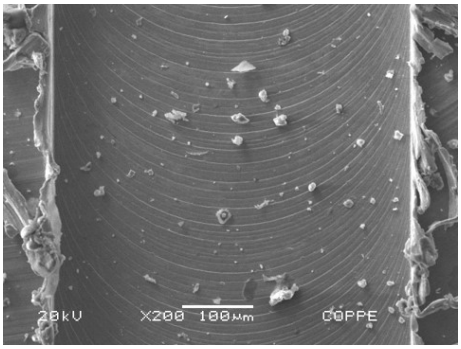

(f) $f_t = 3.0$ μm.

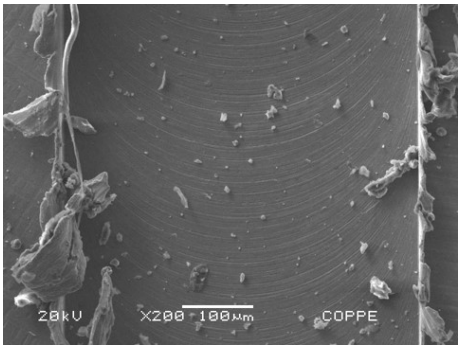

(g) $f_t = 3.5$ μm.

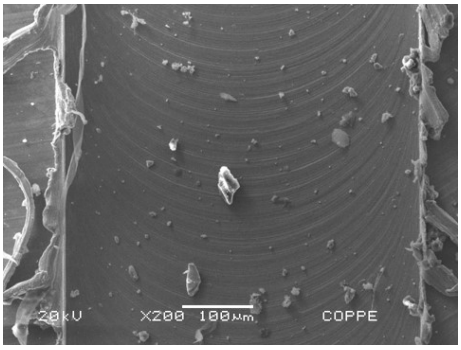

(h) $f_t = 4.0$ μm.

Figure A.2: Groove SEM images for standard Ti-6Al-4V alloy for batch A experiments.

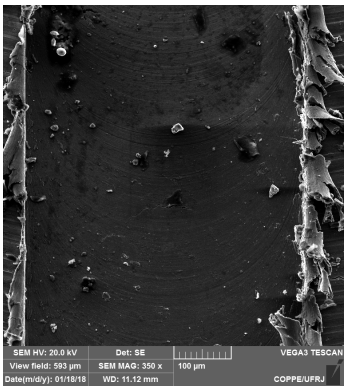

(a) $f_t = 0.5$ μm.

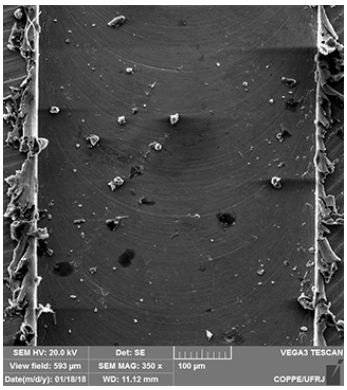

(b) $f_t = 1.0$ μm.

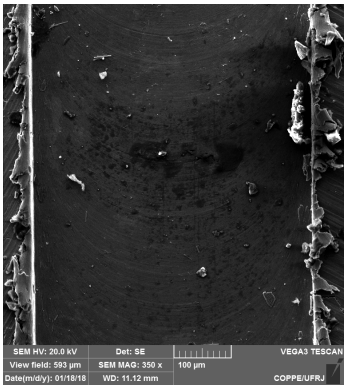

(c) $f_t = 1.5$ μm.

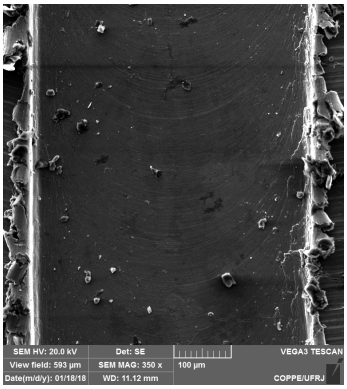

(d) $f_t = 2.0$ μm.

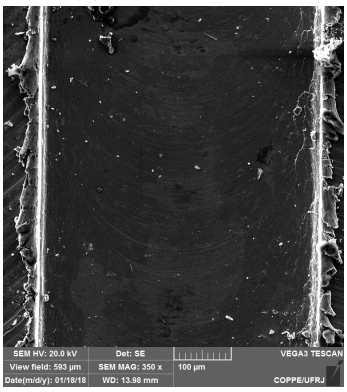

(e) $f_t = 2.5$ μm.

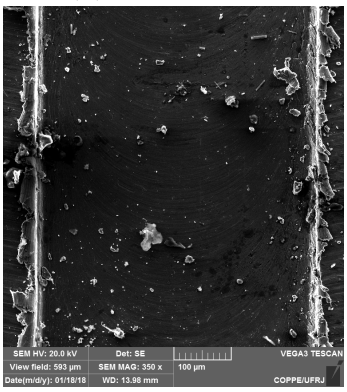

(f) $f_t = 3.0$ μm.

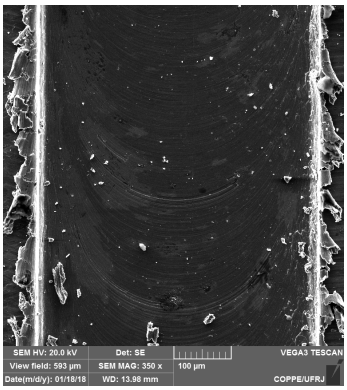

(g) $f_t = 3.5$ μm.

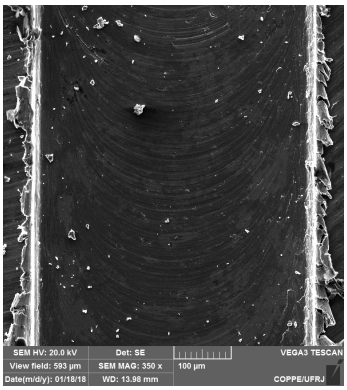

(h) $f_t = 4.0$ μm.

Figure A.3: Groove SEM images for CP-Ti processed by ECAP for batch A experiments.

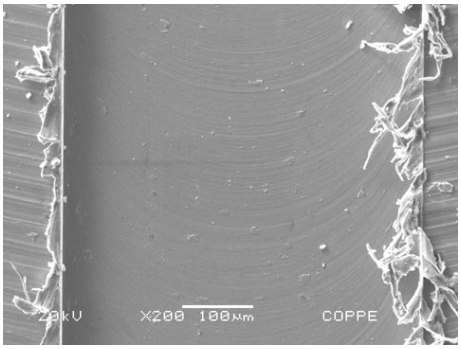

(a) $f_t = 0.5$ μm.

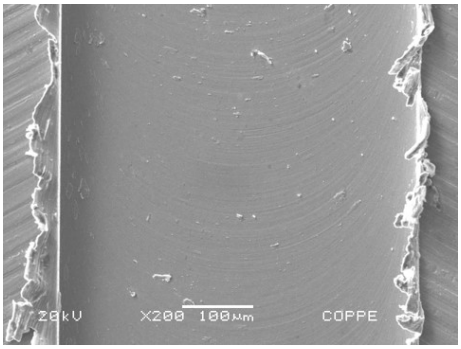

(b) $f_t = 1.0$ μm.

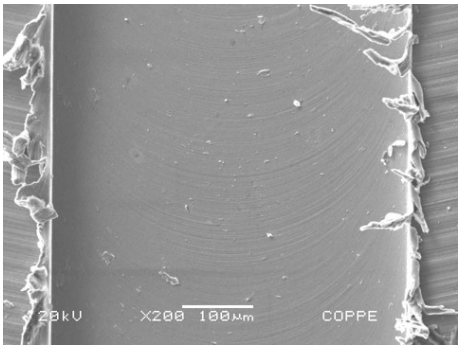

(c) $f_t = 1.5$ μm.

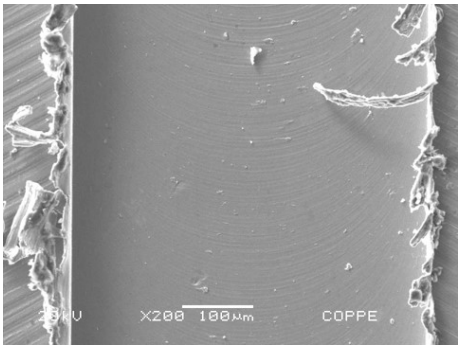

(d) $f_t = 2.0$ μm.

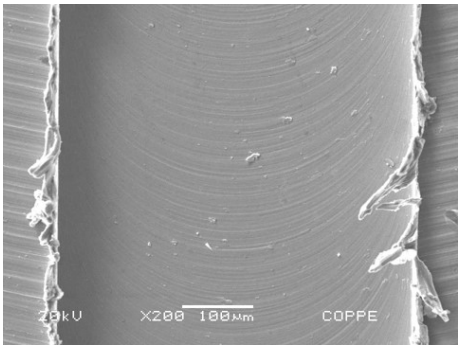

(e) $f_t = 2.5$ μm.

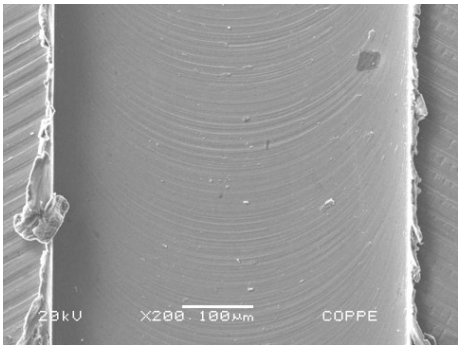

(f) $f_t = 3.0$ μm.

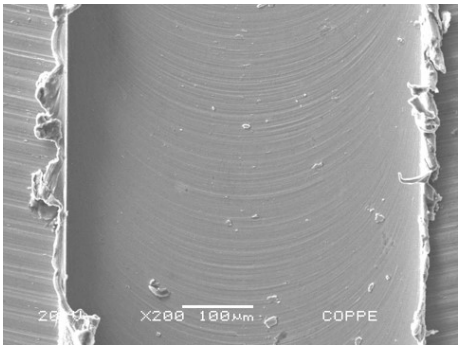

(g) $f_t = 3.5$ μm.

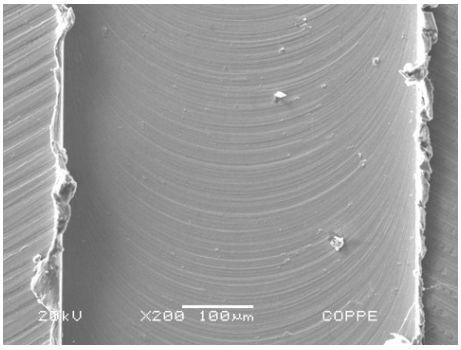

(h) $f_t = 4.0$ μm.

Figure A.4: Groove SEM images for Ti-6Al-4V alloy produced by SLM for batch A experiments.

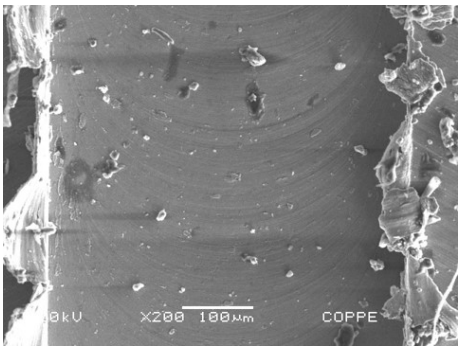

(a) $f_t = 0.5$ μm.

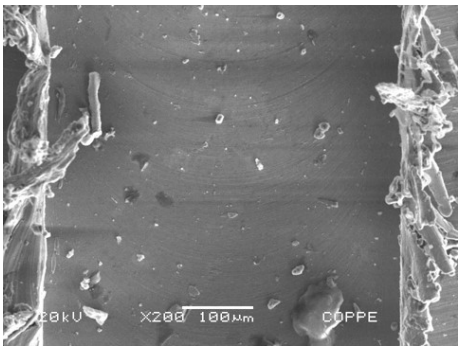

(b) $f_t = 1.0$ μm.

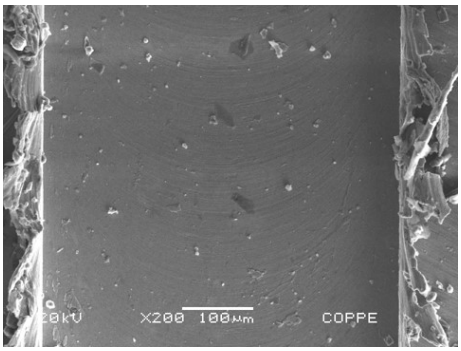

(c) $f_t = 1.5$ μm.

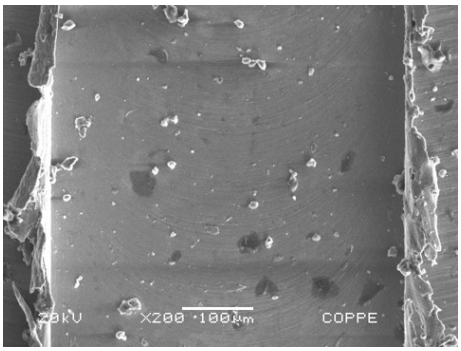

(d) $f_t = 2.0$ μm.

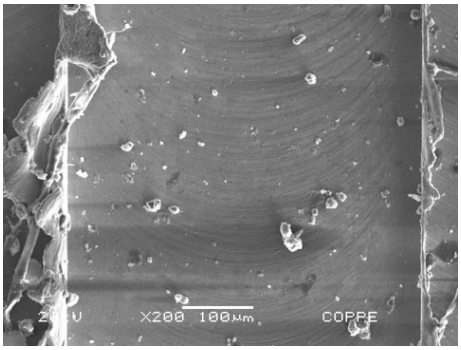

(e) $f_t = 2.5$ μm.

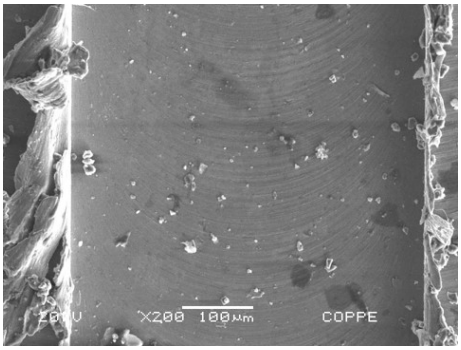

(f) $f_t = 3.0$ μm.

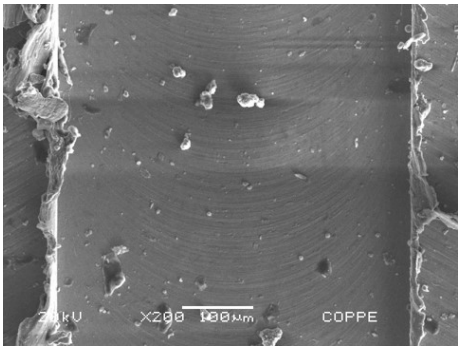

(g) $f_t = 3.5$ μm.

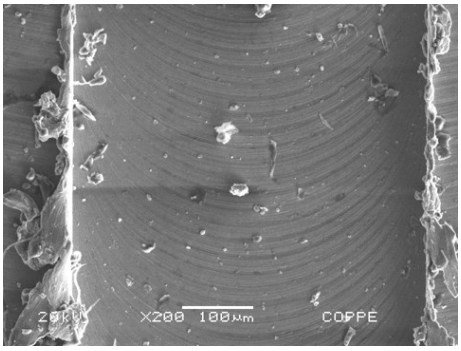

(h) $f_t = 4.0$ μm.

Figure A.5: Groove SEM images for standard CP-Ti for batch B experiments.

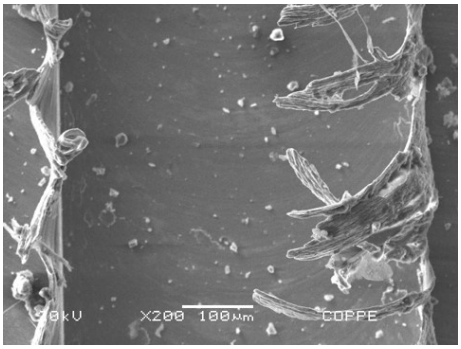

(a) $f_t = 0.5$ μm.

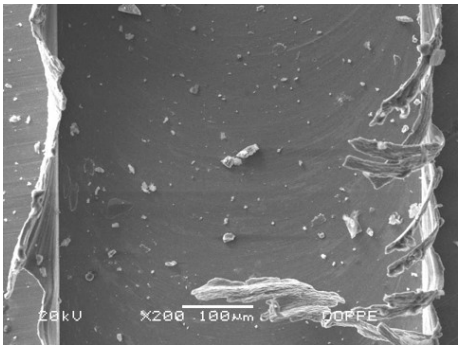

(b) $f_t = 1.0$ μm.

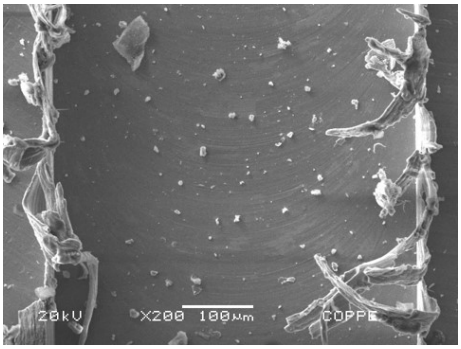

(c) $f_t = 1.5$ μm.

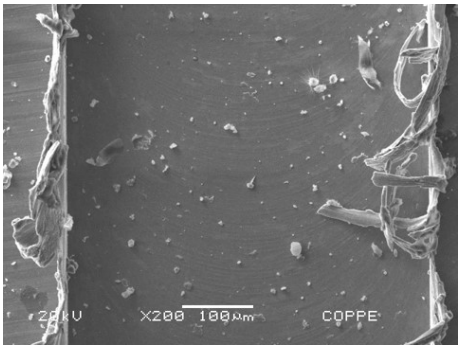

(d) $f_t = 2.0$ μm.

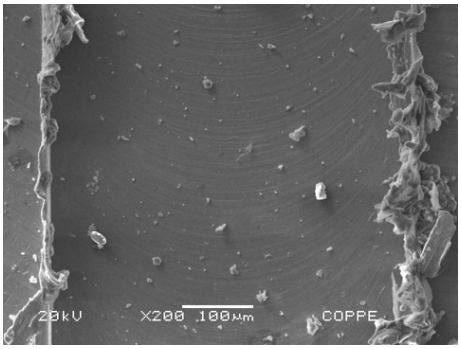

(e) $f_t = 2.5$ μm.

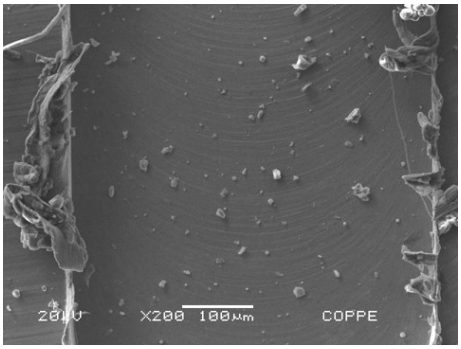

(f) $f_t = 3.0$ μm.

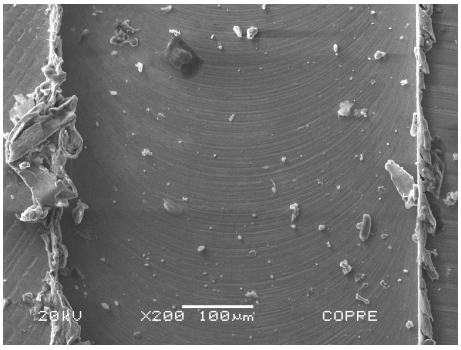

(g) $f_t = 3.5$ μm.

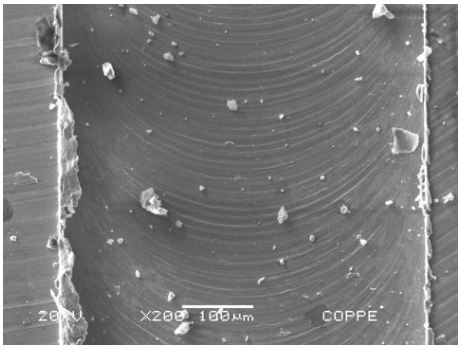

(h) $f_t = 4.0$ μm.

Figure A.6: Groove SEM images for standard Ti-6Al-4V alloy for batch B experiments.

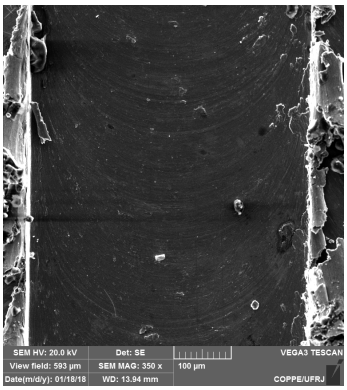

(a) $f_t = 0.5$ μm.

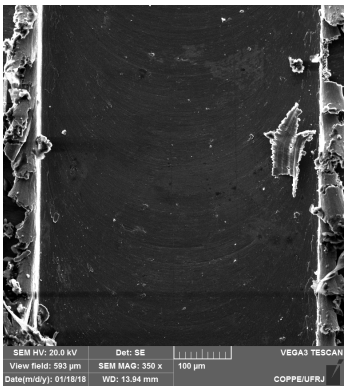

(b) $f_t = 1.0$ μm.

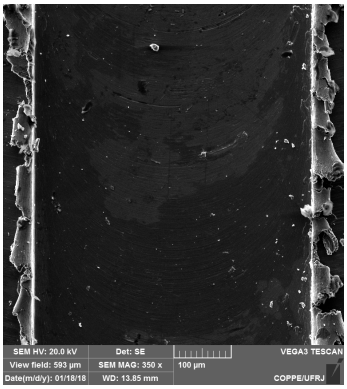

(c) $f_t = 1.5$ μm.

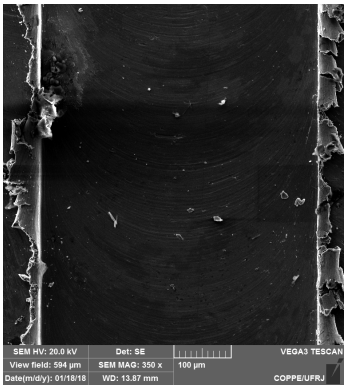

(d) $f_t = 2.0$ μm.

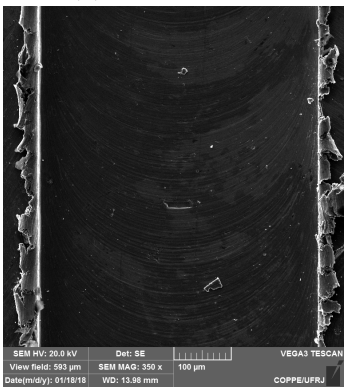

(e) $f_t = 2.5$ μm.

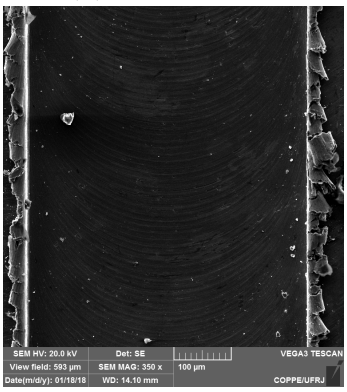

(f) $f_t = 3.0$ μm.

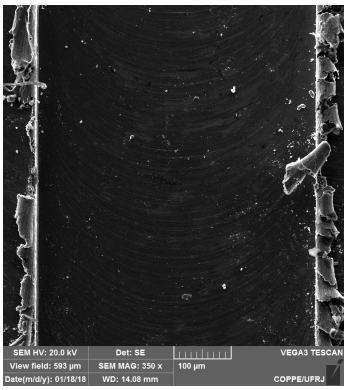

(g) $f_t = 3.5$ μm.

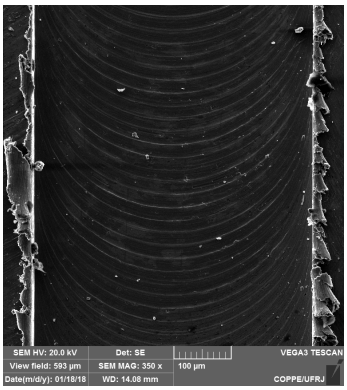

(h) $f_t = 4.0$ μm.

Figure A.7: Groove SEM images for CP-Ti processed by ECAP for batch B experiments.

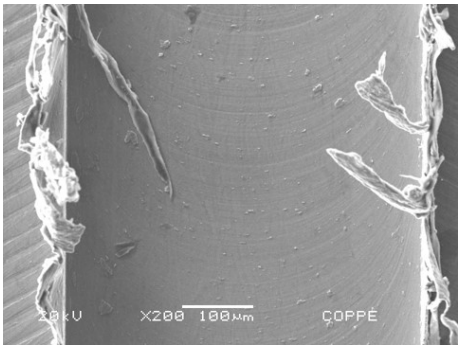

(a) $f_t = 0.5$ μm.

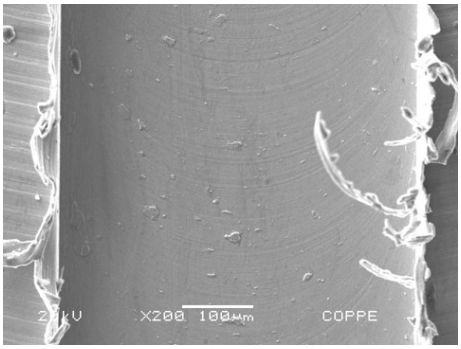

(b) $f_t = 1.0$ μm.

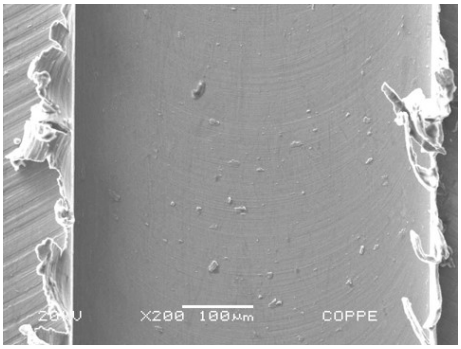

(c) $f_t = 1.5$ μm.

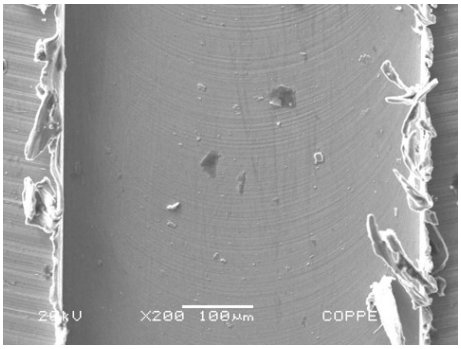

(d) $f_t = 2.0$ μm.

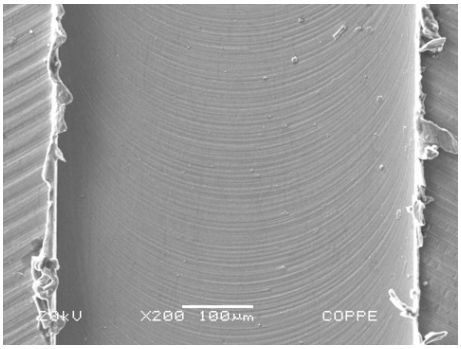

(e) $f_t = 2.5$ μm.

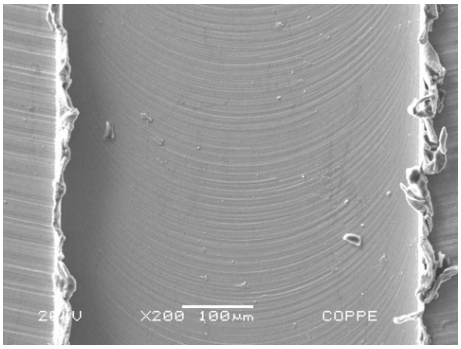

(f) $f_t = 3.0$ μm.

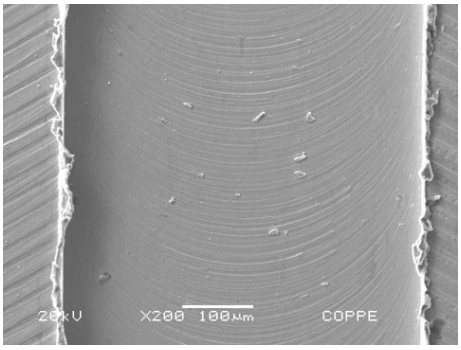

(g) $f_t = 3.5$ μm.

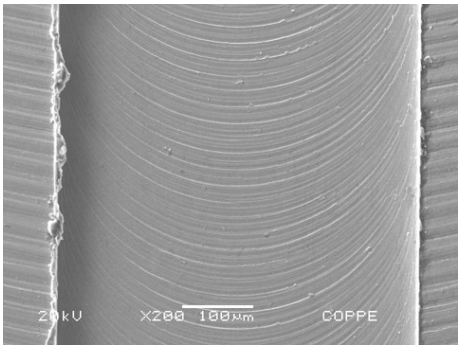

(h) $f_t = 4.0$ μm.

Figure A.8: Groove SEM images for Ti-6Al-4V alloy produced by SLM for batch B experiments.

Appendix B

Microchips images

This appendix presents the optical microscope images of the microchips collected during the micromilling experiments for all the materials studies in this work.

They are presented as follows:

- Figure B.1 - microchips of standard commercially pure titanium grade 2;
- Figure B.2 - microchips of standard Ti-6Al-4V alloy;
- Figure B.3 - microchips of commercially pure titanium grade 2 processed by equal channel angular pressing;
- Figure B.4 - microchips of Ti-6Al-4V alloy produced by selective laser melting.

(a) $f_t = 0.5$ μm.

(b) $f_t = 1.0$ μm.

(c) $f_t = 1.5$ μm.

(d) $f_t = 2.0$ μm.

(e) $f_t = 2.5$ μm.

(f) $f_t = 3.0$ μm.

(g) $f_t = 3.5$ μm.

(h) $f_t = 4.0$ μm.

Figure B.1: Chips analysis for standard CP-Ti.

(a) $f_t = 0.5$ μm.

(b) $f_t = 1.0$ μm.

(c) $f_t = 1.5$ μm.

(d) $f_t = 2.0$ μm.

(e) $f_t = 2.5$ μm.

(f) $f_t = 3.0$ μm.

(g) $f_t = 3.5$ μm.

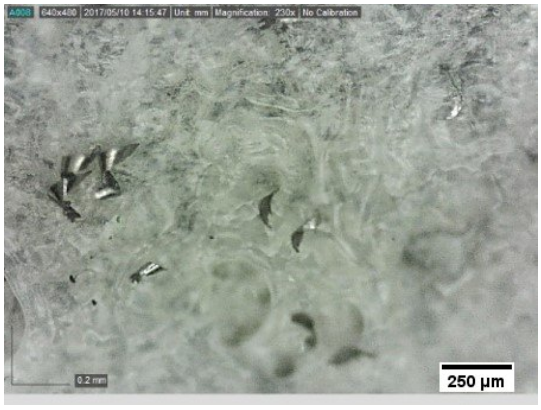

(h) $f_t = 4.0$ μm.

Figure B.2: Chips analysis for standard Ti-6Al-4V.

(a) $f_t = 0.5$ μm.

(b) $f_t = 1.0$ μm.

(c) $f_t = 1.5$ μm.

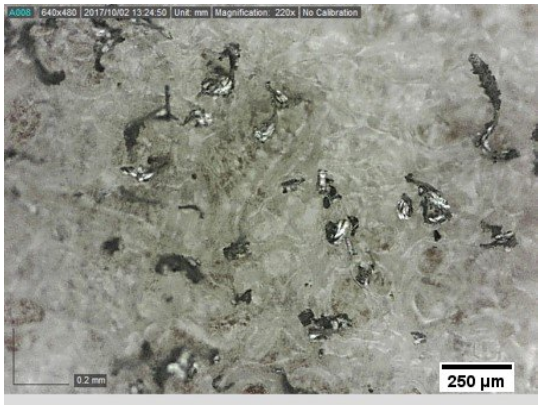

(d) $f_t = 2.0$ μm.

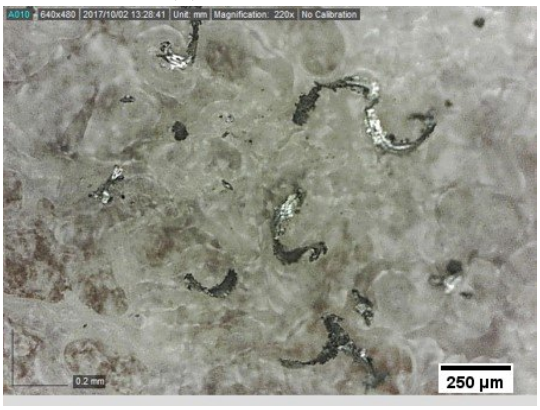

(e) $f_t = 2.5$ μm.

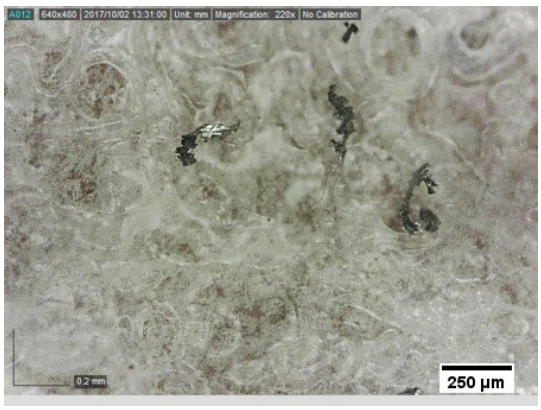

(f) $f_t = 3.0$ μm.

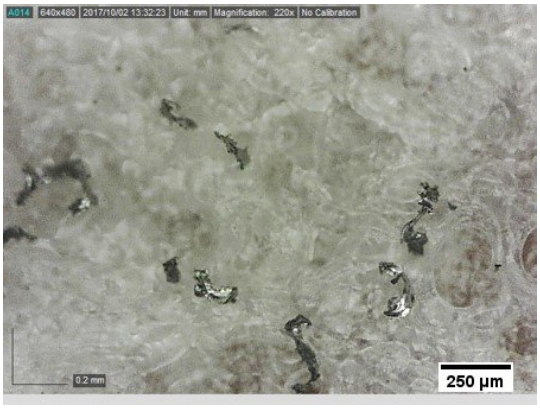

(g) $f_t = 3.5$ μm.

(h) $f_t = 4.0$ μm.

Figure B.3: Chips analysis for CP-Ti processes by ECAP.

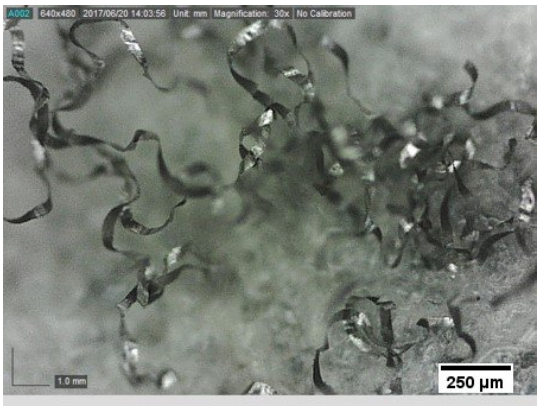

(a) $f_t = 0.5$ μm.

(b) $f_t = 1.0$ μm.

(c) $f_t = 1.5$ μm.

(d) $f_t = 2.0$ μm.

(e) $f_t = 2.5$ μm.

(f) $f_t = 3.0$ μm.

(g) $f_t = 3.5$ μm.

(h) $f_t = 4.0$ μm.

Figure B.4: Chips analysis for Ti-6Al-4V produced by SLM.